AD

USAAVLABS TECHNICAL REPORT 70-36

MECHANISMS OF SAND AND DUST EROSION IN GAS TURBINE ENGINES

C. E. Smeltzer
M. E. Gulden
S. S. McElmurry
W. A. Compton

August 1970

U. S. ARMY AVIATION MATERIEL LABORATORIES
FORT EUSTIS, VIRGINIA

CONTRACT DAAJ02-68-C-0056

SOLAR DIVISION OF INTERNATIONAL HARVESTER COMPANY
SAN DIEGO, CALIFORNIA

DISCLAIMERS

The findings in this report are not to be construed as an official Department of the Army position unless so designated by other authorized documents.

When Government drawings, specifications, or other data are used for any purpose other than in connection with a definitely related Government procurement operation, the United States Government thereby incurs no responsibility nor any obligation whatsoever; and the fact that the Government may have formulated, furnished, or in any way supplied the said drawings, specifications, or other data is not to be regarded by implication or otherwise as in any manner licensing the holder or any other person or corporation, or conveying any rights or permission, to manufacture, use, or sell any patented invention that may in any way be related thereto.

Unclassified

Security Classification

DOCUMENT CONTROL DATA - R & D

(Security classification of title, body of abstract and indexing annotation must be entered when the overall report is classified)

1. ORIGINATING ACTIVITY *(Corporate author)*
Solar Division of International Harvester Company
San Diego, California

2a. REPORT SECURITY CLASSIFICATION
Unclassified

2b. GROUP

3. REPORT TITLE
MECHANISMS OF SAND AND DUST EROSION IN GAS TURBINE ENGINES

4. DESCRIPTIVE NOTES *(Type of report and inclusive dates)*
Final Report July 1968 - December 1969

5. AUTHOR(S) *(First name, middle initial, last name)*
Charles E. Smeltzer Scott S. McElmury
Mary E. Gulden William A. Compton

6. REPORT DATE	7a. TOTAL NO. OF PAGES	7b. NO. OF REFS
August 1970	293	30

8a. CONTRACT OR GRANT NO.
DAAJ02-68-C-0056

b. PROJECT NO.
Task 1G162203D14413

c.

d.

9a. ORIGINATOR'S REPORT NUMBER(S)
USAAVLABS Technical Report 70-36

9b. OTHER REPORT NO(S) *(Any other numbers that may be assigned this report)*
Solar Report Number RDR 1625-6

10. DISTRIBUTION STATEMENT
This document is subject to special export controls, and each transmittal to foreign governments or foreign nationals may be made only with prior approval of U. S. Army Aviation Materiel Laboratories, Fort Eustis, Virginia 23604.

11. SUPPLEMENTARY NOTES

12. SPONSORING MILITARY ACTIVITY
U. S. Army Aviation Materiel Laboratories
Fort Eustis, Virginia

13. ABSTRACT
This program emphasizes the materials science approach to understanding ductile erosion mechanisms. The first part is experimental, studying the effects upon solid-particle erosion of pertinent material and environmental variables; namely, target alloy composition, strength level, and imposed strain; dust particle variety, size, concentration, velocity, and kinetic energy; and carrier-gas composition, impingement angle, and true temperature. Erosion test conditions simulate erosive environments encountered in gas turbine service. Experimental erosion data are compared with weight losses predicted by existing theories on particulate erosion. The second part is diagnostic, a study of visible phenomena associated with the erosion processes using electron microscopy. Phenomenological evidence obtained from the erosion surfaces and erosion products is used to define (probable) physical models of the ductile erosion mechanism. A mathemathical model for the ductile erosion mechanism has been developed also. Important mechanism-related findings are: For a given erosion system, erosion per particle is directly proportional to particle kinetic energy ($\propto Mu^2$). The efficiency of available energy utilization by the erosion process is a function of dust particle variety and impingement angle, but not of engineering strength, for a given target material. The efficacy of (particle) energy translation into the metal removal process remains constant over wide ranges of particle mass and particle energy. Erosion thresholds have been identified, indicating a certain minimum particle energy is require to activate the erosion mechanism. The energy absorbed by the target is translated into both metal deformation and metal removal, the metal deformed (per impact) typically being 300-400 times greater in volume than that removed or eroded. Two mechanisms of erosion have been induced from evidence of intense heat and pressure. The first is the splattering of sub-micron-size droplets of molten target metal. The second is the mechanical bonding of highly plastic target metal to the particle surface.

DD FORM 1 NOV 68 1473 REPLACES DD FORM 1473, 1 JAN 64, WHICH IS OBSOLETE FOR ARMY USE.

Unclassified

Security Classification

14. KEY WORDS	LINK A		LINK B		LINK C	
	ROLE	WT	ROLE	WT	ROLE	WT
Ductile erosion mechanisms						
Solid-particle erosion						
Gas turbine engines						
Target alloy composition						
Engineering variables						
Erosive environments						

DDC REPORT BIBLIOGRAPHY SEARCH CONTROL NO. /JOANE

AD-876 584 21/5
SOLAR SAN DIEGO CALIF

MECHANISMS OF SAND AND DUST EROSION IN GAS TURBINE ENGINES. (U)

DESCRIPTIVE NOTE: FINAL REPT. JUL 68-DEC 69,
AUG 70 295P SMELTZER,CHARLES E. ;GULDEN, MARY E. ;MCELMURY,SCOTT S. ;COMPTON,WILLIAM A.;
REPT. NO. RDR-1625-6
CONTRACT: DAAJ02-68-C-0056
PROJ: DA-1-G-162203-D-144
TASK: 1-G-162203-D-14413
MONITOR: USAAVLABS TR-70-36

UNCLASSIFIED REPORT

DESCRIPTORS: (*GAS TURBINES, INGESTION(ENGINES)), DUST, SAND, ENVIRONMENTAL TESTS, GAS TURBINE BLADES, EROSION (U)

THE APPROACH TO SOLVING THE PROBLEM OF DUST EROSION HAS BEEN TO STUDY THE MECHANICS OF EROSION (I.E., THE ACTUAL PHYSICAL EVENTS OCCURRING AT THE EROSION SURFACE) AS A LOGICAL MEANS OF IDENTIFYING THE PROPERTIES OF THE BLADE (TARGET) MATERIAL AND THE DUST SUSPENSION THAT CONTROL THE EROSION PROCESSES. THIS EROSION MECHANISM STUDY IS OUTLINED AND DISCUSSED IN THE REPORT. (AUTHOR) (U)

DEPARTMENT OF THE ARMY
HEADQUARTERS US ARMY AVIATION MATERIEL LABORATORIES
FORT EUSTIS, VIRGINIA 23604

The research described herein was conducted by the Solar Division of International Harvester Company, San Diego, California, under U. S. Army Contract DAAJ02-68-C-0056. The work was performed under the technical management of David B. Cale, Propulsion Division, U. S. Army Aviation Materiel Laboratories.

Appropriate technical personnel of this Command have reviewed this report and concur with the conclusions and recommendations contained herein.

The findings outlined herein will be given consideration in the planning of future efforts in the area of sand and dust erosion of gas turbine engines.

Task 1G162203D14413
Contract DAAJ02-68-C-0056
USAAVLABS Technical Report 70-36
August 1970

MECHANISMS OF SAND AND DUST EROSION IN GAS TURBINE ENGINES

Final Report

Solar RDR 1625-6

By

C. E. Smeltzer

M. E. Gulden

S. S. McElmury

W. A. Compton

Prepared by

Solar Division of International Harvester Company
San Diego, California

for

U. S. ARMY AVIATION MATERIEL LABORATORIES
FORT EUSTIS, VIRGINIA

ABSTRACT

This two-part program emphasizes the materials science approach to understanding ductile erosion mechanisms. The first part is an experimental phase, studying the effects upon solid-particle erosion (of compressor hardware) of pertinent material and environmental variables; namely, target alloy composition, strength level, and imposed strain; dust particle variety, size, concentration, velocity, and kinetic energy; and carrier-gas composition, impingement angle, and true temperature. Erosion test conditions were chosen to simulate typical ranges of engineering variables and erosive environments encountered in gas turbine service. Experimental erosion data are compared with calculated weight losses predicted by existing theories on particulate erosion. The second part of the program is a diagnostic phase, programmed to detect and study visible phenomena associated with the erosion processes, using high magnification electron microscopy. Phenomenological evidence obtained from the erosion surfaces and erosion products is used to define (probable) physical models of the ductile erosion mechanism. A mathematical model for the ductile erosion mechanism has been developed also, using information from both the diagnostic and experimental programs.

Important mechanism-related findings are

- For a given erosion system, erosion per particle is directly proportional to particle kinetic energy ($\propto Mu^2$). The apparent efficiency of available energy utilization by the erosion (target metal removal) process is a function of dust particle variety and impingement angle, but not of engineering strength, for a given target material. The efficacy of (particle) energy translation into the metal removal process remains constant over wide ranges of particle mass and particle energy.

- The erosion mechanism ceases to function for fine particles ($\leq 20\mu$) below about 100-200 fps, the exact cutoff velocity depending upon particle variety, size, and target alloy. This erosion threshold suggests that a certain minimum particle energy is necessary to activate the erosion mechanism.

- Corner-oriented particle impacts cause the preponderance of erosion damage to metal targets.

- The energy absorbed by the target is translated into both metal deformation and metal removal, the metal deformed (per impact) typically being 300-400 times greater in volume than that removed or eroded.

- Two probable erosion processes have been induced from the phenomenological study. Both processes rely upon the intense heat generated by kinetic energy conversion on particle impact. The first is the splattering of sub-micron-size droplets of molten target metal from the impact crater. The second is the mechanical bonding of highly plastic target metal to the particle surface.

TABLE OF CONTENTS

TABLE OF CONTENTS (Cont)

LIST OF ILLUSTRATIONS

LIST OF ILLUSTRATIONS (Cont)

LIST OF ILLUSTRATIONS (Cont)

LIST OF ILLUSTRATIONS (Cont)

LIST OF ILLUSTRATIONS (Cont)

LIST OF ILLUSTRATIONS (Cont)

LIST OF ILLUSTRATIONS (Cont)

LIST OF ILLUSTRATIONS (Cont)

LIST OF ILLUSTRATION (Cont)

LIST OF ILLUSTRATIONS (Cont)

LIST OF TABLES

LIST OF TABLES (Cont)

LIST OF SYMBOLS

A	specific turbine engine constant, $mg\mu hr/ft^3$
C	dust concentration, mg/ft^3
C_A	dust concentration: weight striking target surface per unit time, $mg/ft^2/sec$
C_B	dust concentration: number of particles striking target surface per unit time, $particles/ft^2/sec$
C_{std}	dust concentration in ambient air, mg/ft^3
$C_{p,g}$	specific heat of carrier gas, BTU/lb-° F
$C_{p,t}$	specific heat of target, cal/gm-°C
d	dust particle size (diameter or cube edge), μ
d_m	maximum particle diameter, μ
d_p	effective particle diameter assuming a spherical particle, ft
E	average erosion weight loss/single particle impact, $mg \times 10^{-8}$
E_V	average erosion volume loss/single particle impact, $cm^3 \times 10^{-11}$
F	dust particle force exerted on target, lb
g	gravitational constant, ft/sec^2
H_F	latent heat of fusion, cal/gm
J	mechanical equivalent of heat, ft-lb/BTU
K	basic erosion system constant
K_d	systems constant excluding particle size effect
K_M	systems constant including particle mass = $K\rho V_p^n$ = KM when n = 1
$K_{R,1}$	erosion constant for mechanism 1 (splattering) = $\phi(90 \text{ deg})\eta/Q$, gm/ft-lb

$K_{R,2}$	erosion constant for mechanism 2 (bonding) = $\phi(90 \text{ deg})\zeta/Q$ gm/ft-lb
K_u	systems constant including velocity = $K\rho u^m$
k	systems constant for brittle targets
L	turbine engine life, hr
l	penetration of initial particle contact below target surface, cm
M	mass of dust particle, mg
m	exponent of particle velocity
N	total weight of dust ingested, mg
n	exponent of dust particle volume
P	gas pressure, atm or psi
P_1	standard air pressure, atm or psi
P_s	static gas pressure in test chamber, psi
P_T	total gas pressure in Kiel probe, mm of Hg or psi
Q	energy required to melt 1 gram of target, cal
q	exponent of particle size
Re	Reynolds number
r	dust particle radius, μ
S	nozzle length, ft
S_o	$U\tau$, gas velocity times time constant (particle range, ft)
T	temperature of gas stream, °F
T_1	standard air temperature, °F
U	gas velocity, fps

u	particle velocity, fps
u_h	residual horizontal component of particle velocity after impact, fps
u_{th}	threshold velocity below which erosion stops, fps
V_g	gas volume, ft^3
V_p	median particle volume, cm^3
W	weight of target melted by mass N, gm
W_R	total weight of target removed by all erosion mechanisms, gm
$W_{R,1}$	weight of target removed by splattering, gm
$W_{R,2}$	weight of target removed by bonding, gm
X	flow parameter of the Weibull fracture strength distribution
x	exponent of velocity ratio
y	exponent of particle kinetic energy parameter
α	dust particle impingement angle, deg
α_1	compressor air inlet angle, deg
β_1	compressor blade inlet angle, deg
β_2	compressor blade outlet angle, deg
γ	ratio of specific heats of the carrier gas at constant pressure and volume
δ	energy needed to remove a unit volume of target material (cutting wear)
ζ	fraction of melted target material that escapes by bonding to dust particle
η	fraction of splattered material that escapes the target surface
ϵ	erosion factor: target weight loss/weight of dust impacted, mg/gm

ϵ_V	volume erosion factor: target volume loss/weight of dust impacted, cm^3/gm
ϵ_1	erosion factor due to splattering, mg/gm
ϵ_2	erosion factor due to bonding, mg/gm
θ	compressor blade camber angle, $\beta_1 - \beta_2$
λ	ratio of particle velocity to carrier-gas velocity
μ_{air}	absolute viscosity of air, lb/hr-ft
ξ	energy needed to remove a unit volume of target material (deformation wear)
ρ	density of dust particle, gm/cm^3
ρ_{air}	density of air, lb/ft^3
σ	minimum flow stress of target, psi
τ	time constant: $\rho d_p^2/18\mu_{air}$, msec
ϕ	probability that a dust particle will be snagged by the target
ψ	probability for splattering the molten target metal

INTRODUCTION

Small gas turbines powering helicopters, hovercraft, etc., over dusty, unimproved land areas routinely ingest up to 25 pounds of sand and dust every hour of low-altitude operation. Consequently, many billions of high-velocity, abrasive dust particles impact the critical airfoil surfaces of compressor blades and vanes every hour, eroding away the thin metal tips and trailing edges. The inevitable result is progressive and rapid degradation of engine performance, often to the extent of premature engine failure within 10-20 percent of the normal overhaul time. The accelerated replacement of erosion-damaged helicopter turbines in Southeast Asia currently costs the U. S. Government about $150 million a year.

Two approaches may be used to combat this problem. One is to develop a filtration system that will remove most of the solid particles from the main air stream. The other is to design blading materials that are not appreciably affected by solid particle erosion. Some compromise is possible where advancements are made in both areas. Dust filters and separators invariably decrease engine efficiency and require constant maintenance. Therefore, the optimum solution would appear to be new compressor materials with significantly improved innate erosion resistance. The proper design of these materials will require better understanding of the basic mechanisms of dust erosion and detailed characterization of the critical material properties and environmental conditions that influence erosion.

The metallic materials used for present-day compressor vanes and blading do not possess adequate, intrinsic resistance to dust erosion. Just why these high-strength materials (namely, 12-17 percent Cr stainless steels and titanium alloys) are not erosion-resistant is not clear. The basic key to establishing the requisites of an inherently erosion-resistant material is believed to be a thorough understanding of the mechanism(s) of erosion. In this investigation, the approach to solving the problem of dust erosion has been to study the mechanics of erosion (i.e., the actual physical events occurring at the erosion surface) as a logical means of identifying the properties of the blade (target) material and the dust suspension that control the erosion processes. This erosion mechanism study is outlined and discussed in this report.

BACKGROUND

REVIEW OF CONCEPTS DERIVED FROM PRIOR EROSION STUDIES

High-velocity, particulate erosion of material surfaces has been treated as an engineering-mechanics problem assuming inelastic collisions by previous investigators such as Finnie (Ref. 1 and 4), Bitter (Ref. 5), Wood and Espenschade (Ref. 6), and Neilson and Gilchrist (Ref. 7). In these prior studies, it has been assumed that a significant portion of the kinetic energy of each impacting particle will be absorbed by the target, resulting in target material removal; i.e., erosion. Two different modes of erosion are distinguished empirically for two different classes of target materials. The "ductile" mode (typical of most metals) is characterized by maximum erosion occurring at some intermediate angle between 0-90 degrees impingement, usually 20-30 degrees (Figure 1). This situation has suggested that the erosion mechanism might be one of cutting or micromachining, with a sharp corner of the individual particle acting as a miniature single-point machine tool (Figure 2). The "brittle" mode (typical of glasses and ceramics) is characterized by the erosion

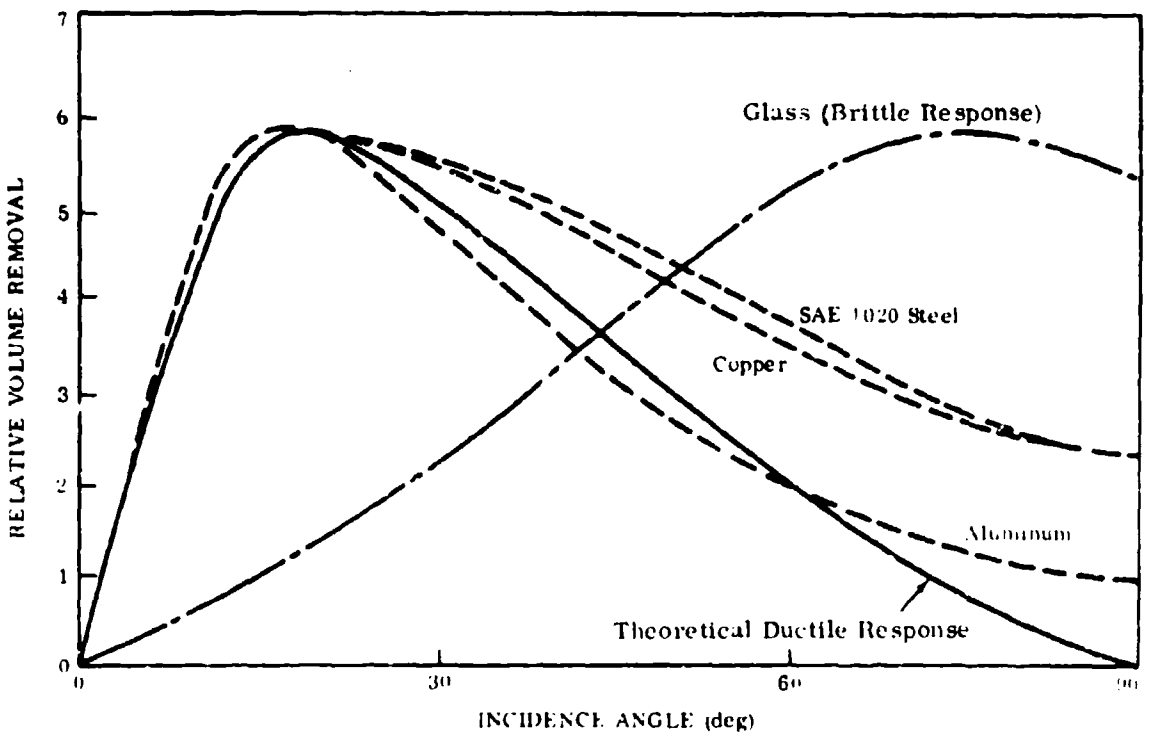

Figure 1. Predicted and Experimental Variation of Volume Removal With Incidence Angle for Various Ductile and Brittle Materials.

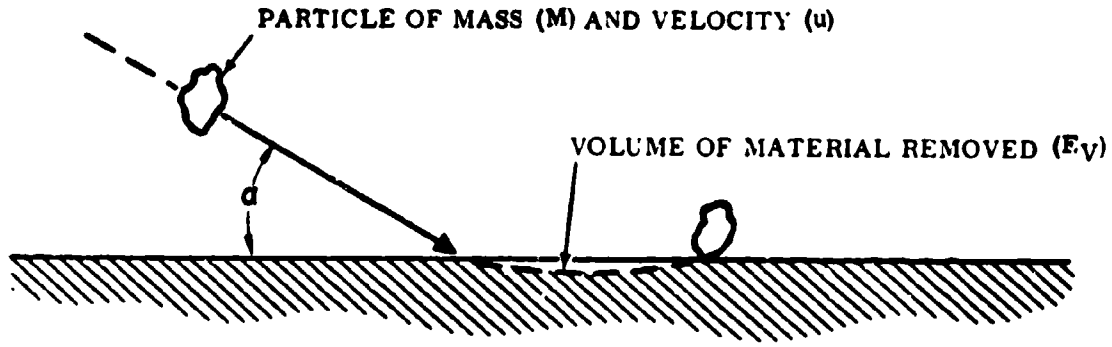

$$E_V = K f(\alpha) \frac{Mu^2}{\sigma} \quad \text{FOR DUCTILE MATERIALS}$$

$$E_V = K f(\alpha) \frac{Mu^{3.3 \text{ to } 6.5}}{\sigma} \quad \text{FOR BRITTLE MATERIALS}$$

where σ = minimum flow stress of the target material

K = a constant for the specific erosion system

Figure 2. Equations of Motion for Dust Erosion.

rate increasing with ascending impingement angle, up to a maximum at normal (90 degree) impingement (Figure 1). Intuitively, this situation has suggested that the erosion mechanism might be one of constant battering or fatigue of the target surface (associated with the normal component of particle force), leading eventually to surface and subsurface cracking and spalling of the target. The brittle mode of erosion has been validated reasonably well by microstructural examination of target surfaces (Ref. 2). However, no authentication of the micromachining hypothesis of ductile erosion has been found in the literature. Inasmuch as all current compressor blade materials react in the ductile mode, it was reasoned that the ductile mode of erosion should warrant more attention and study at this early stage of understanding.

Finnie and coworkers (Ref. 1) have proposed equations of motion for angular particles cutting through a ductile target surface. The basic equation attempts to predict erosion weight or volume loss per individual dust particle collision as being directly proportional to the total available kinetic energy of the particle ($\propto Mu^2$) and inversely proportional to the minimum flow or shear stress (σ) of the target material.

$$\text{Erosion loss} = Kf(\alpha) \frac{Mu^2}{\sigma} \qquad (1)$$

where K = constant for specific erosion system

$f(\alpha)$ = function of incidence angle

M = dust particle mass

u = dust particle velocity

σ = minimum flow stress of target material surface at test temperature

Presumably, the higher the material's flow stress, the greater its resistance to micromachining forces and the smaller the chip formed. Finnie's equation also predicts that erosion loss should be proportional to the mass (or volume for constant particle density) of the impacting particle, as well as proportional to the square of the particle's velocity. The influence of impingement angle was indicated, but not defined mathematically.

For better curve fitting of experimental erosion data (Figure 1), and to factor in the effect of impingement angle upon ductile targets, Bitter (Ref. 5) and Neilson and Gilchrist (Ref. 7) have modified Finnie's original equation as follows:

Bitter:

$$\frac{N}{M} E_V = 1/2 \frac{N(u \sin\alpha - u_{th})^2}{\xi} \qquad (2)$$

Neilson and Gilchrist:

$$\frac{N}{M} E_V \frac{1/2N(u^2 \cos^2\alpha - u_h^2)}{\delta} + \frac{1/2N(u \sin\alpha - u_{th})^2}{\xi} \qquad (3)$$

where $\frac{N}{M} E_V$ = total erosion per mass, N, of particles, in units of volume loss

$\frac{N}{M}$ = total number of eroding particles

u = velocity of eroding particle

u_{th} = constant, related to a threshold velocity below which erosion stops

u_h = residual horizontal component of particle velocity after impact, which becomes increasingly significant with decreasing impingement angle

ξ = energy needed to remove a unit volume of target material (repeated deformation wear)

β = energy needed to remove a unit volume of target material (cutting wear)

These formulas include the concepts of a particle energy threshold below which "brittle" erosion ceases, and a minimum effective angle of impingement below which "ductile" erosion ceases. Bitter's equation is based solely upon an analysis of brittle or "repeated-deformation" type wear, related by the sine of the impingement angle to the magnitude of the particle force component normal to the target surface. The erosion level predicted by this function increases systematically with increasing impingement angle. Neilson and Gilchrist have extended the formula to include the contribution of the horizontal force component of the particle (related to the cosine of the impingement angle), theoretically associated with the ductile or "cutting" mode of erosion. The erosion level predicted by this function decreases with increasing impingement angle. Neilson and Gilchrist assume that the total erosion obtained is an arithmetic combination of brittle and ductile contributions; therefore, the maximum in erosion loss at an intermediate impingement angle can be predicted. However, the working equations are very complex due to the difficulty in measuring quantities such as δ, K, u_h, and ξ.

In a series of low-velocity dust erosion tests ($\approx$570 fps at RT) with ductile stainless steel targets and a variety of natural soils, the formulae of Finnie and Bitter to predict erosion rate were evaluated under the Allison-Purdue Dust Technology Program (Ref. 8). Although the erosion factors (ϵ)* reportedly were reproducible for each dust type, the conclusion drawn, regarding the formulae to predict erosion rate, was that the soil samples were too heterogeneous. Each soil was comprised of a variety of minerals, each of different density, and with a wide range of particle sizes. A short nozzle was employed; hence the spread in probable particle velocity also was large and uncontrolled. The formulae of Bitter and Finnie are applicable only to homogeneous dust samples of constant particle size, mass, and velocity. Using homogeneous test dusts, Wood and Espenschade (Ref. 6) concluded that the equations of motion postulated by Finnie were valid for ductile target materials.

Sheldon and Finnie (Ref. 2) have also explained theoretically the erosion mechanisms in brittle materials. The volume of material removed per particle, E_v, is predicted to be

$$E_v = k r^{f_1(X)} u^{f_2(X)} \qquad (4)$$

* $\epsilon = \dfrac{\text{Target Weight Loss (mg)}}{\text{Weight of Dust Impacted (gm)}}$

where k = quantity involving target material constants

r = average radius of the impacting particles

u = velocity of the impacting particles

and the exponents, $f_1(X)$ and $f_2(X)$, are prescribed functions of X, the flow parameter of the Weibull fracture strength distribution. Moreover, the same authors have shown that nominally brittle materials, such as glass and hardened tool steel, can be made to react with a ductile erosion response, if the impacting particles are sufficiently small and are at the correct energy levels (Ref. 3). The conclusion drawn was that very small particles most frequently impact in the spaces separating the innate structural defects of the target, whose activation by larger particles causes cracking and brittle response. Hence, plastic flow occurred at near theoretical strength levels with the smaller particles.

The one common point of agreement among prior studies of dust erosion is that the erosion process must involve a net interchange or transferral of energy and momentum from the impacting particles to the metal erosion surface. In other words, a fraction of each dust particle's kinetic energy is converted into other energy forms at the impact interface, resulting in physical removal (i.e., erosion) of target material. The probable energy translations postulated (not mutually exclusive) are (1) localized heating of dust particles and/or impact surface, (2) plastic deformation (including cutting and tearing) or cracking of impact surfaces by the moving dust particle, (3) shattering or spinning of the dust particle, and (4) net transfer of energy and momentum to the blade. Of these four energy forms, numbers one and two were thought to contribute most to the erosion mechanism.

EXPLORATORY STUDIES AT SOLAR

Prompted by problems of dust erosion damage to Solar turbines, occurring in Southeast Asia as well as in dusty desert areas throughout the world, Solar embarked on an exploratory erosion testing program to

- Identify some of the critical material and environmental variables controlling dust erosion for future detailed study.

- Determine the validity of the postulated equations of motion.

A simple test rig was constructed to feed controlled amounts of test dusts (different particle sizes and varieties) into a high-velocity air stream, which could be brought to impinge upon selected flat target materials at preset impingement angles (Figure 3). The airstream was maintained in a 3/8-inch I.D. by 2-foot-long acceleration nozzle. The target weight and volume losses then were compared with the losses predicted by the erosion formulae (Ref. 9 and 10).

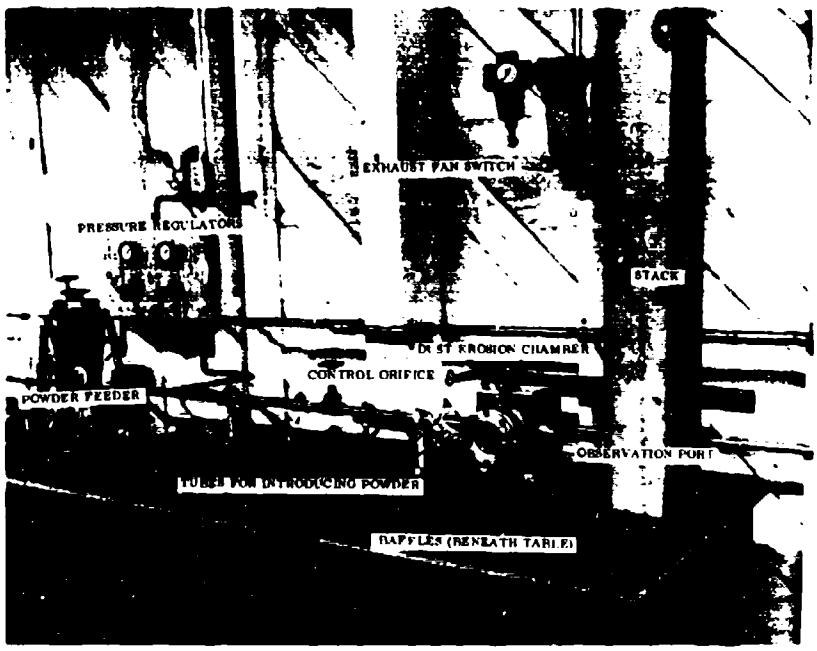

Figure 3. Existing Dust Erosion Rig.

The effect of particle velocity variation was tested using three different test dusts high in silica (see Table I) against two different ductile metallic targets, annealed 2024 aluminum alloy and annealed 410 stainless steel. Impingement angles were 30 and 60 degrees. Generally, the data verified the predicted velocity-squared relationship of Finnie's simple equation of motion (Figure 4) for the two particle velocities, 650 fps and 850 fps. Hence, particle kinetic energy was confirmed to be a key factor in the erosion process.

Another series of target materials of widely different metallurgical properties was tested to determine the importance of flow strength variation upon erosion behavior. These included annealed (low strength) and fully heat treated (high strength) aluminum alloys, a titanium alloy, and a variety of iron- and nickel-base alloys with RT flow strengths ranging from ≈20,000 to ≈280,000 psi. All of these diverse target materials yielded erosion losses of the same approximate order by weight, although the titanium and aluminum alloys lost somewhat more by volume due to density variation (Figure 5). This was felt to be remarkable, inasmuch as erosion losses predicted from flow strength differences should have resulted in nearly order of magnitude changes in erosion; for example, between TRIP steel at 280,000 psi yield strength and annealed 410 stainless steel at 35,000 psi yield strength. It was concluded that some material property (or properties) not significantly altered by those metallurgical processes affecting strength (e.g., heat treatment or cold work) must

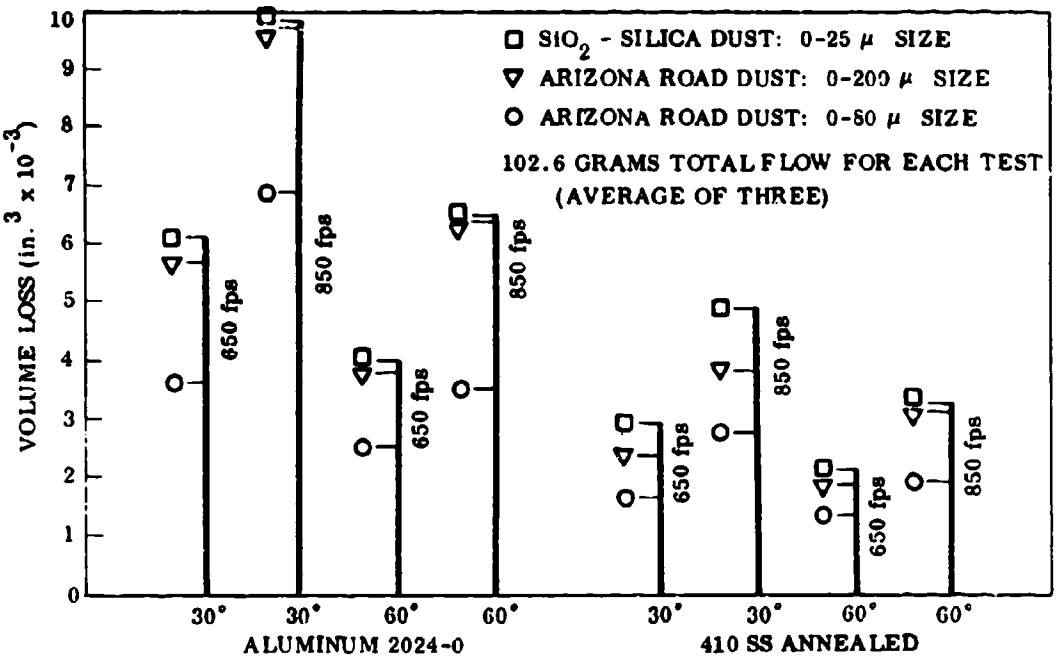

Figure 4. Volume Loss Versus Velocity for Three Types of Dust.

be controlling a material's innate erosion resistance. Such properties as melting temperature, specific heat, thermal diffusivity, and elastic modulus would therefore be suspect.

However, it was difficult to assess what influence these and related target material properties might have on erosion, in the absence of detailed visual information with which to substantiate erosion mechanics. Light microscopy and electron microscopy studies of eroded target surfaces were conducted to obtain insight in this heretofore neglected area. The most obvious visual phenomena recorded were surface "ripples", formed transverse to particle flow on both aluminum and steel targets at the lower impingement angles (20-45 degrees) (Figure 6). In general, the lower the incidence angle, the greater the peak-to-peak distance of the ripple configuration and the deeper the troughs; but no clear connection between ripple formation and erosion mechanism was evident. Finnie and Kabil (Ref. 11) have hypothesized ripple formation on the basis of surface instability.

Electron microscopy examination of erosion surfaces at high magnifications (2400-10,000X) revealed extensive surface deformation, ostensibly due to superimposed impact craters. The aluminum and steel surfaces were notably similar, and surface deformation (roughness) apparently increased with increasing impingement angle (Figures 7 and 8). Ripple crests were especially rough, because of the effectively high incidence angle (Figure 9). Perhaps of greatest importance, no evidence

TABLE I. PHYSICAL PROPERTIES OF TEST DUSTS

Dust Particles	Specific Gravity (gm/cc)	Size Range (μ)	Hardness
SiO_2 Powder	2.39	0 to 25 - 100%	900 to 950 DPH_{50} gm 68 to 70 R_c
Arizona (Fine) Road Dust (~70% SiO_2)	2.46	0 to 5 - 39% 5 to 10 - 18% 10 to 20 - 16% 20 to 40 - 18% 40 to 80 - 9%	1260 to 1420 DPH_{50} gm 74 to 77 R_c
Arizona (Coarse) Road Dust (~70% SiO_2)	2.41	0 to 10 - 24% 10 to 20 - 14% 20 to 40 - 23% 40 to 80 - 30% 80 to 200 - 9%	1260 to 1420 DPH_{50} gm 74 to 77 R_c

was found to support the micromachining concept, either in the form of machining grooves or machined chips. This finding correlated with the previous erosion data that indicated insensitivity of erosion behavior to flow strength variation. However, the extremely fluid and heavily worked appearance of the erosion surfaces suggested that the surface metal was hot, at least transiently, during erosion, so that high-temperature material properties could be involved in the erosion process.

Because of the marked discrepancies between existing theories of erosion and actual erosion behavior, it was concluded that more diagnostic work, preferably of a materials science nature, was required to define the actual erosion mechanics on ductile target surfaces.

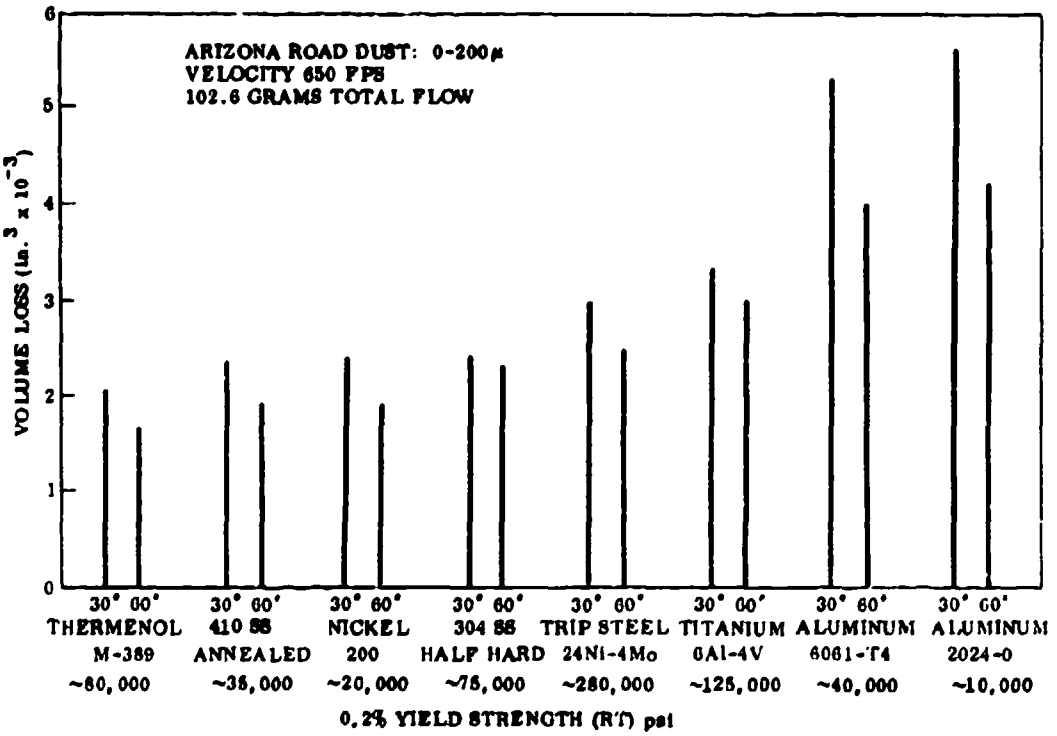

Figure 5. Volume Loss for Various Compressor Materials.

Direction of Particle Motion

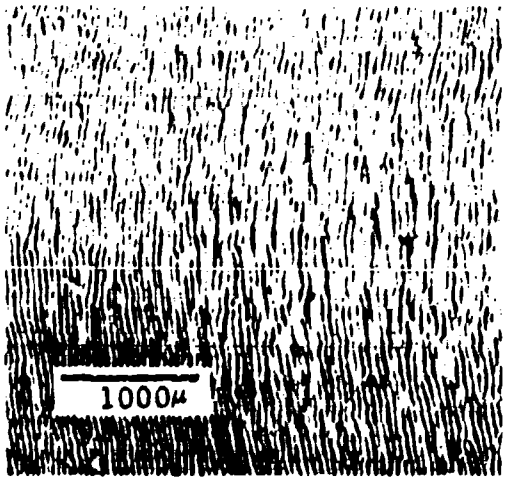

PLAN VIEW
Magnification: 20X

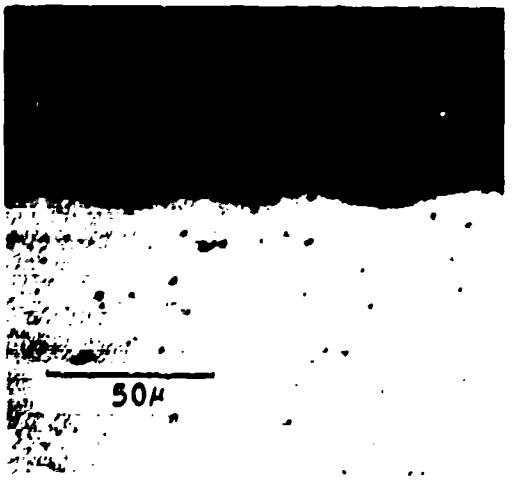

VERTICAL SECTION
Magnification: 500X

SiO_2 DUST 0 to 25μ 650 fps 30 DEGREES

Figure 6. Surface Ripples on Aluminum Alloy; Type 2024-0.

Direction of Particle Motion

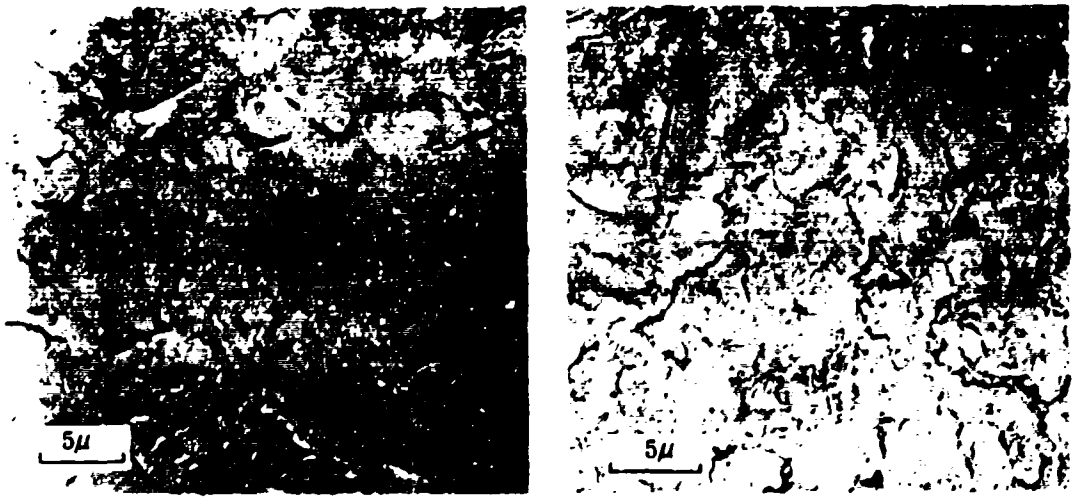

Type 410 Stainless Steel Type 2024-0 Aluminum

SiO_2 DUST 0 to 25μ 650 fps Magnification: 2400X

Figure 7. Surface Replicas After Erosion; 30 Degrees.

Direction of Particle Motion

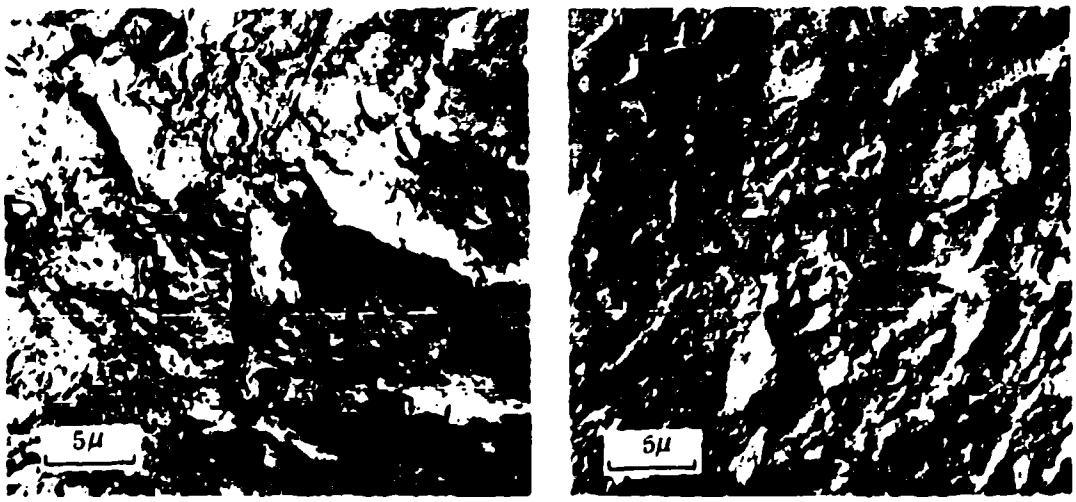

Type 410 Stainless Steel Type 2024-0 Aluminum

SiO_2 DUST 0 to 25μ 650 fps Magnification: 2400X

Figure 8. Surface Replicas After Erosion; 60 Degrees.

Direction of Particle Motion →

SiO_2 Dust 0 to 25μ
650 fps 30 deg
Magnification: 2400X

Figure 9. Ripple Crest on Type 2024-0 Aluminum.

PROGRAM OBJECTIVES AND PLAN

The principal objectives of the subject dust erosion study are as follows:

1. Identify and then define the various mechanisms of erosion associated with high-velocity dust particles striking a ductile metallic target. The initial mechanism definition would be in terms of physical models or sequences of physical events occuring at the erosion interface.

2. Develop mathematical expressions for the erosion mechanisms, relating erosion losses to identifiable control variables introduced by the carrier gas, the dust particles in suspension, and the target materials themselves. Provided the erosion behavior can be well defined, construct nomographs incorporating the important control variables to enable the design engineer to predict erosion behavior of candidate compressor materials under specific operating conditions.

3. Based upon success in meeting the preceding objectives, provide the necessary guide lines to enable development of new engineering materials and/or coatings with superior resistance to sand and dust erosion.

Professor I. Finnie of the University of California, Berkeley, was retained as special consultant to assist in the interpretation of test results and phenomenological findings.

A materials science approach to the problem was emphasized. The program consisted of two parallel parts: (1) an experimental erosion program designed to evaluate the effects of selected material and environmental variables upon measured erosion losses and behavior, and (2) a laboratory diagnostic program to correlate measured erosion behavior with observable physical phenomena associated with the erosion surface, the spent dust particles, and collected erosion products. This report stresses the findings and correlations of the diagnostic program, because they have furnished insight essential to the synthesis of physical models and mathematical treatment of erosion. The conventional electron microscope and scanning electron microscope were the principal diagnostic tools employed. These instruments enable magnification of erosion surfaces and erosion products many thousands of times, so that erosion phenomena can be clearly resolved.

The experimental phase of the erosion program was divided into six separate tasks or series. Each series had the primary objective of determining the influence of a specific environmental or material variable or combination of variables upon erosion loss. The secondary objective was to check the validity of concepts derived from prior erosion studies. A special erosion test facility was constructed to simulate (and control) as closely as possible the erosion conditions in a high-performance compressor. Environmental variables included a wide range of gas velocities (compressed air, argon, helium, or helium-air at 100 to 1500 fps) and variable true temperatures of the carrier gas (RT - 700° F). Target materials were chosen to include current candidate alloys for compressor blades and vanes [namely, a 12-Cr stainless steel (type 410) and a 17-Cr precipitation-hardening stainless steel (17-7 PH), a high-strength titanium alloy (Ti-6Al-4V), and a high-strength aluminum alloy (2024 Al)]. Capability to stress the target specimens in tension up to 60 percent of their 0.2-percent yield strengths during erosion testing was provided. This variable simulated the levels of blade stress encountered in typical compressor operation.

The test dusts were carefully selected and controlled. Naturally occurring surface dusts representative of both the American desert and Vietnam were included, as well as metallographic grade p alumina. Coarse Arizona Road Dust, a standard test dust for auto air filters (≈69 percent SiO_2), was classified into four different mesh sizes (0-43μ, 43-74μ, 74-148μ, and 148-210μ) to study particle mass and size effects. A laterite soil from Pleiku, Vietnam, was obtained and classified into particle-size ranges similar to the Arizona Road Dust. The laterite is a mixture of hydrous iron and aluminum oxides, and has been reputed to be the most troublesome and erosive variety of dust in Vietnam. Dust concentrations were chosen to match the ranges normally encountered in service applications.

The following outline lists the principal material and environmental variables studied in the experimental program:

Test Series	Principal Variables	Secondary Variables
I	Strength level and heat-treat condition of each target alloy	1) Angle of impingement 2) Test dust variety 3) Target alloy
II	1) Carrier-gas true temperature 2) Dust particle velocity	1) Angle of impingement 2) Dust concentration 3) Target alloy

Test Series	Principal Variables	Secondary Variables
III	1) Dust particle mass and size 2) Dust particle velocity 3) Dust particle energy 4) Dust particle variety	1) Angle of impingement 2) Carrier-gas true temperature 3) Target alloy
IV	1) Dust concentration 2) Dust particle velocity 3) Dust particle size	1) Carrier-gas true temperature 2) Target alloy
V	Tensile stress applied to target specimen	1) Angle of impingement 2) Target alloy
VI	Oxygen concentration in the carrier gas	1) Angle of impingement 2) Target alloy

In addition, a special test series was conducted to search for possible erosion thresholds associated with lower levels of particle energy and particle size. This work, in conjunction with Test Series III, also provided useful information for the diagnostic phase of the program.

EXPERIMENTAL ANALYSIS AND PROCEDURES

ANALYSIS OF EROSIVE ENVIRONMENTS ENCOUNTERED IN TURBINE COMPRESSORS

This analysis has two different aspects. The first has to do with a physical description of typical dust clouds generated by helicopter rotor downwash, sand storms, turbine-powered off-highway vehicles, etc., that can be ingested into the turbine power plant. Field studies on turbines operating in dusty environments also were included to quantify the erosion damage potential of particulate clouds. This information is necessary to select pertinent levels of dust particle mass, size, concentration, and total dust weight for the experimental program. The second aspect of the analysis is concerned with what happens to the dust suspension after it is ingested into the compressor, in terms of pressurization, heating, and acceleration of the carrier gas, centrifugal segregation of dust particles, probable angles of impact with compressor blades and vanes, changes in oxygen pressure and activity, etc. Again, these data are required to select meaningful limits for the erosion test variables described in the program plan.

Field Studies on Turbines in Dusty Environments

Turbines typically encounter dust environments in primary power applications for off-highway land vehicles (Ref. 12 and 13), for helicopter and V/STOL aircraft over unimproved landing areas (Ref. 14, 15, and 16), and for stationary gas pumping stations and auxiliary power units in remote desert regions (Ref. 17 and 18). In terms of economic importance, military helicopter applications in Southeast Asia account for the greatest number of turbines suffering severe erosion damage (Ref. 19).

Measurements of dust concentrations in clouds formed by an H-21 helicopter in stationary hovering (1- to 10-foot heights) at Yuma, Arizona, and Ft. Benning, Georgia, have yielded average concentrations ranging from 2 to 4 mg/ft^3 (average) near the rotor hub to 12 to 19 mg/ft^3 (average) near the area of rotor blade overlap (Ref. 16). Dust concentrations increased by a factor of 3 during takeoff and landing maneuvers, and by a factor of 5 with another helicopter operating nearby (Ref. 16). It should be noted also that the ingested dust is further concentrated within the compressor by centrifugal action, which "throws a majority of the sand to the outer portion of the annulus, resulting in extremely high concentrations" near the blade tips (Ref. 14). Sand from these sites is normally high in silica, with an average specific gravity of 2.4 to 2.6. Typical particle size distribution of airborne dusts were: 98 to 100 percent $< 200\mu$; 40 to 60 percent $< 100\mu$; 15 to 40 percent $< 50\mu$; and 5 to 10 percent $< 15\mu$. Particles larger than 500μ were not

airborne (Ref. 16). Other references cite similar dust concentrations and ranges, (Ref. 14, 15, 16, and 17). The principal difference in Southeast Asia is that the dusts are predominantly lateritic minerals (Ref. 14) (mixtures of hydrous aluminum oxides and iron oxides).

Of the quantitative erosion studies upon actual turbines, some of the most relevant field work was conducted by Montgomery and Clark (Ref. 16), who determined erosion rates as a function of dust particle size and concentration for a Solar Mars gas turbine. This study showed that within limits of repeatability, the erosion factor

$$\epsilon = \frac{\text{grams weight loss}}{\text{grams dust ingested}}$$

appears constant for any realistic dust concentration up to 13 mg/ft^3 (Figure 10). From this information they were able to predict the turbine life as being proportional to a constant, which is representative of the engine type, and inversely proportional to the product of the dust concentration and the particle size according to the relation

$$L = \frac{A}{C \times d_m} = \frac{1.38}{C \times d_m} \qquad (5)$$

where L = engine life in hours

A = constant (1.38 for the Mars engine)

C = dust concentration in mg/ft^3

d_m = maximum particle size in microns

It was reasoned from this relation that all particles above 2 to 3 microns should be filtered from the air stream to ensure an acceptable turbine life expectancy for high dust concentration areas. This requirement is shown in Figure 11 where the particle size is plotted versus engine life for different concentrations. Although this is specifically for the Mars engine, it remains the most relevant published data on the effect of particle size and concentration on engine life. For this particular engine, particle sizes larger than 10 microns must be filtered from the inlet air to give a reasonable life.

Biachini and Koschman of Allison also carried out field studies of dust erosion in the T63 turbine using 0 to 200-micron (Arizona Road (AR) Dust, coarse) dust particles, initially at 15 mg/ft^3 (Ref. 20). They found that engine power decreased almost linearly with the total dust ingested, and that this function was apparently

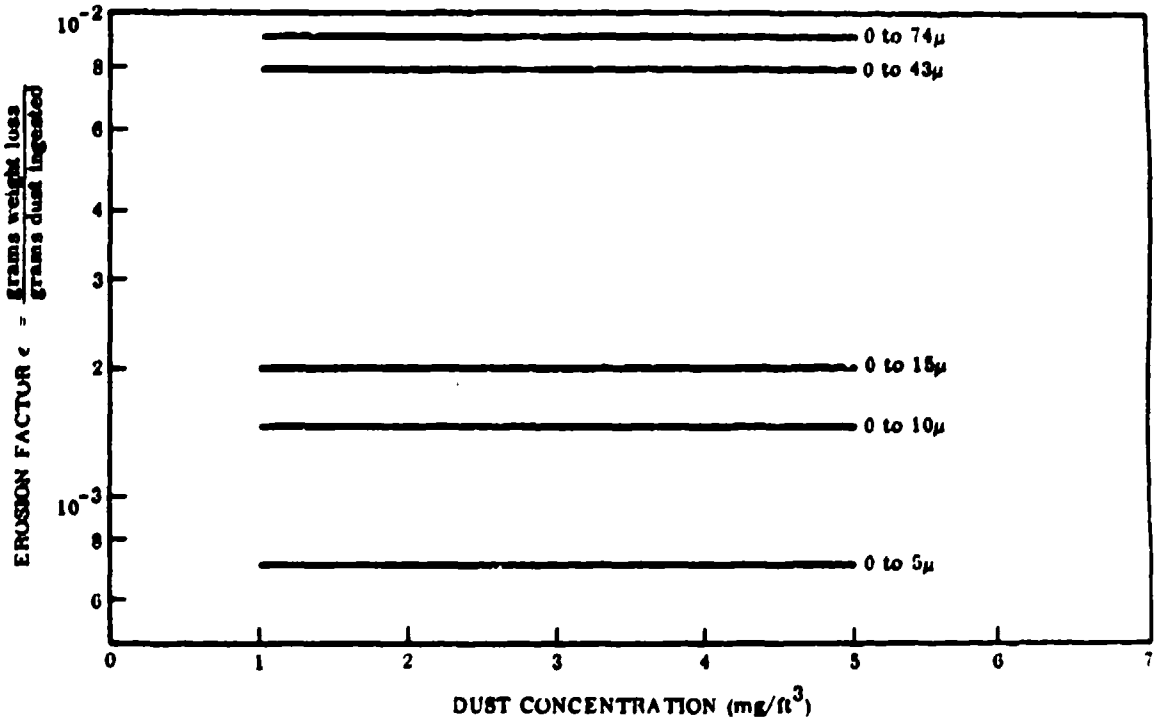

Figure 10. Erosion Factor Versus Concentration for Each Particle Size.

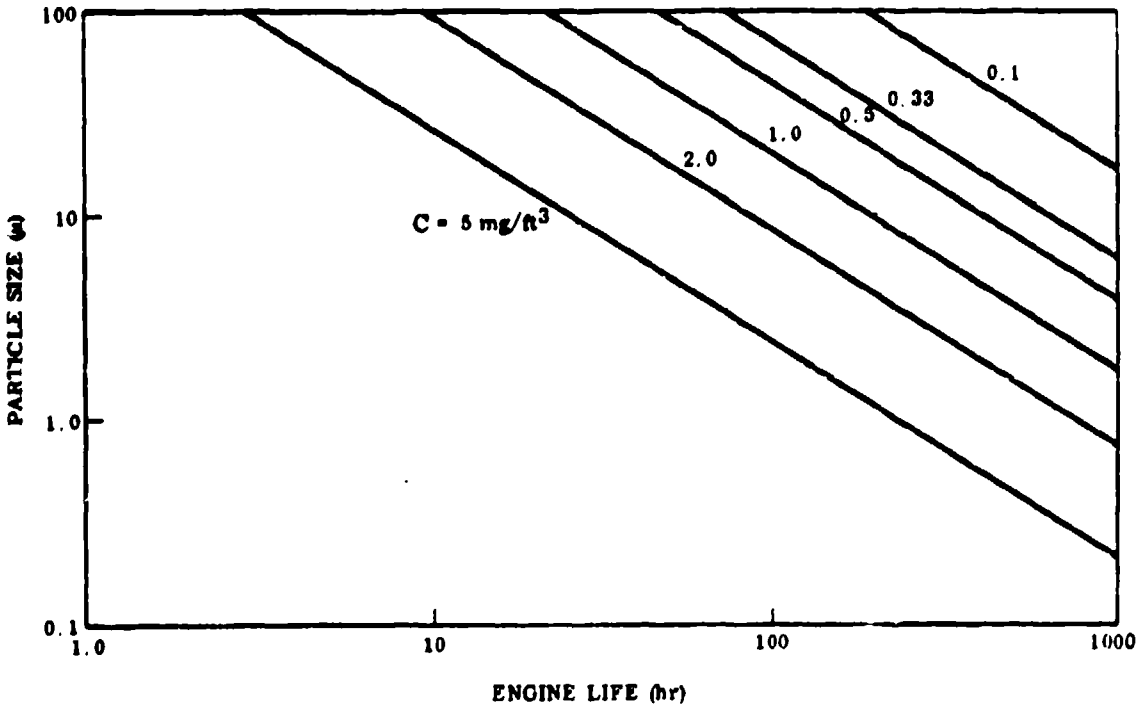

Figure 11. Engine Life Versus Particle Size for a Mars Gas Turbine Engine.

independent of the dust concentration (Figure 12). Also, they noted that particles up to 10 microns in size had only a small effect on engine power. On the other hand, the erosion effects of 0-80 micron dust (AR fine) and 0-200 micron dust (AR coarse) were severe, but not discernibly different.

Rapp and Rosenthal of General Electric (Ref. 14) also found that power degradation and the number of safe landings could be directly related to the pounds of dust ingested. Compressor blade and vane erosion was severe on engines without inertial filters (Southeast Asian operations). As a general rule, large particles caused substantial damage to the first stage blades, all along the leading edges. Large particles were apparently shattered by impact with the first stage blades and accelerated to high velocities through the latter stages, so that erosion past the first stage proved similar regardless of initial particle size ingested. Because of centrifugal effects, the site of blade damage was progressively transferred to the blade tips and trailing edges, the higher the stage. To counteract erosion, General Electric experimented with hard blade coatings, the most successful of which were an electro-deposited hard Cr plate and a beryllium diffusion coating. Embrittling side effects prevented their general application to AM-355 and similar stainless steel alloys blades, however (Ref. 14).

A difference of opinion exists over the effectiveness of small dust particles (≤15 microns) in eroding turbine components. Mr. J. M. Clark, Jr., of the Southwest Research Institute cites data (Ref. 21) which shows that, in 660 hours of ingesting 0-5 micron dust at a concentration of only 0.33 mg/ft^3, a gas turbine was destroyed as an operational unit. He discounted arguments that very fine dust particles were decelerated or deflected significantly by the boundary layer on airfoil surfaces. G. Thomas, also of Southwest Research Institute, has published data showing that a Solar turbine (Model T-221N-1) was erosion damaged sufficiently to become inoperable after running 132 hours with an inertial separator on the air inlet (Ref. 18). Ninety percent of the dust ingested into the turbine was determined to be ≤14 microns. Based upon other data (Ref. 14, 20, and 22), engine manufacturers such as General Electric and Allison feel that engine erosion is a minor problem with particles smaller than 10-15 microns. Hence, they stress that properly maintained inertial separators and mechanical filters should be adequate to effectively nullify the erosion problem. (The inertial filter has a marked cutoff in efficiency somewhere between 10-15 microns.)

In summation, the concentration of dust in the air ingested over unimproved air strips varies normally between ≈2-100 mg/ft^3, depending upon the dust variety and other environmental factors. The size of dust particles ingested ranges widely between less than 1 micron diameter and about 200 microns diameter. Screens and centrifugal separators are capable of removing most of the dust above 60μ size,

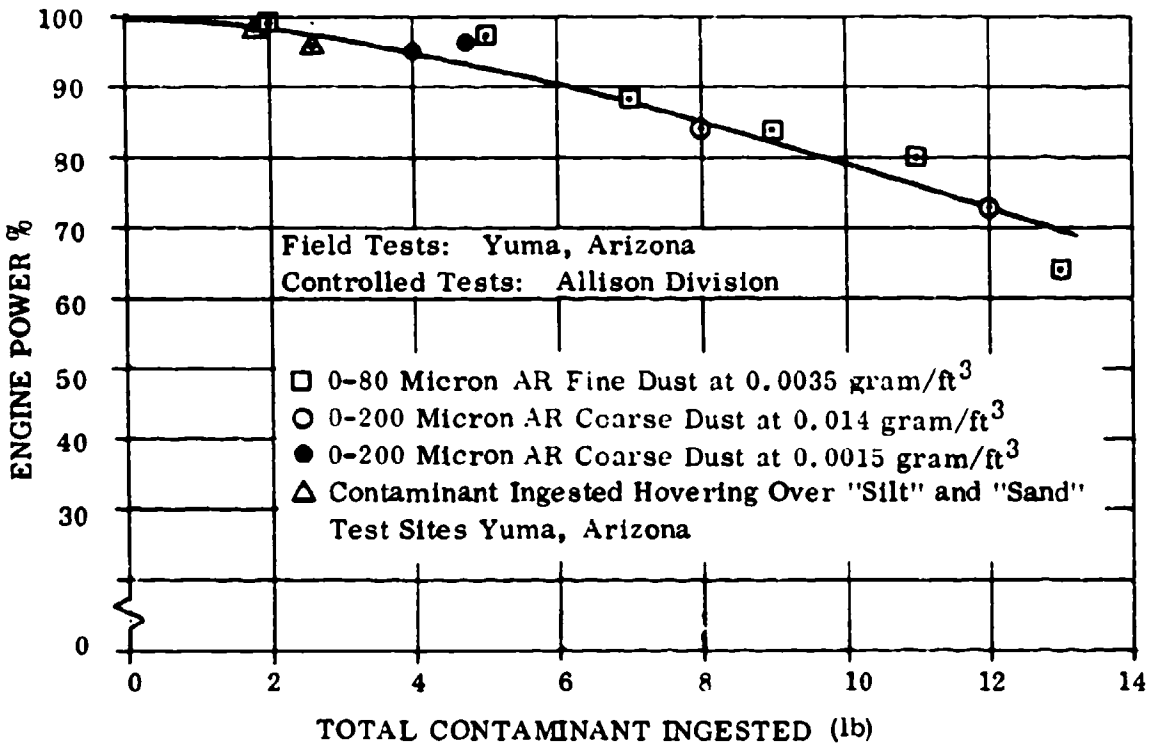

Figure 12. T63-A-5A Engine Sand and Dust Ingestion Tests; Comparison of Erosion Effects From Field Tests and Controlled Ingestion Tests.

so that experimental emphasis can logically be placed upon particles in the 0-60μ range. The most common dust varieties encountered are those sandy soils characterized by high silica content, typical of American desert and coastal regions (e.g., the Arizona Road Dusts, marketed by A.C. Spark Plug, Division of General Motors), and the lateritic soils of Southeast Asia.

The conclusions to be drawn from the published data regarding the effect of ingested dust on gas turbine performance are summarized as follows:

- Serious erosion of gas turbine components will be caused by ingestion of airborne dust generated by average military operations in unimproved areas. Efficient air filters will be required on all gas turbines to remove dust particles above 2 to 3 microns in diameter if improved erosion-resistant materials are not available.

- Anticipated gas turbine life varies inversely as the product of the maximum particle size and the dust concentration, and the erosion factor is independent of the rate of ingestion (i.e., dust concentration).

- The total erosion is independent of dust concentration within realistic limits, and is a direct function of the total weight of ingested dust of any given particle size for a given gas turbine. In the particle size range of airborne particles, there is negligible erosion of the inducer section of the compressor impeller or other areas where the absolute velocity of the entrained dust is low.

- A simple cycle gas turbine demonstratec little or no external evidence (by observation or readout) of complete destruction by dust erosion prior to the point of complete failure. Vibration of gas turbines does not appear to increase until almost total destruction of the rotating components by dust erosion has occurred.

Field studies give only a generalized or end view of the erosion phenomena, with limited potential for insight into the basic mechanisms of erosion. This is because erosion in a turbine occurs over a wide and changing range of conditions that are difficult to control directly as variables.

Program Guide Lines Based Upon Compressor Environments

To appreciate the range of aerodynamic conditions experienced by typical compressor blades and vanes, several compressor parameters are examined here. An example of this study is contained in Table II. For the typical blade shape (Figure 13), the difference between the blade inlet and outlet angles ($\beta_1 - \beta_2$) relative to the turbine axis gives a camber angle of the blade, θ. This difference has been listed for front, central, and latter rotor stages for three sections through the blades of one of Solar's gas turbine engines (Saturn, 1100 hp). The relative air inlet angles, taking into account the relative air velocities of the air and rotating blade, are also listed together with the relative air velocities through the compressor stages. The pressure at a given stage and the temperature are also shown in Table II. The angle of incidence of the air relative to the rotating blade is always positive, varying from 0.2 to 5.5 degrees for the stages listed. Therefore, impinging particles always hit on the leading edge or concave side of the blade; the convex side is effectively shadowed from dust erosion. Also, the maximum angle at which particles strike the concave side is given by θ. This angle varies from a maximum of 46.5 degrees at the hub on the fourth stage rotor to a minimum of 6.0 degrees at the tip on the first stage. Therefore, erosion impingement angles vary roughly between 5 and 50 degrees with a mean impingement angle in the region of 30 degrees on rotating blades, which is close to the maximum wear rate angle for ductile materials. Thus, ductile materials are a poor choice for the concave side if this mechanism persists in the velocity range being investigated.

TABLE II. TYPICAL COMPRESSOR BLADE DATA IN AN AXIAL COMPRESSOR

Stage	Section Through Blade	Blade Inlet Angle β_1 (deg)	Blade Outlet Angle β_2 (deg)	Camber Angle $\theta = \beta_1 - \beta_2$ (deg)	Air Inlet Angle α_1 (deg)	Leading Edge Incidence Angle $\alpha_1 - \beta_1$ (deg)	Relative Air Velocity (fps)	Pressure (psia)	Temperature (°R)
Rotor 1	Hub	41.4	0.8	40.6	46.9	5.5	1100	14.7	540
	Mean	50.0	33.2	16.8	55.1	5.1			
	Tip	56.5	50.5	6.0	60.6	4.1			
Rotor 4	Hub	48.5	2.0	46.5	50.2	1.7	1010	34.5	707
	Mean	52.1	21.4	30.7	54.5	2.4			
	Tip	57.3	35.7	21.6	58.0	0.7			
Rotor 8	Hub	54.1	25.1	29.0	54.3	0.2	920	85.5	945
	Mean	54.8	34.4	20.4	57.0	2.2			
	Tip	57.1	41.1	16.0	59.5	2.4			

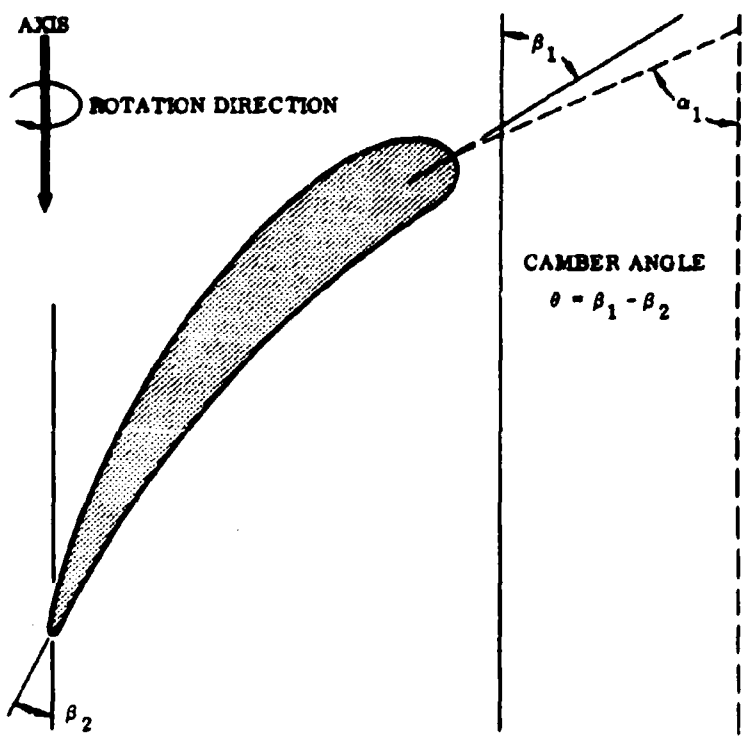

Figure 13. Typical Axial Compressor Blade.

Typically, the camber angle for stator vanes is higher than for rotor blades. In fact, the camber angle on the Saturn engine is an average of about 45 degrees from the front to the rear stages at both the hub and tip. The higher camber angle means more turning of the gas; thus there is a greater probability of solid particles striking the concave surface. Since the heavier dust particles are centrifuged to the outer diameter, it has been observed that the highest erosion rate occurs on stator vanes on the latter stages, which corresponds very well with what can be predicted from the known erosion rate data.

The static or true gas temperatures in the compressor can be as high as 600° - 800° F due to adiabatic heating. Relative velocities can reach 1100 to 1500 fps. These velocities are significantly higher than any previously investigated, ≈800 fps. The total pressure and activity of oxygen increase by a factor of almost 6 in the Saturn gas turbine and can increase up to 15 or 16 times in higher performance compressors. It was felt that this increased oxygen concentration could have significant effect on erosion characteristics, particularly if the target oxidation rate affects dust erosion characteristics. Another important consideration is that tensile stress in the rotating blades may have some effect on erosion rates. The additional surface energy associated with stress application could conceivably influence erosion, inasmuch as rate of kinetic energy transfer at the erosion interface appears to be one factor controlling erosion.

In summation, the most advanced, high-efficiency compressors are designed to convert intake air at ambient pressure and temperature to about 16 atmospheres and ≈800° F progressively through 10-16 stages. Gas velocities reach a maximum at about 1100-1500 fps. The high pressure, temperature, and velocity of air in the latter stages will likely increase its chemical reactivity with respect to metallic blade and vane surfaces; hence the desirability to evaluate erosion behavior under these high-limit conditions. The impingement angle of air upon concave airfoil surfaces varies between 5 degrees and about 50 degrees, while the impingement angle upon the leading edge surface of first stage blades approaches 90 degrees. Typical stress levels in compressor blades vary from about 60 to 40 percent of the design yield stress (at service temperature), from the blade tip to near the blade root.

ACCELERATION CHARACTERISTICS OF DUST PARTICLES

To simulate in the laboratory the high-velocity gas and particle flow within a compressor, dust particles first were metered into a high-pressure, moderate-to-high-velocity gas stream (air, helium, or helium-air, flowing in a 1- to 2-inch-diameter tube). The resultant dust suspension was then made to pass through a subsonic acceleration tube or barrel (1/4 in. to 3/8 in. diameter) of sufficient

length to allow the dust particles to accelerate to the desired test velocities. Approximately 1/2 inch from the muzzle of the barrel and in the direct path of the jet stream, the flat surface of each target specimen was positioned at a predetermined impingement angle.

Considerable effort was devoted to analyzing the acceleration characteristics of dust particles introduced into the high-velocity fluids employed. A general aerodynamic solution based upon empirical relations was developed to predict the minimum barrel lengths required to accelerate different varieties of dust particles up to fluid velocity, using the air and helium-air mixtures planned for the experimental program (see Appendixes I and II). Examples are worked out showing the possibilities of minimizing barrel length by using fluid velocities higher than the ultimate particle velocities desired. For the largest particle sizes ($\approx 200\mu$) and highest velocities (1000-1100 fps), it was shown that barrel lengths of 20-400 feet may be required where particle velocity and gas velocity are equal, but these length requirments were reduced appreciably by employing over-speed gas. The principal assumptions made, regarding this analysis, are:

- The dust particles react as Stokesian spheres. (The angular dust particles used should actually accelerate somewhat faster than spheres.)
- Internal friction effects within the barrel are negligible.
- The discharge coefficient of the subsonic nozzle is 1.00.
- Gas velocity 1/2-inch downstream from the nozzle discharge is uniform over the effective projected area of the jet.

Gas velocities were monitored with a 1/32-inch-diameter Kiel probe (Pitot tube with 1/8-inch-diameter collector) at various positions in the jet stream. Gas velocity (U) was computed from the Kiel probe total pressure (P_t) using the standard formula

$$\frac{U}{\sqrt{T}} = \sqrt{2g \cdot J \cdot C_{p,g}\left[1-\left(\frac{P_s}{P_t}\right)^{\frac{\gamma-1}{\gamma}}\right]} \qquad (6)$$

where P_s = static pressure of the gas in the test chamber

T = temperature of the gas stream

g = gravitational constant

J = mechanical equivalent of heat

$C_{p,g}$ = specific heat of the carrier gas at constant pressure

γ = ratio of specific heats of the carrier gas at constant pressure and at constant volume

Empirically derived gas charts of $U/\sqrt{T}$ versus P_t/P_s were employed.

An analysis was made of the engineering properties of helium-air mixtures (Appendix II). Helium-air mixtures were used as propellant gases for gas velocities above 1000 fps at room temperature to avoid undesirable choking and shock wave phenomena at and near the sonic velocity of the air propellant (Figure 131 of Appendix II). Thermodynamic properties and parameters such as specific heat, gas constant, specific heat ratio (γ), molecular weight, absolute viscosity and limiting sonic velocities are computed and plotted for a wide variety of helium-air mixtures at different test temperatures. These data were used to calculate required nozzle lengths and diameters for the higher speed tests. In general, the particle velocities from the aerodynamic computations are listed in the report, in terms of the velocity of the median-size particle within a given particle-size distribution and/or the limiting velocities of the smallest and largest particles within the same distribution.

To determine the maximum barrel length required for erosion testing, a set of examples was worked out for particles of Arizona Road Dust, in sizes ranging from 10μ to 75μ and ultimate particle velocities (u) from 500 to 1000 fps. The particles were assumed to have been introduced into room-temperature air of uniform velocity (U) and at 1 atmosphere static pressure. Inasmuch as the viscosity and drag coefficient increase with increasing gas temperature, the minimum required barrel lengths would be longest for the room-temperature tests. The results of these computations are shown graphically in Figures 14 through 18. It can be seen that reasonable nozzle lengths ($\leq$10 feet) are possible for values of $u/U = \lambda$ in the range of 0.80 to 0.90 for all test conditions. A 2-foot-iong nozzle can provide particle velocities up to 1000 fps for particle sizes up to 25μ diameter when $\lambda = 0.90$ or up to 50μ diameter when $\lambda = 0.80$, (Figure 18). A 75-micron particle requires approximately a 3.5-foot nozzle to reach 800 fps ($\lambda = 0.80$), but would require a 9.8-foot nozzle to accelerate to 1000 fps ($\lambda = 0.90$), because of the sonic velocity limitation of the air carrier gas. Similar computations for particles as large as 200μ indicated that u/U ratios need not fall

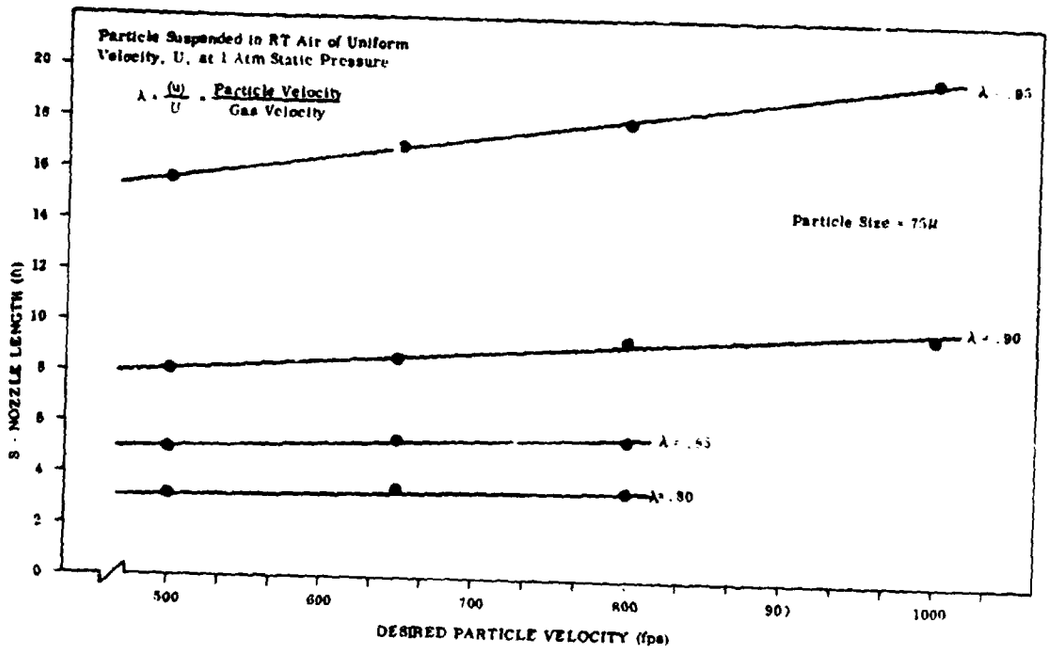

Figure 14. Nozzle Length Required to Accelerate Particle of Arizona Road Dust to Desired Velocity.

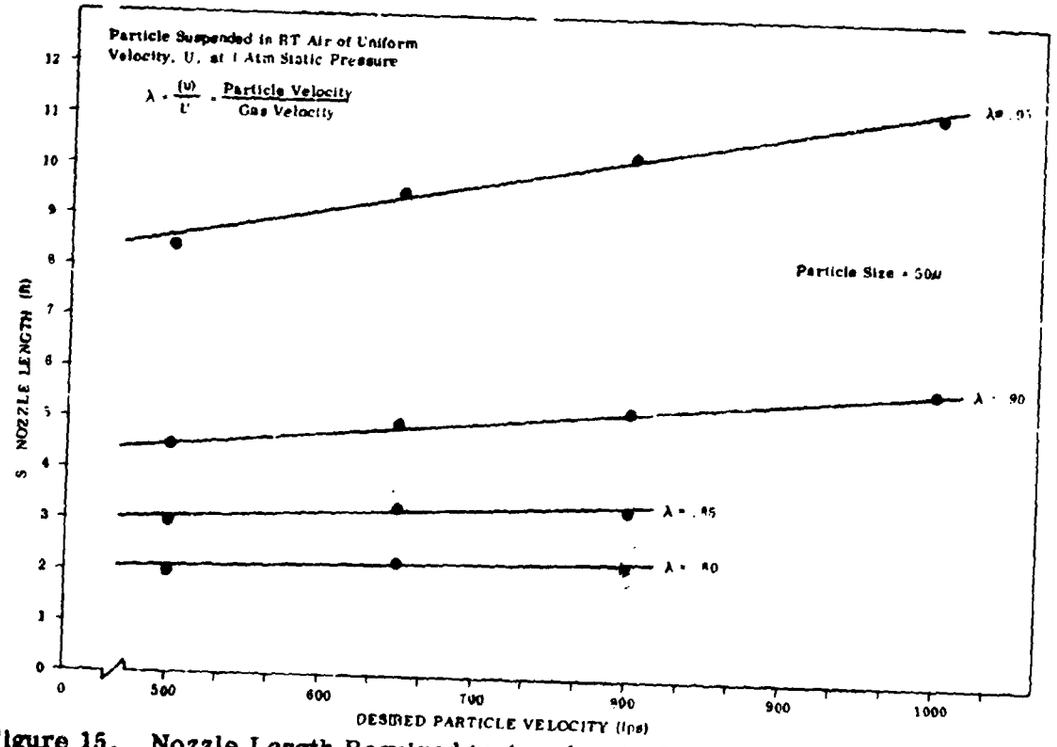

Figure 15. Nozzle Length Required to Accelerate Particle of Arizona Road Dust to Desired Velocity.

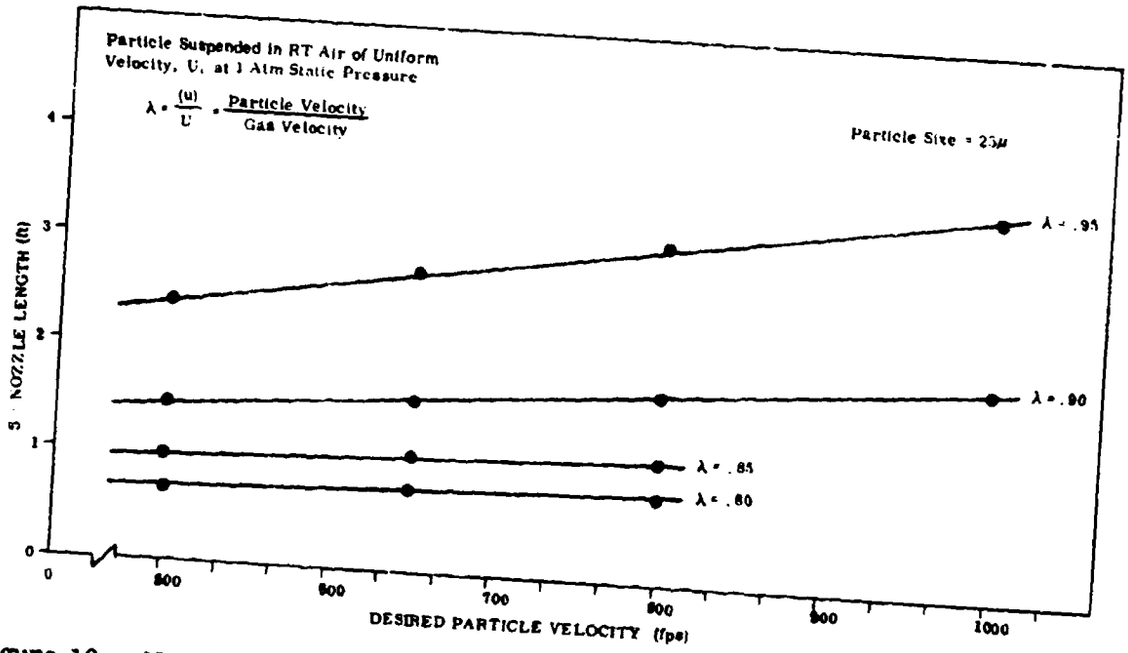

Figure 16. Nozzle Length Required to Accelerate Particle of Arizona Road Dust to Desired Velocity.

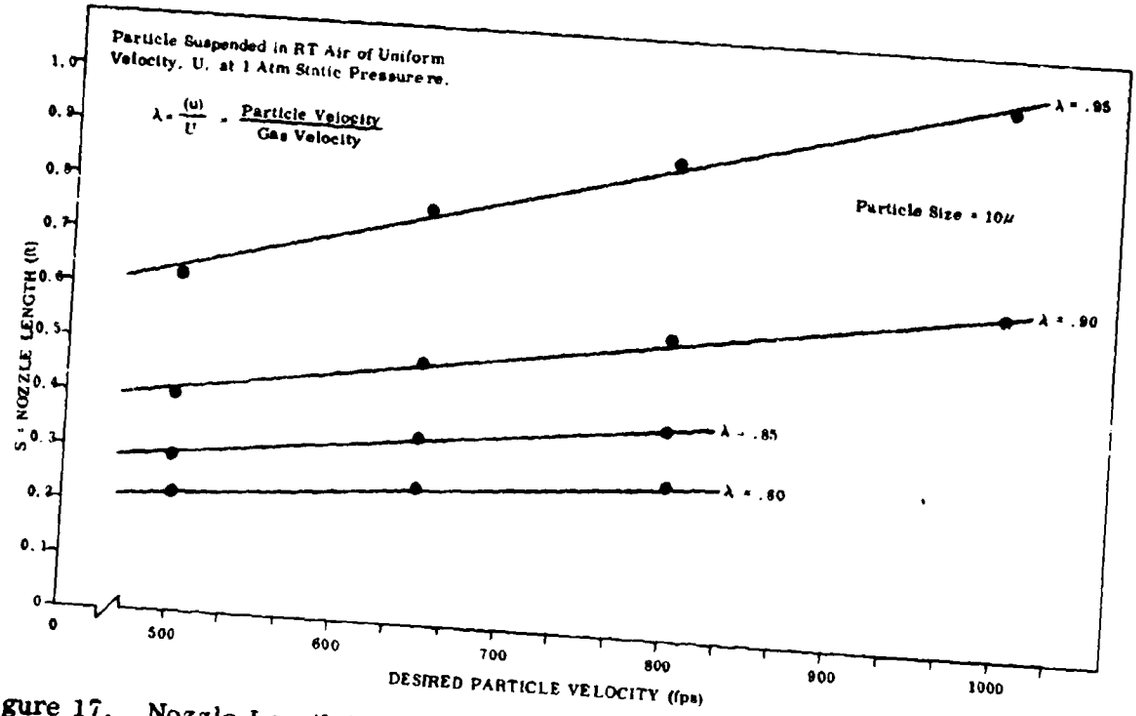

Figure 17. Nozzle Length Required to Accelerate Particle of Arizona Road Dust to Desired Velocity.

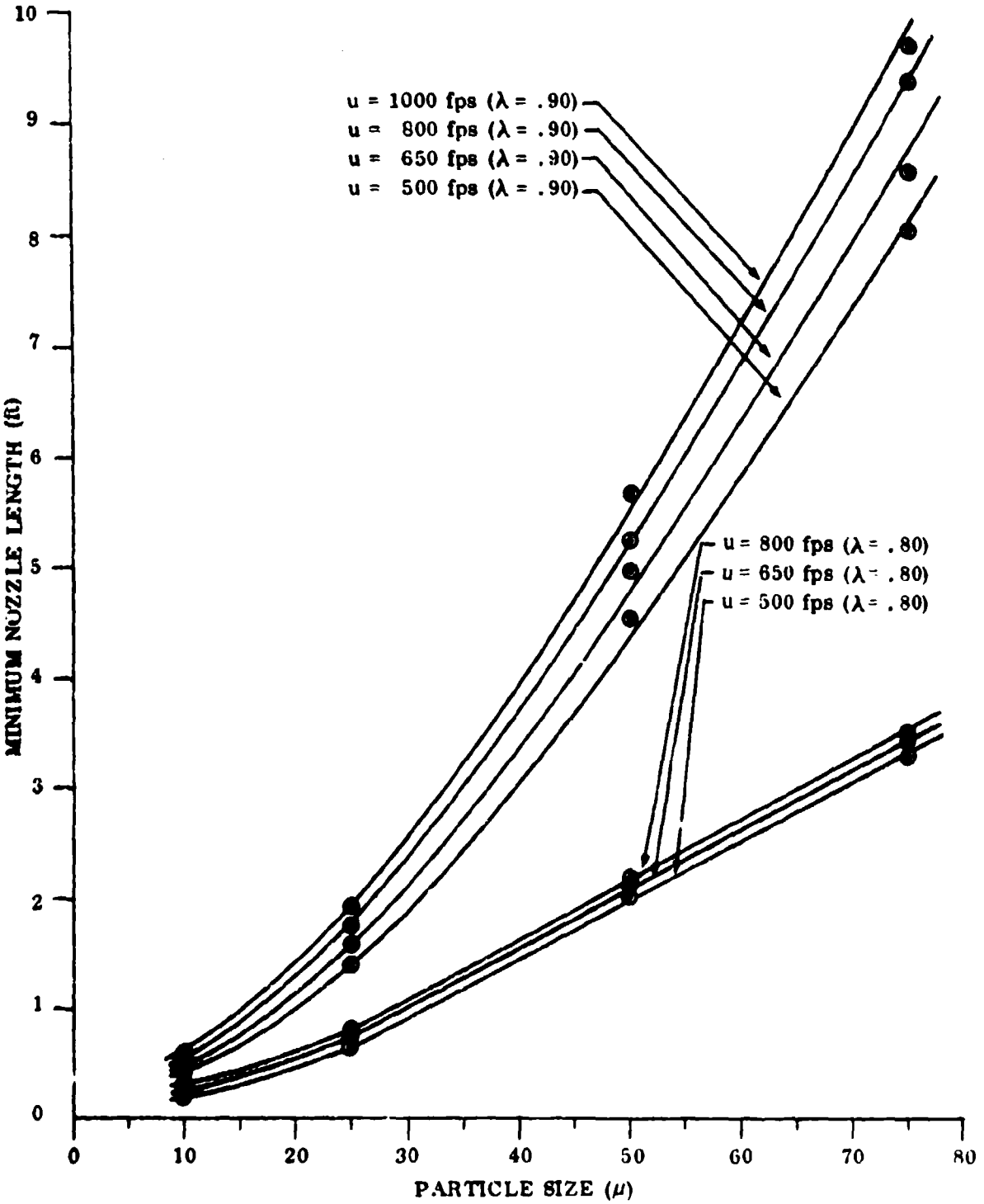

Figure 18. Variation in Required Nozzle Length With Particle Size, for Desired Particle Velocity.

below 0.70 for desired particle velocities up to 800 fps, using a 10-foot-long acceleration barrel. Therefore, a 10-foot-long barrel was adopted as standard for most erosion testing, and only the u/U ratio varied as needed.

Typical working curves of carrier-gas velocity (U) versus corresponding particle velocity (u) are shown in Figures 19 and 20 for silica or Arizona Road Dust particles r nging from 5μ up to 208μ diameter.

EROSION TEST FACILITY AND TEST PROCEDURES

The construction of a special erosion test rig was necessary to accommodate the high gas velocities and pressures, the high temperatures, and the target stressing capability required to simulate the erosion environment in a turbine compressor. A schematic of the erosion facility is shown in Figure 21. Because the analysis of particle acceleration dynamics (Appendix I) had shown the need for long nozzle and barrel lengths (on the order of 10 feet), it was decided to locate the gas heater and precision powder feeder on a second-floor deck directly above the test chamber. In this way, vertical nozzles up to 10 feet in length could be positioned between the control orifice (which monitors mass flow rate of gas) and the top of the test chamber. A vertical nozzle also provides a symmetrical erosion pattern on the target by avoiding gravity effects.

In a typical test run, compressed shop air or a bottled combination of air and helium (premixed) is fed into 2-inch-diameter inlet pipes to the control point. Here, the flow is regulated to match the desired test condition. For example, a 1 atmosphere room temperature test at 850 fps gas velocity would require a mass flow of about 1.9 lb of air per minute; while an otherwise similar test at 1500 fps would require about 1.2 lb of gas per minute (75% He/25% air mixture). Lower velocity tests require proportionately lower flows, while higher velocity tests require proportionately higher flows. For elevated-temperature tests, the regulated flow then is passed through a heat exchanger (12 kw rating, electrical heating elements) for heating the gas to the desired test temperature of 400° or 700° F. The rate of heat input is controlled by a thermocouple attached to the back of the target specimen. The carrier-gas true temperature, first measured by a bare thermocouple on the front of the specimen within the gas jet, is controlled during the test by another thermocouple on the back of the target. Thermally insulated pipe conducts the heated gas from the heat exchanger into the acceleration nozzle (also insulated) and the test chamber; see Figures 21, 22, and 23. In room temperature testing the heat exchanger is bypassed. When the gas and specimen temperatures are at the correct levels as well as the gas velocity (as measured by a Pitot tube at the

nozzle exit), the powder feeder is turned on to initiate the test.*

The two main functions of the 1/4-inch I.D. by 10-foot-long acceleration barrel (Figure 22) are to accelerate the test dust particles, fed near the barrel entrance, up to the desired test velocities at the barrel exit, and to direct a cylindrical jet of the resultant dust suspension to impinge upon a flat target surface (1 inch by 2 inch) preset at a prescribed incidence angle between 20 and 90 degrees.

The distance from the specimen center line to the nozzle orifice was held constant at 1/2 inch. The dust concentration was controlled between $\approx$5-200 mg/ft^3, the normal range for dust clouds encountered in helicopter service. The maximum velocities of particles leaving the 10-foot-long acceleration nozzle were computed using aerodynamic formulas. Target erosion losses were measured and compared in terms of total target weight loss (mgs), corresponding target volume loss (cm^3 x 10^3), or target weight loss per gram of dust impacted. This last parameter is termed the erosion factor "ϵ" and is a bulk measure of the efficiency of the erosion process.

The exhaust gases from the test chamber were channeled selectively through a bifurcated duct (Figures 22 and 23). During the main part of a test run, the gas was conducted (right-hand path) through a series of centrifugal separators and baffles to remove the larger dust particles, and ultimately through a water trap to collect the finer particles, prior to entering the exhaust stack. For a few minutes of each run, the exhaust gas was diverted to the left path and through a 1 micron glass-fabric filter to collect used dust and eroded fragments of the target material for study.

Other features of the facility include adaptability to varying nozzle lengths (1/2-foot to 10 feet) and internal diameters (0.250 to 0.375 inch), a large glass view port to observe and photograph erosion phenomena, and a structurally reinforced test chamber with 5-ton hydraulic ram coupled to a tensile-grip specimen holder to transmit tensile stress to the specimen.

---

* The powder feeder used in Test Series II of the main program was a special unit designed and built by Giannini Scientific Corporation of Santa Ana, California. It is a rotary-wheel volume-metering unit which feeds precise quantities of test dust into the gas stream at the continuously controllable rate of 9.0 to 210 grams of silica or AR dust per hour. It worked well for powders of 50μ size or larger, but had a tendency to clog for the finer dust fractions ($\leq$50μ). Consequently, a mechanically simpler, gravity-feed unit was designed and built at Solar for the balance of the test program (Series III-VI). This feeder is described in Appendix III.

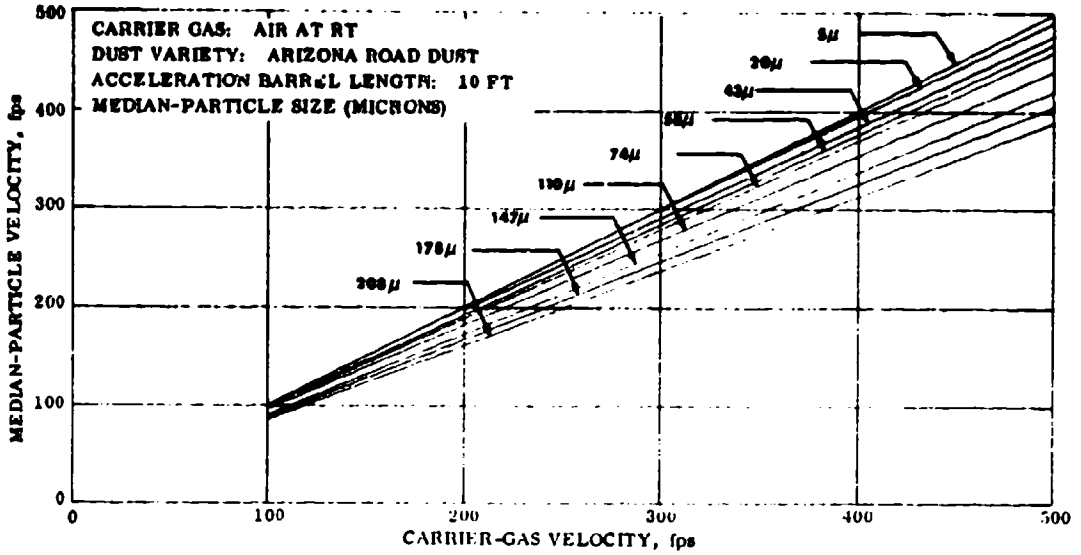

Figure 19. Correlation of Carrier-Gas Velocity With Dust Particle Velocity.

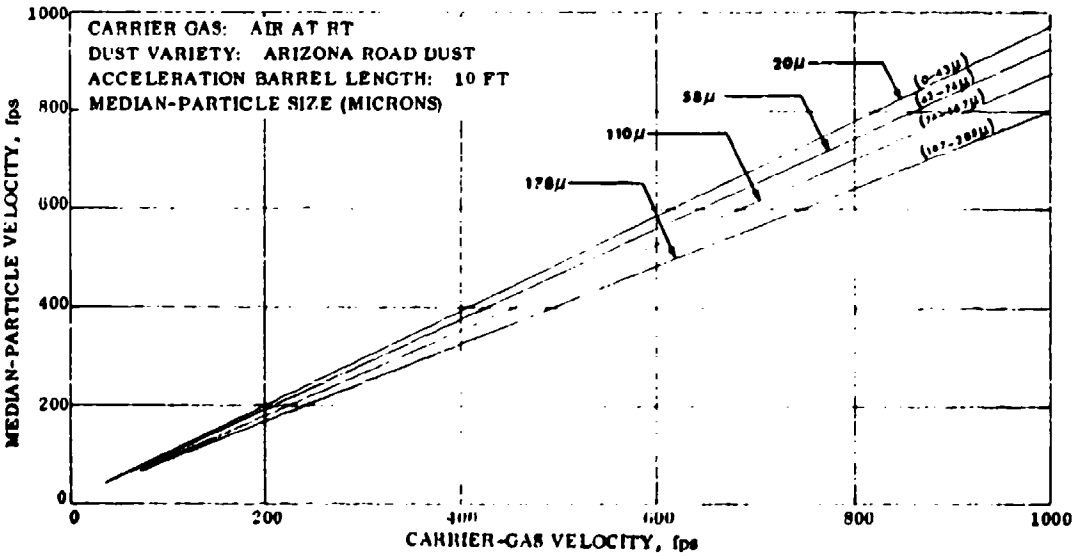

Figure 20. Correlation of Carrier-Gas Velocity With Dust Particle Velocity.

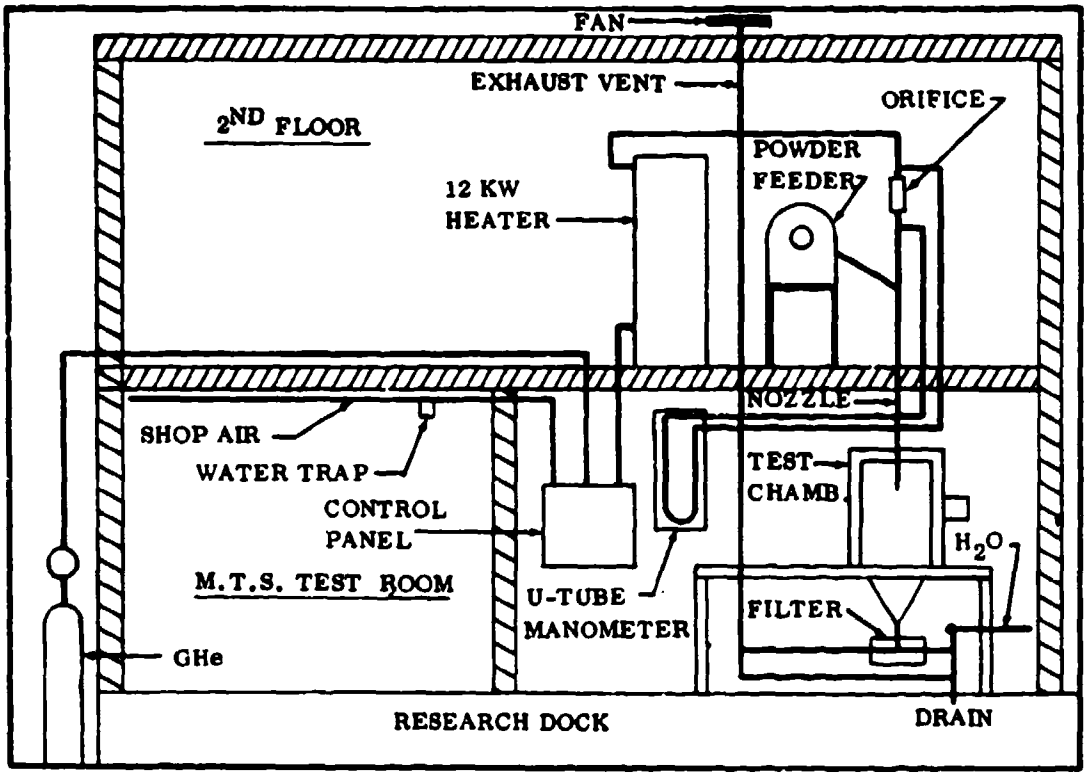

Figure 21. Schematic of New Erosion Test Facility.

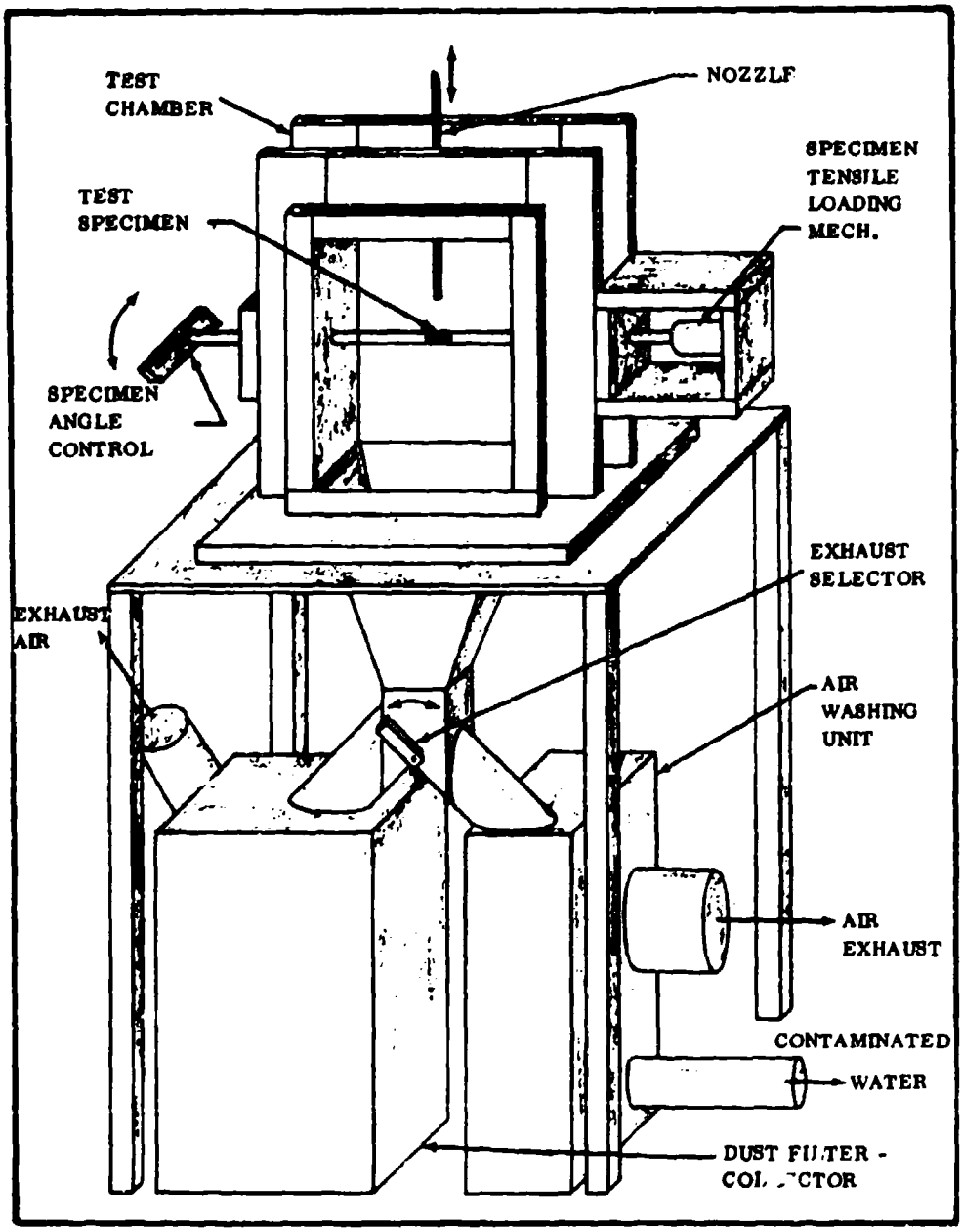

Figure 22. Schematic of Erosion Test Chamber and Dust Collection System.

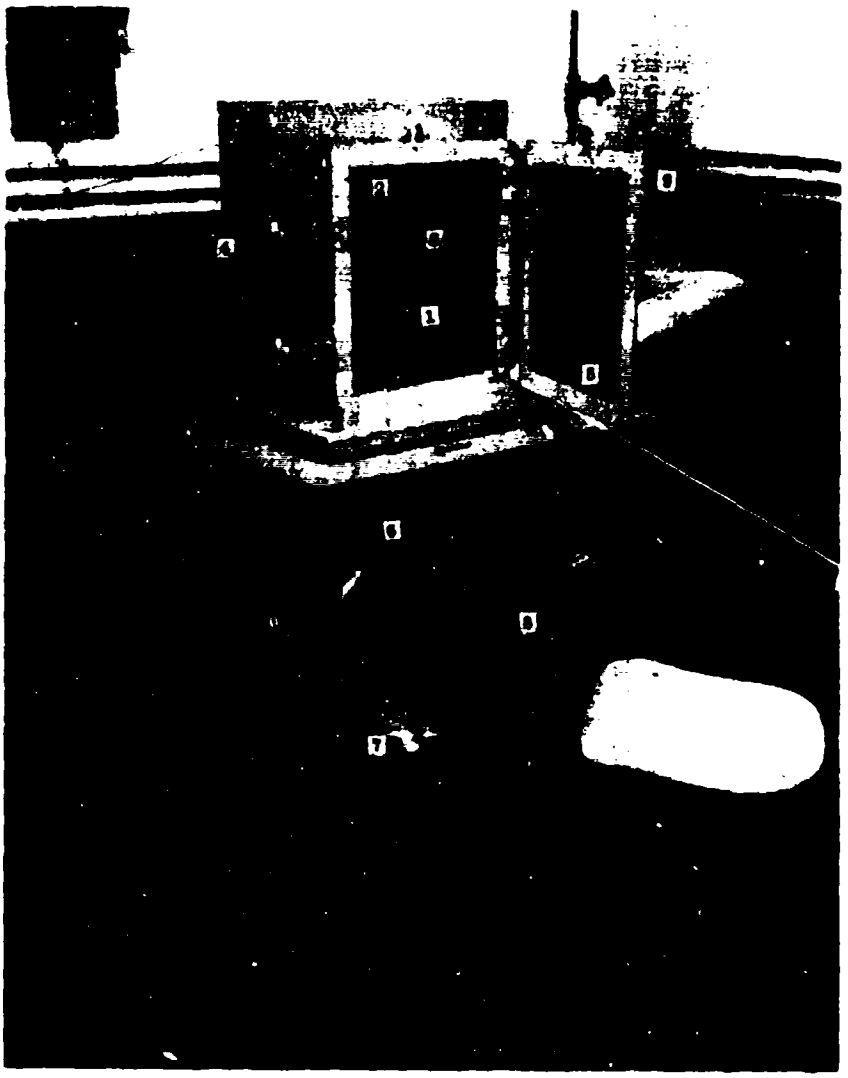

1. Erosion Test Chamber
2. Nozzle
3. Specimen Holder
4. Impingement Angle Control
5. Test Chamber Door, With View Port
6. Exhaust Path Selector
7. Collection Filter for Dust and Erosion Products
8. Exhaust Gas Scrubbing Unit
9. Exhaust Stack

Figure 23. Test Chamber and Dust Collection System (New Erosion Test Facility).

Series I testing was carried out using the existing erosion test rig described on page 7, while the larger test facility was under construction. This existing rig was modified only with a gravity-feed dust meter similar to that described in Appendix III (Compare Figures 3 and 24). The two rigs operate very similarly, the principal difference being a shorter, 3/8-inch I.D. by 2.0-foot-long acceleration nozzle, positioned horizontally (existing rig, Figure 24). Series I tests were conducted at sufficiently low particle velocities (500 and 650 fps) to permit the shorter acceleration distance.

Prior to Series I testing, carrier-gas velocity profiles were measured in the erosion test chamber at various distances (1/4 inch - 1 inch) from the nozzle exit. Maximum air velocity at the exit was maintained at 810 fps (Figure 25). Based upon these profiles, a nozzle exit to target specimen distance of 1/2 inch was chosen for testing. At this point, the maximum air velocity is still high (≈800 fps) and the velocity profile is reasonable flat over a lateral distance of about 0.20 inch on either side of the jet center line. This distance also makes specimen rotation convenient, with minimal back-pressure effects.

Employing the general solutions for particle acceleration developed in Appendix I, the following sample calculation is shown for the determination of required air velocity (U) at the nozzle exit for particle velocity (u) to be 650 fps (50μ Al_2O_3 dust). For the sake of realism, the lowest value of $u/U = \lambda$ arbitrarily permitted is 0.70. The maximum nozzle length that can be accommodated by the existing test rig is 2.0 feet (therefore, let S = required nozzle length for $\lambda = 0.70$).

Accelerating Particle: 50μ Al_2O_3, metallographic grade

Reynolds Number: $$R_e = \frac{U\, d_p\, \rho_{air}}{\mu_{air}} = 1.05\, U$$

where d_p = effective particle diameter assuming a spherical particle (ft)

ρ_{air} = density of air at 60° F and 1 atmosphere static pressure
= 0.0765 lb/ft^3

μ_{air} = absolute viscosity of air at 60° F and 1 atmosphere static pressure
= 0.0432 lb/hr-ft

Time Constant, $\tau = \rho d_p^{\,2}/18\mu_{air}$

where ρ = particle density = 4.0 x 62.4 lb/ft^3

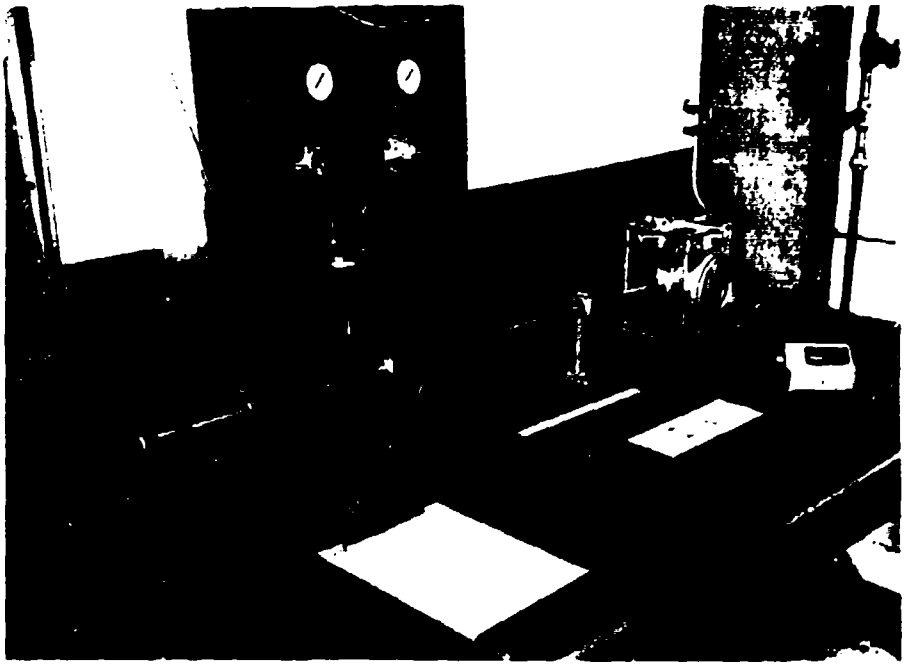

Figure 24. Existing Erosion Test Rig Setup for Series I Testing (Note 2-Foot Nozzle Between Arrows).

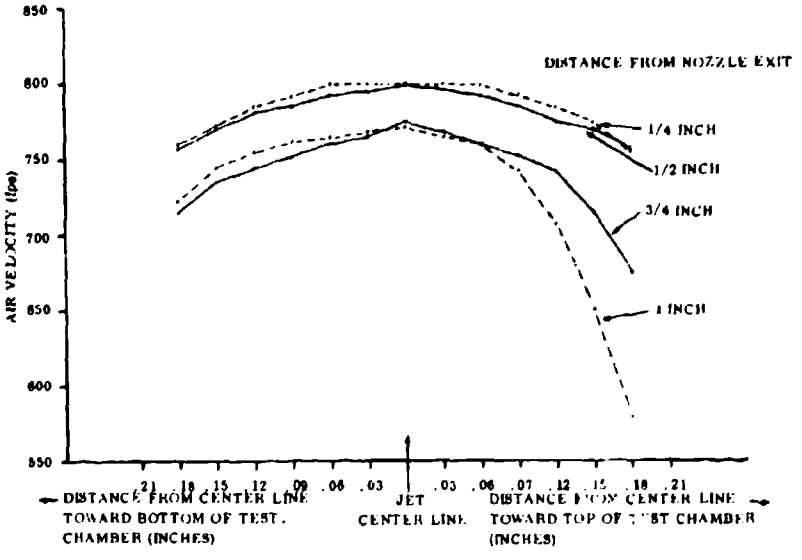

Figure 25. Gas Velocity Profiles of the Air Jet Used in Series I Tests.

In this situation,

$u = 650$ fps

$S = 2.0$ ft (maximum)

$\tau = 31.6$ milliseconds

$R_e = 1.05\ U$

$S_o = U\tau = 0.031\ U$ ft

Inasmuch as $\lambda = u/U$ is restricted to 0.70 minimum, and this minimum value will yield the lowest corresponding value for required nozzle length, S is determined from the curves in Appendix I.

where $\lambda = u/U = 0.70$

$\therefore U = 930$ fps

$R_e = 975$

$S/S_o = 0.070$

$S_o = 28.8$ ft

$S = 2.02$ ft

From the first trial calculation, it can be seen that an air velocity of 930 fps is required for a nozzle length of 2.02 feet.

SELECTION AND PREPARATION OF TEST DUSTS AND TARGET MATERIALS

Target Materials

Target materials were chosen on the basis of their applicability as compressor blade and vane alloys. Current usage is predominantly with the martensitic types of stainless steels, although the future trend is toward alloys of titanium and aluminum, because of weight advantages.

The high-strength, corrosion-resistant stainless steels (Type 410, 17-7 PH, AM-350, etc.) can be considered definite candidates for all stages of compressor blading, operating from room temperature and 1 atmosphere static pressure up to 800° F and 16 atmospheres. The newer precipitation hardening steels, such as 17-7 PH and AM-350, offer advantages in strength/density, general corrosion and stress corrosion resistance as well as maximum operating temperature (i.e., 1200° F versus 1000° F) over the more commonly used 410 or 403 stainless.

Aluminum or titanium, attractive for their lighter weight and comparable strength/density and modulus/density ratios, would safely experience narrower ranges of gas temperature, pressure, and velocity because of maximum service temperature limitations. Even the stronger forged aluminum alloys, such as types 2024, 6066, and 7075, lose useful strength rapidly above 350°-400° F, which restricts their application to the first few stages (maximum metal temperature of ≈375° F and maximum static pressure of ≈4 atmospheres). Likewise, the better current titanium alloys (e.g., Ti-6Al-4V or Ti-8Al-1Mo-1V) cannot be applied confidently above about 700° F, even though their short-term tensile strengths are retained well up to 1000° F. The reason for the lower temperature limitation is inordinately low creep strengths above 700° F; dimensional instability cannot be tolerated in close-running, highly stressed, rotating blade applications. Surface oxidation and embrittlement of titanium in long-term service can also be problems above 700° F. With these restrictions, titanium alloys could be applied reliably only to the intermediate compressor stages (maximum metal temperature of ≈675° F and maximum static pressure of ≈10 atmospheres).

In spite of their different limitations in compressor applications, however, all aluminum, titanium, and steel alloy targets were erosion tested under similar regimes of temperature, particle velocity, etc. This was done to obtain direct comparisons of their relative erosion behaviors in order to study erosion mechanisms on all candidate alloy bases (i.e., Fe, Al, and Ti).

The target alloys ultimately selected were representative of current and advanced compressor blade materials: two stainless steels (types 410 and 17-7 PH), one titanium alloy (Ti-6Al-4V), and one aluminum alloy (type 2024).

A sufficient quantity of each target material was procured in single-sheet form (0.080 inch thickness) for the entire experimental program. The target alloys were purchased to proper Aerospace Material Specifications (AMS): AMS-4911A (Ti-6Al-4V, annealed), AMS-5055 (type 410 stainless steel, annealed), AMS-5528A (Type 17-7 PH stainless steel, annealed), and AMS-4035D (type 2024 aluminum alloy, annealed). The surface finish of the sheet alloys was designated 2D, except for the aluminum alloy which was Medium Matte (etched).

Standard target specimens (each 0.080 inch by 1 inch by 2 inch) were machined from the main sheets and heat treated either to the annealed (soft, low strength) condition or a typical service condition (relatively hard, high strength) prior to being erosion tested. The heat treatments and their effects upon target hardness and RT yield strengths are given in Table III.

TABLE III. TARGET MATERIALS: HARDNESS AND STRENGTH VARIATION WITH HEAT TREATMENT

Target Alloy (Heat Treatment Designation)	Condition	Average Hardness (RT) Rockwell Number			Typical 0.2% Yield Strength, RT (ksi)
		A	B	C scale	
Aluminum Alloy (2024-0)	Annealed[1]	10.0	1	--	11
(2024-T6)	Service Heat[2] Treatment	48.5	78	--	55
Ti-6Al-4V	Annealed[3]	66.5	--	32	125
Ti-6Al-4V	Service Heat[4] Treatment	71.5	--	42	165
410 Stainless Steel	Annealed [5]	52.0	84	--	35
410 Stainless Steel	Service Heat[6] Treatment	64.5	--	28	120
17-7 PH Stainless Steel	Annealed[7]	53.5	97	--	50
17-7 PH Stainless Steel	Service Heat[8] Treatment	71.5	--	42	185

(1) 775° F, 2-3 hrs, FC at 50° F/hr to 500° F, AC
(2) 920° F, 45 min, water quench to RT; age at 375° F, 16 hrs
(3) 1300° -1650° F, 1 hr (inert atmosphere; controlled colling per AMS-4911B)
(4) 1650° F, 20 min (inert atmosphere), water quench to RT + 900° F, 5 hrs (inert atmosphere) FC
(5) 1550° F, 1 hr, FC at 24-50° F/hr to 1100° F, then AC to RT
(6) 1750° F, 30 min, AC to RT + Temp at 1100° F for 2 hrs
(7) 1900° F, 1-2 hrs, AC (Condition A)
(8) 1400° F, 1-1/2 hrs, AC to below 60° F but above 32° F, hold 1 hr + 1050° F, 1-1/2 hrs, AC (Condition TH)

Test Dusts

Two varieties of surface soil were selected to represent the most troublesome dusts occurring in nature: Arizona Road Dust, supplied by AC Spark Plug Division of General Motors Corporation, and a lateritic soil from Pleiku, Vietnam, representative of Southeast Asia. Arizona Road Dust is a heterogeneous mixture of minerals collected from the Arizona desert region (Table IV). The principal constituents are silica (SiO_2, $\approx 68.5\%$) and alumina (Al_2O_3, $\approx 16.0\%$). Laterite is a heterogeneous and variable mixture of hydrous aluminum oxides and iron oxides. A request was made to the Contracting Officer for information regarding the most troublesome variety or varieties of laterite in Vietnam. It was reported that laterite from the Central Highlands of Vietnam appeared to be the most erosive species from helicopter experience. Pleiku is in this region. Other erosive soils collected from beach and lowland areas of Vietnam showed a marked similarity to the Arizona Road Dust, particularly with regard to their high silica contents (Appendix IV).

A third test dust selected was metallographic grade, pure alumina powder, a commercial abrasive. Alumina is appreciably harder, stronger and more refractory than silica, and it was chosen to help determine whether these properties influence erosiveness. Alumina is also compatible with the programmed evaluation of laterite soils, which have a high alumina content. Figure 26 is a macrophotograph of a sample of the metallographic grade alumina. The particles are quite blocky and angular, and have maximum width dimensions ranging from about 40 to 80 microns. About 70 percent lie within the 40-50-micron range (240 grit).

Eight hundred pounds of coarse Arizona Road Dust (No. 1543637, Table IV) were ordered and sent to Michigan Technological University, Houghton, Michigan, for subsequent grading and classification to desired particle size fractions (0-43μ, 43-74μ, 74-147μ, and 147-210μ). This order supplied sufficient test dusts for all test series.

The fractions were prepared by a combination of air classification and dry screening. Wet screening (originally planned) was not employed because of the tendency of the fines to cake and the difficulties involved in recovering and drying the solids. The weights of the individual fractions obtained from the 800 pounds of starting material were as follows:

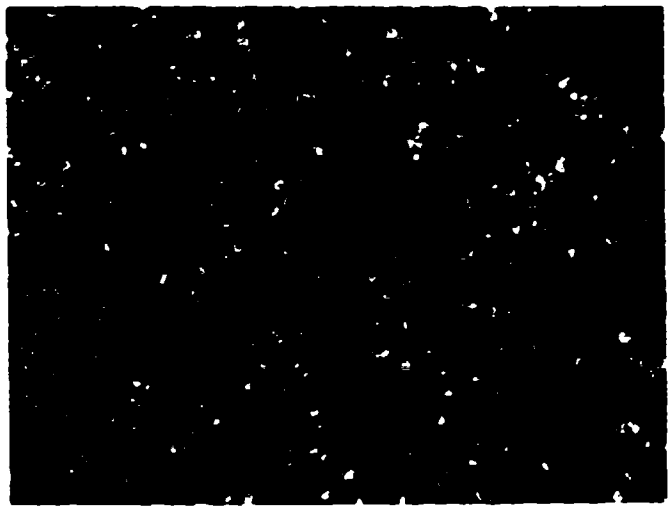

Figure 26. Macrophotograph of Metallographic Grade Alumina Powder, 240 Grit. Magnification: 25X

Fraction	Weight (lb)
-43 microns (-325 mesh)	489.0
-74/+43 microns (-200/+325 mesh)	146.0
-147/+74 microns (-100/+200 mesh)	134.0
-208/+147 microns (-65/+100 mesh)	13.5
+208 microns (+65 mesh)	1.1
Total	783.6

Screen analyses (size distributions) of the various fractions are listed below:

	Percent Composition (Wt) of Nominal Fraction			
Fraction	-43μ	-74/+43μ	-147/+74μ	-208/+147μ
+208μ	0.00	0.00	0.00	0.01
-208/+147μ	0.00	0.00	0.40	**94.35**
-147/+74μ	0.05	4.82	**95.43**	5.62
-74/+43μ	3.50	**81.92**	4.10	0.02
-43μ	**96.45**	13.26	0.07	0.00
Totals	100.00	100.00	100.00	100.00

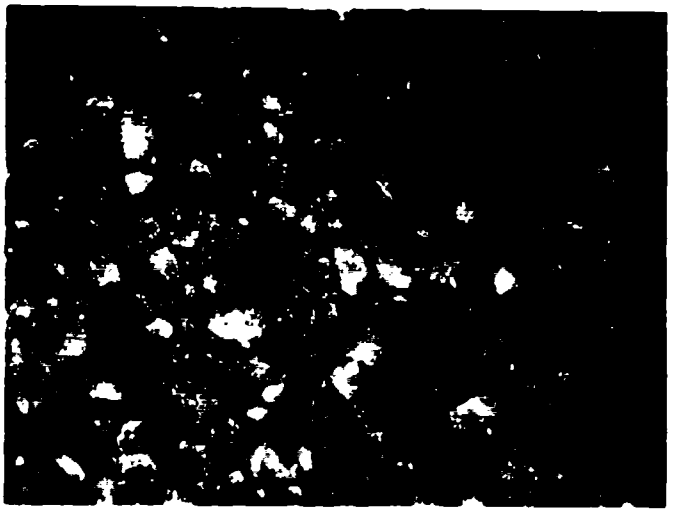

Figure 27. Macrophotograph of Arizona Road Dust (74-147μ). Magnification: 25X

The typical angular forms of the constituent silica particles in the Arizona Road Dust are very evident in Figure 27.

A search for a suitable lateritic variety of test dust was conducted. Samples of three different Vietnamese soils were obtained from the U.S. Army Aviation Systems Command: one from Cam Ranh Bay, another from Pleiku, and the third from An Khe. On the basis of chemical analyses performed by the Army and microscopic examination at Solar, the soils from Cam Ranh Bay and An Khe are not laterites, but are high in silica sand (77-95%), with a total compositional make-up very similar to the Arizona Road Dusts. The soil from Pleiku was concluded to be lateritic in nature, with a silica content (free and combined) of only 36.7 percent. The soil is characterized by a preponderance of spherical or angular aggregates (pisolites) made up of very fine constituent particles, typical of laterites. X-ray fluoresence analysis at Solar indicated the following approximate concentrations (by weight) of metallic elements: iron (25%), aluminum (13%), silicon (20%), titanium (1%), potassium (1%), with traces of calcium and manganese. This analysis indicates a laterite soil of about equal proportions of iron and aluminum (hydrous) oxides, on an atomic basis. A petrographic analysis of the Pleiku soil was requested of the minerology and soil specialists at Michigan Technological University, Houghton, Michigan. Their analyses are given in Appendix IV. The petrographic study stated that the Pleiku soil consists of approximately 80-90 percent tropical "clay" in angular aggregates typically 30-100 microns in size. (The balance is predominantly particles of quartz (≤10%), and feldspar, both mostly ≥50μ). The constituent particles of the aggregates are too fine (colloidal) to be resolved by light microscopy (≤1.0 micron). Presumably the "clay" or laterite base is a mixture of hydrous iron and aluminum oxides,

TABLE IV. SPECIFICATION SHEET FOR ARIZONA ROAD DUST

Classified from natural Arizona dust. Prepared by the AC Spark Plug Division, General Motors Corporation, Flint, Michigan. Particle-size distribution determined with Roller Air Analyzer.

RAW DUST AS RECEIVED FROM PHOENIX, ARIZONA

Particle-Size Distribution		Chemical Analysis		Average Wet Screen Analysis	
0 - 5 Microns	4.6%	Ignition Loss	2.68%	-325 Screen	38.3%
5 - 10 "	3.0%	SiO_2	68.47%	-200 to 325 Screen	14.0%
10 - 20 "	5.8%	Fe_2O	4.58%	-150 to 200 Screen	6.1%
20 - 40 "	23.8%	Al_2O_3	15.98%	-100 to 150 Screen	5.0%
Over 40 "	62.7%	MgO	0.77%	- 70 to 100 Screen	6.0%
		CaO	2.91%	- 50 to 70 Screen	4.6%
		Total Alkalis as Na_2O	4.61%	- 30 to 50 Screen - 14 to 30 Screen	11.2% 14.8%

STANDARDIZED TEST DUST AS PREPARED

1543094 - Fine Grade Particle-Size Distribution		1543637-Coarse Grade Particle-Size Distribution	
0 to 5 Microns	39 ± 2%	0 to 5 Microns	12 ± 2%
5 to 10 "	18 ± 3%	5 to 10 "	12 ± 3%
10 - 20 "	16 ± 3%	10 - 20 "	14 ± 3%
20 - 40 "	18 ± 3%	20 - 40 "	23 ± 3%
40 - 80 "	9 ± 3%	40 - 80 "	30 ± 3%
		80 - 200 "	9 ± 3%

based upon its preponderance in the soil sample, its brown color, and the X-ray fluorescence analysis of the total soil samples. Laterite is usually described as a variable mixture of very finely divided (often colloidal) limonite ($FeO(OH) \cdot nH_2O$) and bauxite (approx. $Al(OH)_3$). Both of these hydrous aluminum and iron oxides are of variable compositions, frequently with appreciable impurity content. Laterite is a common variety of weathered, sedimentary soil in wet, tropical countries, and is extremely stable. When wet, it is soft and pliable, like clay in appearance. When it dries out, it reverts to quite hard and porous aggregates, which tend to form adhesive concretions on surfaces.

One hundred pounds of the Pleiku soil were obtained for test purposes. Subsequently, the dust was graded and classified by dry screening the soil at Solar into size fractions similar to the Arizona Road Dust.

TECHNIQUES OF ELECTRON MICROSCOPY FOR EROSION SURFACES

The main purpose of this phase of the investigation was to observe the physical alteration of target metal surfaces resulting from the impact of individual dust particles as well as the superimposed impacts of many particles. The phenomenological evidence thus obtained proved to be useful for determining the probable events constituting the erosion mechanism.

After erosion testing, two stage replicas were made of the target surfaces using germanium as the shadowing material and carbon for structural support. The replicas were viewed in a Phillips 100C electron microscope operated at 80 K.V. Some erosion surfaces were viewed directly with the Cambridge "Stereoscan" scanning electron microscope.

To study individual dust particle impacts, a very small weight of powder or dust was used to produce only about 10,000 impacts per specimen. This contrasts markedly with the 50- to 80-million superimposed particle impacts typical of the standard erosion test surfaces.

To ensure that the structural features observed in the electron microscope were only a function of particle impact and not a result of as-processed target surface roughness, the test coupons were carefully polished with 1.0μ Al_2O_3 powder prior to erosion testing.

EROSION TEST RESULTS AND DISCUSSION

TEST SERIES I - EFFECTS OF VARIABLE METALLURGICAL STRUCTURE AND STRENGTH OF THE TARGET ALLOY

The principal objectives of Series I testing were to characterize the type of erosion response (ductile or brittle) and the incidence angle for maximum erosion loss for each target material. An essential part of this work was studying the influence of metallurgical structure on erosion response and rate. Target materials were tested in their softest, weakest condition (annealed structures) as well as heat treated to significantly higher strength and hardness levels (Table III).

All tests were conducted in triplicate with room temperature air as the carrier gas. Gas velocity was standardized at 810 fps, with a calculated particle velocity at the target surface of 500 fps for nominally 50-micron alumina (Al_2O_3) dust and 650 fps for 43-74-micron Arizona Road Dust (also nominally 50 microns). Microscopic examination of the two test dusts revealed that they were essentially identical in particle size, so that the effects of dust variety and density could be ascertained at a constant particle energy and particle size.

The carrier-gas velocity was chosen so that the kinetic energy levels of individual 50-micron particles of both Al_2O_3 and SiO_2 dusts are approximately the same. Each particle's energy is proportional to the product of its density and the square of its predicted velocity prior to impact.

$$SiO_2: \quad 2.45 \text{ gm/cc} \times (650 \text{ ft/sec})^2 = 1.07 \times 10^6$$

$$Al_2O_3: \quad 4.00 \text{ gm/cc} \times (500 \text{ ft/sec})^2 = 1.00 \times 10^6$$

The predicted velocity for SiO_2 particles (2-foot nozzle) is higher than for Al_2O_3 particles because of silica's lower density (Appendix I).

An intermediate dust concentration of 19 mg/ft^3 STP (80 mg/ft^3 at the nozzle exit) was selected for a preliminary study of the influence of test duration upon erosion rate for all annealed target materials. Cumulative test times of 5, 10, and 15 minutes were programmed on single specimens with total dust charges of 15.0, 30.0, and 45.0 grams, respectively (see Figures 28 through 31). The objective was to determine a suitable test time (and dust charge) from the linear portion of the cumulative erosion loss versus cumulative time relation, remote from transient starting phenomena, etc. For all target materials and all impingement angles tested (20, 30, 45, 60, and 90 degrees), the linearity of the test data was remarkably good, with 30 degrees impingement developing the maximum rate of erosion. Consequently, the intermediate test time of 10 minutes and dust charge of 30.0 grams

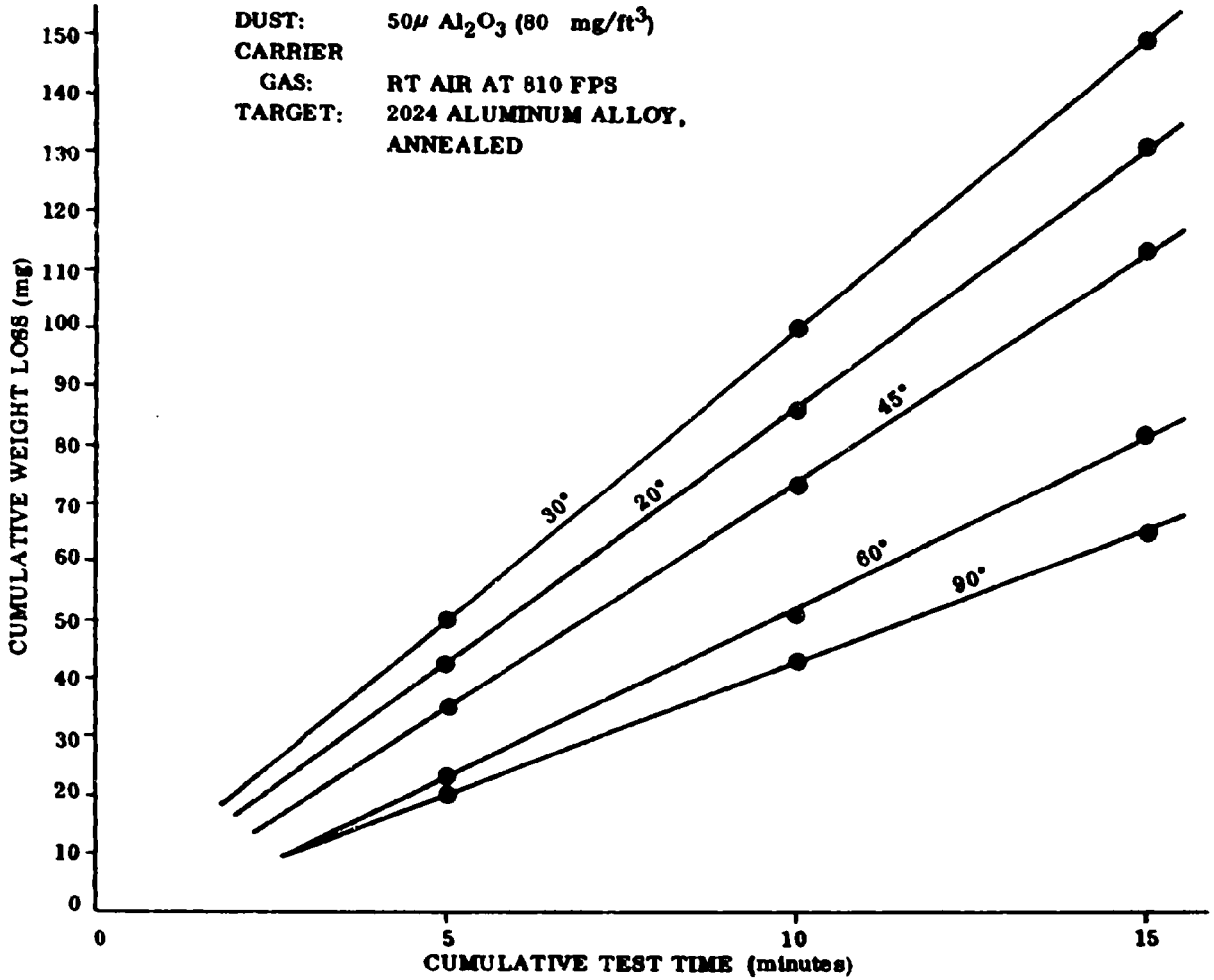

Figure 28. Cumulative Erosion Weight Loss Versus Cumulative Test Time. Test Series I - Preliminary.

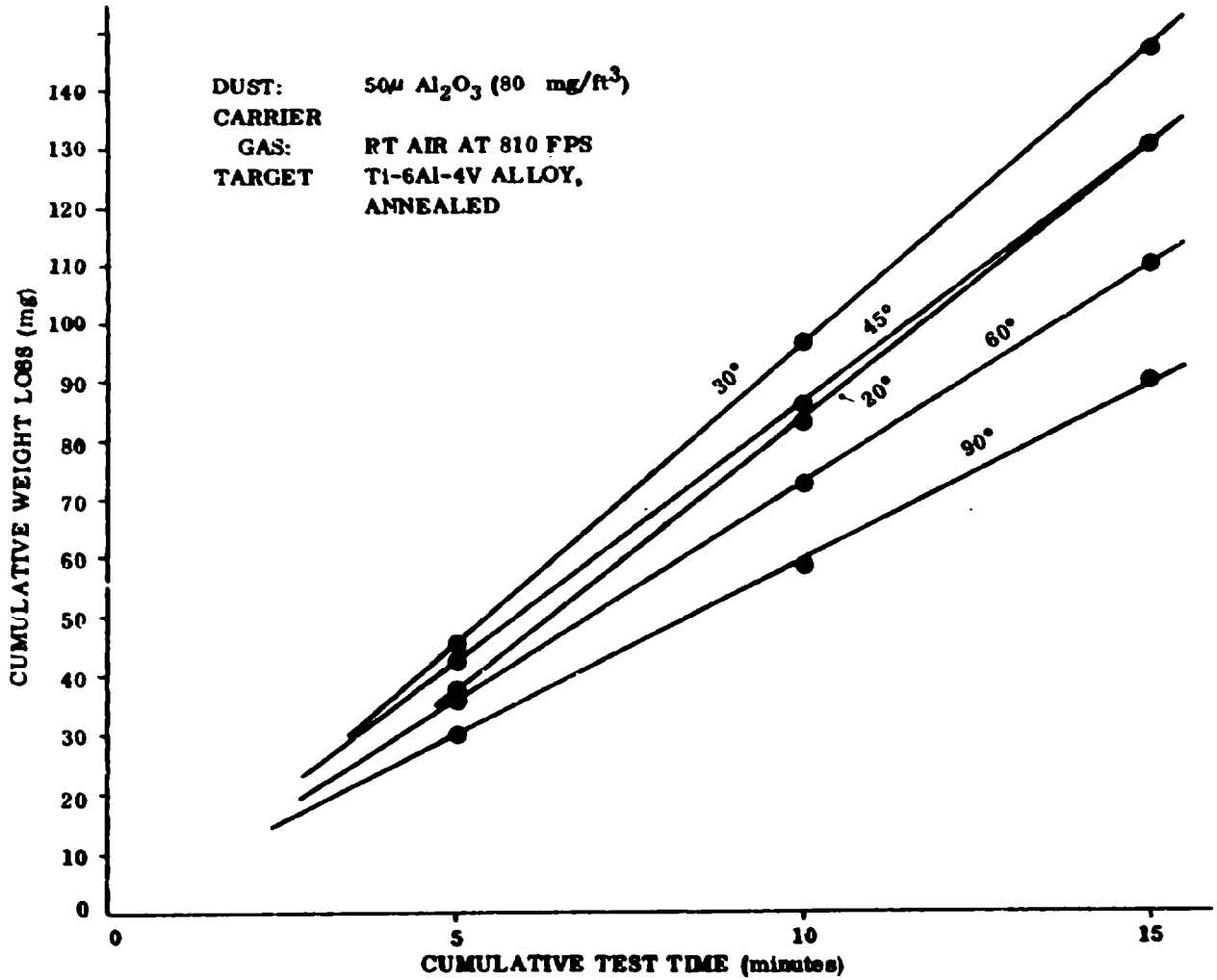

Figure 29. Cumulative Erosion Weight Loss Versus Cumulative Test Time. Test Series I - Preliminary.

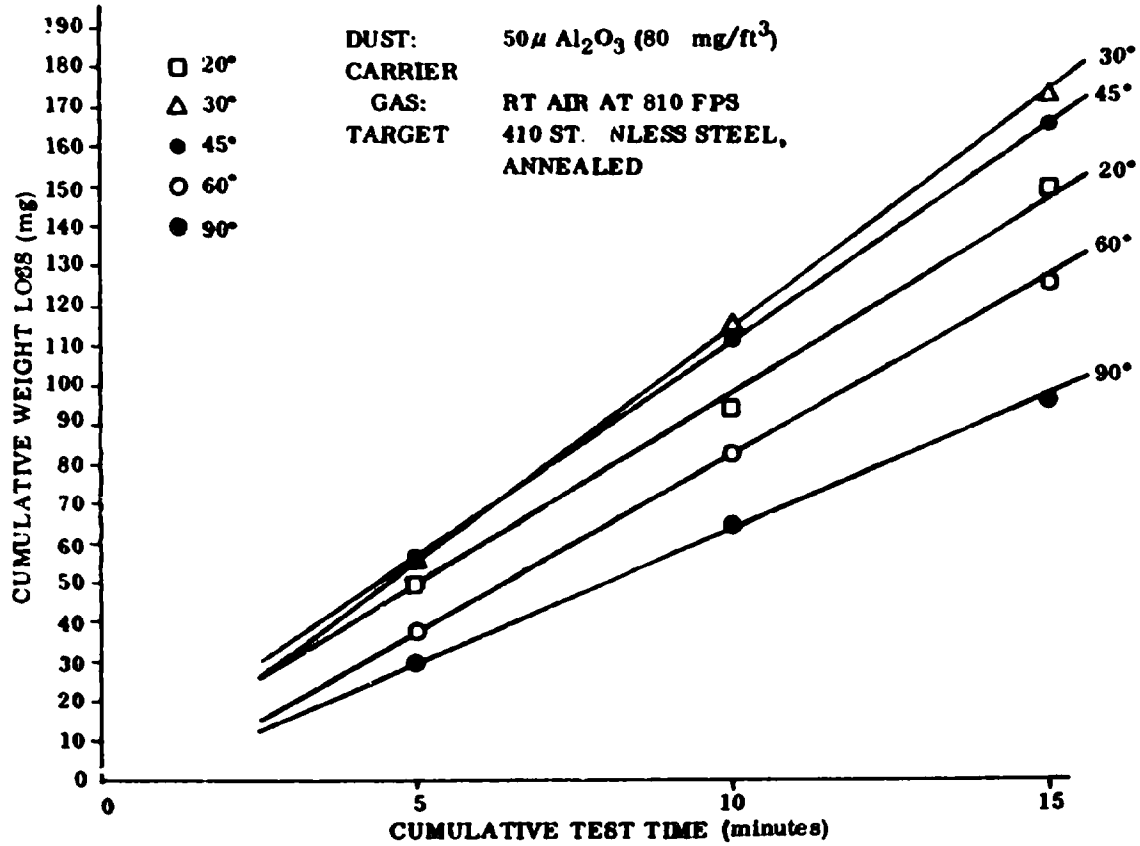

Figure 30. Cumulative Erosion Weight Loss Versus Cumulative Test Time. Test Series I - Preliminary.

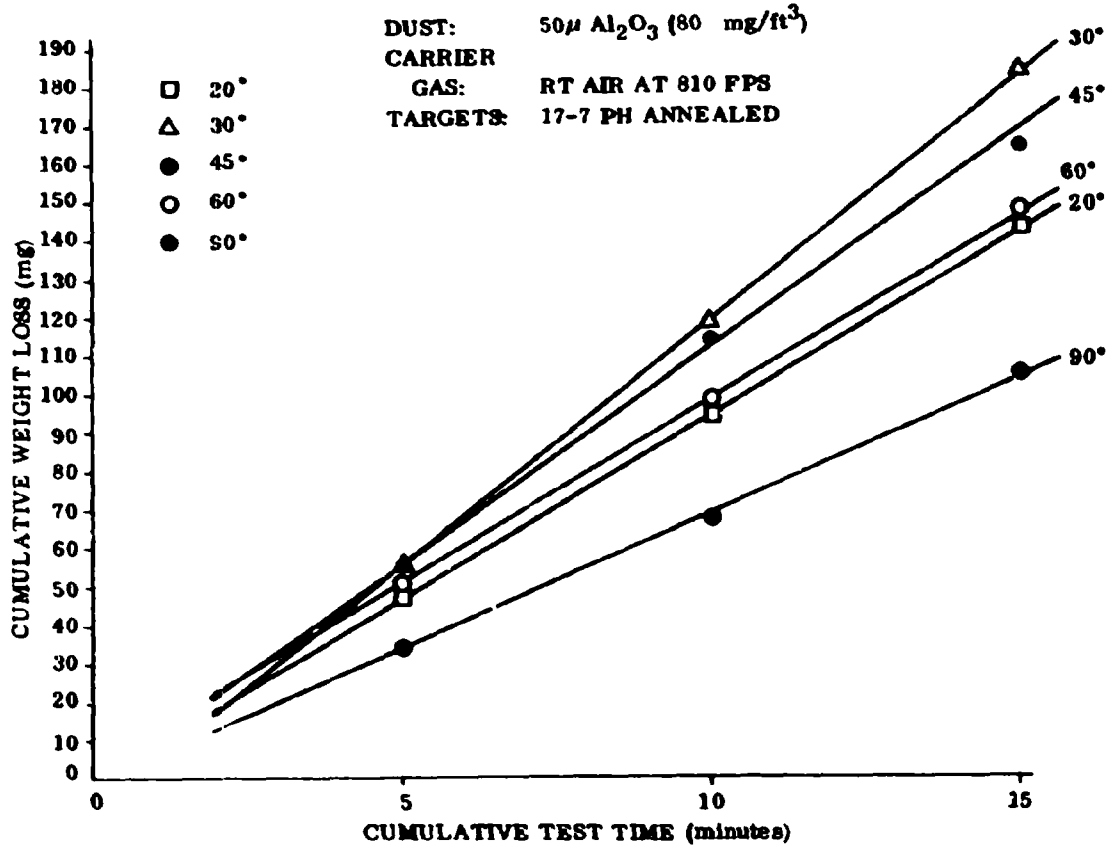

Figure 31. Cumulative Erosion Weight Loss Versus Cumulative Test Time. Test Series I - Preliminary.

were chosen as standard for Series I testing, along with the intermediate dust concentration of 19 mg/ft^3 STP.

The original plan for the main program called for testing at the following angles of incidence: 10, 20, 30, 45, 60, and 90 degrees. During the testing, it became apparent that the maximum rates of erosion occur between the angles of 20 and 45 degrees. Therefore, two additional intermediate angles were added to the test plan (25 and 37.5 degrees), and the 10-degree impingement angle was dropped. In an attempt to factor out operator and equipment bias, the majority of the erosion tests were conducted using a random order of testing. To determine the importance of random testing, one incidence angle with alumina dust (37.5 degrees) and two incidence angles with Arizona Road Dust (30 and 37.5 degrees) were tested in a numerical (sequential) testing order for comparison. No apparent differences in the scatter or other characteristic form of the test data distribution due to testing order were noted (see Tables V and VI). Consequently, random testing order was not employed in subsequent test series.

Erosion data in terms of target weight loss, target volume loss, and average erosion factor have been tabulated (see Tables V and VI for results with alumina dust and Arizona Road Dust, respectively). Target weight loss or target volume loss versus impingement angle are plotted in Figures 32 through 35. In Figure 32, the erosion data for the annealed and the fully heat treated conditions (averages) are shown separately. In subsequent figures, all data for the annealed and fully heat treated conditions are averaged together for each target material.

Effect of Impingement Angle Variation

All of the target materials, whether annealed or fully heat treated, typically exhibited ductile erosion responses. (The ductile response is characterized by the maximum erosion loss occurring at an intermediate angle, normally between 20 and 45 degrees.) For the specimens tested with Al_2O_3 dust, maximum losses occurred at the 30-degree angle (single exception, 410 stainless steel at 37.5 degrees). Specimens tested with Arizona Road Dust uniformly showed peak losses at the 37.5-degree angle (compare Figures 32, 33, 34, and 35).

Effect of Metallurgical Condition of Target Alloy

If erosion is related to target heat-treat condition, the appreciable differences in yield (minimum flow) strengths between the annealed and fully heat-treated conditions for the target alloys (see Table III) should produce correspondingly marked differences in the measured erosion factors. For example, in the fully heat treated conditions, the two steels and the aluminum alloy have room-temperature strengths ≈3.0-4.5 times higher than in the annealed conditions. For room-temperature

TABLE V. SERIES I TEST DATA, 50μ ALUMINA TEST DUST

Erosion Test Data - Series No. 1
Nozzle Dia. 3/8 in. Nozzle Length 2 ft
Nozzle Pressure 47 psi Line Pressure 67 psi
Gas Composition Shop Air Gas Temperature RT
Barometric Pressure Sea Level Powder Feeder Pressure and Setting: 30 psi
(Total Weight of Dust Consumed per Test = 30.0 gm)

Specimen Number	Target Material	Median-Particle Velocity (fps)	Impingement Angle (deg)	Dust Variety	Dust Concentration (mg/ft^3)	Test Duration (min)	Nominal Initial Specimen Weight (gm)	Specimen Volume loss ($cm^3 \times 10^{-3}$)	Specimen Weight loss (mg)	Erosion Factor, ε ($\times 10^{-3}$)
• 4	2024-0	500	20	Al_2O_3	80.	10.	7.40		77.4	
5	Al Alloy	500	20	(50μ)	80.	10.	7.40		65.3	
6	(An-									
	nealed)	500	20		80.	10.	7.40		75.4	
Average								26.4	72.7	
• 22	2024-T6	500	20	Al_2O_3	80.	10.	7.40		85.9	
23	Al Alloy	500	20	(50μ)	80.	10.	7.40		81.1	
24	(S.T. and									
	Aged)	500	20		80.	10.	7.40		59.9	
Average								27.2	75.2	
Overall Averages								26.8	74.0	2.48
• 1	2024-0	500	25	Al_2O_3	80.	10.	7.40		104.0	
2	(An-			(50μ)						
	nealed)	500	25		80.	10.	7.40		98.2	
3		500	25		80.	10.	7.40		112.8	
Average								28.1	105.0	
• 19	2024-T6	500	25	Al_2O_3	80.	10.	7.40		92.9	
20	(S.T. &			(50μ)						
	Aged)	500	25		80.	10.	7.40		93.6	
21		500	25		80.	10.	7.40		98.9	
Average								34.4	95.1	
Overall Averages								36.3	100.1	3.34

• Random Testing Order

TABLE V - Continued

Erosion Test Data - Series No. 1
Nozzle Dia. 3/8 in. Nozzle Length 2 ft
Nozzle Pressure 47 psi Line Pressure 67 psi
Gas Composition Shop Air Gas Temperature RT
Barometric Pressure Sea Level Powder Feeder Pressure and Setting: 30 psi
(Total Weight of Dust Consumed per Test = 30.0 gm)

	Specimen Number	Target Material	Median-Particle Velocity (fps)	Impingement Angle (deg)	Dust Variety	Dust Concentration (mg/ft^3)	Test Duration (min)	Nominal Initial Specimen Weight (gm)	Specimen Volume loss ($cm^3 \times 10^{-3}$)	Specimen Weight loss (mg)	Erosion Factor, ε ($\times 10^{-3}$)
•	7	2024-0	500	30	Al_2O_3	80.	10.	7.40		105.2	
	8	(An-			(50μ)						
		nealed)	500	30		80.	10.	7.40		94.1	
	9		500	30		80.	10.	7.40		104.4	
	Average								36.7	101.2	
•	25	2024-T6	500	30	Al_2O_3	80.	10.	7.40		113.0	
	26	(S.T. &	500	30	(50μ)	80.	10.	7.40		114.4	
	27	Aged)	500	30		80.	10.	7.40		94.8	
	Average								39.0	107.4	
	Overall Averages								37.8	104.3	3.48
••	AL1	2024-0	500	37.5	Al_2O_3	80.	10.	7.40		106.1	
	AL2	(An-			(50μ)						
		nealed	500	37.5		80.	10.	7.40		104.7	
	AL3		500	37.5		80.	10.	7.40		101.5	
	Average								37.7	104.1	
••	AL4	2024-T6	500	37.5	Al_2O_3	80.	10.	7.40		98.8	
	AL5	(S. T. &	500	37.5	(50μ)	80.	10.	7.40		100.7	
	AL6	Aged)	500	37.5		80.	10.	7.40		99.2	
	Average								36.1	99.5	
	Overall Averages								36.9	101.9	3.39
•	10	2024-0	500	45	Al_2O_3	80.	10.	7.40		96.5	
	11	(An-			(50μ)						
		nealed)	500	45		80.	10.	7.40		76.6	
	12		500	45		80.	10.	7.40		79.1	
	Average								30.51	84.1	

• Random Testing Order ••Sequential Testing Order

TABLE V - Continued

Erosion Test Data - Series No. I
Nozzle Dia. 3/8 in. Nozzle Length 2 ft
Nozzle Pressure 47 psi Line Pressure 67 psi
Gas Composition Shop Air Gas Temperature RT
Barometric Pressure Sea Level Powder Feeder Pressure and Setting: 30 psi
(Total Weight of Dust Consumed per Test = 30.0 gm)

	Specimen Number	Target Material	Median-Particle Velocity (fps)	Impingement Angle (deg)	Dust Variety	Dust Concentration (mg/ft^3)	Test Duration (min)	Nominal Initial Specimen Weight (gm)	Specimen Volume loss ($cm^3 \times 10^{-3}$)	Specimen Weight loss (mg)	Erosion Factor, ϵ ($\times 10^{-3}$)
*	28	2024-T6	500	45	Al_2O_3	80.	10.	7.40		100.1	
	29	(S. T. &	500	45	(50μ)	80.	10.	7.40		60.9	
	30	Aged)	500	45		80.	10.	7.40		87.5	
	Average								30.0	82.8	
	Overall Averages								30.3	83.5	2.78
*	13	2024-0	500	60	Al_2O_3	80.	10.	7.40		62.1	
	14	(An-			(50μ)						
		nealed)	500	60		80.	10.	7.40		103.0	
	15		500	60		80.	10.	7.40		65.1	
	Average								27.8	76.7	
*	31	2024-T6	500	60	Al_2O_3	80.	10.	7.40		83.3	
	32	(S. T. &	500	60	(50μ)	80.	10.	7.40		70.8	
	33	Aged)	500	60		80.	10.	7.40		64.9	
	Average								26.4	73.0	
	Overall Averages								27.1	74.9	2.50
*	16	2024-0	500	90	Al_2O_3	80.	10.	7.40		50.6	
	17	(An-			(50μ)						
		nealed)	500	90		80.	10.	7.40		51.6	
	18		500	90		80.	10.	7.40		75.5	
	Average								21.4	59.2	
*	34	2024-T6	500	90	Al_2O_3	80.	10.	7.40		41.9	
	35	(S. T. &	500	90	(50μ)	80.	10.	7.40		49.9	
	36	Aged)	500	90		80.	10.	7.40		52.5	
	Average								17.4	48.1	
	Overall Averages								19.4	53.7	1.79

* Random Testing Order

TABLE V - Continued

Erosion Test Data - Series No. I
Nozzle Dia. 3/8 in. Nozzle Length 2 ft
Nozzle Pressure 47 psi Line Pressure 67 psi
Gas Composition Shop Air Gas Temperature RT
Barometric Pressure Sea Level Powder Feeder Pressure and Setting: 30 psi
(Total Weight of Dust Consumed per Test = 30.0 gm)

	Specimen Number	Target Material	Median-Particle Velocity (fps)	Impingement Angle (deg)	Dust Variety	Dust Concentration (mg/ft^3)	Test Duration (min)	Nominal Initial Specimen Weight (gm)	Specimen Volume loss ($in^3 \times 10^{-3}$)	Specimen Weight loss (mg)	Erosion Factor, ε ($\times 10^{-3}$)
*	40	Ti-6Al-4V	500	20	Al_2O_3	80.	10.	12.10		86.6	
	41	(An-			(50μ)						
		nealed)(1)	500	20		80.	10.	12.10		79.4	
	42		500	20		80.	10.	12.10		82.9	
	Average								18.8	83.0	
*	58	Ti-6Al-4V	500	20	Al_2O_3	80.	10.	12.10		83.3	
	59	(S. T. &	500	20	(50μ)	80.	10.	12.10		91.8	
	60	Aged)(2)	500	20		80.	10.	12.10		82.7	
	Average								19.4	85.9	
	Overall Averages								19.1	84.5	2.82
*	37	(1)	500	25	Al_2O_3	80.	10.	12.10		101.8	
	38		500	25	(50μ)	80.	10.	12.10		82.5	
	39		500	25		80.	10.	12.10		89.9	
	Average								20.6	91.4	
*	55	(2)	500	25	Al_2O_3	80.	10.	12.10		90.2	
	56		500	25	(50μ)	80.	10.	12.10		92.0	
	57		500	25		80.	10.	12.10		94.6	
	Average								20.8	92.3	
	Overall Averages								20.7	91.9	3.06
*	43	(1)	500	30	Al_2O_3	80.	10.	12.10		117.7	
	44		500	30	(50μ)	80.	10.	12.10		105.8	
	45		500	30		80.	10.	12.10		114.5	
	Average								25.4	112.7	

* Random Testing Order

TABLE V - Continued

Erosion Test Data - Series No. 1
Nozzle Dia. 3/8 in. Nozzle Length 2 ft
Nozzle Pressure 47 psi Line Pressure 67 psi
Gas Composition Shop Air Gas Temperature RT
Barometric Pressure Sea Level Powder Feeder Pressure and Setting: 30 psi
(Total Weight of Dust Consumed per Test = 30.0 gm)

	Specimen Number	Target Material	Median-Particle Velocity (fps)	Impingement Angle (deg)	Dust Variety	Dust Concentration (mg/ft^3)	Test Duration (min)	Nominal Initial Specimen Weight (gm)	Specimen Volume loss ($cm^3 \times 10^{-3}$)	Specimen Weight loss (mg)	Erosion Factor, ϵ ($\times 10^{-3}$)
*	61	(2)	500	30	Al_2O_3	80.	10.	12.10		115.4	
	62		500	30	(50μ)	80.	10.	12.10		113.3	
	63		500	30		80.	10.	12.10		102.3	
	Average								25.0	110.3	
	Overall Averages								25.2	111.5	3.72
**	T17	(1)	500	37.5	Al_2O_3	80.	10.	12.10		96.4	
	T18		500	37.5	(50μ)	80.	10.	12.10		89.0	
	T19		500	37.5		80.	10.	12.10		94.8	
	Average								21.1	93.4	
**	T110	(2)	500	37.5	Al_2O_3	80.	10.	12.10		103.1	
	T111		500	37.5	(50μ)	80.	10.	12.10		103.7	
	T112		500	37.5		80.	10.	12.10		101.1	
	Average								23.2	102.6	
	Overall Averages								22.2	98.0	3.26
*	46	(1)	500	45	Al_2O_3	80.	10.	12.10		93.1	
	47		500	45	(50μ)	80.	10.	12.10		91.4	
	48		500	45		80.	10.	12.10		79.2	
	Average								19.9	87.9	
*	64	(2)	500	45	Al_2O_3	80.	10.	12.10		114.3	
	65		500	45	(50μ)	80.	10.	12.10		101.7	
	66		500	45		80.	10.	12.10		90.7	
	Average								23.1	102.2	
	Overall Averages								21.5	95.1	3.17

* Random Testing Order **Sequential Testing Order

TABLE V - Continued

Erosion Test Data - Series No. 1
Nozzle Dia. 3/8 in. Nozzle Length 2 ft
Nozzle Pressure 47 psi Line Pressure 67 psi
Gas Composition Shop Air Gas Temperature RT
Barometric Pressure Sea Level Powder Feeder Pressure and Setting: 30 psi
(Total Weight of Dust Consumed per Test = 30.0 gm)

Specimen Number	Target Material	Median-Particle Velocity (fps)	Impingement Angle (deg)	Dust Variety	Dust Concentration (mg/ft^3)	Test Duration (min)	Nominal Initial Specimen Weight (gm)	Specimen Volume loss (cm^3)	Specimen Weight loss (mg)	Erosion Factor, ϵ ($\times 10^{-3}$)
49	(1)	500	60	Al_2O_3	80.	10.	12.10		71.6	
50		500	60	(50μ)	80.	10.	12.10		85.3	
51		500	60		80.	10.	12.10		69.9	
Average								17.1	75.6	
67	(2)	500	60	Al_2O_3	80.	10.	12.10		76.7	
68		500	60	(50μ)	80.	10.	12.10		76.4	
69		500	60		80.	10.	12.10		80.3	
Average								17.6	77.8	
Overall Averages								17.4	76.7	2.56
52	(1)	500	90	Al_2O_3	80.	10.	12.10		84.6	
53		500	90	(50μ)	80.	10.	12.10		58.4	
54		500	90		80.	10.	12.10		67.6	
Average								15.9	70.2	
70	(2)	500	90	Al_2O_3	80.	10.	12.10		63.0	
71		500	90	(50μ)	80.	10.	12.10		63.9	
72		500	90		80.	10.	12.10		62.6	
Average								14.3	63.2	
Overall Averages								15.1	66.7	2.22
112	(1) (Annealed)	500	90	Al_2O_3 (50μ)	80.	10.	12.10		91.8	
113		500	90		80.	10.	12.10		90.8	
114		500	90		80.	10.	12.10		87.0	
Average								16.2	89.9	

*Random Testing Order

TABLE V - Continued

Erosion Test Data - Series No. I
Nozzle Dia. 3/8 in. Nozzle Length 2 ft
Nozzle Pressure 47 psi Line Pressure 67 psi
Gas Composition Shop Air Gas Temperature RT
Barometric Pressure Sea Level Powder Feeder Pressure and Setting: 30 psi
(Total Weight of Dust Consumed per Test = 30.0 gm)

Specimen Number	Target Material	Median-Particle Velocity (fps)	Impingement Angle (deg)	Dust Variety	Dust Concentration (mg/ft^3)	Test Duration (min)	Nominal Initial Specimen Weight (gm)	Specimen Volume loss ($cm^3 \times 10^{-3}$)	Specimen Weight loss (mg)	Erosion Factor, ϵ ($\times 10^{-3}$)
* 130	17-7PH	500	20	Al_2O_3	80.	10.	19.70		95.7	
131	(Precipi-	500	20	(50μ)	80.	10.	19.70		84.4	
132	tation	500	20		80.	10.	19.70		81.9	
	Hard-									
	ened) (4)									
Average								11.4	87.3	
Overall Average								11.8	90.1	3.00
* 109	(3)	500	25	Al_2O_3	80.	10.	19.70		106.3	
110		500	25	(50μ)	80.	10.	19.70		101.4	
111		500	25		80.	10.	19.70		96.5	
Average								13.3	101.4	
* 127	(4)	500	25	Al_2O_3	80.	10.	19.70		112.6	
128		500	25	(50μ)	80.	10.	19.70		126.5	
129		500	25		80.	10.	19.70		118.1	
Average								15.7	119.7	
Overall Average								14.5	110.6	3.68
* 115	(3)	500	30	Al_2O_3	80.	10.	19.70		124.4	
114		500	30	(50μ)	80.	10.	19.70		115.8	
117		500	30		80.	10.	19.70		137.4	
Average								16.5	125.9	
* 133	(4)	500	30	Al_2O_3	80.	10.	19.70		111.6	
134		500	30	(50μ)	80.	10.	19.70		112.3	
135		500	30		80.	10.	19.70		130.9	
Average								15.5	118.6	
Overall Average								16.0	122.2	4.08

* Random Testing Order

TABLE V - Continued

Erosion Test Data - Series No. I

Nozzle Dia. 3/8 in. Nozzle Length 2 ft

Nozzle Pressure 47 psi Line Pressure 67 psi

Gas Composition Shop Air Gas Temperature RT

Barometric Pressure Sea Level Powder Feeder Pressure and Setting: 30 psi

(Total Weight of Dust Consumed per Test = 30.0 gm)

	Specimen Number	Target Material	Median-Particle Velocity (fps)	Impingement Angle (deg)	Dust Variety	Dust Concentration (mg/ft^3)	Test Duration (min)	Nominal Initial Specimen Weight (gm)	Specimen Volume loss ($cm^3 \times 10^{-3}$)	Specimen Weight loss (mg)	Erosion Factor, ϵ ($\times 10^{-3}$)
**	PH-19	(3)	500	37.5	Al_2O_3	80.	10.	19.70		121.4	
	PH-20		500	37.5	(50μ)	80.	10.	19.70		109.4	
	PH-21		500	37.5		80.	10.	19.70		117.6	
	Average								15.2	116.1	
**	PH-22	(4)	500	37.5	Al_2O_3	80.	10.	19.70		115.8	
	PH-23		500	37.5	(50μ)	80.	10.	19.70		120.5	
	PH-24		500	37.5		80.	10.	19.70		124.6	
	Average								15.8	120.3	
	Overall Average								15.5	118.2	3.94
*	118	(3)	500	45	Al_2O_3	80.	10.	19.70		120.4	
	119		500	45	(50μ)	80.	10.	19.70		107.5	
	120		500	45		80.	10.	19.70		111.7	
	Average								14.9	113.2	
*	136	(4)	500	45	Al_2O_3	80.	10.	19.70		122.0	
	137		500	45	(50μ)	80.	10.	19.70		116.6	
	138		500	45		80.	10.	19.70		103.3	
	Average								14.9	114.0	
	Overall Average								14.9	113.6	3.78
*	121	(3)	500	60	Al_2O_3	80.	10.	19.70		100.3	
	122		500	60	(50μ)	80.	10.	19.70		125.0	
	123		500	60		80.	10.	19.70		98.9	
	Average								14.2	108.1	

* Random Testing Order ** Sequential Testing Order

TABLE V - Continued

Erosion Test Data - Series No. I
Nozzle Dia. 3/8 in. Nozzle Length 2 ft
Nozzle Pressure 47 psi Line Pressure 67 psi
Gas Composition Shop Air Gas Temperature RT
Barometric Pressure Sea Level Powder Feeder Pressure and Setting: 30 psi
(Total Weight of Dust Consumed per Test = 30.0 gm)

Specimen Number	Target Material	Median-Particle Velocity (fps)	Impingement Angle (deg)	Dust Variety	Dust Concentration (mg/ft^3)	Test Duration (min)	Nominal Initial Specimen Weight (gm)	Specimen Volume loss ($cm^3 \times 10^{-3}$)	Specimen Weight loss (mg)	Erosion Factor, ϵ ($\times 10^{-3}$)
• 139	(4)	500	60	Al_2O_3	80.	10.	19.70		101.7	
140		500	60	(50μ)	80.	10.	19.70		121.7	
141		500	60		80.	10.	19.70		99.6	
Average								14.1	107.7	
Overall Average								14.2	107.9	3.60
• 124	(3)	500	90	Al_2O_3	80.	10.	19.70		83.4	
125		500	90	(50μ)	80.	10.	19.70		93.6	
126		500	90		80.	10.	19.70		70.6	
Average								10.8	82.5	
• 142	(4)	500	90	Al_2O_3	80.	10.	19.70		87.3	
143		500	90	(50μ)	80.	10.	19.70		75.0	
144		500	90		80.	10.	19.70		74.1	
Average								10.3	78.8	
Overall Average								10.6	80.7	2.69
• 70	410 S.S.	500	20	Al_2O_3	80.	10.	19.00		80.4	
77	(An-			(50μ)						
	nealed)(5)	500	20		80.	10.	19.00		90.2	
78		500	20		80.	10.	19.00		88.8	
Average								11.0	86.5	
• 94	410 S.S.	500	20	Al_2O_3	80.	10.	19.00		84.9	
95	(Quenched	500	20	(50μ)	80.	10.	19.00		84.4	
96	& Tem-	500	20		80.	10.	19.00			
	pered)(6)								112.3	
Average								12.5	97.2	
Overall Average								11.9	91.9	3.06

• Random Testing Order

TABLE V – Continued

Erosion Test Data - Series No. 1
Nozzle Dia. 3/8 in. Nozzle Length 2 ft
Nozzle Pressure 47 psi Line Pressure 67 psi
Gas Composition Shop Air Gas Temperature RT
Barometric Pressure Sea Level Powder Feeder Pressure and Setting: 30 psi
(Total Weight of Dust Consumed per Test = 30.0 gm)

	Specimen Number	Target Material	Median-Particle Velocity (fps)	Impingement Angle (deg)	Dust Variety	Dust Concentration (mg/ft^3)	Test Duration (min)	Nominal Initial Specimen Weight (gm)	Specimen Volume loss ($cm^3 \times 10^{-3}$)	Specimen Weight loss (mg)	Erosion Factor, ε ($\times 10^{-3}$)
•	73	(5)	500	25	Al_2O_3	80.	10.	19.00		109.2	
	74		500	25	(50μ)	80.	10.	19.00		113.8	
	75		500	25		80.	10.	19.00		105.1	
	Average								14.1	109.4	
•	91	(6)	500	25	Al_2O_3	80.	10.	19.00		119.4	
	92		500	25	(50μ)	80.	10.	19.00		97.3	
	93		500	25		80.	10.	19.00		89.0	
	Average								13.2	101.9	
	Overall Average								13.6	105.7	3.52
•	79	(5)	500	30	Al_2O_3	80.	10.	19.00		116.0	
	80		500	30	(50μ)	80.	10.	19.00		105.1	
	81		500	30		80.	10.	19.00		106.9	
	Average								14.1	109.3	
•	97	(6)	500	30	Al_2O_3	80.	10.	19.00		109.4	
	98		500	30	(50μ)	80.	10.	19.00		105.3	
	99		500	30		80.	10.	19.00		119.0	
	Average								14.4	111.6	
	Overall Average								14.4	110.4	3.68
••	RR-13	(5)	500	37.5	Al_2O_3	80.	10.	19.00		124.7	
	RR-14		500	37.5	(50μ)	80.	10.	19.00		128.0	
	RR-15		500	37.5		80.	10.	19.00		125.0	
	Average								16.4	125.9	

• Random Testing Order •• Sequential Testing Order

TABLE V - Continued

Erosion Test Data - Series No. 1
Nozzle Dia. 3/8 in. Nozzle Length 2 ft
Nozzle Pressure 47 psi Line Pressure 67 psi
Gas Composition Shop Air Gas Temperature RT
Barometric Pressure Sea Level Powder Feeder Pressure and Setting: 30 psi
(Total Weight of Dust Consumed per Test = 30.0 gm)

	Specimen Number	Target Material	Median-Particle Velocity (fps)	Impingement Angle (deg)	Dust Variety	Dust Concentration (mg/ft^3)	Test Duration (min)	Nominal Initial Specimen Weight (gm)	Specimen Volume loss ($cm^3 \times 10^{-3}$)	Specimen Weight loss (mg)	Erosion Factor, ϵ ($\times 10^{-3}$)
**	88-16	(6)	300	37.5	Al_2O_3	80.	10.	19.00		126.4	
	88-17		300	37.5	(50μ)	80.	10.	19.00		128.7	
	88-18		300	37.5		80.	10.	19.00		115.0	
	Average								15.9	123.4	
	Overall Average								16.1	124.7	4.15
*	82	(6)	300	45	Al_2O_3	80.	10.	19.00		107.3	
	83		300	45	(50μ)	80.	10.	19.00		126.6	
	84		300	45		80.	10.	19.00		97.9	
	Average								14.7	113.9	
*	100	(6)	100	45	Al_2O_3	80.	10.	19.00		104.2	
	101		100	45	(50μ)	80.	10.	19.00		117.3	
	102		100	45		80.	10.	19.00		111.4	
	Average								14.2	111.0	
	Overall Average								14.5	112.5	3.75
*	85	(6)	500	60	Al_2O_3	80.	10.	19.00		80.7	
	86		500	60	(50μ)	80.	10.	19.00		106.6	
	87		500	60		80.	10.	19.00		84.6	
	Average								11.7	90.7	
*	103	(6)	500	90	Al_2O_3	80.	10.	19.00		101.9	
	104		500	90	(50μ)	80.	10.	19.00		87.5	
	105		500	90		80.	10.	19.00		95.3	
	Average								12.2	94.9	
	Overall Average								12.0	92.8	3.09

* Random Testing Order ** Sequential Testing Order

TABLE V - Continued

Erosion Test Data - Series No. 1
Nozzle Dia. 3/8 in. Nozzle Length 2 ft
Nozzle Pressure 47 psi Line Pressure 67 psi
Gas Composition Shop Air Gas Temperature RT
Barometric Pressure Sea Level Powder Feeder Pressure and Setting: 30 psi
(Total Weight of Dust Consumed per Test = 30.0 gm)

Specimen Number	Target Material	Median-Particle Velocity (fps)	Impingement Angle (deg)	Dust Variety	Dust Concentration (mg/ft^3)	Test Duration (min)	Nominal Initial Specimen Weight (gm)	Specimen Volume loss ($cm^3 \times 10^{-2}$)	Specimen Weight loss (mg)	Erosion Factor, ϵ ($\times 10^{-3}$)
88	(5)	500	90	Al_2O_3	80.	10.	19.00		94.0	
89		500	90	(50μ)	80.	10.	19.00		63.6	
90		500	90		80.	10.	19.00		68.4	
Average								9.7	76.3	
106	(6)	500	90	Al_2O_3	80.	10.	19.00		69.1	
107		500	90	(50μ)	80.	10.	19.00		67.4	
108		500	90		80.	10.	19.00		73.0	
Average								9.9	76.5	
Overall Average								9.8	75.9	2.53

* Random Testing Order

TABLE VI. SERIES I TEST DATA - ARIZONA ROAD DUST

Erosion Test Data - Series No. 1 (43-74μ)
Nozzle Dia. 3/8 in. Nozzle Length 2 ft
Nozzle Pressure 47 psi Line Pressure 67 psi
Gas Composition Shop Air Gas Temperature RT
Barometric Pressure Sea Level Powder Feeder Pressure and Setting: 30 psi
(Total Weight of Dust Consumed per Test = 30.0 gm)

	Specimen Number	Target Material	Median-Particle Velocity (fps)	Impingement Angle (deg)	Dust Variety	Dust Concentration (mg/ft^3)	Test Duration (min)	Nominal Initial Specimen Weight (gm)	Specimen Volume loss ($cm^3 \times 10^{-3}$)	Specimen Weight loss (mg)	Erosion Factor, ε ($\times 10^{-3}$)
*	X-10	2024-0	650	20	Arizona	80.	10.	7.40		57.5	
	X-44	Al Alloy	650	20	Road	80.	10.	7.40		51.1	
	X-46	(An-			Dust						
		nealed)	650	20	(43-74μ)	80.	10.	7.40		55.7	
	Average								19.9	54.8	1.83
**	X-49	2024-0	650	30	Arizona	80.	10.	7.40		73.7	
	X-50	Al Alloy	650	30	Road	80.	10.	7.40		74.3	
	X-51	(An-			Dust						
		nealed)	650	30	(43-74μ)	80.	10.	7.40		76.6	
	Average								27.1	74.9	
**	X-52	2024-T6	650	30	Arizona	80.	10.	7.40		72.2	
	X-53	Al Alloy	650	30	Road	80.	10.	7.40		72.4	
	X-54	(S. T. &			Dust						
		Aged)	650	30	(43-74μ)	80.	10.	7.40		72.9	
	Average								26.4	72.5	
	Overall Average								26.8	73.7	2.46
**	X-25	2024-0	650	37.5	Arizona	80.	10.	7.40		77.7	
	X-26	Al Alloy	650	37.5	Road	80.	10.	7.40		78.6	
	X-27	(An-			Dust						
		nealed)	650	37.5	(43-74μ)	80.	10.	7.40		77.6	
	Average								27.9	77.0	

* Random Testing Order ** Sequential Testing Order

TABLE VI - Continued

Erosion Test Data - Series No. 1 (43-74μ)
Nozzle Dia. 3/8 in. Nozzle Length 2.0
Nozzle Pressure 47 psi Line Pressure 67 psi
Gas Composition Shop Air Gas Temperature RT
Barometric Pressure Sea Level Powder Feeder Pressure and Setting: 30 psi
(Total Weight of Dust Consumed per Test = 30.0 gm)

Specimen Number	Target Material	Median-Particle Velocity (fps)	Impingement Angle (deg)	Dust Variety	Dust Concentration (mg/ft³)	Test Duration (min)	Nominal Initial Specimen Weight (gm)	Specimen Volume loss ($cm^3 \times 10^{-3}$)	Specimen Weight loss (mg)	Erosion Factor, ($\times 10^{-3}$)
** X-28	2024-T6	650	37.5	Arizona	80.	10.	7.40		77.0	
X-29	Al Alloy	650	37.5	Road	80.	10.	7.40		74.6	
X-30	(S. T. &			Dust						
	Aged)	650	37.5	(43-74μ)	80.	10.	7.40		77.0	
Average								27.7	76.5	
Overall Average								27.4	76.8	2.50
* X-26	2024-0	650	45.	Arizona	80.	10.	7.40		64.0	
X-27	(An-			Road						
	nealed)	650	45.	Dust	80.	10.	7.40		68.0	
X-47		650	45.	(43-74μ)	80.	10.	7.40		66.0	
Average								24.1	66.5	2.22
* X-18	2024-0	650	90.	Arizona	80.	10.	7.40		52.6	
X-23	(An-			Road						
	nealed)	650	90.	Dust	80.	10.	7.40		51.0	
X-42		650	90.	(43-74μ)	80.	10.	7.40		44.1	
Average								14.1	49.0	1.66
* X-17	2024-0	650	90.	Arizona	80.	10.	7.40		41.0	
X-29	(An-			Road						
	nealed)	650	90.	Dust	80.	10.	7.40		41.0	
X-45		650	90.	(43-74μ)	80.	10.	7.40		41.0	
Average								12.1	41.0	1.11

* Random Testing Order ** Sequential Testing Order

TABLE VI - Continued

Erosion Test Data - Series No. 1 (43-74μ)
Nozzle Dia. 3/8 in. Nozzle Length 2 ft
Nozzle Pressure 47 psi Line Pressure 67 psi
Gas Composition Shop Air Gas Temperature RT
Barometric Pressure Sea Level Powder Feeder Pressure and Setting: 30 psi
(Total Weight of Dust Consumed per Test = 30.0 gm)

Specimen Number	Target Material	Median-Particle Velocity (fps)	Impingement Angle (deg)	Dust Variety	Dust Concentration (mg/ft^3)	Test Duration (min)	Nominal Initial Specimen Weight (gm)	Specimen Volume loss ($cm^3 \times 10^{-3}$)	Specimen Weight loss (mg)	Erosion Factor, ε ($\times 10^{-6}$)
• X-2	Ti-6Al-4V	650	20.	Arizona	80.	10.	13.10		44.0	
X-4	(An-			Road						
	nealed)(1)	650	20.	Dust	80.	10.	13.10		46.0	
X-41		650	20.	(43-74μ)	80.	10.	13.10		47.8	
Average								10.3	45.6	1.52
•• X-55	Ti-6Al-4V	650	30.	Arizona	80.	10.	13.10		60.2	
X-56	(An-			Road						
	nealed)(1)	650	30.	Dust	80.	10.	13.10		57.6	
X-57		650	30.	(43-74μ)	80.	10.	13.10		59.5	
Average								13.4	59.1	
•• X-58	Ti-6Al-4V	650	30.	Arizona	80.	10.	13.10		60.4	
X-59	(S. T. &	650	30.	Road	80.	10.	13.10		60.8	
X-60	Aged)(2)	650	30.	Dust	80.	10.	13.10		61.1	
Average				(43-74μ)				13.7	60.8	
Overall Average								13.6	60.0	2.00
•• X-31	(1)	650	37.5	Arizona	80.	10.	13.10		64.1	
X-32		650	37.5	Road	80.	10.	13.10		61.4	
X-33		650	37.5	Dust	80.	10.	13.10		63.0	
Average				(43-74μ)				14.1	62.8	
•• X-34	(2)	650	37.5	Arizona	80.	10.	13.10		63.7	
X-35		650	37.5	Road	80.	10.	13.10		62.8	
X-36		650	37.5	Dust	80.	10.	13.10		62.6	
Average				(43-74μ)				14.4	62.6	
Overall Average								14.3	62.1	2.10

• Random Testing Order •• Sequential Testing Order

TABLE VI - Continued

Erosion Test Data - Series No. 1 (43-74μ)
Nozzle Dia. 3/8 in. Nozzle Length 2 ft
Nozzle Pressure 47 psi Line Pressure 67 psi
Gas Composition Shop Air Gas Temperature RT
Barometric Pressure Sea Level Powder Feeder Pressure and Setting: 30 psi
(Total Weight of Dust Consumed per Test = 30.0 gm)

Specimen Number	Target Material	Median-Particle Velocity (fps)	Impingement Angle (deg)	Dust Variety	Dust Concentration (mg/ft^3)	Test Duration (min)	Nominal Initial Specimen Weight (gm)	Specimen Volume loss ($cm^3 \times 10^{-2}$)	Specimen Weight loss (mg)	Erosion Factor, ε ($\times 10^{-3}$)
• X-9	Ti-6Al-4V	650	45.	Arizona	80.	10.	12.10		57.2	
X-11	(An-	650		Road						
	nealed)(1)	650	45.	Dust	80.	10.	12.10		58.4	
X-14			45.	(43-74μ)	80.	10.	12.10		61.0	
Average								13.3	58.9	1.98
• X-6	(1)	650	60.	Arizona	80.	10.	12.10		51.2	
X-20		650	60.	Road	80.	10.	12.10		52.0	
X-48		650	60.	Dust (43-74μ)	80.	10.	12.10		53.7	
Average								11.9	52.7	1.76
• X-4	(1)	650	90.	Arizona	80.	10.	12.10		43.6	
X-64		650	90.	Road	80.	10	12.10		43.0	
X-68		650	90.	Dust (43-74μ)	80.	10.	12.10		45.2	
Average								9.9	43.9	1.46
• X-88	17-7PH	650	30.	Arizona	80.	10.	19.70		60.7	
X-26	(An-			Road						
	nealed)(3)	650	30.	Dust	80.	10.	19.70		57.8	
X-88		650	30.	(43-74μ)	80.	10.	19.70		59.1	
Average								7.9	59.1	1.97
•• X-67	17-7PH	650	30.	Arizona	80.	10.	19.70		68.4	
X-66	(An-			Road						
	nealed)(4)	650	30.	Dust	80.	10.	19.70		72.1	
X-69		650	30.	(43-74μ)	80.	10.	19.70		73.5	
Average								9.4	71.3	

• Random Testing Order •• Sequential Testing Order

TABLE VI - Continued

Erosion Test Data - Series No. 1 (43-74μ)
Nozzle Dia. 3/8 in. Nozzle Length 2 ft
Nozzle Pressure 47 psi Line Pressure 67 psi
Gas Composition Shop Air Gas Temperature RT
Barometric Pressure Sea Level Powder Feeder Pressure and Setting: 30 psi
(Total Weight of Dust Consumed per Test = 30.0 gm)

	Specimen Number	Target Material	Median-Particle Velocity (fps)	Impingement Angle (deg)	Dust Variety	Dust Concentration (mg/ft^3)	Test Duration (min)	Nominal Initial Specimen Weight (gm)	Specimen Volume loss ($cm^3 \times 10^{-3}$)	Specimen Weight loss (mg)	Erosion Factor, ε ($\times 10^{-3}$)
**	X-70	17-7PH	650	30	Arizona	80.	10.	19.70		72.8	
	X-71	(Precipi-	650	30	Road	80.	10.	19.70			
		tation			Dust					76.2	
	X-72	Hardened)	650	30	(43-74μ)	80.	10.	19.70		75.6	
	Average								9.8	74.9	
	Overall Average								9.6	73.1	2.38
**	X-	17-7PH	650	37.5	Arizona	80.	10.	19.70		76.0	
	X-	(An-			Road						
		nealed)	650	37.5	Dust	80.	10.	19.70		77.2	
	X-		650	37.5	(43-74μ)	80.	10.	19.70		79.5	
	Average								10.5	78.2	
**	X-	17-7PH	650	37.5	Arizona	80.	10.	19.70		78.6	
	X-	(Precipi-	650	37.5	Road	80.	10.	19.70			
		tation)			Dust					75.7	
	X-	Hardened)	650	37.5	(43-74μ)	80.	10.	19.70		77.0	
	Average								10.2	77.1	
	Overall Average								10.4	77.7	2.59
*	X-12	17-7PH	650	45.	Arizona	80.	10.	19.70		78.1	
	X-27	(An-			Road						
		nealed)	650	45.	Dust	80.	10.	19.70		73.3	
	X-35		650	45.	(43-74μ)	80.	10.	19.70		67.7	
	Average								9.6	73.0	2.43

* Random Testing Order **Sequential Testing Order

TABLE VI - Continued

Erosion Test Data - Series No. 1 (43-74μ)
Nozzle Dia. 3/8 in. Nozzle Length 2 ft
Nozzle Pressure 47 psi Line Pressure 67 psi
Gas Composition Shop Air Gas Temperature RT
Barometric Pressure Sea Level Powder Feeder Pressure and Setting: 30 psi
(Total Weight of Dust Consumed per Test = 30.0 gm)

Specimen Number	Target Material	Median-Particle Velocity (fps)	Impingement Angle (deg)	Dust Variety	Dust Concentration (mg/ft^3)	Test Duration (min)	Nominal Initial Specimen Weight (gm)	Specimen Volume loss ($cm^3 \times 10^{-3}$)	Specimen Weight loss (mg)	Erosion Factor, ε ($\times 10^{-3}$)
X-12	17-7PH	650	60.	Arizona	80.	10.	19.70		66.0	
X-19	(An-			Road						
	nealed)	650	60.	Dust	80.	10	19.70		66.7	
X-30		650	60.	(43-74μ)	80.	10.	19.70		62.9	
Average								8.6	65.2	2.17
X-21	17-7PH	650	90.	Arizona	80.	10.	19.70		55.4	
X-24	(An-			Road						
	nealed)	650	90.	Dust	80.	10	19.70		52.6	
X-42		650	90.	(43-74μ)	80.	10.	19.70		49.8	
Average								6.9	52.6	1.75
X-7	410 S.S.	650	30.	Arizona	80.	10.	19.00		51.2	
X-33	(An-			Road						
	nealed)	650	30.	Dust	80.	10.	19.00		52.0	
X-39		650	30.	(43-74μ)	80.	10.	19.00		55.0	
Average								6.8	52.7	1.76
X-61	410 S.S.	650	30.	Arizona	80.	10.	19.00		62.9	
X-62	(An-			Road						
	nealed)	650	30.	Dust	80.	10.	19.06		68.3	
X-63		650	30.	(43-74μ)	80.	10.	19.00		69.7	
Average								8.7	67.0	

* Random Testing Order ** Sequential Testing Order

TABLE VI - Continued

Erosion Test Data - Series No. 1 (43-74μ)
Nozzle Dia. 3/8 in. Nozzle Length 2 ft
Nozzle Pressure 47 psi Line Pressure 67 psi
Gas Composition Shop Air Gas Temperature RT
Barometric Pressure Sea Level Powder Feeder Pressure and Setting: 30 psi/4
(Total Weight of Dust Consumed per Test = 30.0 gm)

Specimen Number	Target Material	Median-Particle Velocity (fps)	Impingement Angle (deg)	Dust Variety	Dust Concentration (mg/ft^3)	Test Duration (min)	Nominal Initial Specimen Weight (gm)	Specimen Volume loss (cm^3 x 10^{-3})	Specimen Weight loss (mg)	Erosion Factor, ε (x 10^{-3})
** X-64	410 S.S.	650	30	Arizona	80.	10.	19.00		74.8	
X-65	(Quenched	650	30	Road	80.	10.	19.00		69.0	
X-66	and Tem-			Dust						
	pered)	650	30	(43-74μ)	80.	10.	19.00		68.9	
Average								9.2	70.9	
Overall Average								9.0	69.0	2.30
** X-37	410 S.S.	650	37.5	Arizona	80.	10.	19.00		76.8	
X-38	(An-			Road						
	nealed)	650	37.5	Dust	80.	10.	19.00		71.1	
X-39		650	37.5	(43-74μ)	80.	10.	19.00		73.0	
Average								9.5	73.5	
** X-40	410 S.S.	650	37.5	Arizona	80.	10.	19.00		73.6	
X-41	(Quenched	650	37.5	Road	80.	10.	19.00		72.5	
X-42	and Tem-			Dust						
	pered)	650	37.5	(43-74μ)	80.	10.	19.00		74.0	
Average								9.5	73.4	
Overall Average								9.5	73.5	2.45
* X-26	410 S.S.	650	45.	Arizona	80.	10.	19.00		70.3	
X-36	(An-			Road						
	nealed)	650	45.	Dust	80.	10.	19.00		67.5	
X-40		650	45.	(43-74μ)	80.	10.	19.00		71.0	
Average								9.0	69.6	2.32

* Random Testing Order ** Sequential Testing Order

TABLE VI - Continued

Erosion Test Data - Series No. 1 (43-74μ)
Nozzle Dia. 3/8 in. Nozzle Length 2 ft
Nozzle Pressure 47 psi Line Pressure 67 psi
Gas Composition Shop Air Gas Temperature RT
Barometric Pressure Sea Level Powder Feeder Pressure and Setting: 30 psi
(Total Weight of Dust Consumed per Test = 30.0 gm)

Specimen Number	Target Material	Median-Particle Velocity (fps)	Impingement Angle (deg)	Dust Variety	Dust Concentration (mg/ft^3)	Test Duration (min)	Nominal Initial Specimen Weight (gm)	Specimen Volume loss ($cm^3 \times 10^{-3}$)	Specimen Weight loss (mg)	Erosion Factor, ε ($\times 10^{-3}$)
X-1	410 S.S.	650	60.	Arizona	80.	10.	19.00		61.9	
X-5	(An-			Road						
	nealed)	650	60.	Dust	80.	10.	19.00		65.4	
X-18		650	60.	(43-74μ)	80.	10.	19.00		62.1	
Average								8.2	63.1	2.10
X-3	410 S.S.	650	90.	Arizona	80.	10.	19.00		45.0	
X-16	(An-			Road						
	nealed)	650	90.	Dust	80.	10.	19.00		42.4	
X-31		650	90.	(43-74μ)	80.	10.	19.00		44.7	
Average								5.7	44.0	1.47

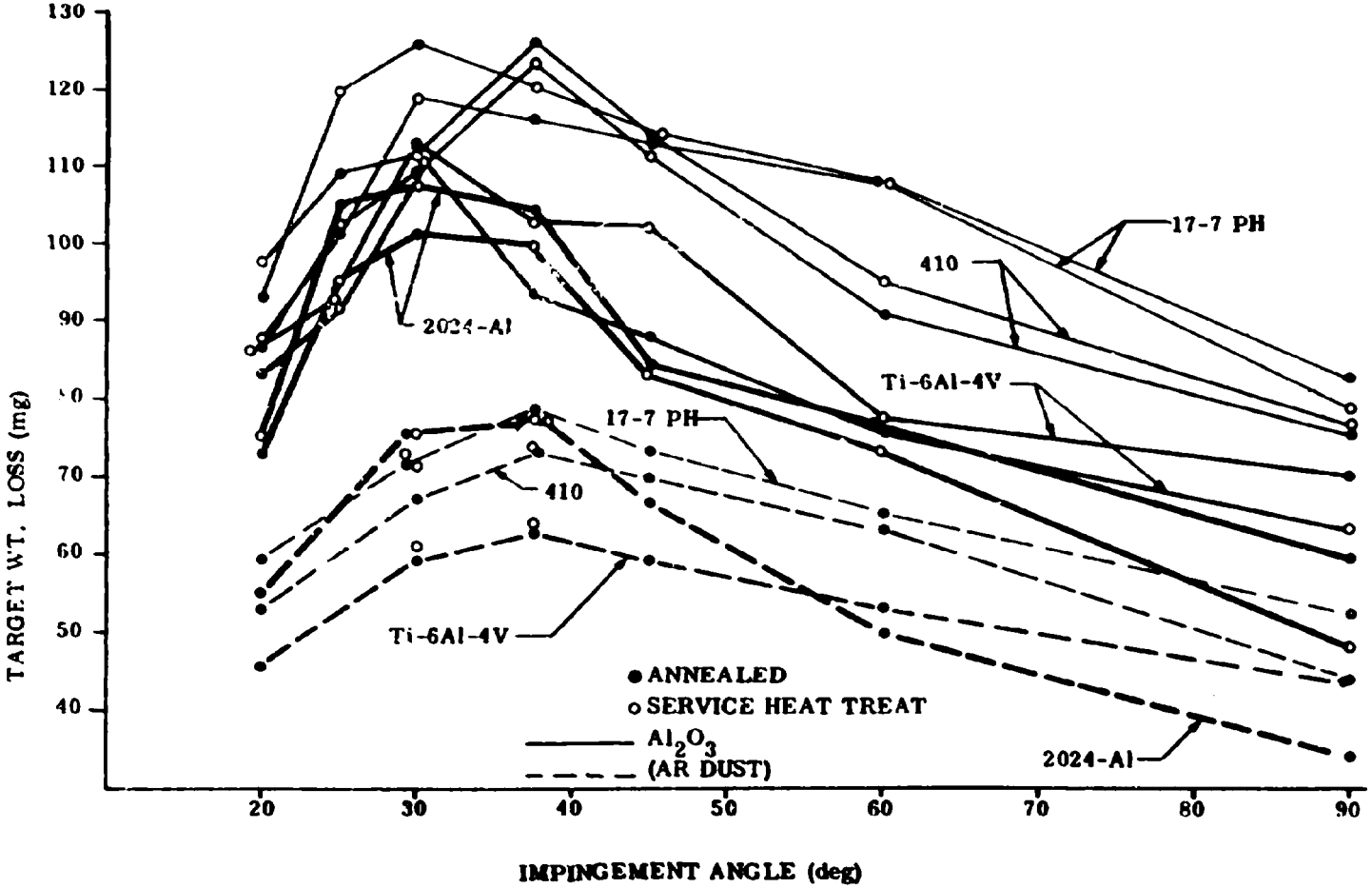

Figure 32. Variation in Target Weight Loss With Impingement Angle (Test Series I).

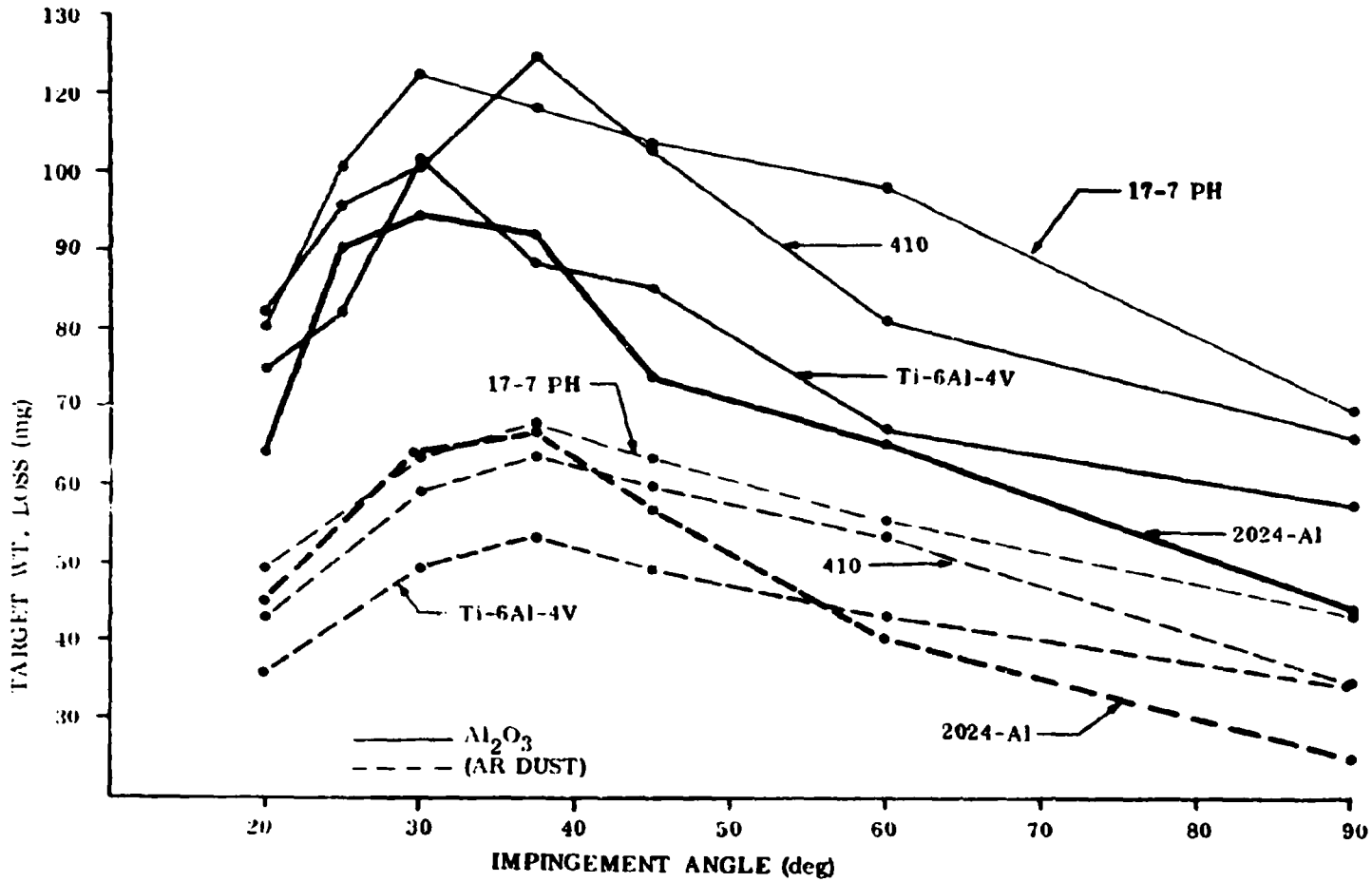

Figure 33. Variation in Average Target Weight Loss With Impingement Angle (Test Series I).

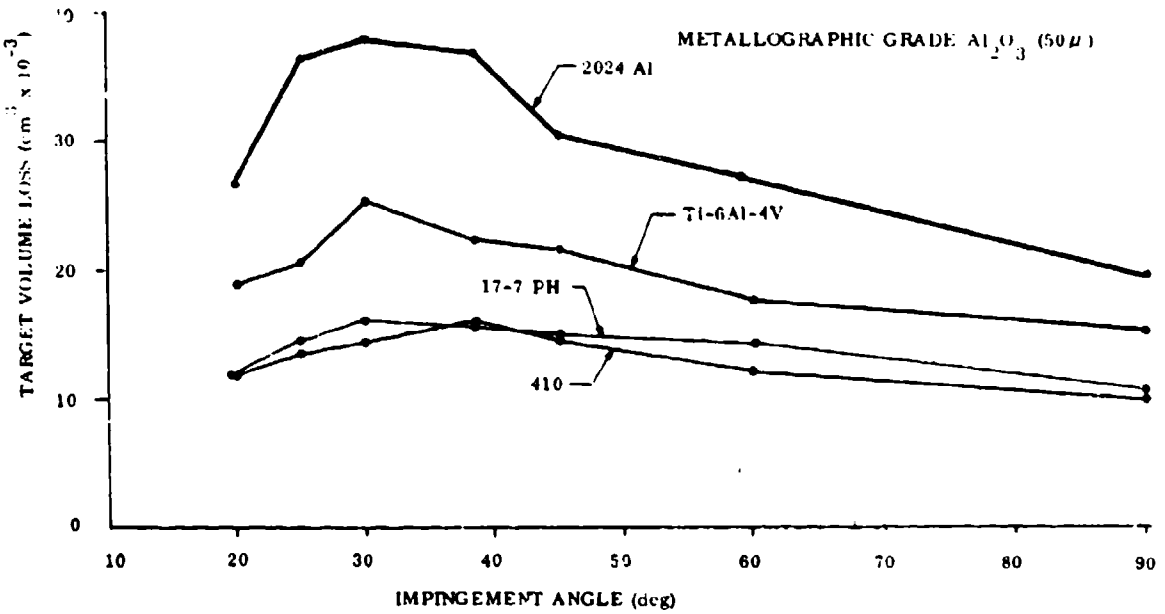

Figure 34. Variation in Average Target Volume Loss With Impingement Angle (Test Series I).

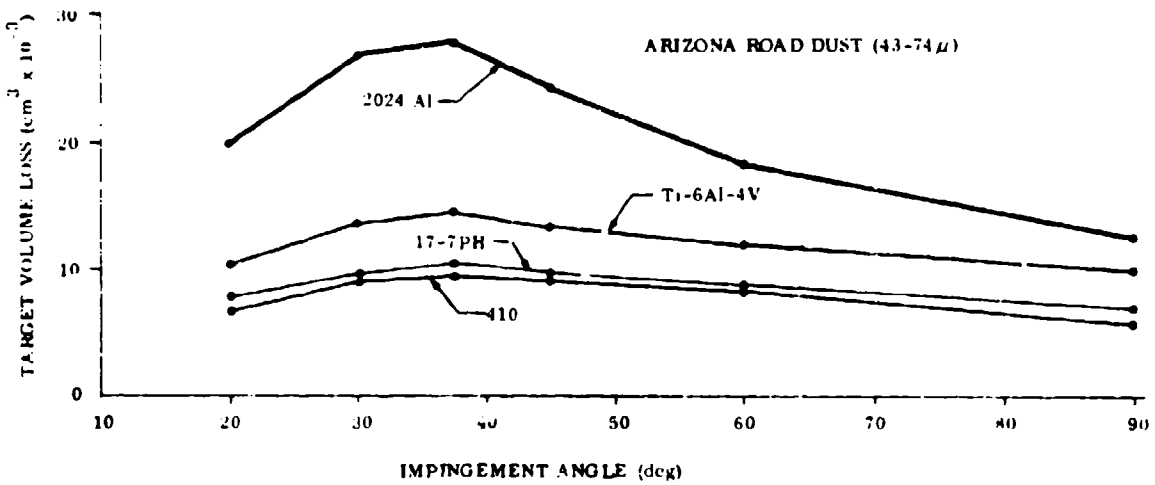

Figure 35. Variation in Average Target Volume Loss With Impingement Angle (Test Series I).

erosion, equation (1) then predicts that the weaker, annealed structures should erode ≈3.0-4.5 times more than the fully heat treated structures. However, erosion weight loss differences were generally less than 5 percent between the annealed and the fully heat treated conditions.

There appears to be no significant difference in erosion characteristics of the annealed specimens and the fully heat treated specimens (see Figure 32). This is true for all target materials and for both dust varieties tested. (Comparisons with Arizona Road Dust were made at the impingement angles of 30 and 37.5 degrees). This statement is based upon comparisons of average weight loss values and the appreciable overlapping of scatter bands at almost all impingement angles. In the few instances where apparent differences might be suspected (≥5 percent differential in average weight loss), about one-half of the incidence angles exhibit higher weight loss for the annealed conditions, the other half for the hardened conditions; hence, no trend was apparent.

When all of the target weight loss data for both heat treat conditions are plotted on separate probability charts for each impingement angle (see Figures 36 through 43), the total data, in most cases, conform reasonably well to the normal distribution for a single population. The conformation is particularly good at impingement angles below 60 degrees. The reproducibility of data is considerably better with the Arizona Road Dust than with alumina dust for all target materials. This was not expected, inasmuch as the more chemically homogeneous alumina should logically have produced less data scatter.

It is apparent that specimen flow strength, which is related to hardness and metallurgical structure, has little bearing on the inherent erosion resistance of a specific target material. At this point, the logical inference was reaffirmed that other properties of the target, not significantly affected by variation in heat-treat condition, must govern the degree of erosion resistance.

Effect of Target Alloy

In the range of impingement angles for maximum target weight loss, all target materials lose about the same maximum amounts (range mean ± 8.7% for Al_2O_3, ± 10.5% for Arizona Road Dust). This is valid in spite of appreciable differences in hardnesses, modulii, densities, strengths, melting points, and basic structures among the four target materials.

Maximum target volume losses show much greater variation from material to material than maximum weight losses due to differences in target densities (Figures 34 and 35).

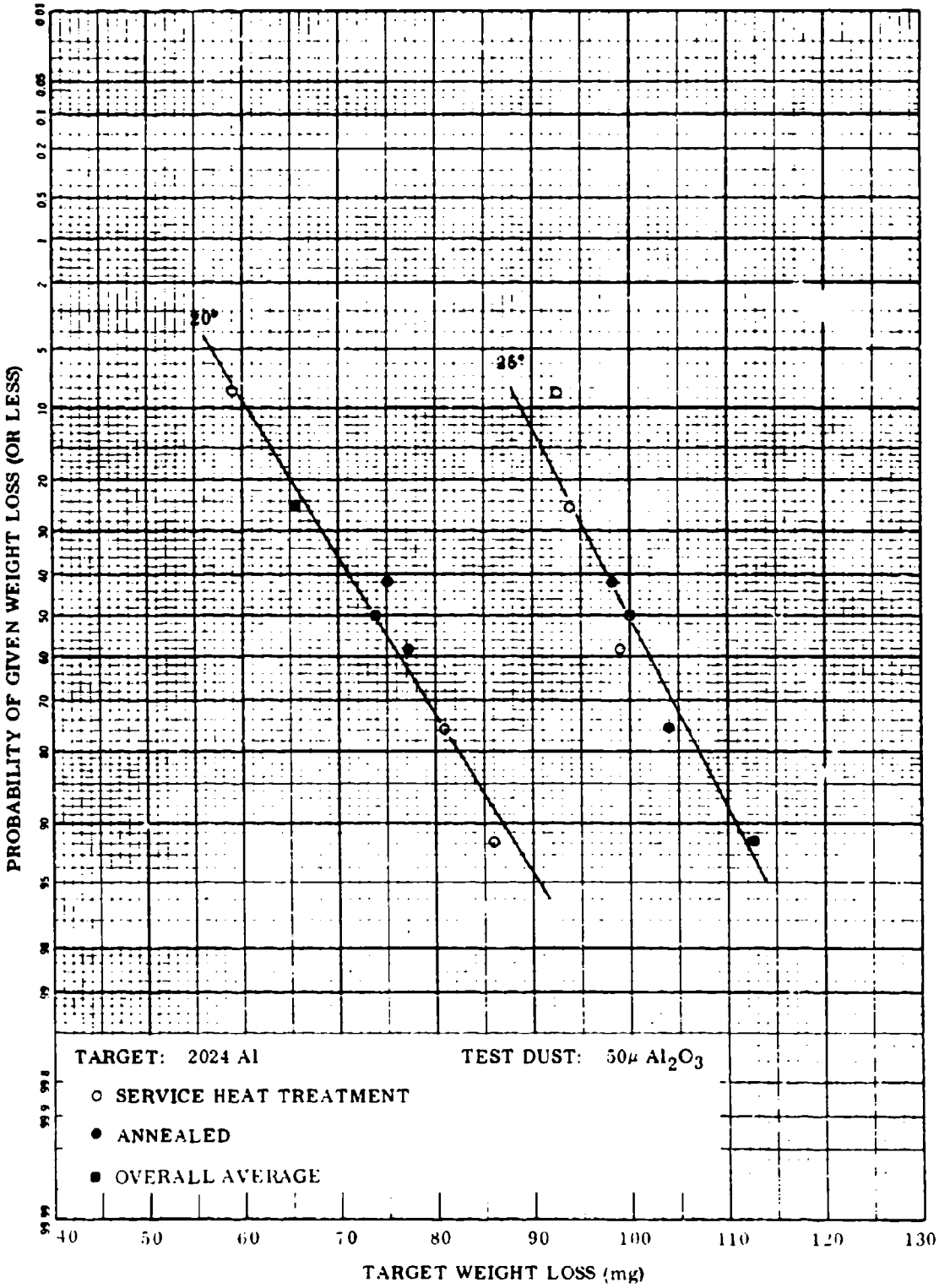

Figure 36A. Probability Plot of Test Series I Data.

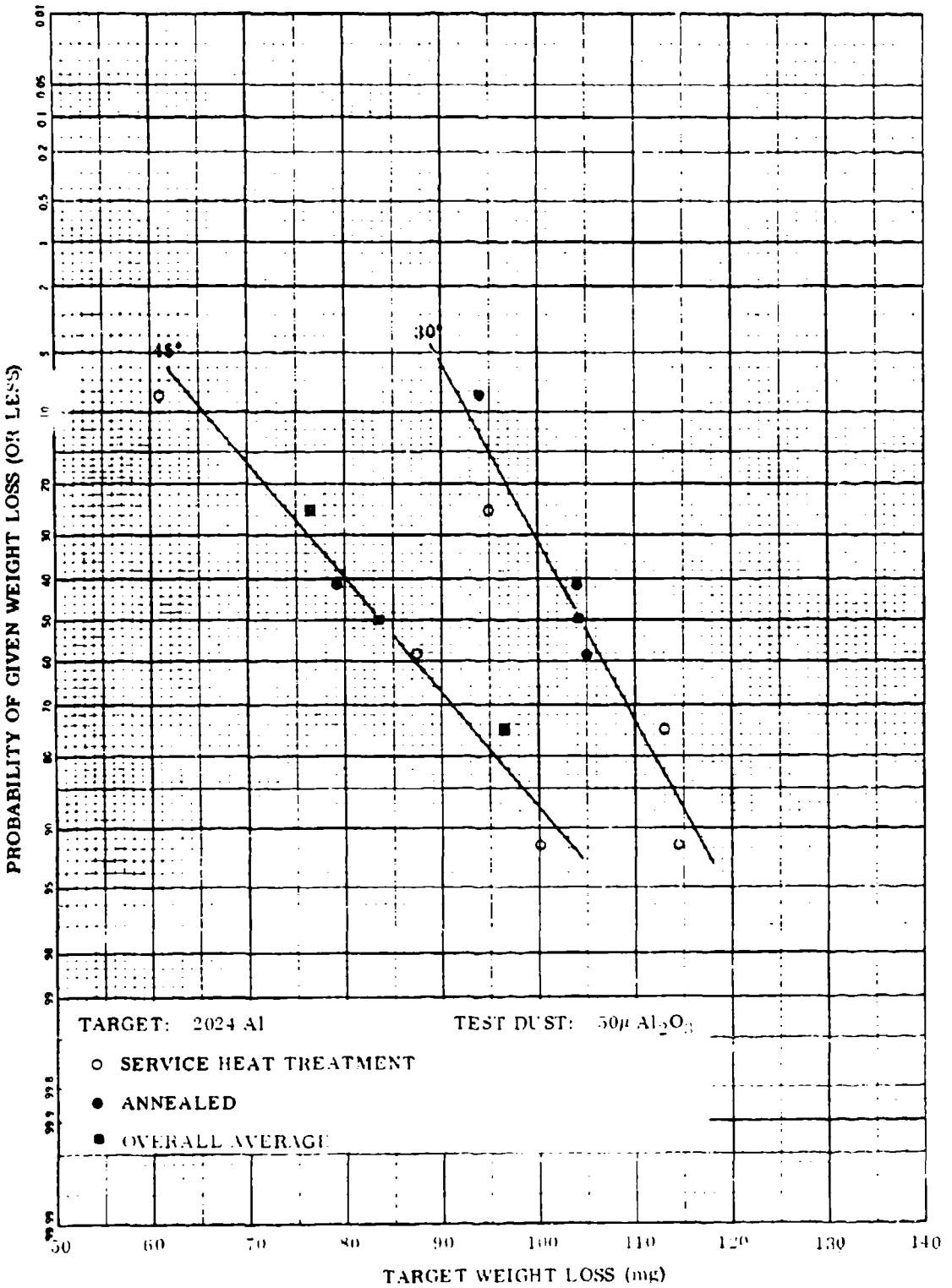

Figure 36B. Probability Plot of Test Series I Data.

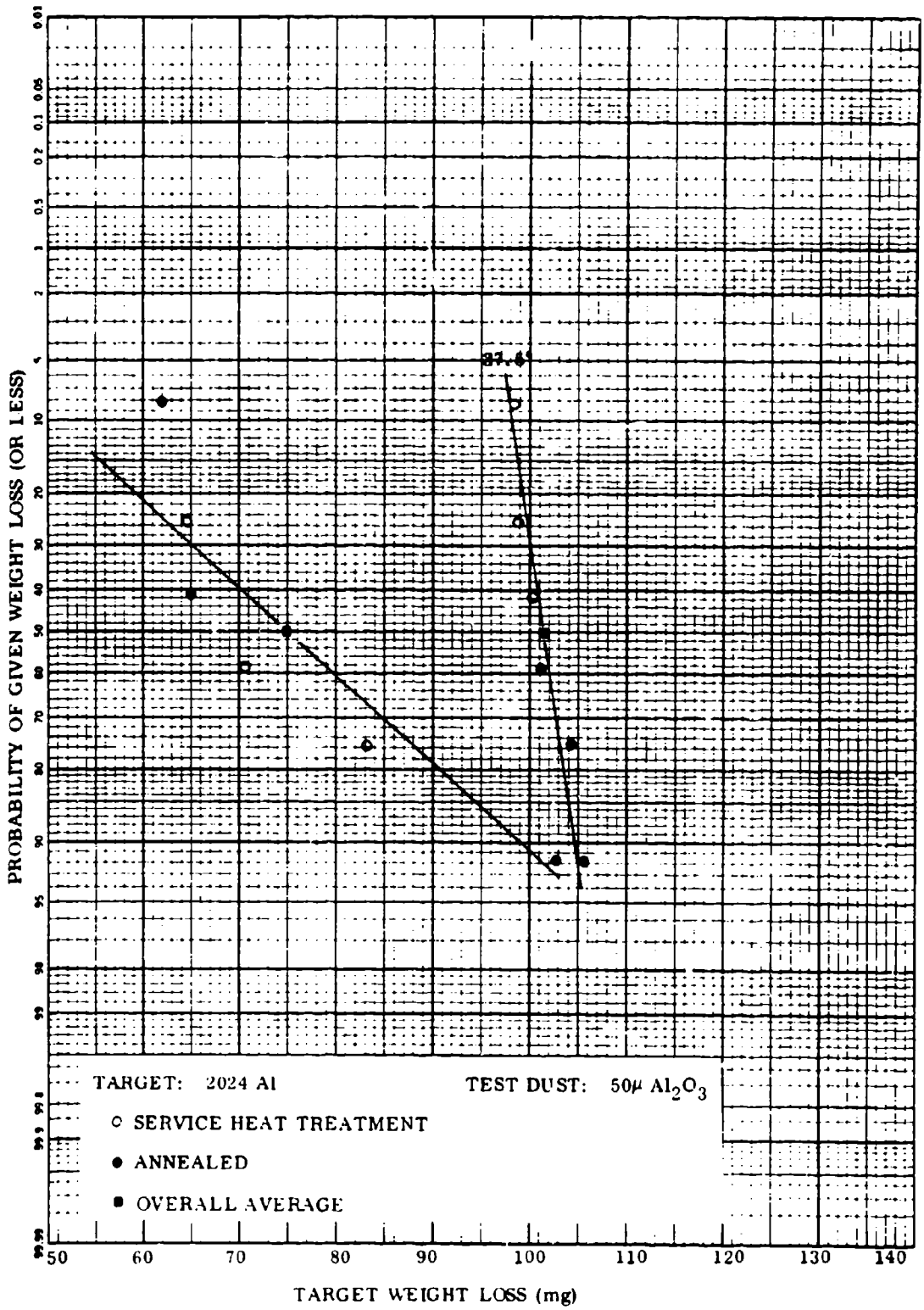

Figure 36C. Probability Plot of Test Series I Data.

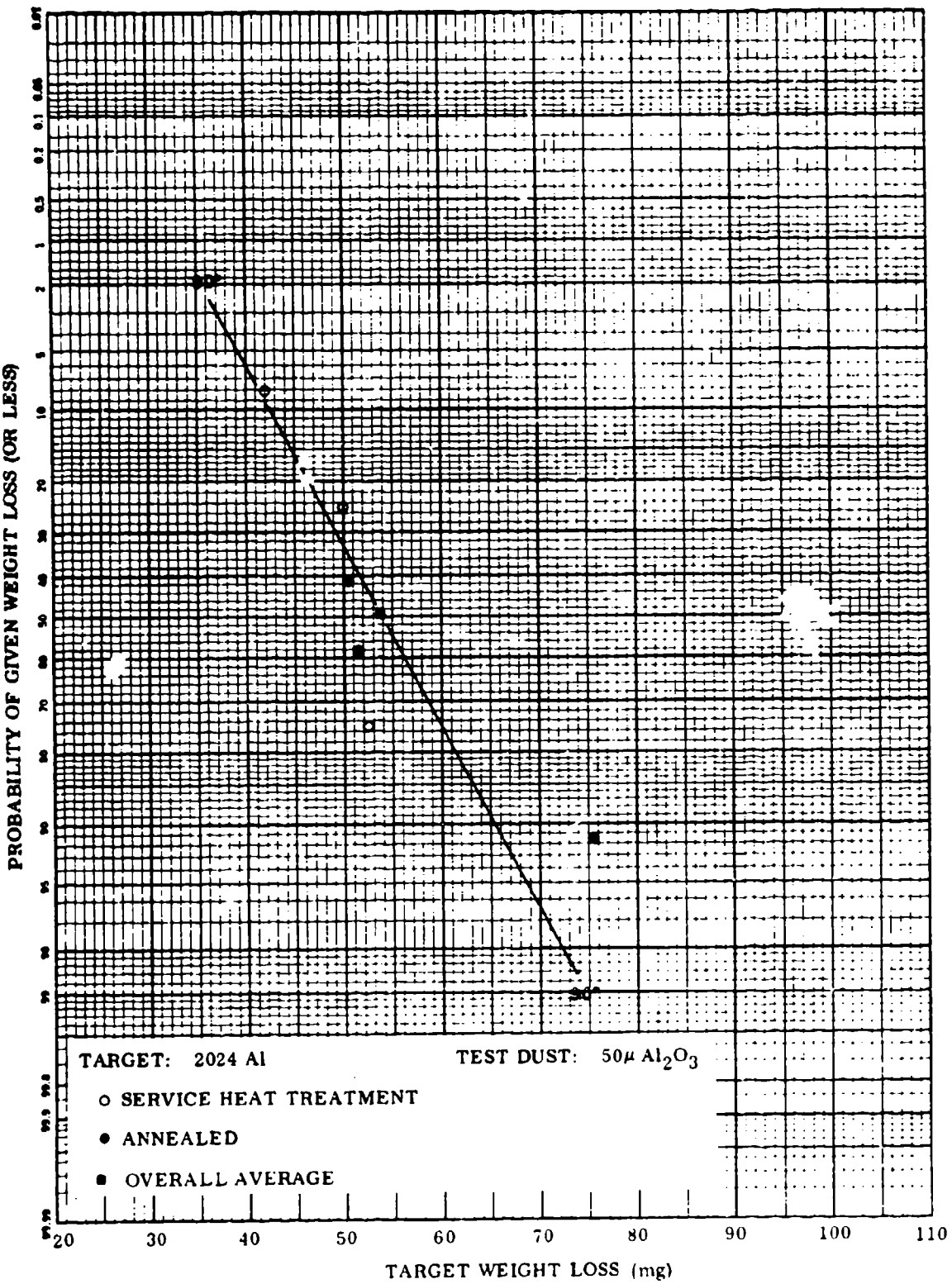

Figure 36D. Probability Plot of Test Series I Data.

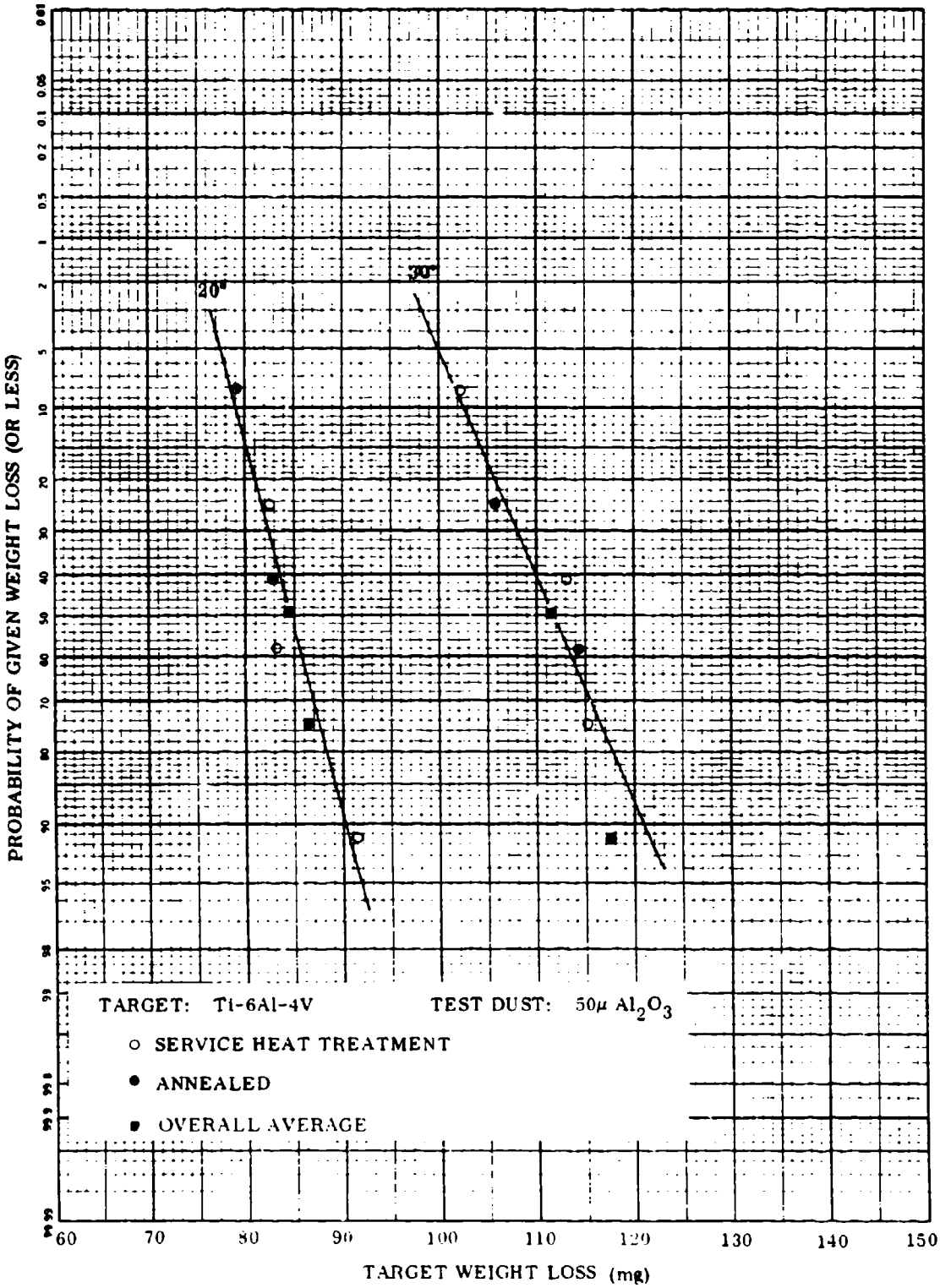

Figure 37A. Probability Plot of Test Series I Data.

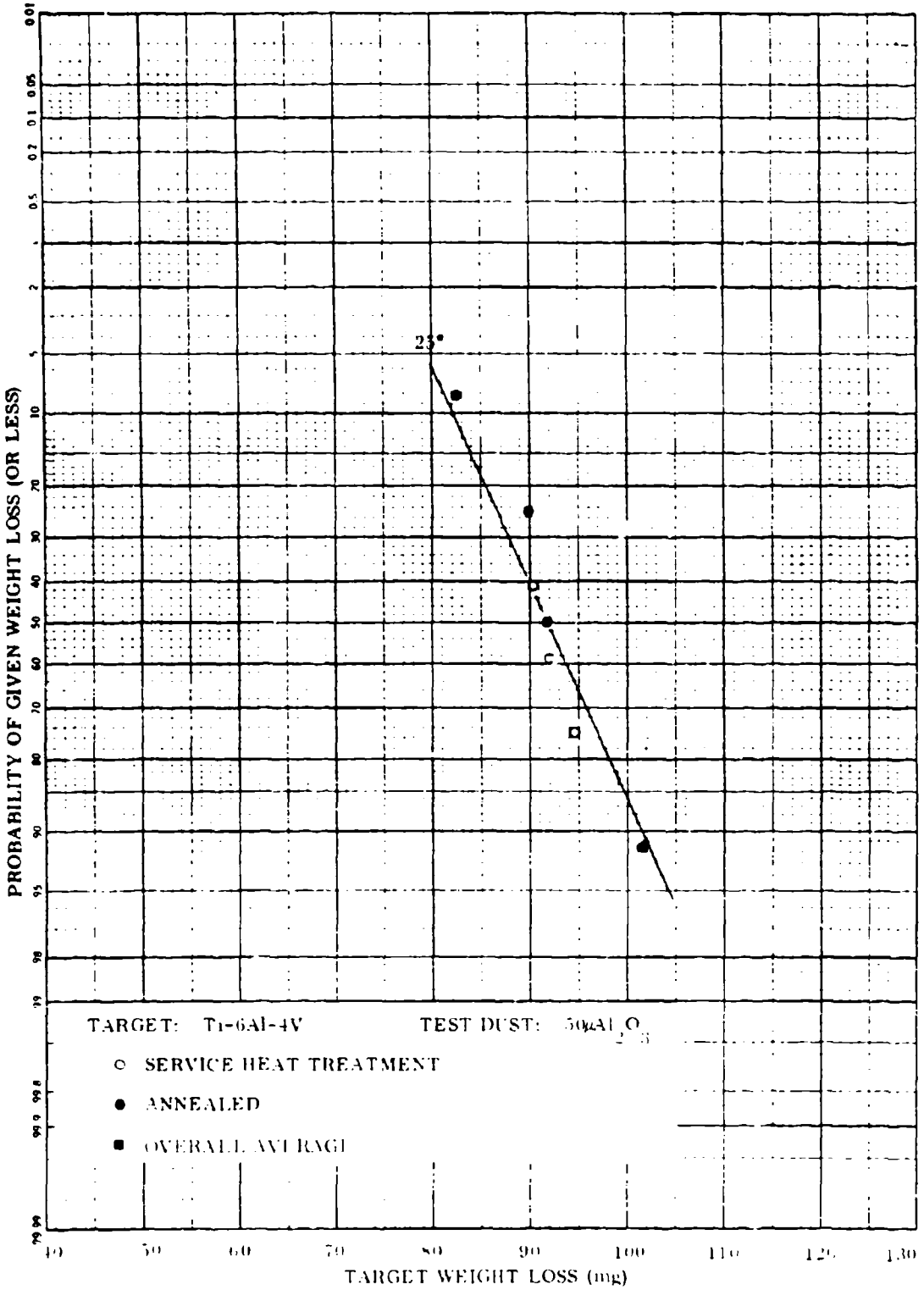

Figure 37B. Probability Plot of Test Series I Data.

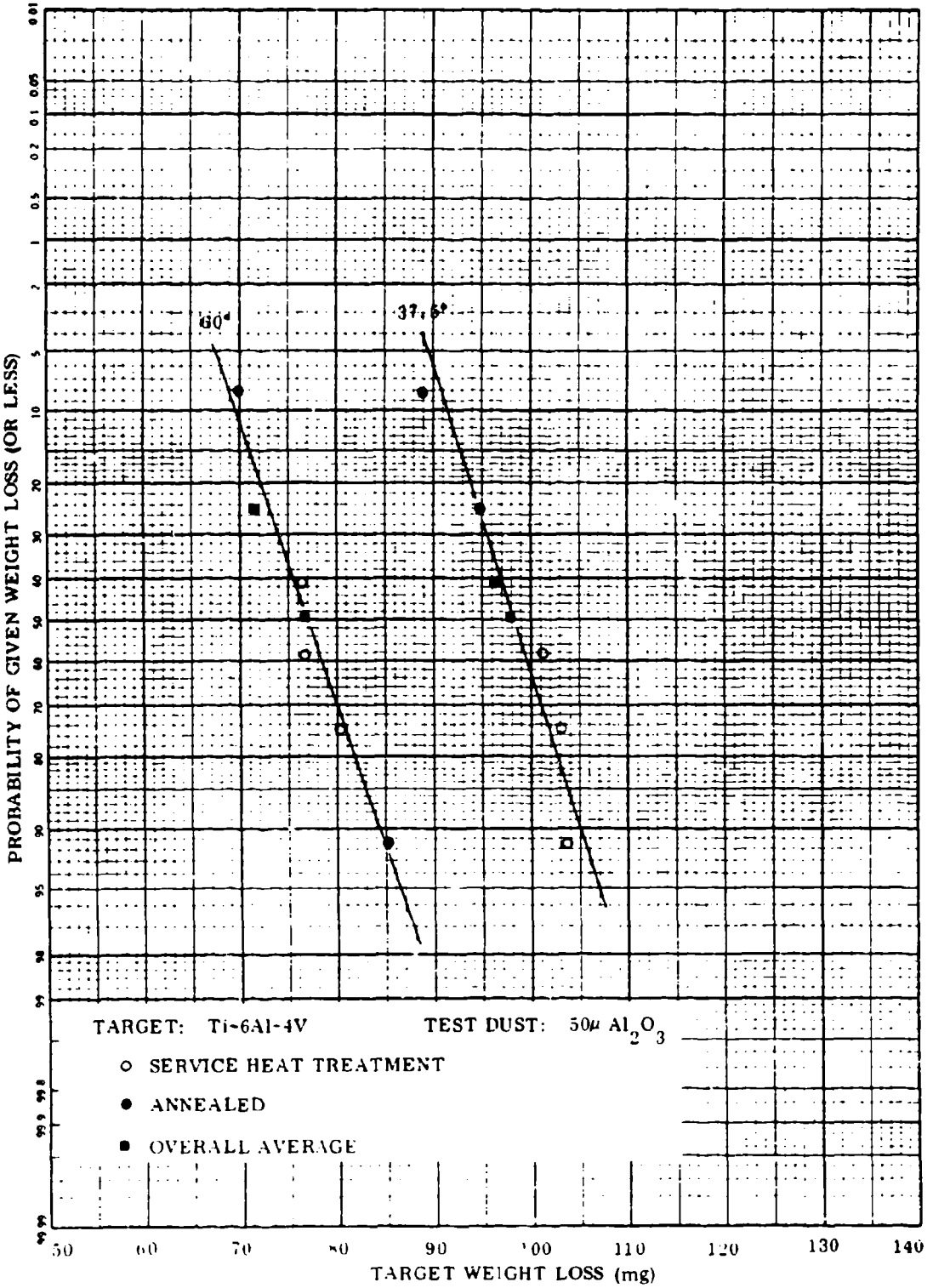

Figure 37C. Probability Plot of Test Series I Data.

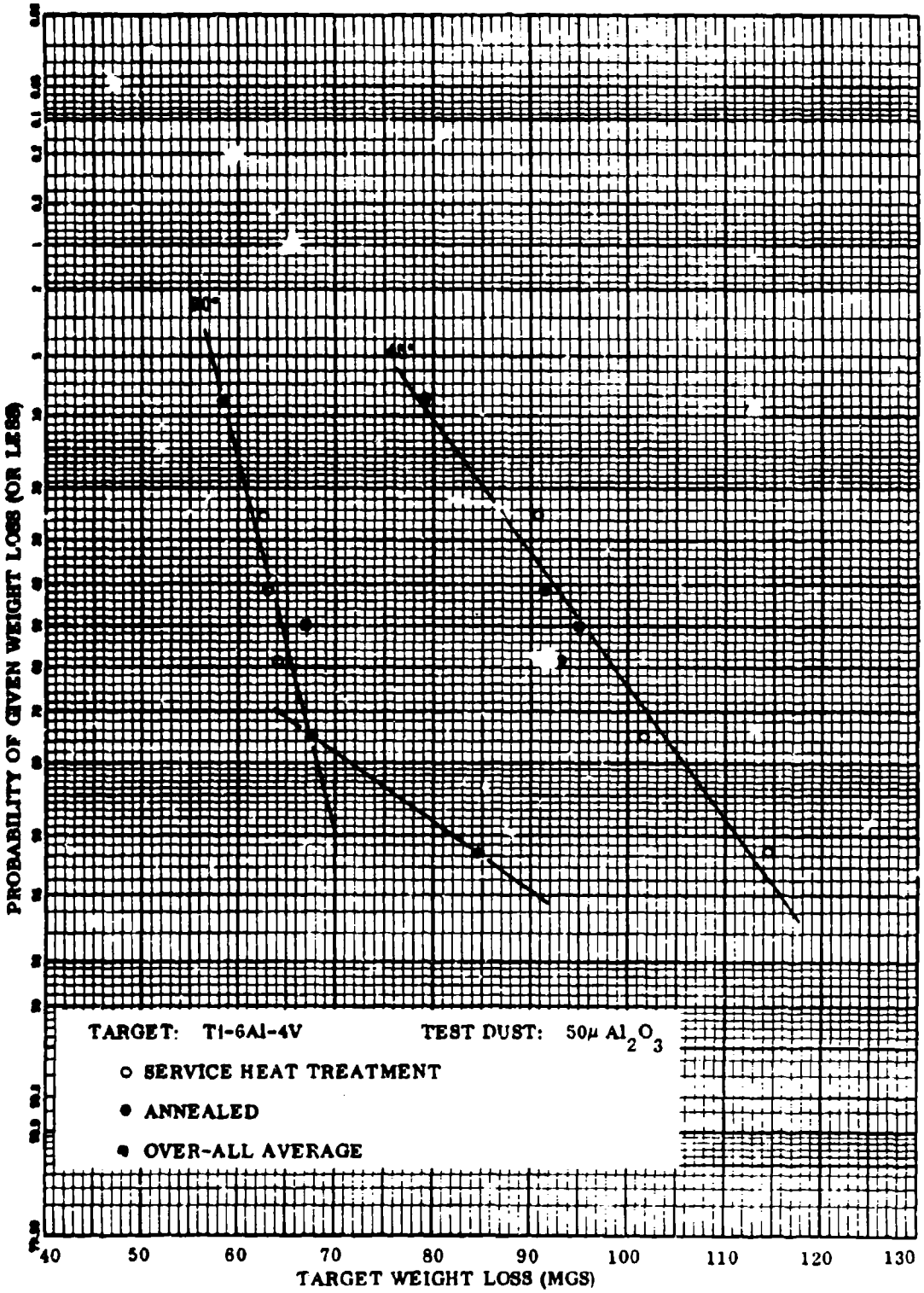

Figure 37D. Probability Plot of Test Series I Data.

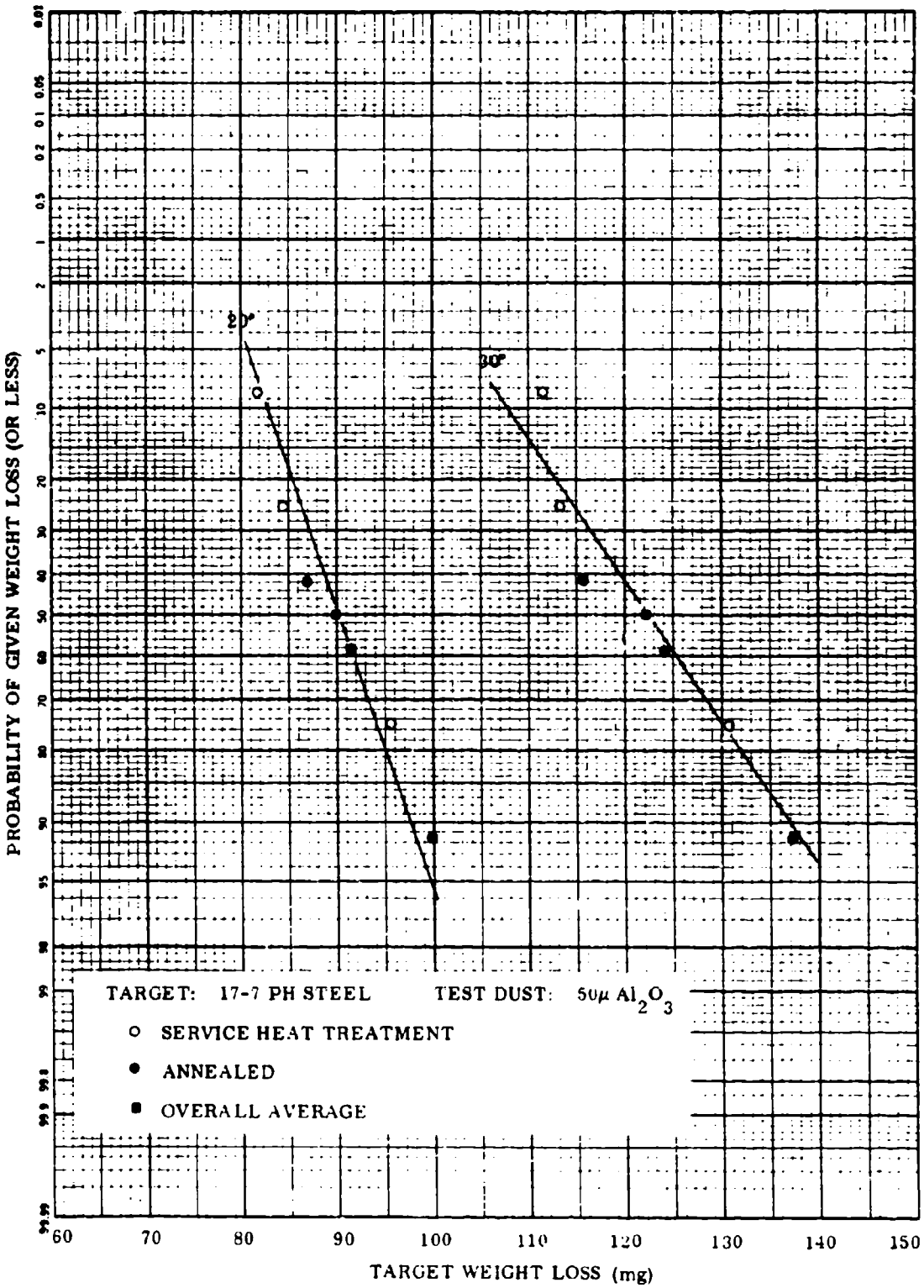

Figure 38A. Probability Plot of Test Series I Data.

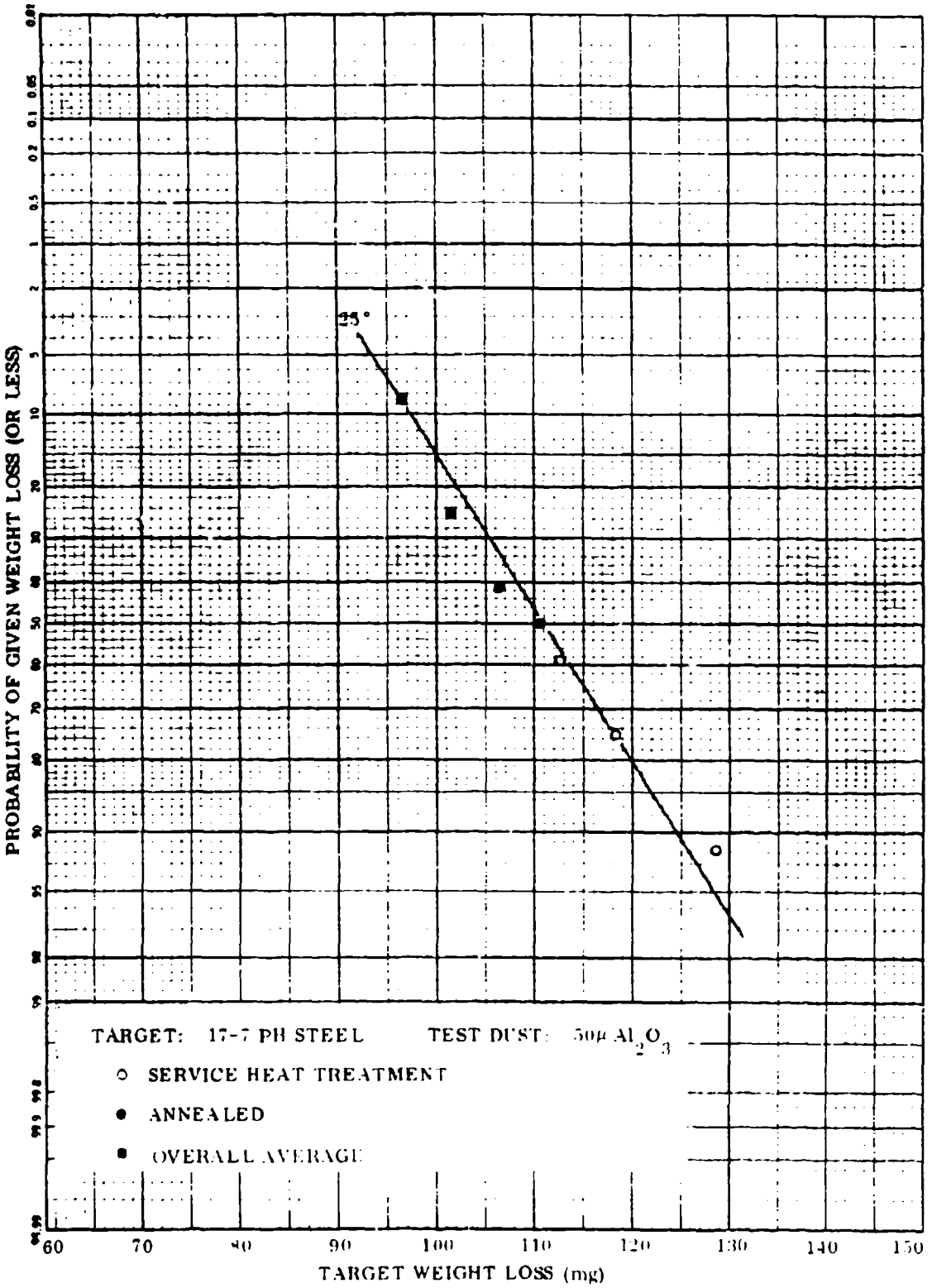

Figure 38B. Probability Plot of Test Series I Data.

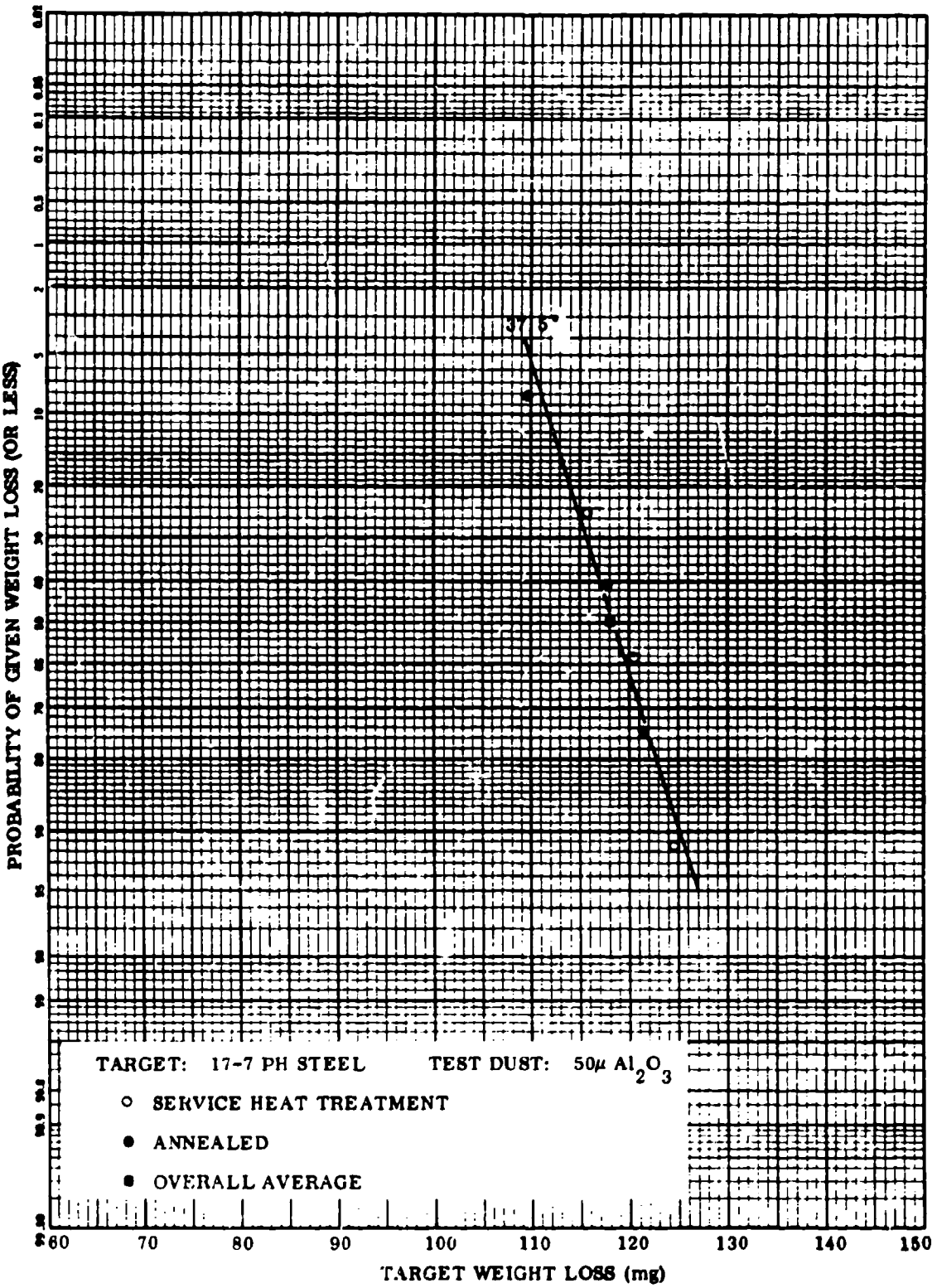

Figure 38C. Probability Plot of Test Series I Data.

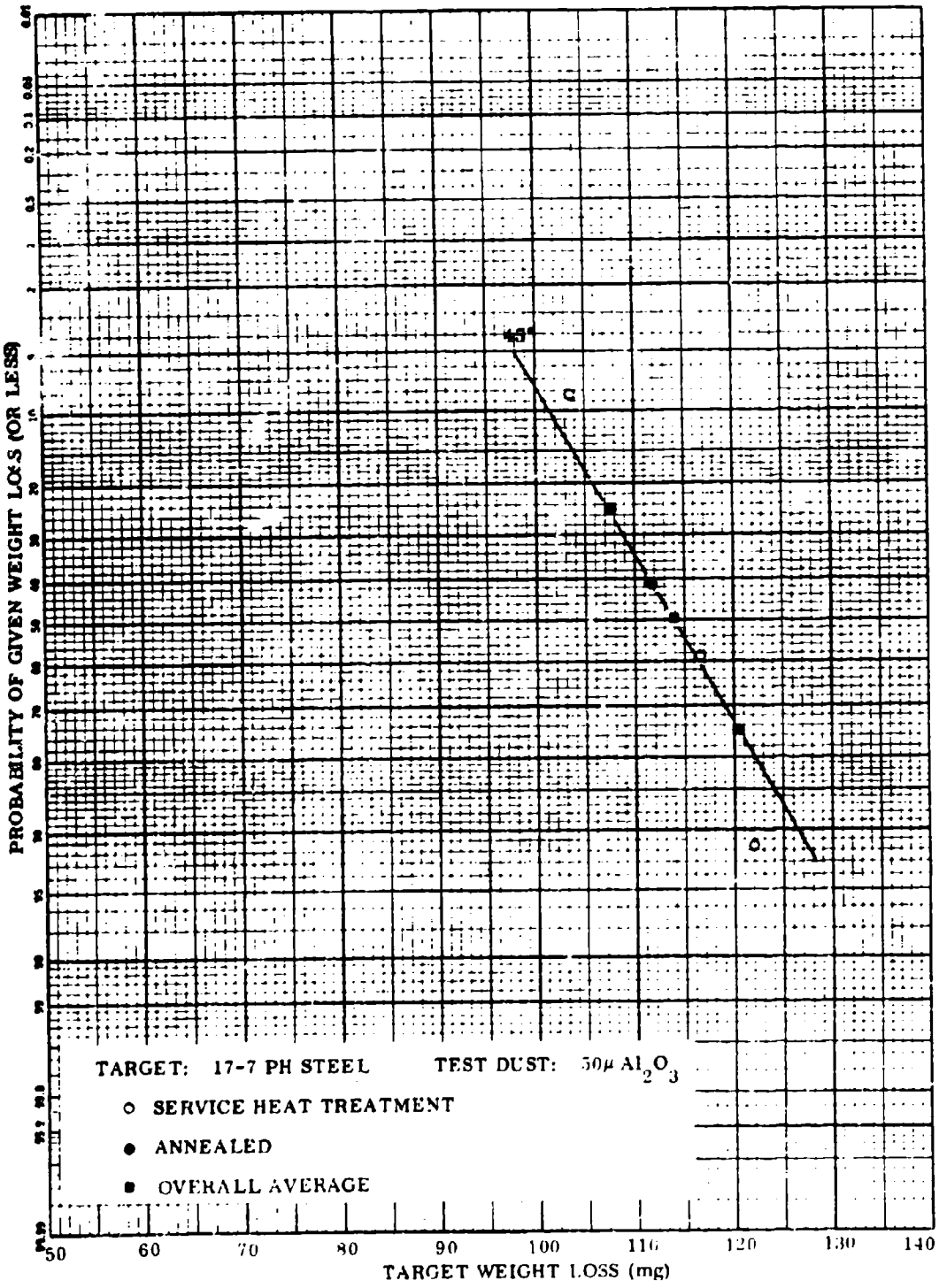

Figure 38D. Probability Plot of Test Series I Data.

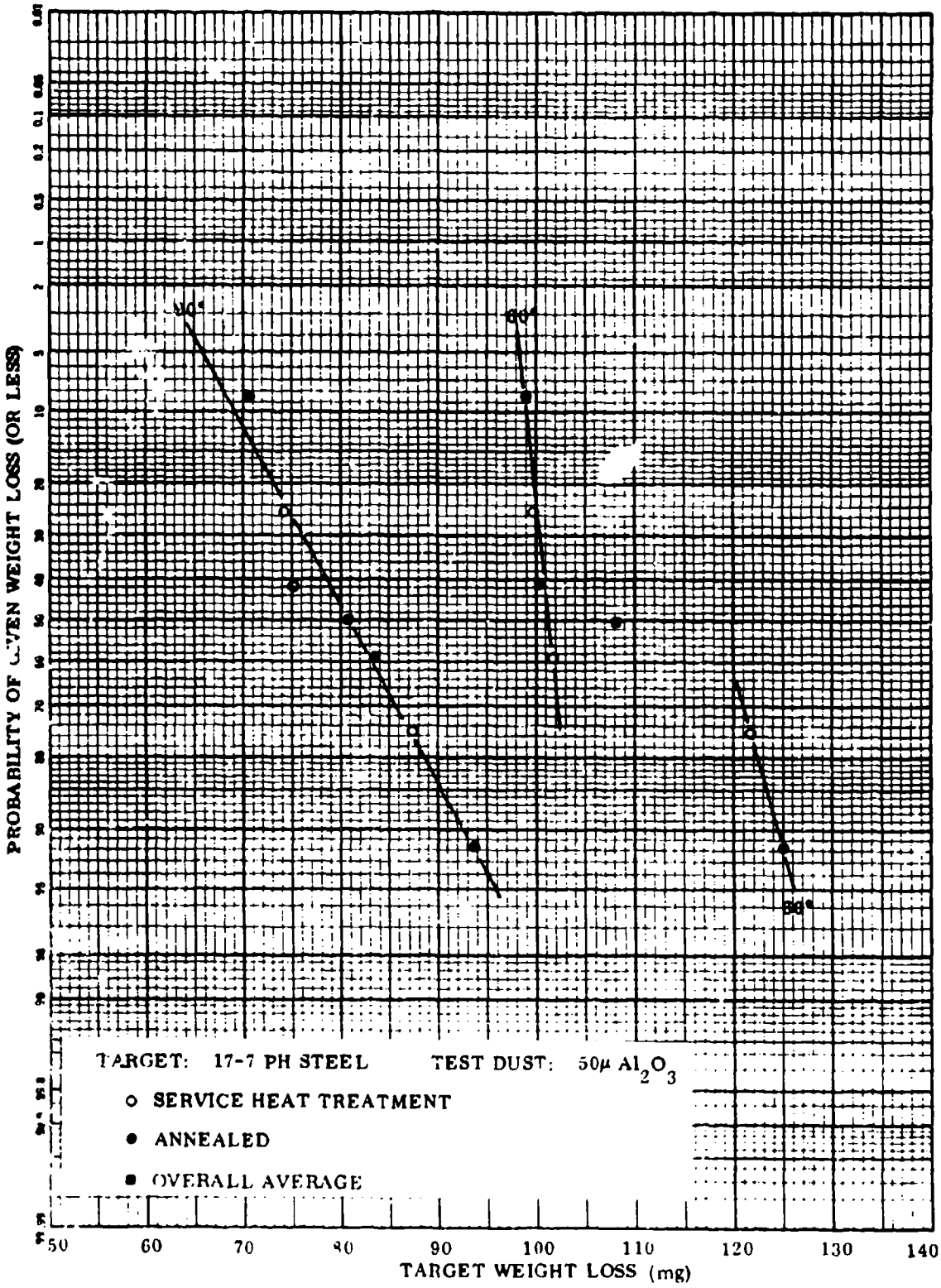

Figure 38E. Probability Plot of Test Series I Data.

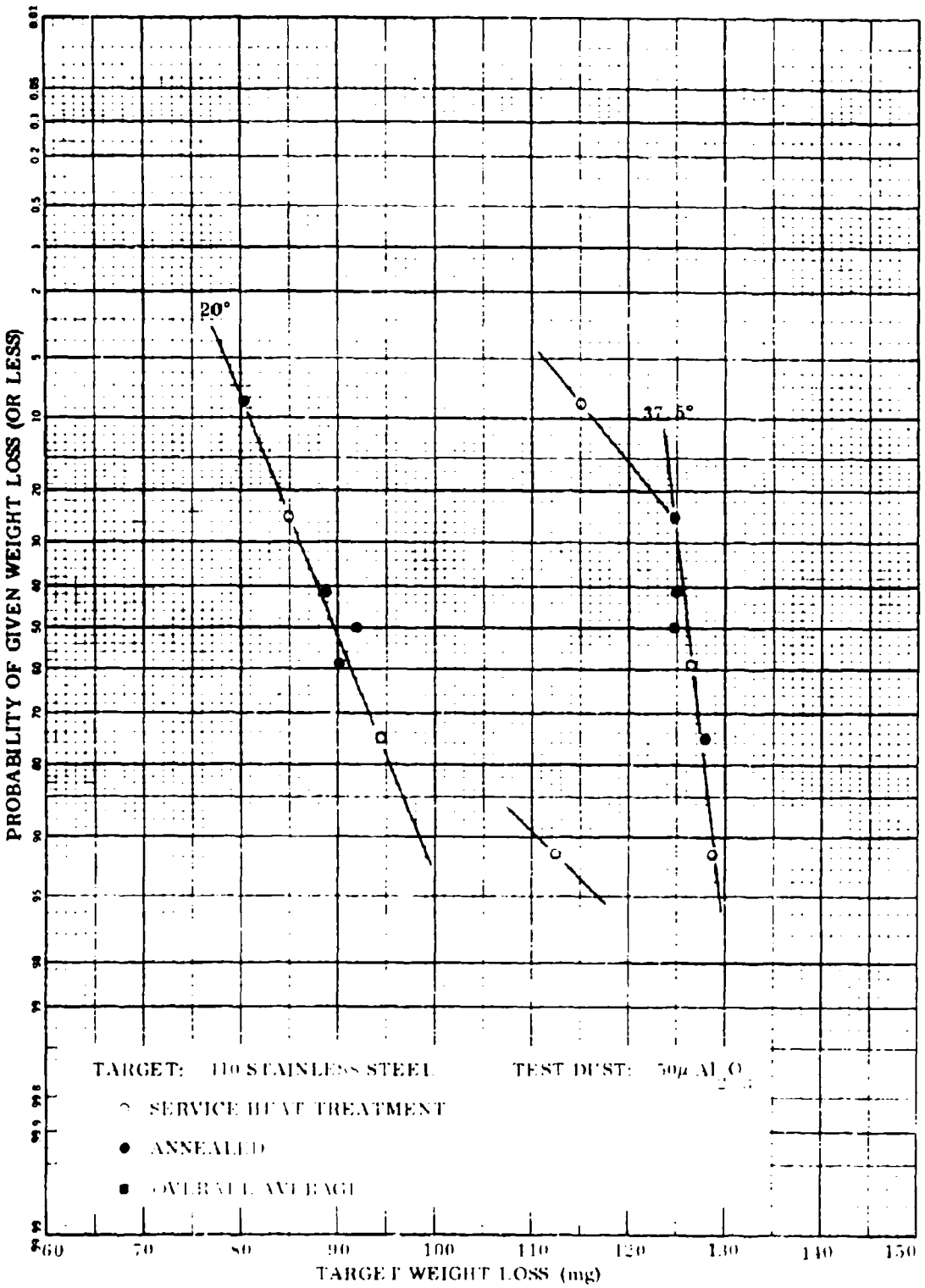

Figure 39A. Probability Plot of Test Series I Data.

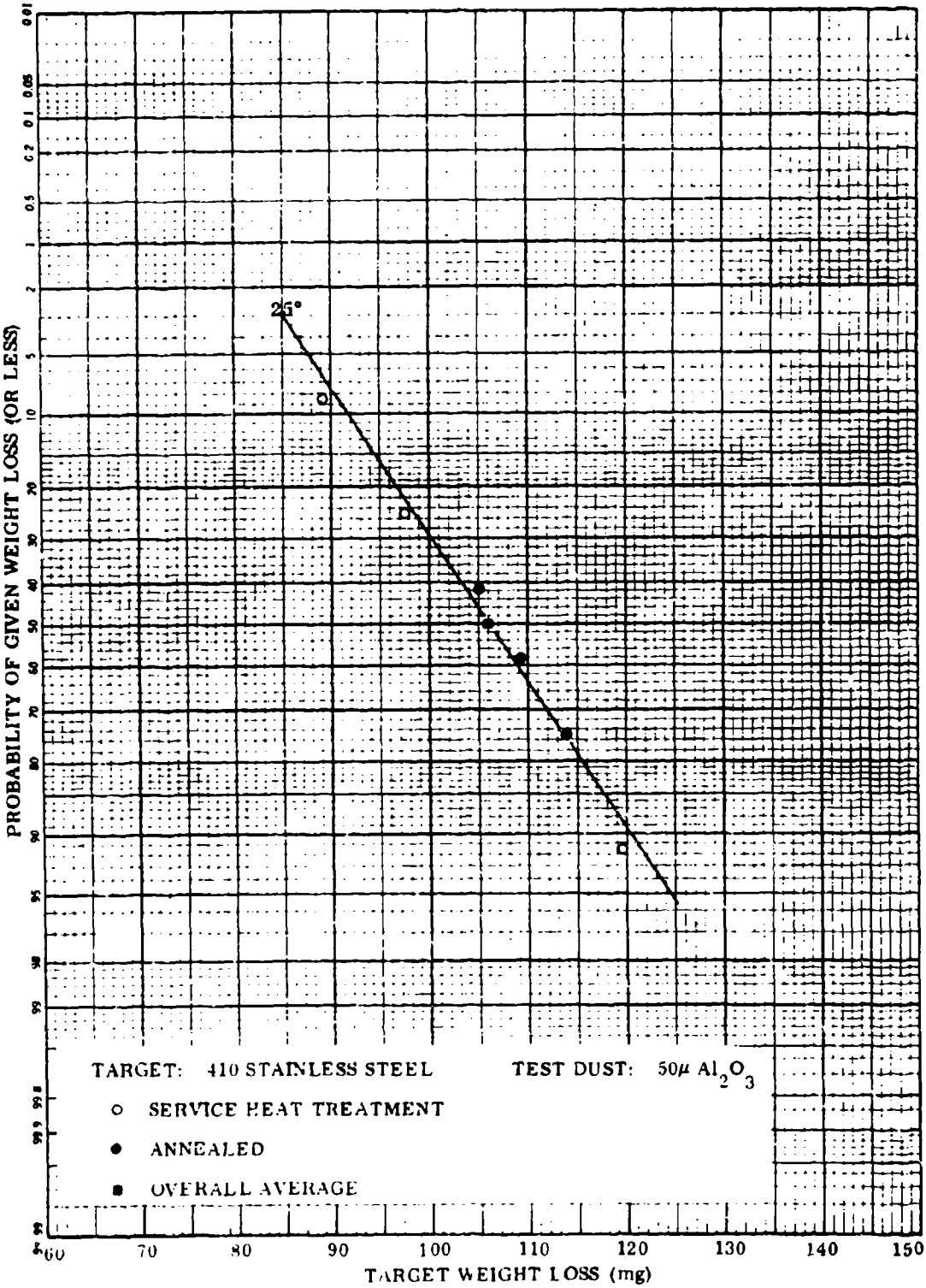

Figure 39B. Probability Plot of Test Series I Data.

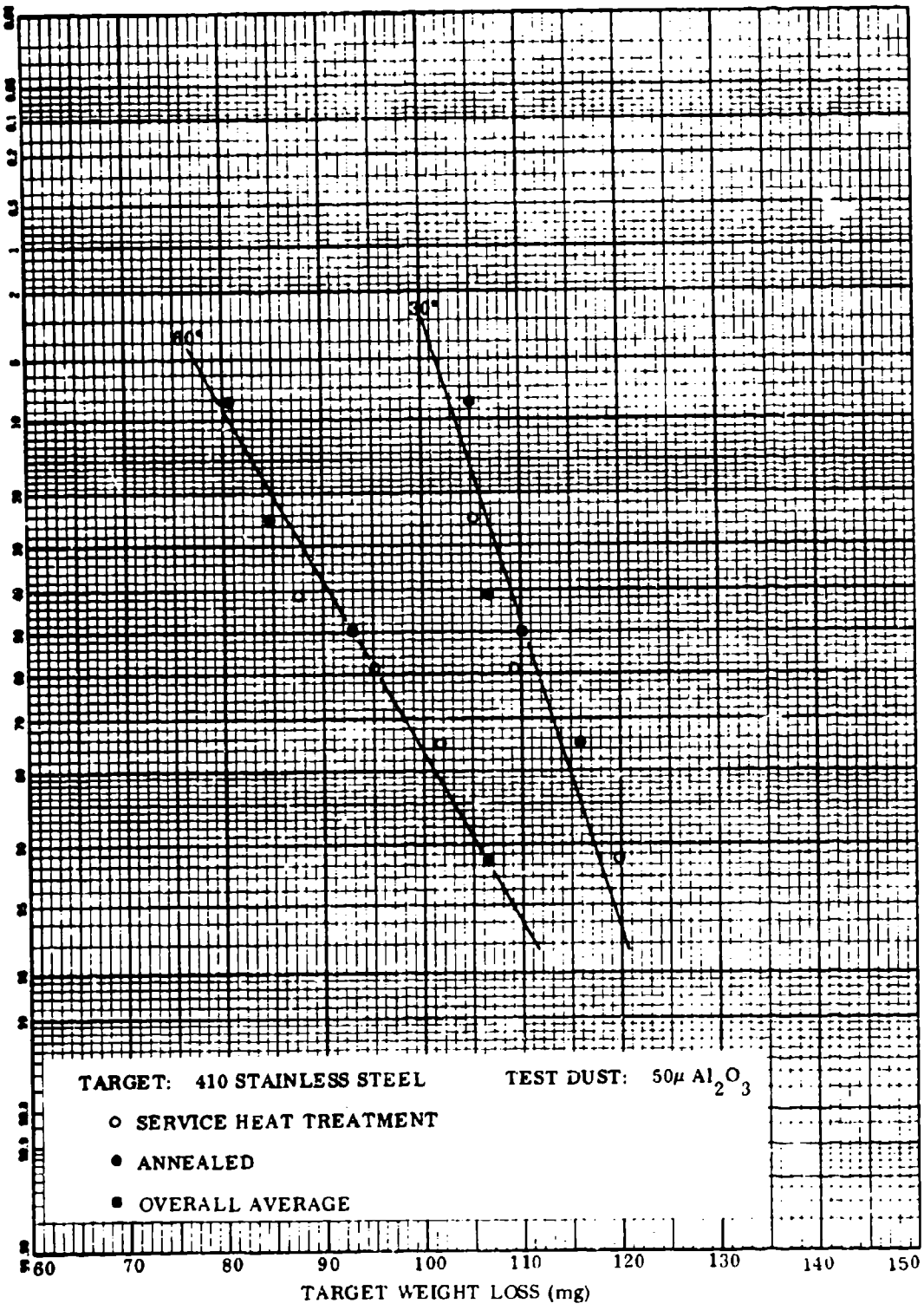

Figure 39C. Probability Plot of Test Series I Data.

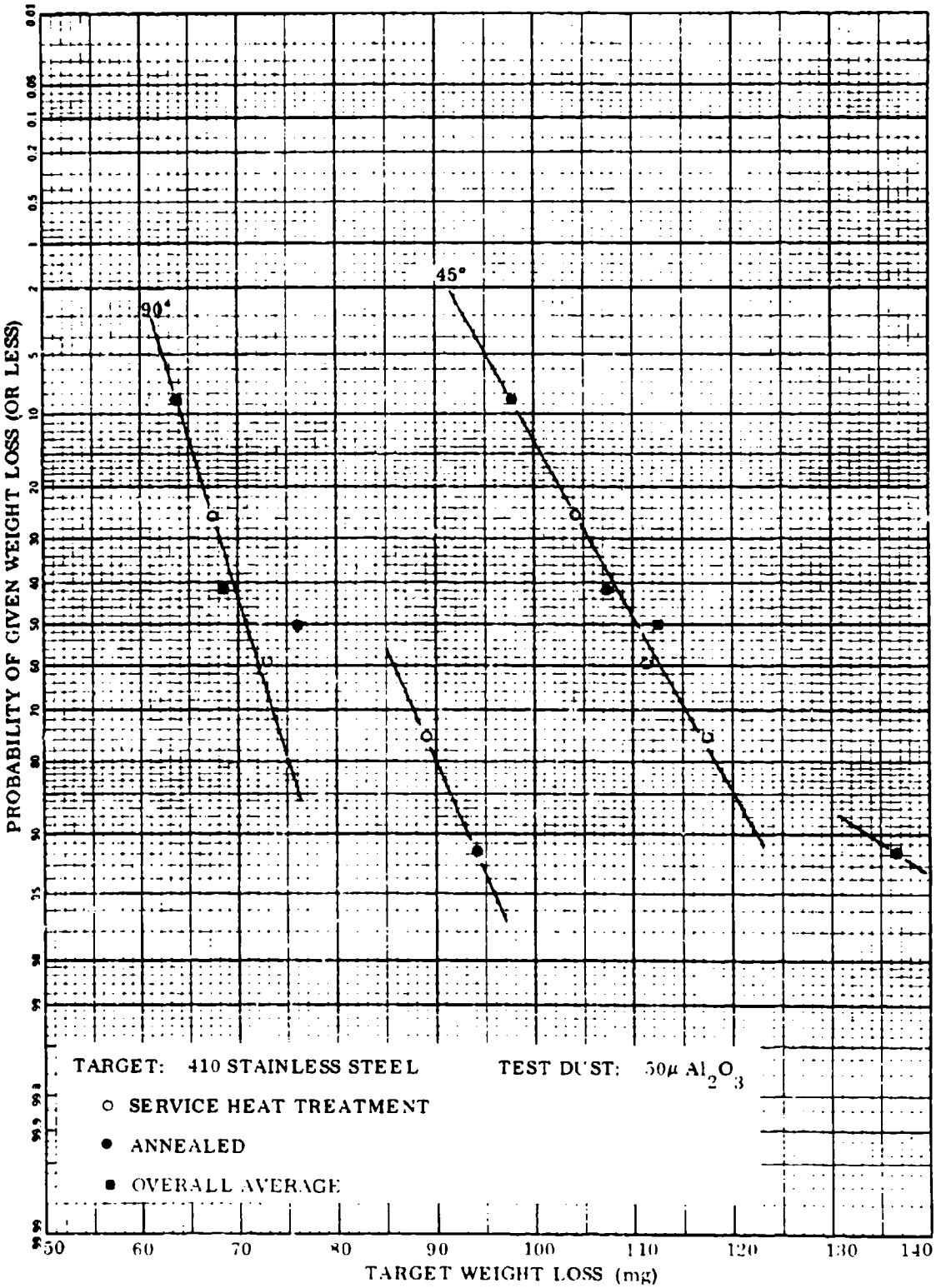

Figure 39D. Probability Plot of Test Series I Data.

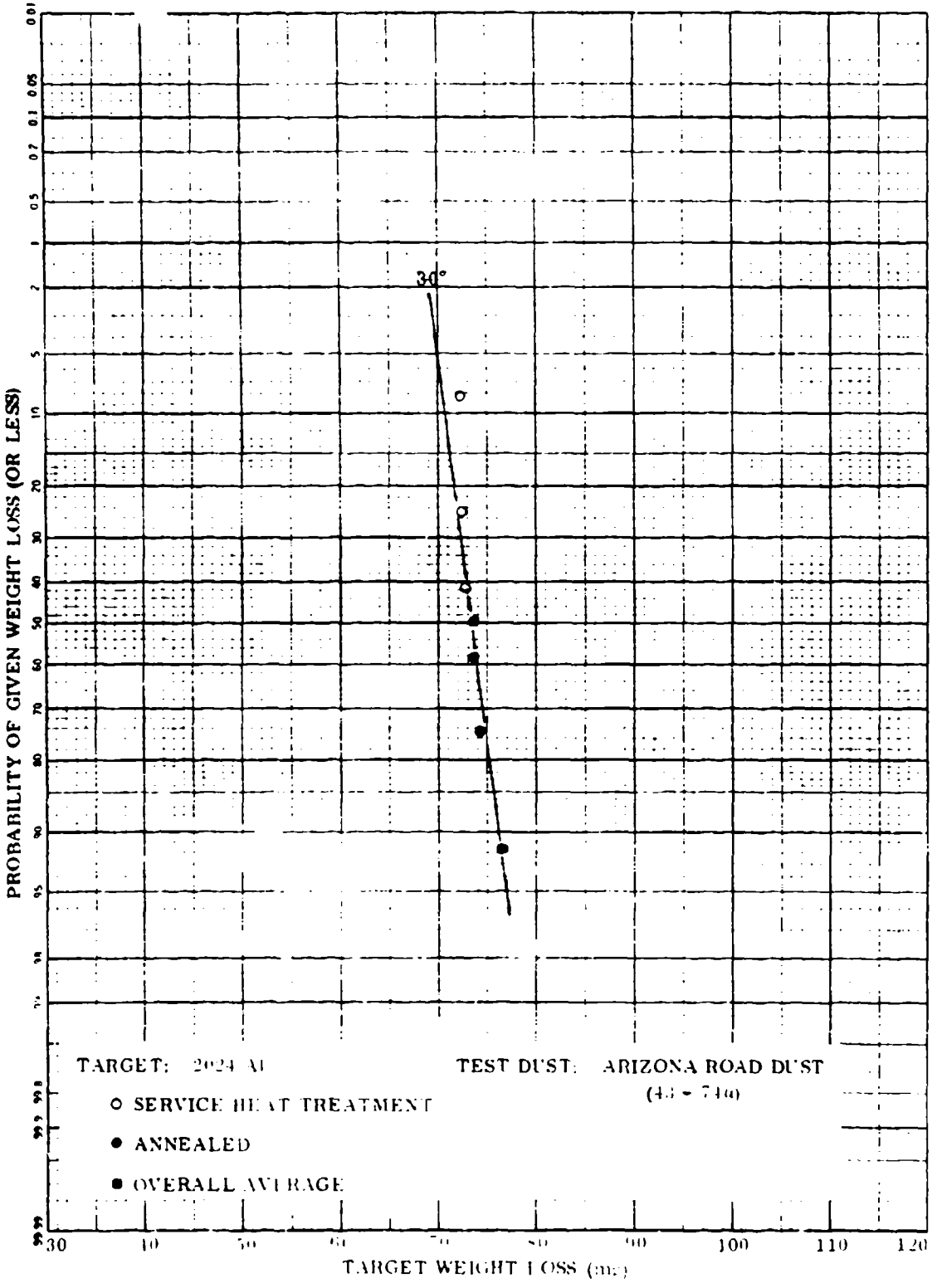

Figure 40A. Probability Plot of Test Series I Data.

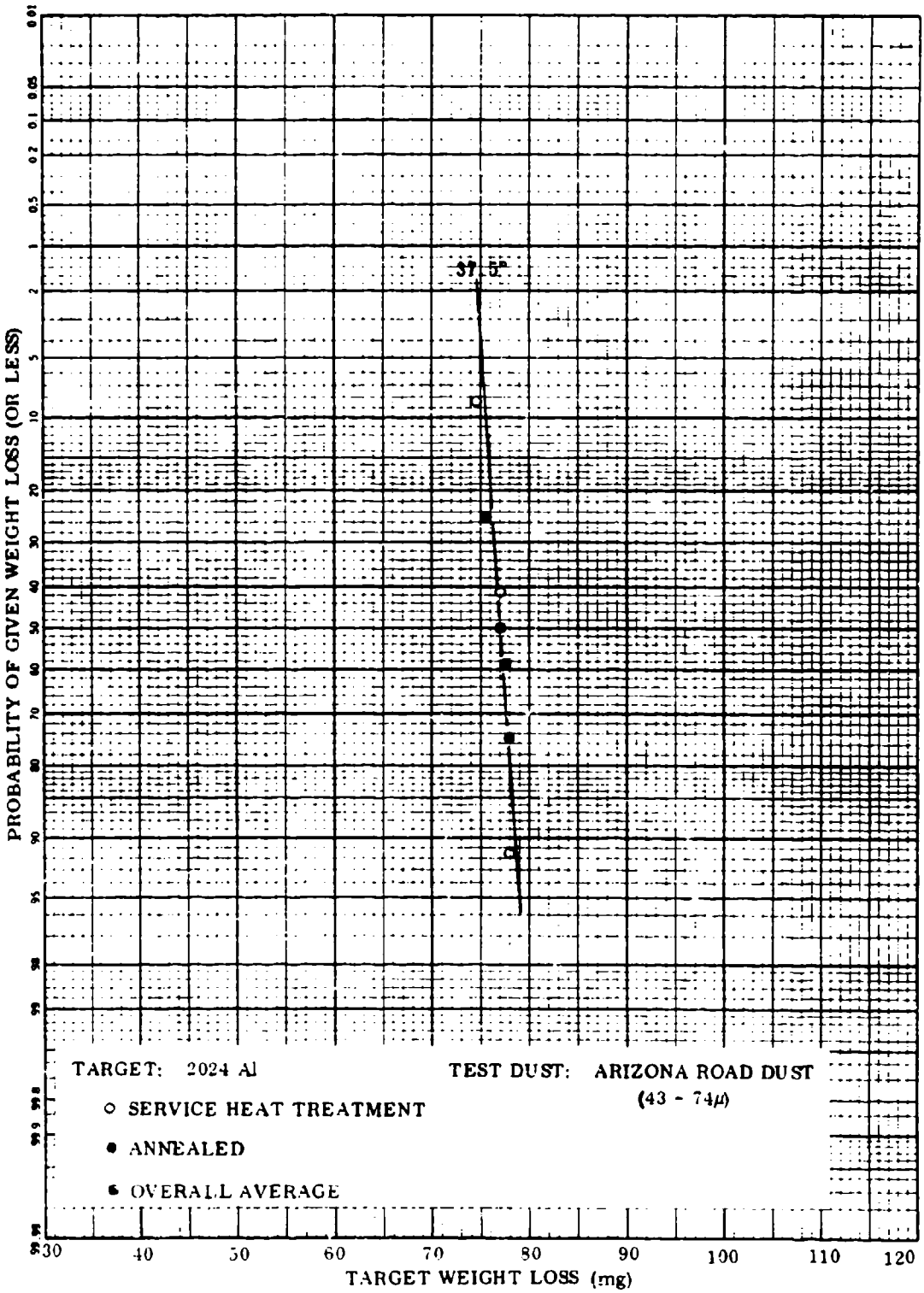

Figure 40B. Probability Plot of Test Series I Data.

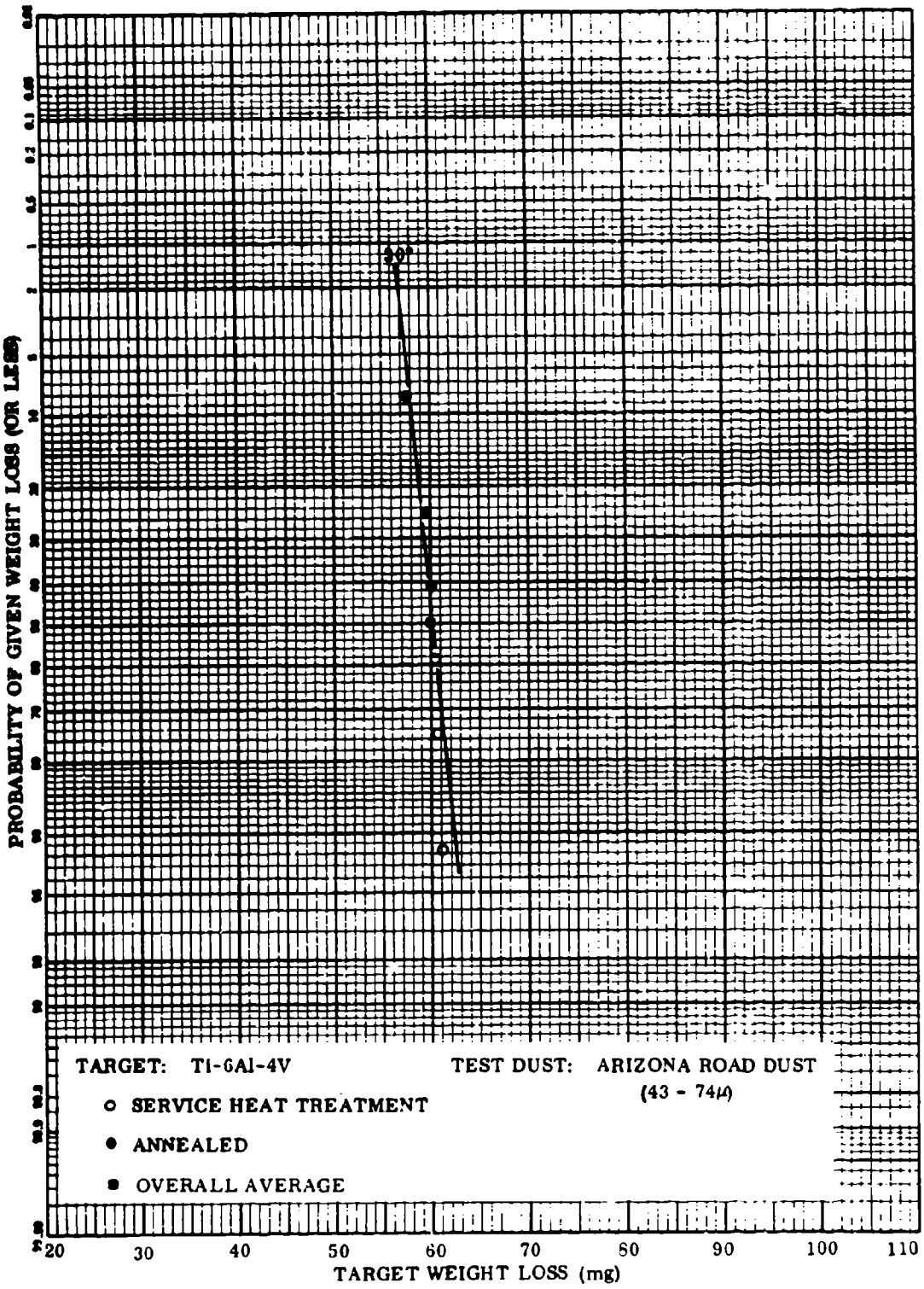

Figure 41A. Probability Plot of Test Series I Data.

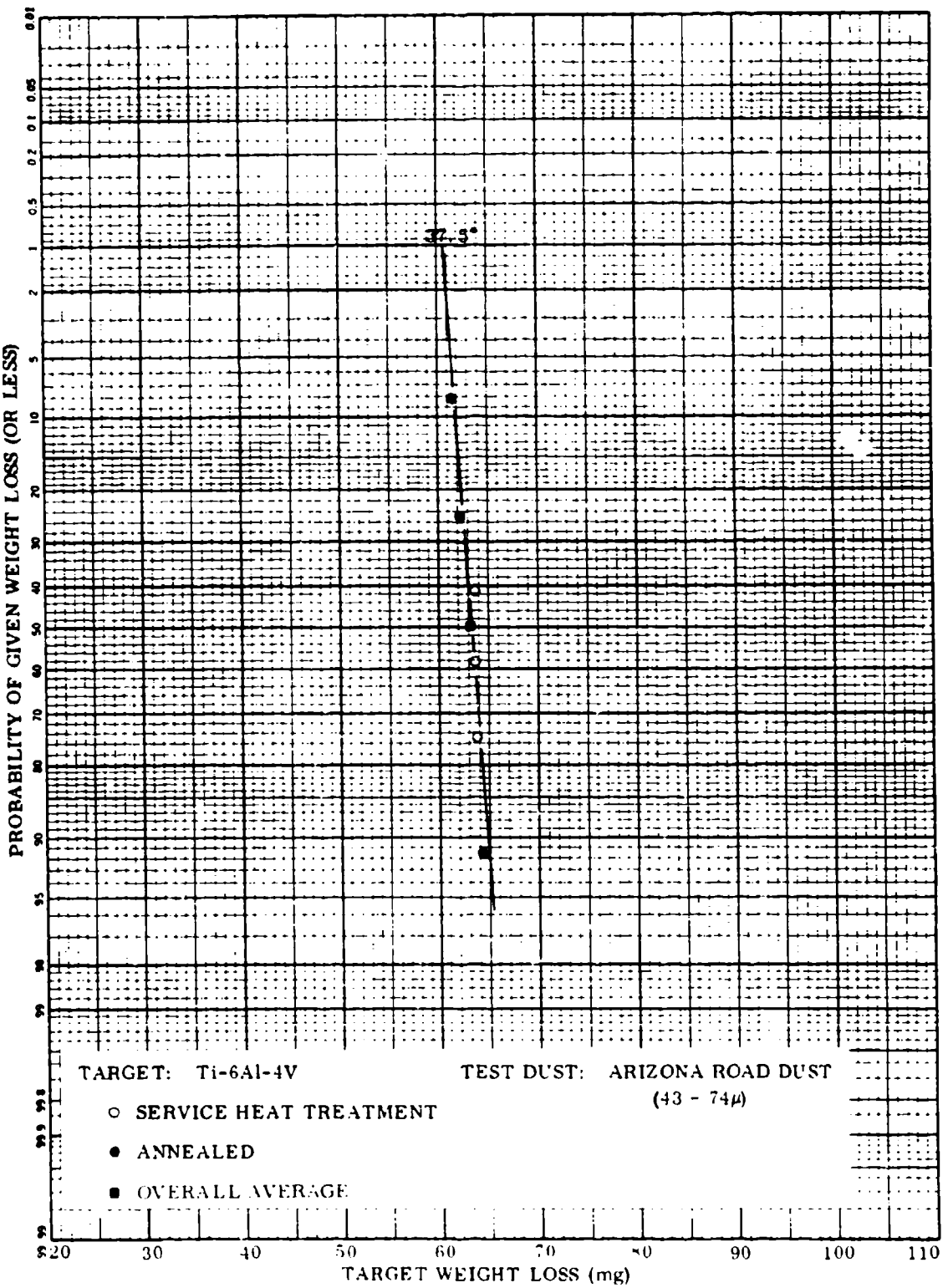

Figure 41B. Probability Plot of Test Series I Data.

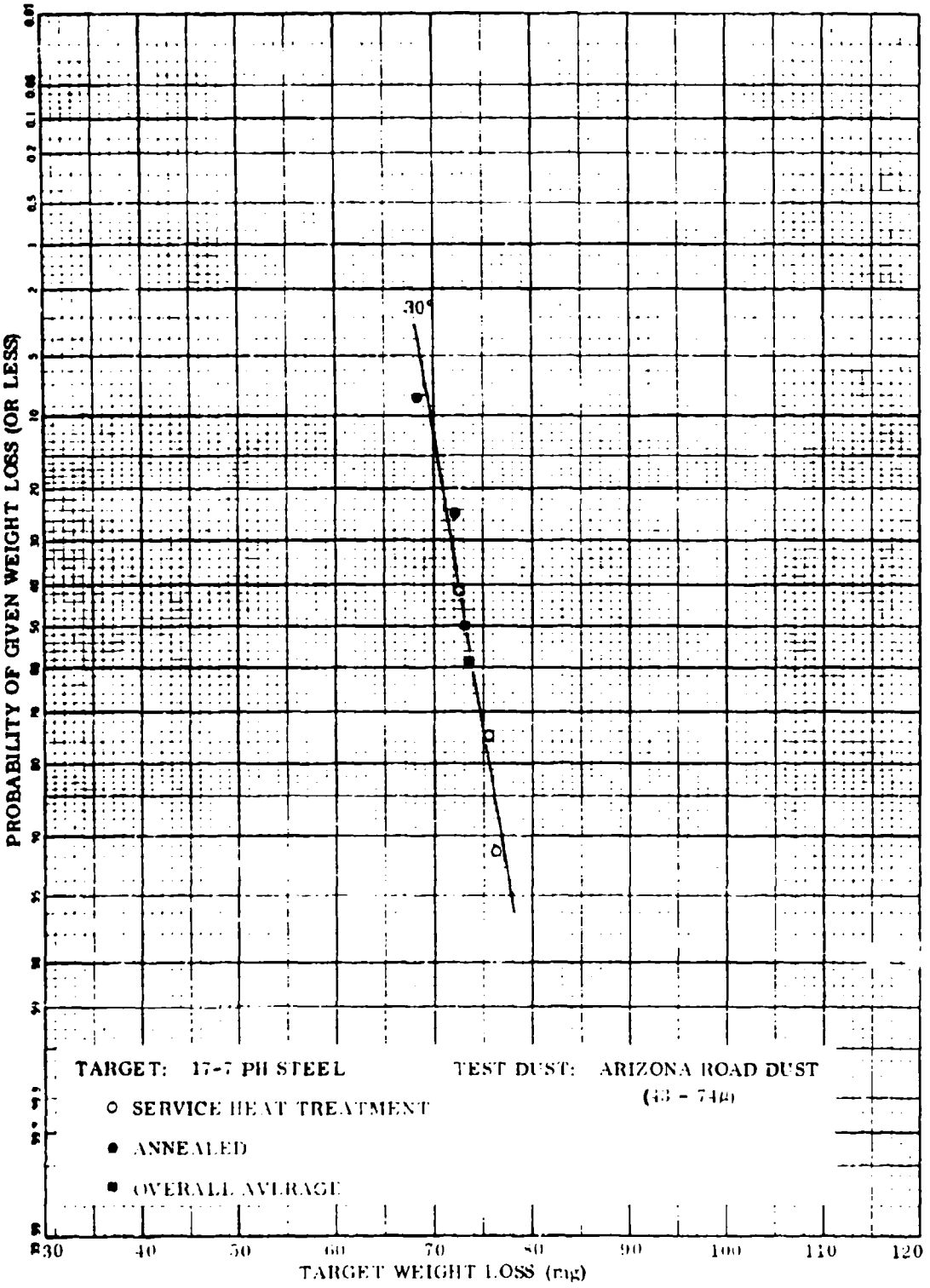

Figure 42A. Probability Plot of Test Series I Data.

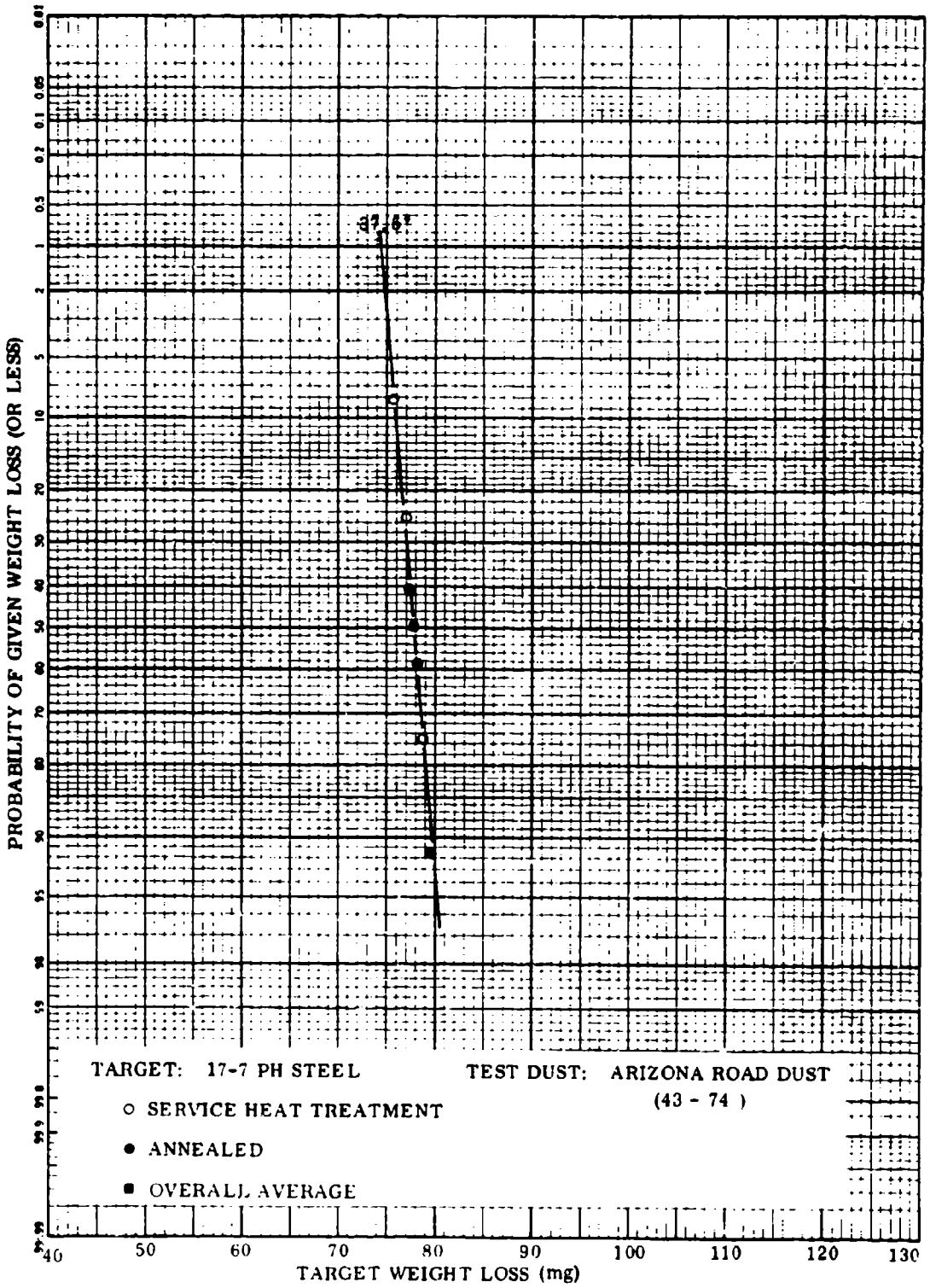

Figure 42B. Probability Plot of Test Series I Data.

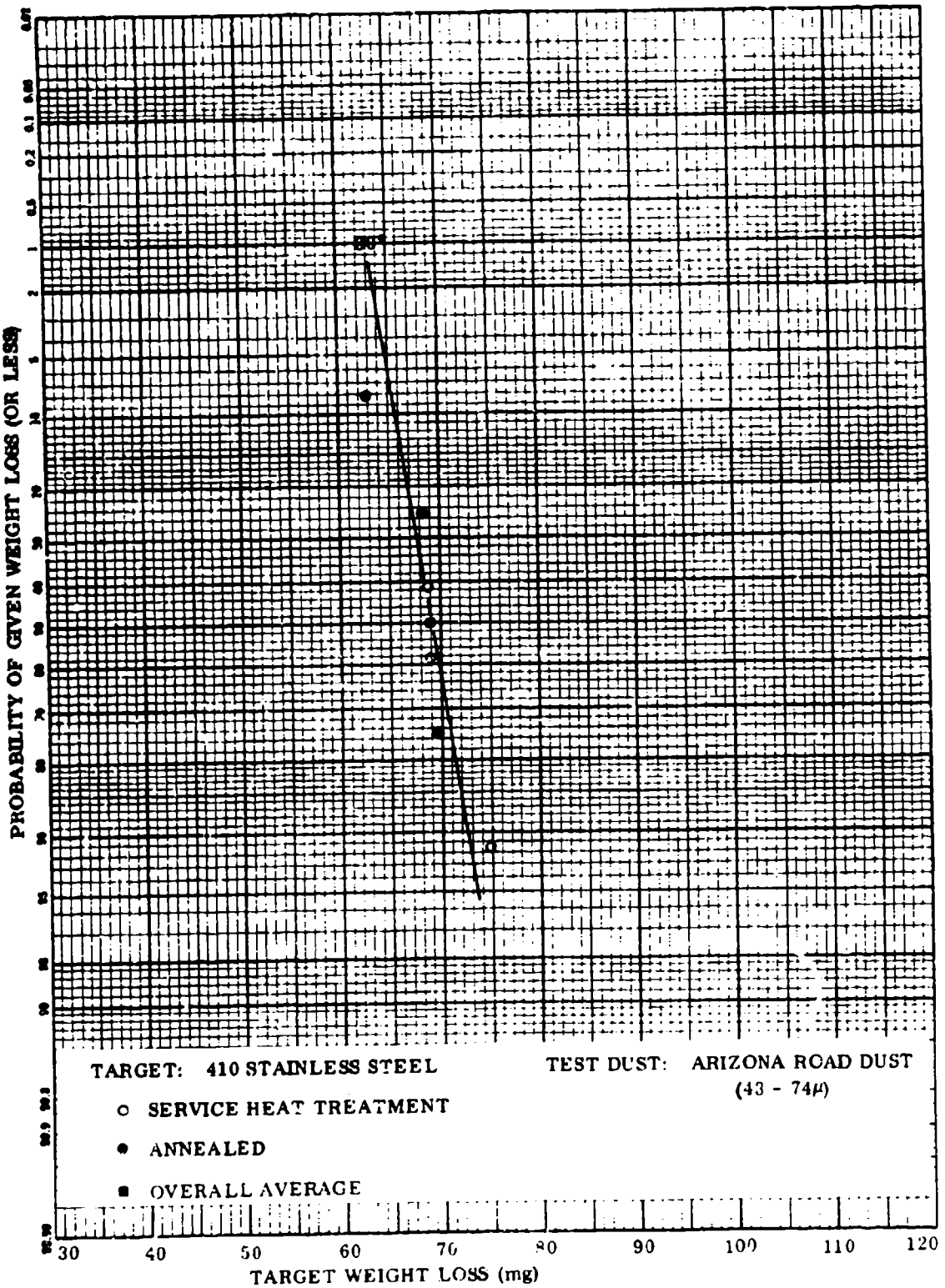

Figure 43A. Probability Plot of Test Series I Data.

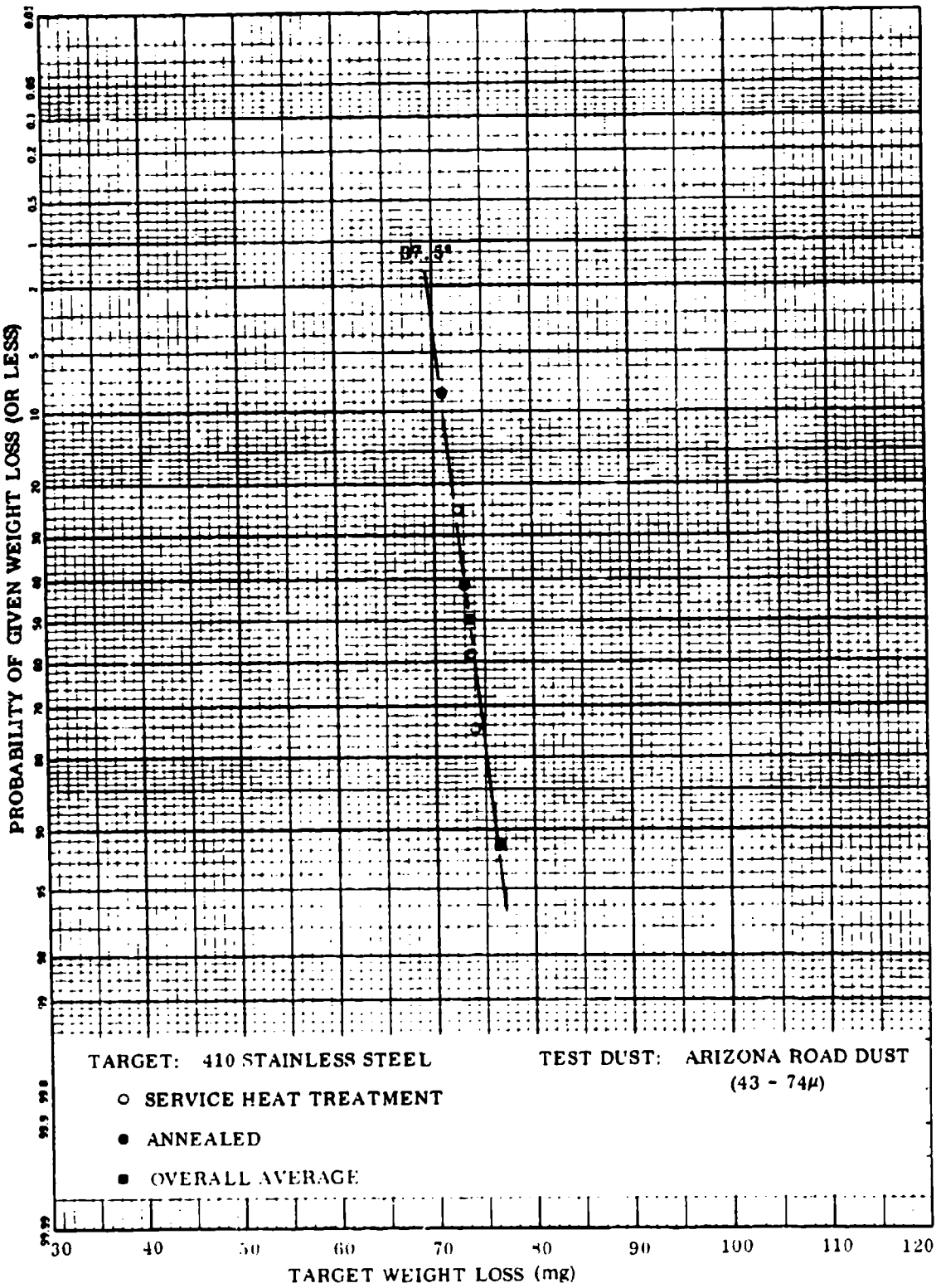

Figure 43B. Probability Plot of Test Series I Data.

Maximum volume losses for the aluminum-alloy target run from about 2.4 (Al_2O_3 dust) to 2.8 (Arizona Road Dust) times the corresponding values for the steel targets, while the titanium-alloy-to-steel volume ratios are 1.6 (Al_2O_3 dust) and 1.5 (Arizona Road Dust). It is felt that volume loss data should be of more importance to the design engineer.

Because of the similar erosion factors obtained regardless of target alloys or metallurgical condition, it was decided to defer investigation of other (possibly controlling) material variables until programmed studies of environmental variables and erosion phenomena were executed. It was anticipated that these studies would furnish needed insight into the materials aspects of the erosion mechanism.

Influence of Test Dust Variety

The influence of dust variety on erosion factor was investigated by comparing the test results for Al_2O_3 and Arizona Road Dust particles of the same nominal diameter (50-micron) under the conditions of these tests (equivalent particle kinetic energy and 1.6 times more Arizona Road Dust particles than Al_2O_3 particles per test). Equation (1) predicts that erosion losses with Arizona Road Dust should be 1.6 times greater than with Al_2O_3, assuming that the system correction factor remains constant. Instead, the actual erosion factors obtained with silica-rich Arizona Road Dust were only 53-75 percent of those obtained with the harder Al_2O_3 dust; the percentage varied with the specific target alloy (Figures 32 and 33).

At the impingement angles for maximum erosion, the Arizona Road Dust is only fractionally as erosive as Al_2O_3 by the following percentages based on target weight loss or erosion factor:

Target	Impingement Angle (Deg)	Percent of Loss (Al_2O_3 = 100)
2024-Al	30	71
	37.5	75
Ti-6Al-4V	30	53
	37.5	64
410 Stainless Steel	30	63
	37.5	58
17.7 PH Stainless Steel	30	60
	37.5	66

The major reason for this difference is believed to be the greater refractoriness and hardness of the fused alumina (2260 $KHN_{100\ gm}$) versus SiO_2 (950 $KHN_{100\ gm}$).

However, another possible explanation is that the Arizona Road Dust is a heterogeneous soil sample of which only ≈68.5 percent (weight) is hard SiO_2 (the balance consisting of appreciably softer minerals). In contrast, the metallographic grade Al_2O_3 is a homogeneous sample consisting of 100 percent highly abrasive alumina.

Even so, the average erosion loss per individual SiO_2 particle impact is only 48-68 percent of the loss attributable to each Al_2O_3 particle impact. It is clear that the variety of dust is a major factor in setting erosion behavior.

Erosion Efficiency

Erosion efficiency per se, as described by the erosion factor, ϵ, is quite low for all test dusts and all target materials (Tables V and VI). The range of ϵ observed was from $1.79 - 4.08 \times 10^{-3}$ for 50-micron alumina dust, and from $1.14 - 2.59 \times 10^{-3}$ for the Arizona Road Dust (43-74-micron). This means that approximately 250 to 1000 parts by weight of dust are required to remove just one part by weight of target material. The erosion efficiency is remarkably poor in view of the high kinetic energy of each impacting particle.

General Discussion

A possible shortcoming of the target weight loss versus impingement angle relation is that it does not consider the variation in impingement area with impingement angle. For example, the target area impacted by particles within the cylinder of the carrier-gas jet is five times as large at 20-degree incidence angle as the area at 90-degree angle (Figure 44). When the erosion data are replotted in terms of weight or volume loss per unit impingement area versus impingement angle, the angle for maximum loss invariably shifts upward. This is at least partially due to the marked increase in target impingement area with decreasing impingement angle, especially below 45 degrees (see Figure 44 and compare Figures 45, 46, and 47). The steel targets reach maximum values for both dust varieties at 60 degree impingement angle, and establish a high plateau of erosion loss between 37.5 and 90 degrees. The titanium and aluminum alloys also establish high plateaus of erosion between 37.5 and 90 degrees with maximums at 60 or 90 degrees (Ti) as opposed to 45 or 60 degrees (Al). (When all of the data were surveyed together, the impingement angle of 37.5 degrees seemed to be a good standard angle to select for future testing, inasmuch as a high level of erosion is obtained at this angle regardless of the method of plotting the data.)

The erosion data plotted here as a function of unit area of target exposed should be of value principally to the design engineer, whereas the previous data plots that characterize erosion response simply as a function of unit weight of dust impacted (also relatable to number of particles impacted) may be of more value to the specialist in materials development. However, both types of plots are needed to describe the erosion behavior.

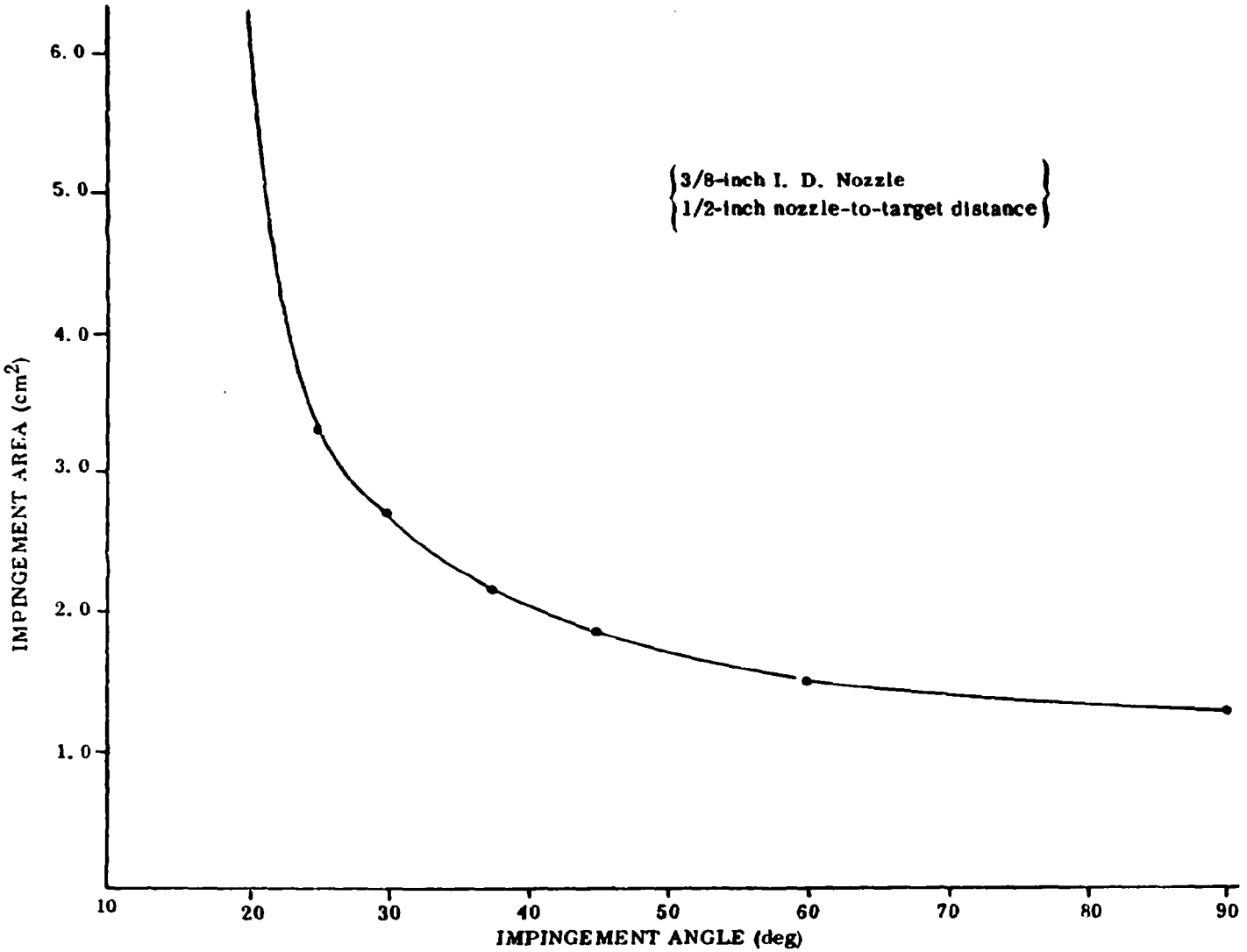

Figure 44. Variation of Target Impingement Area With Impingement Angle.

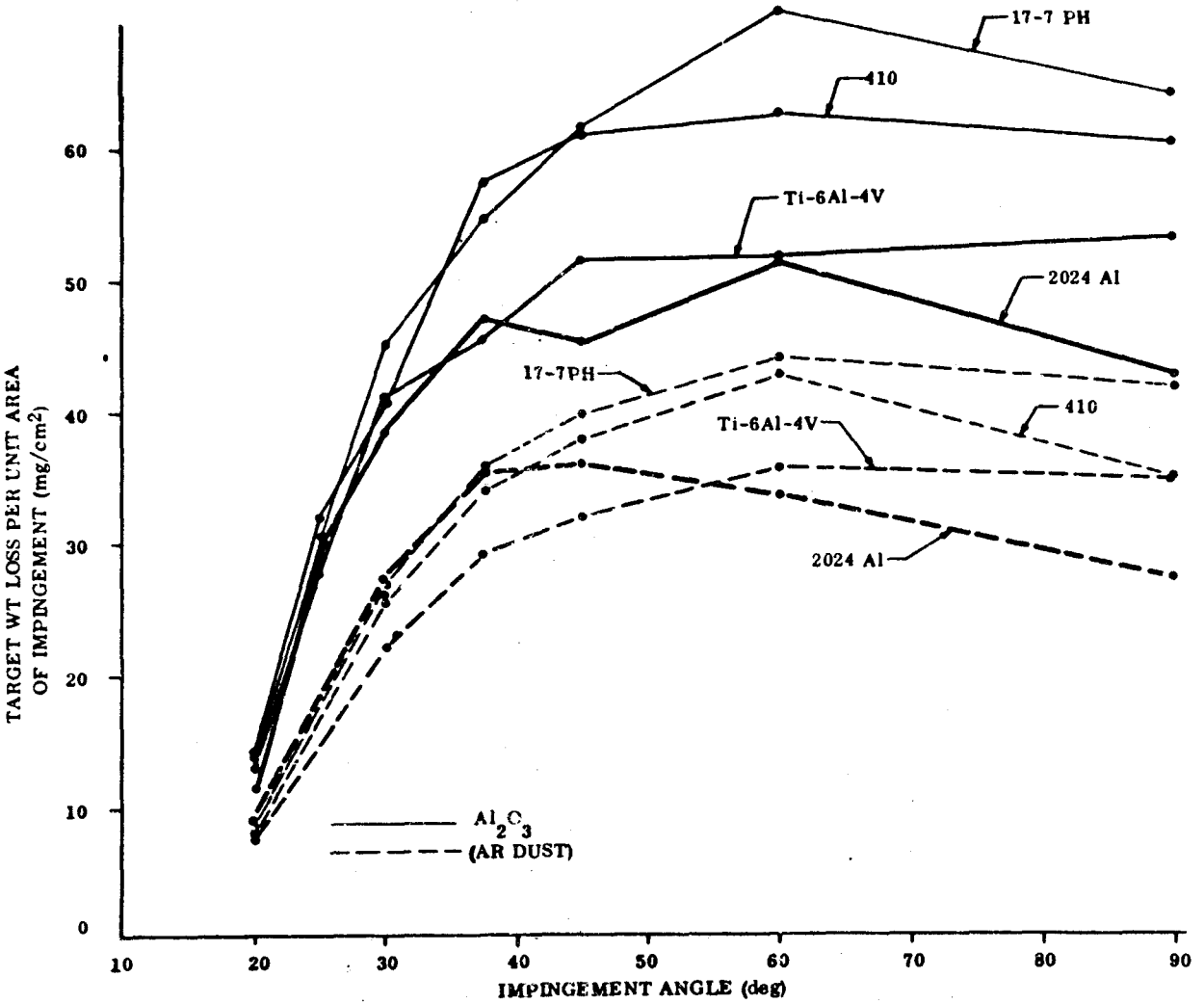

Figure 45. Target Weight Loss per Unit Area of Impingement Versus Impingement Angle (Test Series II).

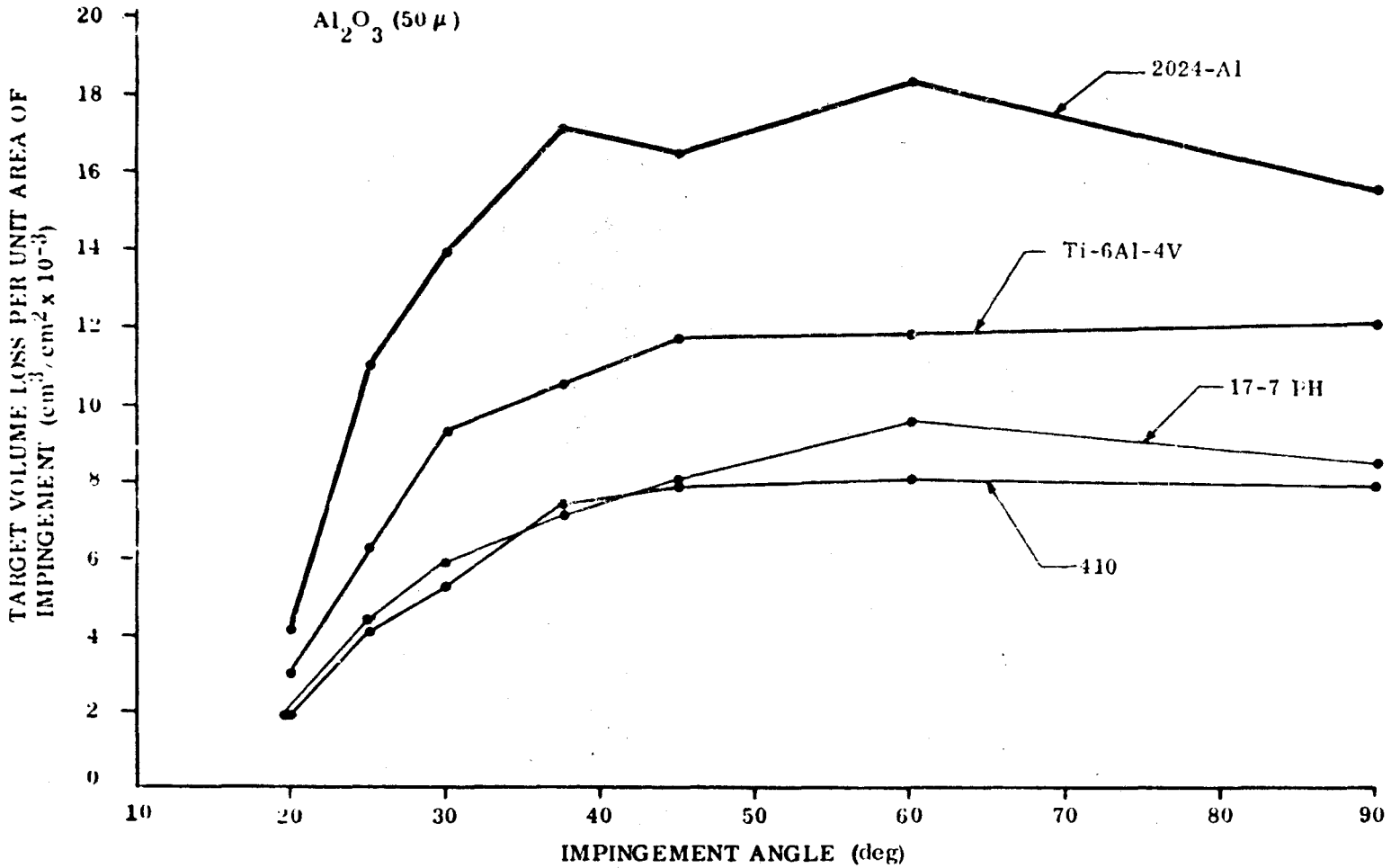

Figure 46. Target Volume Loss per Unit Area of Impingement Versus Impingement Angle (Test Series I).

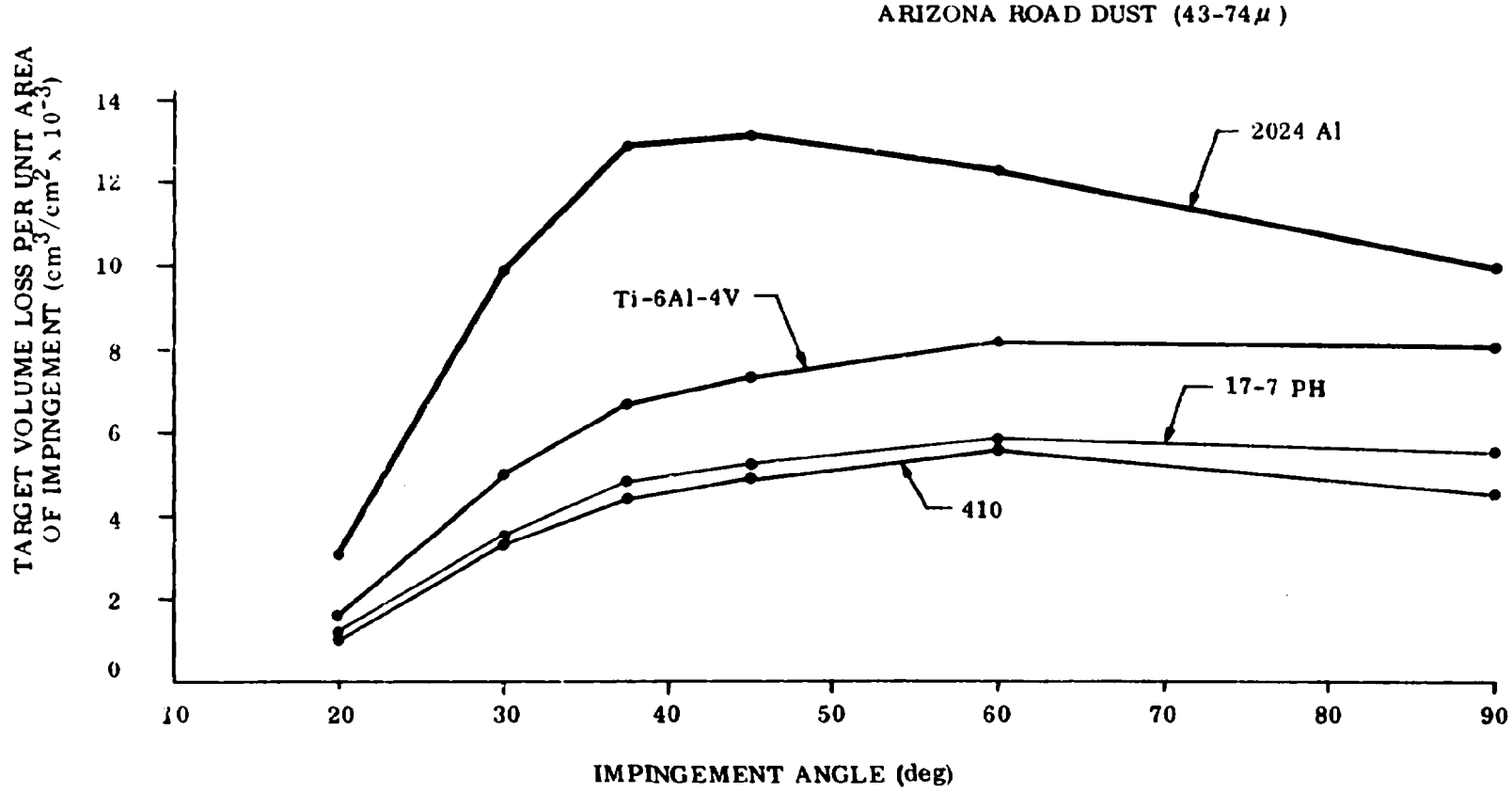

Figure 47. Target Volume Loss per Unit Area of Impingement Versus Impingement Angle (Test Series I).

EFFECTS OF VARYING CARRIER-GAS TRUE TEMPERATURE AND PARTICLE VELOCITY (SERIES II)

Test Series II was designed primarily to determine the effect of varying test temperature and particle velocity upon erosion factor (a bulk or engineering measure of erosion efficiency) and the erosion mechanism. Dust concentration was studied as a secondary variable. Tests were conducted at carrier-gas true temperatures of 80°F (RT), 400°F, and 700°F with computed particle velocities of 650 and 1100 fps. True gas temperature (or stagnation temperature) was taken as the maximum temperature recorded for each test condition by a miniature chromel-alumel (type K) thermocouple, attached to a dummy test target specimen of each target material in the center of the carrier-gas jet impingement area. The center of the target impingement area was maintained at a constant distance (1/2 inch) from the nozzle exit plane, as in ordinary test procedure. The carrier gases employed were compressed air at 700-715 fps[1] (RT, 400°F, and 700°F) and 1200 fps[2] (700°F), and a mixture of 35 percent (wt) He-65 percent (wt) air at 1260 fps[2] (RT). The dust used was specially classified Arizona Road Dust (43-74-micron), maintained at a constant (nozzle) concentration of 40 mg/ft^3 or 25 mg/ft^3. The weight of dust impacted per test was also held constant at 5.40 grams. The test dust was fed at uniform rates into a 10-foot-long nozzle of 1/4-inch I.D. using the Giannini precision powder feeder. It was found that this dust feeder typically fed the nominal charge of test dust with a weight reproducibility of ± 5 percent. Two impingement angles were employed (37.5 and 60 degree) to permit evaluation of the character of erosion response (i.e., "ductile" or "brittle"). Target materials tested were type 2024 aluminum alloy, Ti-6Al-4V titanium alloy, and the two stainless steels, type 410 and 17-7 PH, all in the annealed condition. Three erosion tests were conducted for each test condition.

Effects of Test Temperature

Average test results are plotted in Figures 48 and 51 in the form of weight erosion factor

$$\epsilon = \frac{\text{Target Weight Loss (mg)}}{\text{Weight Dust Impacted (gm)}}$$

---

(1) Carrier-gas velocity calculated to yield a particle velocity of 650 fps in a 10-foot nozzle.

(2) Carrier-gas velocity calculated to yield a particle velocity of 1100 fps in a 10-foot nozzle.

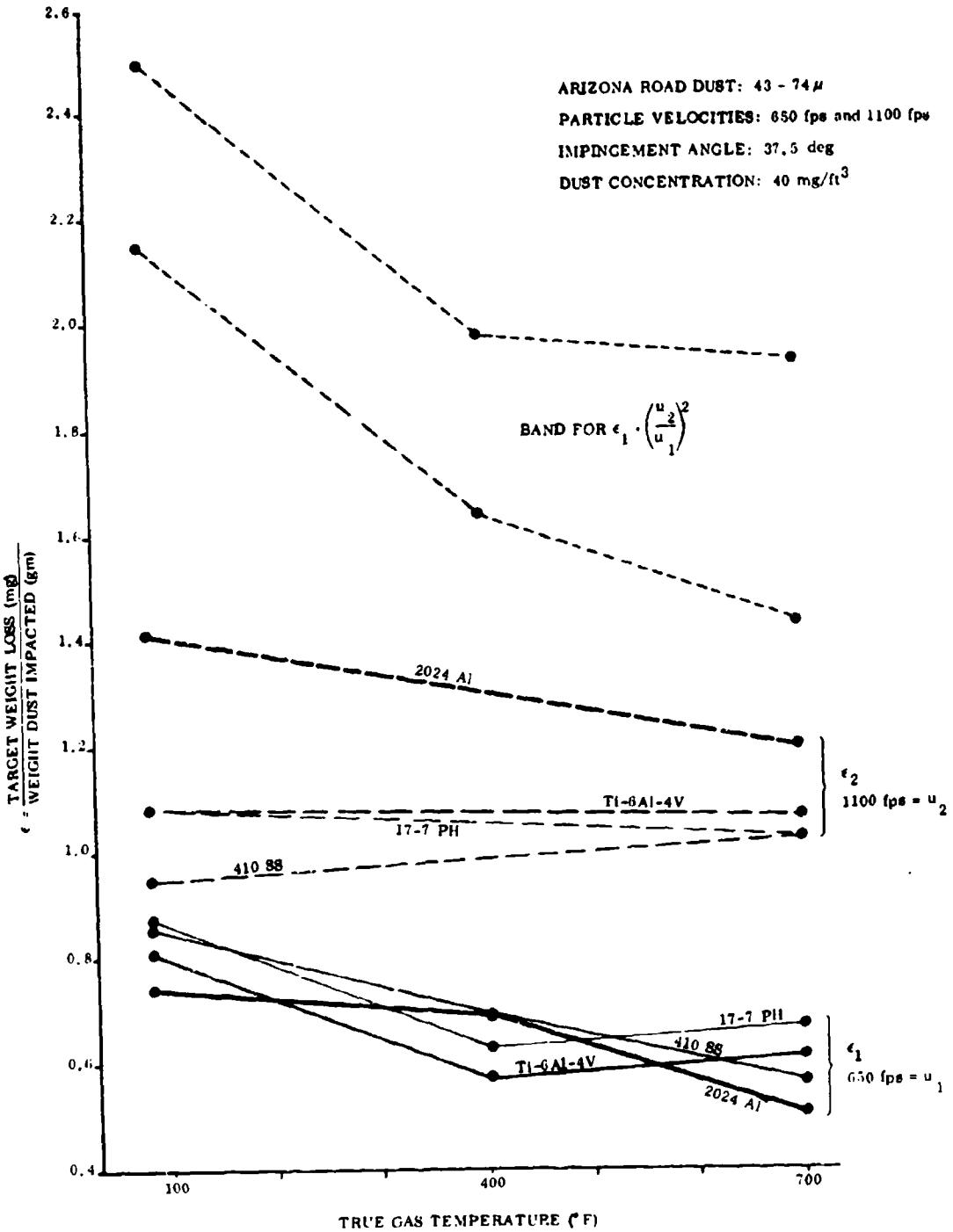

Figure 48. Weight Erosion Factor (ϵ) Versus Carrier-Gas True Temperature (Series II).

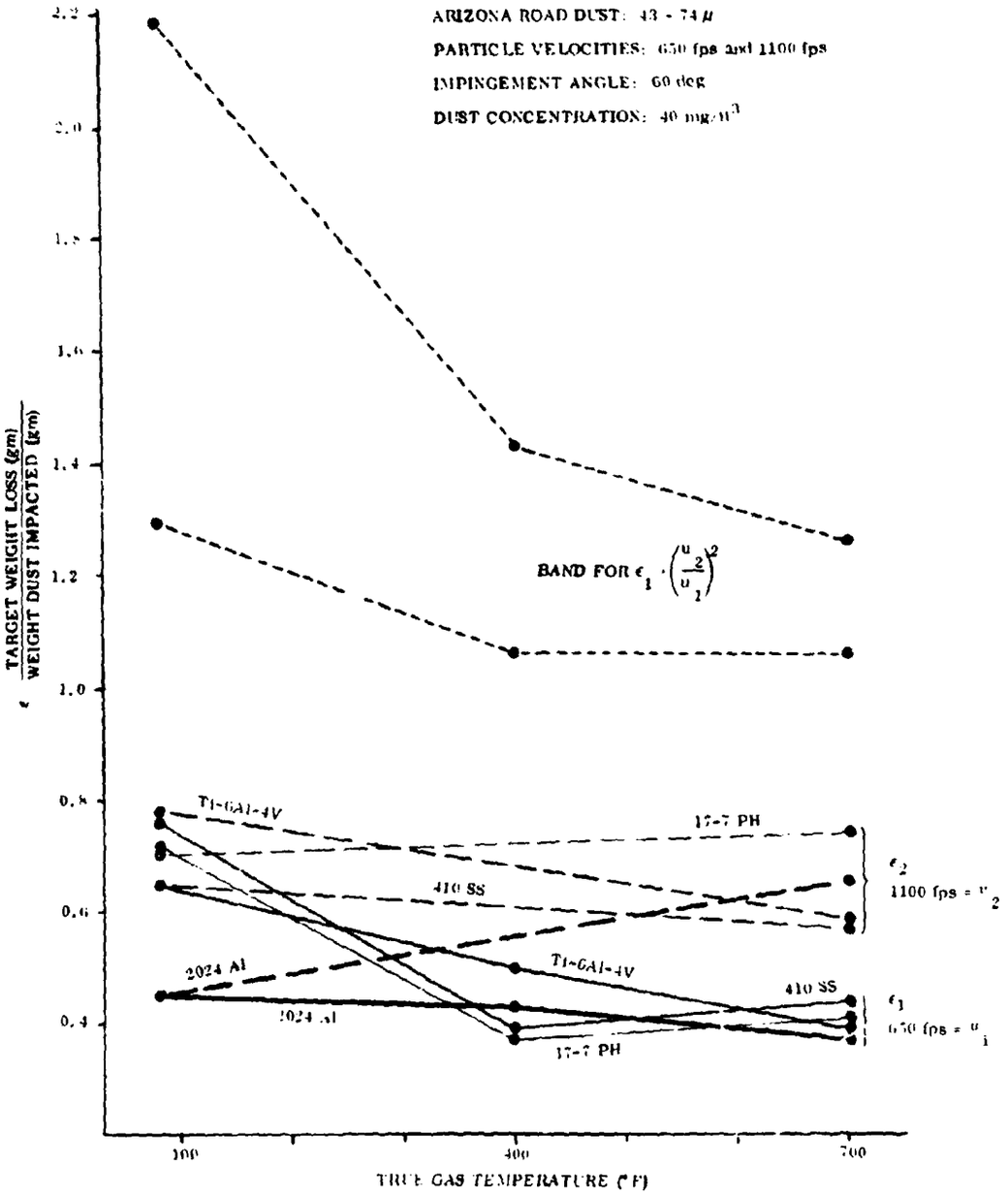

Figure 49. Weight Erosion Factor (ϵ) Versus Carrier-Gas True Temperature (Series II).

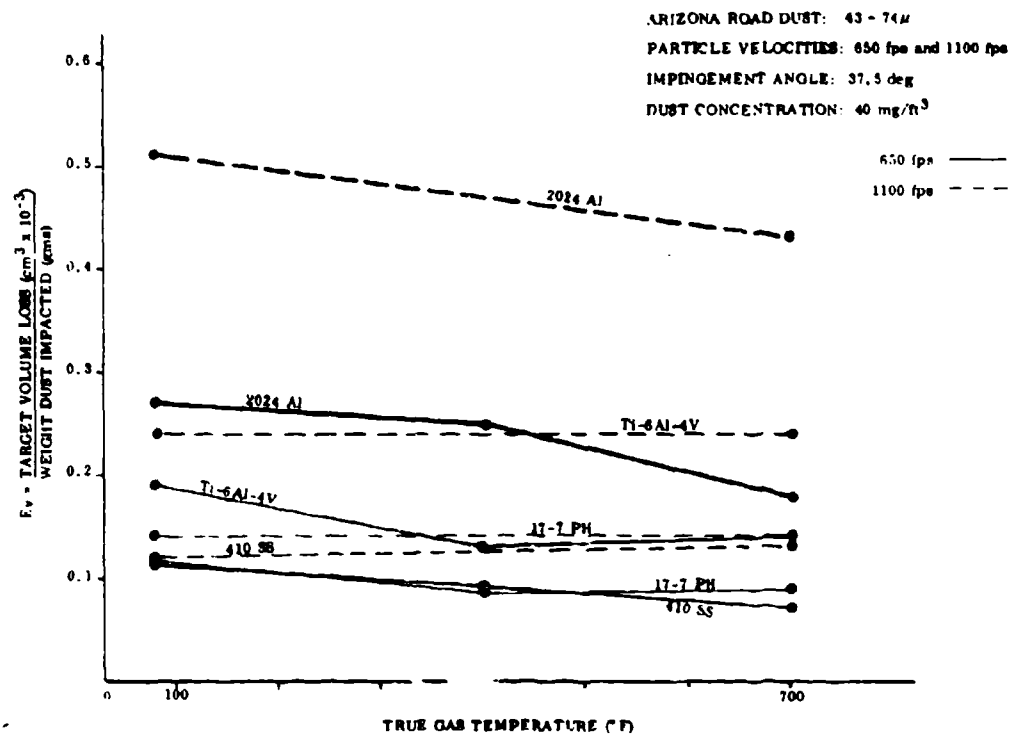

Figure 50. Volume Erosion Factor (ϵ_V) Versus Carrier-Gas True Temperature (Series II).

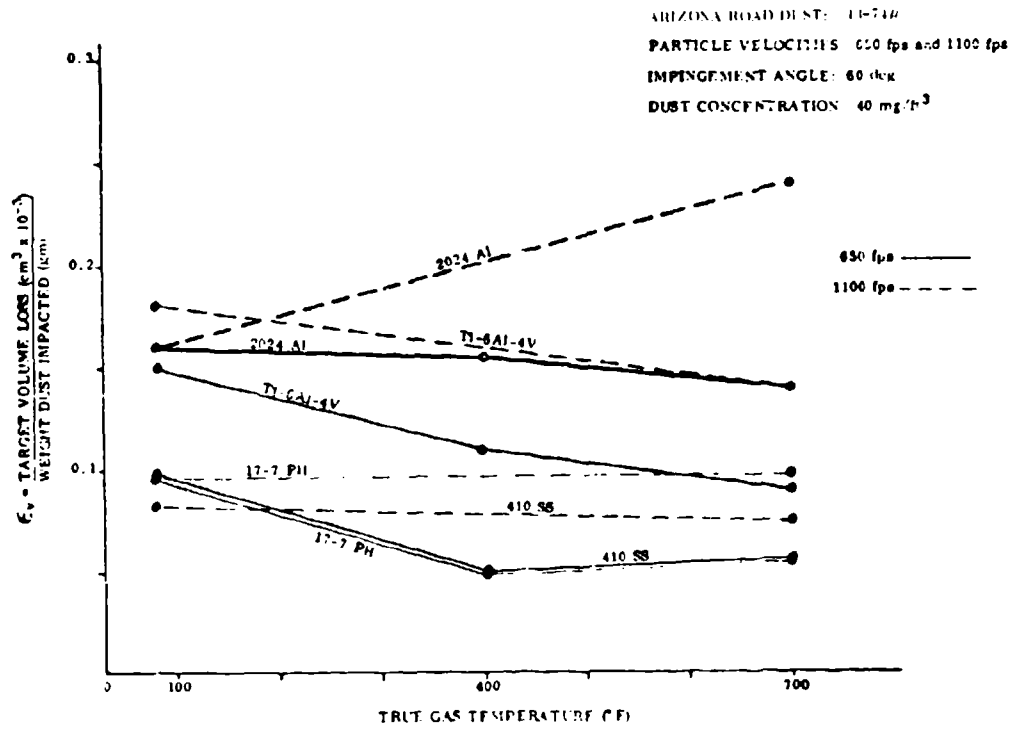

Figure 51. Volume Erosion Factor (ϵ_V) Versus Carrier-Gas True Temperature (Series II).

and volume erosion factor

$$\epsilon_V = \frac{\text{Target Volume Loss } (cm^3 \times 10^{-3})}{\text{Weight Dust Impacted (gm)}}$$

versus true gas temperature for each particle velocity and impingement angle. Test data given in Table VII include average target weight losses and volume losses, average target weight and volume losses per unit impingement area, and weight erosion factor (ϵ) and volume erosion factor (ϵ_V). In Table VII, additional data are presented showing the effect upon erosion of lowering the dust concentration from 40 mg/ft^3 to 25 mg/ft^3 at the higher particle velocity (1100 fps). Figures 52 through 55 are plots of weight erosion factor versus impingement angle for all the target materials at both test velocities and the terminal test temperatures of RT and 700° F.

A significant temperature effect upon erosion loss was observed for about 75 percent of the elevated temperature test conditions (see Table VII), assuming that an average erosion weight loss differing ≥10 percent from the corresponding room-temperature value indicates a significant change. This seems to be a reasonable assumption, inasmuch as individual test values (from triplicate tests) for each test condition normally varied only ± 3 percent to ± 8 percent from the average values reported in Table VII. Over the range of temperatures studied, the maximum changes in average erosion loss over the average room temperature loss run from about (+) 46 percent to (-) 49 percent (Table VIII). Therefore, an order of magnitude change in erosion due to temperature variation is definitely not indicated.

In 17 out of 18 situations showing a significant temperature effect (see Table VIII), the trend was toward reduced erosion losses with increasing temperature. In many cases, erosion was reduced from 20 to almost 50 percent of the RT levels. This trend was not expected, inasmuch as surface flow strengths and energies required to remove target material undoubtedly decrease with increasing surface temperature. It is of interest that dust-free "erosion" tests, conducted at 400° F and 700° F with heated carrier gas alone, resulted in no measurable weight gain due to oxidation for any target. Consequently, it was concluded that surface oxidation did not offset the actual target weight losses due to erosion; hence, the measured decreases in elevated-temperature erosion are real. However, more rapid (light) surface oxidation at elevated temperatures could influence the erosion mechanism; for example, by inhibiting wetting and/or smear-bonding of the semimolten target surface by impacting dust particles ("stop-off" effect), or by effectively raising the melting point and viscosity of the target surface (see "Study of Erosion Phenomena and Synthesis of Erosion Models", page 211 for probable surface reactions). Recent dust erosion testing in Britain (Ref. 23), within a vacuum chamber ($P \approx 1.0 \times 10^{-3}$ Torr), has yielded even higher erosion factors on stainless steels than those obtained in the

TABLE VII. COMPILATION OF SERIES II TEST DATA

Target Material	Impingement Angle (deg)	True Gas Temperature (°F)	Particle Velocity (fps)	Dust Concentration (mg/ft^3) (Nozzle)	Dust Concentration (mg/ft^3) STP	Average Target Weight Loss (mg)	Average Target Volume Loss ($cm^3 \times 10^{-3}$)	Weight Loss per Unit Impingement Area (mg/cm^2)	Volume Loss per Unit Impingement Area ($cm^3 \times 10^{-3}/cm^2$)	Weight Erosion Factor, ϵ (mg/gm)	Volume Erosion Factor, ϵ_v ($cm^3 \times 10^{-3}$/gm)
2024-Al (Annealed)	37.5	RT	650	40	6.5	4.0	1.45	7.9	2.9	0.74	0.27
	60	"	"	"	"	2.4	0.86	6.2	2.3	0.45	0.16
	37.5	400	"	"	14.0	3.7	1.34	7.3	2.6	0.69	0.25
	60	"	"	"	"	2.3	0.84	5.9	2.2	0.43	0.16
	37.5	700	"	"	20.0	2.7	0.98	5.3	1.9	0.50	0.18
	60	"	"	"	"	2.0	0.73	5.1	1.9	0.37	0.14
	37.5	RT	1100	"	5.0	7.6	2.76	14.9	5.4	1.41	0.51
	60	"	"	"	"	2.4	0.88	6.2	2.3	0.45	0.16
	37.5	700	"	"	13.0	6.4	2.32	12.6	4.6	1.19	0.43
	60	"	"	"	"	3.5	1.27	9.0	3.3	0.65	0.24
	37.5	700	"	25	8.1	10.0	3.63	19.6	7.1	1.85	0.67
	60	"	"	"	"	4.0	1.45	10.3	3.7	0.74	0.27
Ti-6Al-4V (Annealed)	37.5	RT	650	40	6.5	4.4	1.60	8.6	1.9	0.81	0.19
	60	"	"	"	"	3.5	0.79	9.0	2.0	0.65	0.15
	37.5	400	"	"	14.0	3.1	0.70	8.1	1.4	0.57	0.13
	60	"	"	"	"	2.7	0.61	6.9	1.6	0.50	0.11
	37.5	700	"	"	20.0	3.3	0.75	6.5	1.5	0.61	0.14
	60	"	"	"	"	2.1	0.48	5.4	1.2	0.39	0.09
	37.5	RT	1100	"	5.0	5.9	1.31	11.4	2.6	1.08	0.24
	60	"	"	"	"	4.2	0.95	10.8	2.4	0.78	0.18
	37.5	700	"	"	13.0	5.7	1.29	11.2	2.5	1.05	0.24
	60	"	"	"	"	3.2	0.73	8.2	1.8	0.59	0.14
	37.5	"	"	25	8.1	6.4	1.45	12.6	2.9	1.19	0.27
	60	"	"	"	"	4.5	1.02	11.5	2.6	0.83	0.19
410 SS (Annealed)	37.5	RT	650	40	6.5	4.6	0.78	9.0	1.2	0.85	0.110
	60	"	"	"	"	4.1	0.53	10.5	1.4	0.76	0.088
	37.5	400	"	"	14.0	3.7	0.48	7.3	0.94	0.69	0.089
	60	"	"	"	"	2.1	0.27	5.4	0.69	0.39	0.050
	37.5	700	"	"	20.0	3.0	0.39	5.9	0.77	0.56	0.072
	60	"	"	"	"	2.4	0.31	6.2	0.79	0.44	0.057
	37.5	RT	1100	"	5.0	5.1	0.66	10.0	1.3	0.95	0.120
	60	"	"	"	"	3.5	0.45	9.0	1.2	0.65	0.083
	37.5	700	"	"	13.0	5.5	0.71	10.4	1.4	1.02	0.130
	60	"	"	"	"	3.1	0.40	7.9	1.0	0.57	0.074
	37.5	"	"	25	8.1	6.3	0.84	12.8	1.7	1.21	0.160
	60	"	"	"	"	4.4	0.57	11.3	1.5	0.82	0.110
17-7 PH (Annealed)	37.5	RT	650	40	6.5	4.7	0.63	9.2	1.2	0.87	0.120
	60	"	"	"	"	3.9	0.52	10.0	1.3	0.72	0.096
	37.5	400	"	"	14.0	3.4	0.46	6.7	0.90	0.63	0.085
	60	"	"	"	"	2.0	0.27	5.1	0.68	0.37	0.050
	37.5	700	"	"	20.0	3.6	0.48	7.1	0.94	0.67	0.089
	60	"	"	"	"	2.2	0.30	5.6	0.77	0.41	0.056
	37.5	RT	1100	"	5.0	5.8	0.77	11.4	1.5	1.08	0.140
	60	"	"	"	"	3.8	0.51	9.7	1.3	0.70	0.095
	37.5	700	"	"	13.0	5.5	0.73	10.8	1.4	1.02	0.140
	60	"	"	"	"	4.0	0.53	10.3	1.4	0.74	0.098
	37.5	700	"	25	8.1	7.1	0.95	13.8	1.9	1.32	0.180
	60	"	"	"	"	4.4	0.59	11.3	1.5	0.82	0.110

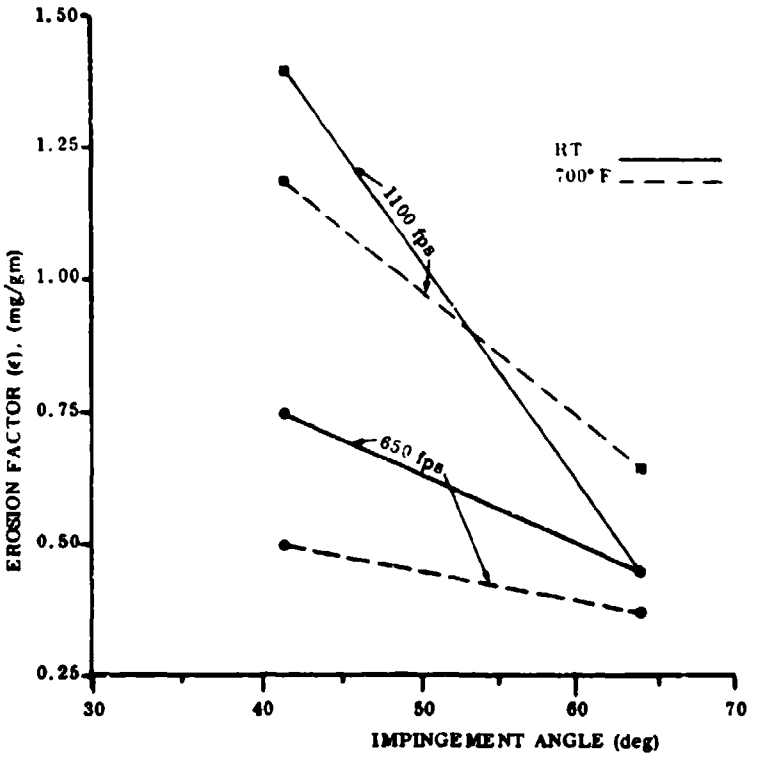

Figure 52. Erosion Factor Versus Impingement Angle at RT and 700° F - 2024 Al Target (Series II).

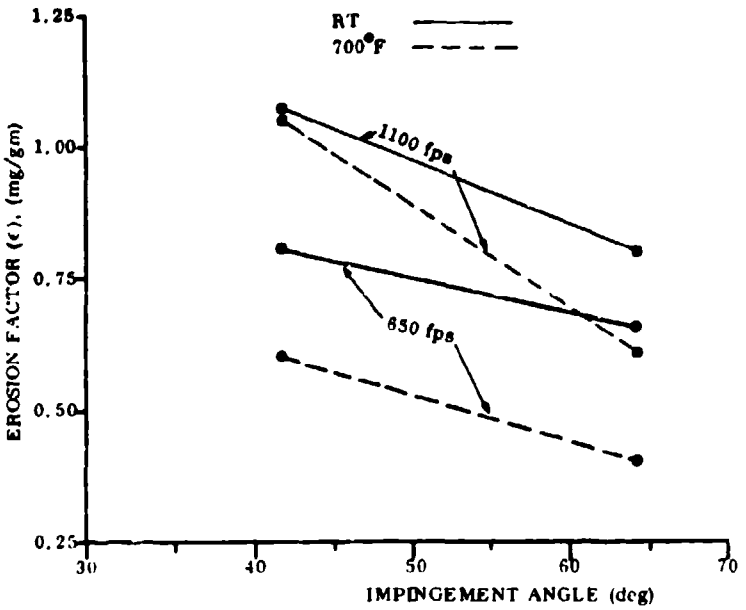

Figure 53. Erosion Factor Versus Impingement Angle at RT and 700° F - Ti-6Al-4V Target (Series II).

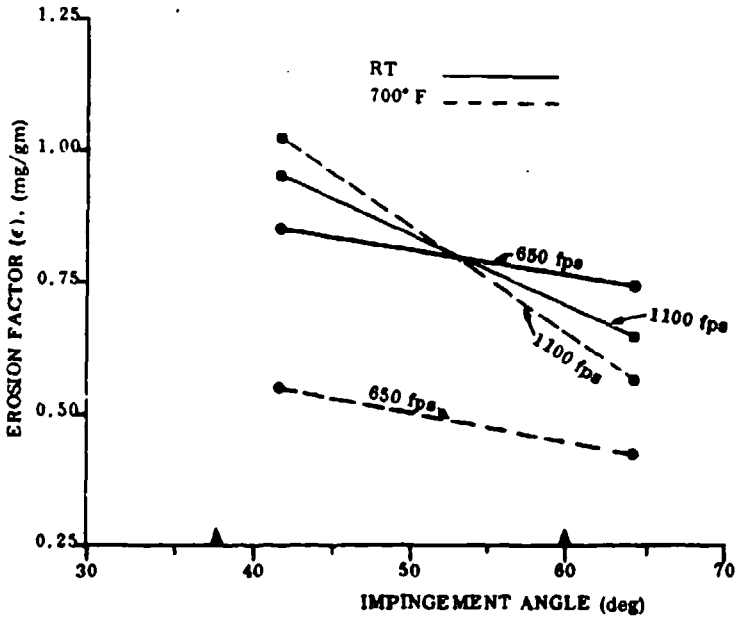

Figure 54. Erosion Factor Versus Impingement Angle at RT and 700° F - 410 SS Target (Series II).

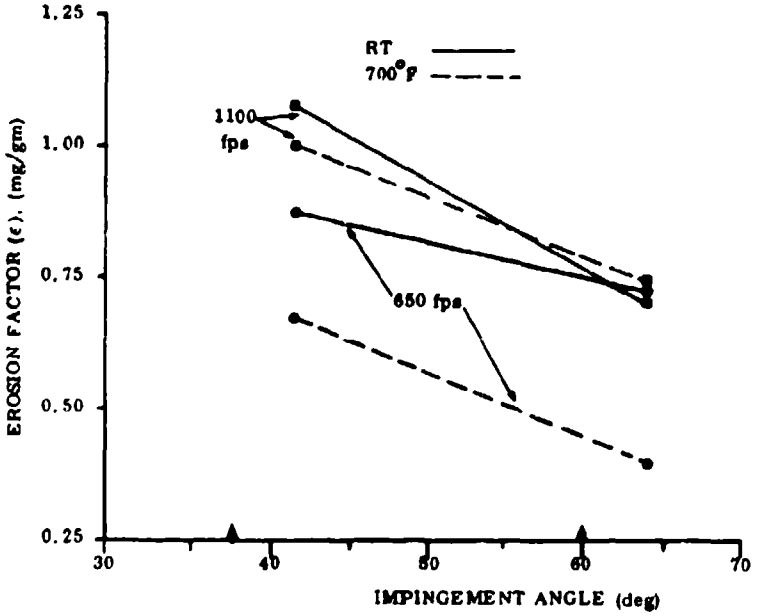

Figure 55. Erosion Factor Versus Impingement Angle at RT and 700° F - 17-7 PH Target (Series II).

TABLE VIII. DIFFERENCE IN AVERAGE TARGET WEIGHT LOSS (%); T Vs. RT

Target Species	T = 400° F				T = 700° F			
	37.5°		60°		37.5°		60°	
	650 fps	1100 fps	650 fps	1100 fps	650 fps	1100 fps	650 fps	1100 fps
2024-Al	(-) 7.5	--	(-) 4.2	--	(-)32.5	(-)15.8	(-)16.7	(+)45.8
Ti-6Al-4V	(-)29.5	--	(-)22.8	--	(-)25.0	(-) 1.7	(-)40.1	(-)23.8
410 SS	(-) 2.6	--	(-)48.8	--	(-)21.1	(+) 7.9	(-)41.5	(-)11.4
17-7 PH	(-) 5.6	--	(-)48.7	--	0.0	(-) 5.2	(-)43.6	(+) 5.3

subject program, which supports the concept that light surface oxidation probably slows down the erosion process, and is definitely not an essential requisite for erosion.

The temperature effect is more complex than it first appears. Although only 2 impingement angles (37.5 and 60 degrees) were tested, it is apparent that temperature markedly affects the shape of the erosion factor versus impingement angle curves. For every target and for the same particle velocity (650 or 1100 fps), the two erosion curves for RT and 700° F have different slopes, and show evidence of convergence and, in some cases, actual crossover at specific angles. Examples are shown in Figures 52 through 55. The angle of crossover varies with target material and velocity, but generally occurs at or above 37.5 degrees. The implication is that, for a given target alloy, elevated temperature erosion could be more severe than RT erosion at certain impingement angles, while just the opposite situation exists at other impingement angles. Dependent variables influencing the specific erosion behavior include not only the temperature and impingement angle, but also the specific target alloy and particle velocity. Obviously, the erosion mechanism must have many interacting and interdependent variables.

Specific temperature effects for each target alloy are discussed below.

The aluminum alloy target exhibited only very slight reductions in erosion at 400° F, but significant reductions (over RT values) in 3 of 4 test conditions at 700° F. Curiously, at the 60-degree impingement angle and the higher (1100 fps) particle velocity, the aluminum alloy experienced a 46-percent increase in erosion loss at 700° F, effectively reversing the trend. This is shown in Figure 52, where the crossover in erosion factor curves for RT and 700° F (1100 fps) occurs between 37.5 and 60

degrees impingement. The convergence of the RT and 700° F curves for 650 fps with increasing impingement angle suggests that they may cross over as well between 60 and 90 degrees impingement. The inference could be drawn that 700° F erosion becomes progressively less severe than RT erosion only below a certain critical impingement angle, the value of which decreases with increasing particle velocity (≈50 degrees at 1100 fps, and between 60 and 90 degrees at 650 fps). Conversely, one might infer that 700° F erosion becomes progressively worse than RT erosion above these critical angles for aluminum. Additional testing would have been required to check out these indications. However, the strong influence of impingement angle is already obvious.

The titanium alloy target showed significant reductions in erosion losses at both 400° F and 700° F (5 out of 6 test conditions). The absence of a temperature effect in the sixth case (700° F, 1100 fps, 37.5 degrees) appears to be related to the imminent crossover of the RT and 700° F erosion-factor curves near this point (see Figure 53). In striking contrast to the aluminum-alloy curves (Figure 52), the titanium-alloy curves appear to be converging in an opposite way that would make 700° F erosion more severe than RT erosion at angles below the critical or crossover points. This is because RT erosion factor curves are dropping at a faster rate than the corresponding 700° F curves in the case of the aluminum alloy; just the opposite is true for the titanium alloy. Clearly, the factors molding the shapes and slopes of the erosion versus impingement angle curves are many and complex; they include all of the variables tested in Series II (test temperature, particle velocity, and target material), and undoubtedly others.

At the lower particle velocity (650 fps), both steel target alloys evidenced lower erosion losses (in the range of 20-49 percent) at 400° F and 700° F than at RT (Table VIII). Figure 54 (410 SS) and Figure 55 (17-7 PH) indicate that the RT and 700° F erosion-factor curves are converging for both steels at 650 fps, and may cross over at impingement angles below 37.5 degrees, in the manner of the titanium alloy. The same figures show that at 1100 fps, the erosion-factor curves for RT and 700° F actually do cross over between 37.5 and 60 degrees; the 410 stainless steel in the manner of the titanium alloy (i.e., 700° F erosion is progressively more severe than RT erosion below the critical or crossover angle) and the 17-7 PH in the manner of the aluminum alloy (i.e., 700° F erosion is progressively less severe than RT erosion below the critical angle). However, it should be noted that the erosion differences recorded at 1100 fps are not very great (Table VIII). This is because the RT and 700° F curves at 1100 fps (410 SS and 17-7 PH) cross over with less differential in relative slopes than do the corresponding 1100 fps curves for the titanium and aluminum alloys (compare Figures 52, 53, 54, and 55).

Measured impingement areas obtained in 400° F and 700° F testing are exactly the same as those obtained in RT testing (Series II), so that the geometry of the carrier-gas jet (cone) is not altered by test temperature variation and is therefore not a

factor in the temperature effect upon erosion. However, because of the complexity of the situation described, it could not be determined just what target (or dust) material properties were actually involved in the test temperature effect upon erosion.

Effects of Particle Velocity

Equation (1) predicts that when a target material is bombarded with the same dust but at two different particle velocities, the ratio of the erosion losses should be proportional to the square of the particle velocity ratios; i.e.,

$$E_{V2}/E_{V1} = \left(\frac{u_2}{u_1}\right)^{x=2} \tag{7}$$

It is evident from Figures 48 and 49 and Table IX that the value of the velocity exponent, x (Series II data), is invariably less than 2.0, and ranges widely between (-) 0.30 and (+) 1.64. In all instances, the exponent, x, is higher at 700°F than at RT, indicating a consistently stronger velocity effect at the elevated temperature for all target alloys. All of the elevated temperature (700°F) tests were conducted with air as the carrier gas. It should be remembered that the high-velocity, room-temperature tests were conducted with helium-air; and if oxidation exerts positive influence on the erosion mechanism, the reduced reactivity of helium-air might have been a contributive factor to the lower velocity exponents at RT. The reduced reactivity of helium-air is not believed to be responsible for the erosion differences at 1100 fps, however, because low-velocity (650 fps) erosion tests conducted with helium-air (aluminum alloy target; RT) yielded erosion losses identical to those of similar tests conducted with pure air as the carrier gas. This supplies additional evidence that target oxidation is not a major factor influencing erosion. It also substantiates the validity of the high-velocity data (RT).

With one exception, the velocity exponent is appreciably greater at the 37.5-degree impingement angle than at the 60-degree angle, indicating that incidence angle as well as temperature may affect the importance of the velocity parameter. This angle relation can be seen in Figures 52 through 55. The shapes of the erosion factor versus impingement angle curves are influenced by the particle velocity in much the same manner as by the test temperature variation (Table X). Most of the slopes of the different velocity curves, between 37.5 and 60 degrees, range randomly between 1.1 and 1.8, confirming ductile response in all cases. (Note that the slopes for Series I and Series II data agree well (Table X). These velocity curves therefore show the same tendency for convergence and crossover toward the higher impingement angles that the temperature curves have shown. At this point,

TABLE IX. EXPONENT (x) OF VELOCITY RATIO;

$$\frac{E_{V2}}{E_{V1}} = \left(\frac{u_2}{u_1}\right)^x$$

Target Material	Room Temperature		700°F	
	37.5°	60°	37.5°	60°
2024-Al	1.22	0.0	1.64	1.07
Ti-6Al-4V	0.53	0.35	1.04	0.83
410 SS	0.56	(-) 0.30	1.15	0.43
17-7 PH	0.91	(-) 0.05	0.81	1.14

it appeared that the actual velocity exponents can range widely, and be either positive or negative depending upon the impingement angle in question.

The above comments regarding velocity effect apply only to the limited data available from Series II testing. It was recognized that the normal data scatter associated with the use of a heterogeneous natural test dust might require more than triplicate testing per condition to evaluate accurately the exponential relationship of equation (7). A better estimate of the true average levels of erosion required to test this equation could be derived from testing ≈20-30 specimens per condition. A better way to estimate the velocity exponent would be to test over a much wider range of particle velocities, particle masses and energies, thereby averaging out the true value of the exponent (if constant) over a large number of well-dispersed data points. This approach was used in Test Series III, which had the primary objective of assessing the effect of particle velocity. A near-constant exponent for particle velocity was derived from Series III work. The Series II data for the velocity variable represented too restricted a particle energy spectrum. That is, the two particle energies compared were too close to obtain an accurate estimate of the slope (velocity exponent) for the various E_V versus (log) u relations.

Effects of Dust Concentration

Erosion tests were conducted previously at Solar that demonstrated the existence of a dust concentration effect upon erosion factor at room temperature. It was found that RT erosion factors were increased systematically (≈26-30%) by reducing nozzle dust concentration through the range 160.0 - 53.3 mg/ft^3. In order to gage the

TABLE X. VARIATION IN THE RATIO

$$\frac{\epsilon_{37.5°}}{\epsilon_{60°}}$$

FOR SERIES I AND II TEST DATA

Target Material	Temperature (°F)	Particle Velocity (fps)	$\frac{\epsilon_{37.5°}}{\epsilon_{60°}}$	
			Series II Data	Series I Data
2024-Al	RT	650	1.6	1.5
	"	1100	3.1	---
	400	650	1.6	---
	700	650	1.4	---
	"	1100	1.8	---
Ti-6Al-4V	RT	650	1.2	1.2
	"	1100	1.4	---
	400	650	1.1	---
	700	650	1.6	---
	"	1100	1.8	---
410 SS	RT	650	1.1	1.2
	"	1100	1.5	---
	400	650	1.8	---
	700	650	1.3	---
	700	1100	1.8	---
17-7 PH	RT	650	1.2	1.2
	"	1100	1.5	---
	400	650	1.7	---
	700	650	1.6	---
	"	1100	1.4	---

nce of dust concentration upon erosion factor at an elevated temperature, 700° F
on tests were conducted upon each target alloy at 1100 fps and impingement
s of 37.5 and 60 degrees. The tests were similar to previous Series II tests,
ith a nozzle dust concentration of only 25.0 mg/ft^3, rather than the standard
mg/ft^3 (see Table VII). Test duration was increased correspondingly to permit
alent quantities of dust (5.40 gm) to impact all the targets. The test data in
: VII show that significant (≥10%) increases in erosion factor due to reduced
ntration were the rule for every test condition at 700° F. The increases, rang-
om 11 to 55 percent, are tabulated in Table XI.

pparent potency of the dust concentration effect at all temperatures underscores
nportance of controlling a constant nozzle dust concentration throughout each
eriod as well as from test to test to obtain strictly comparable erosion data.
nderlying reason for the dust concentration effect has remained a mystery,
gh it is discussed in detail in Test Series IV. Unfortunately, it is virtually
ssible to control a meaningful dust concentration in the 10,000 particle surveys,
study of the surface phenomena associated with the concentration effect by
ron microscopy was not feasible.

t of Nozzle Geometry Upon Erosion Factor

s I testing was carried out with a 3/8-inch I. D. nozzle of 2-foot length. Series
ting was conducted with a smaller diameter nozzle (1/4-inch I. D.) of greater
h (10 feet). (The changes in nozzle geometry were made to attain carrier-gas
ities higher than 700-800 fps and dust particle velocities higher than 650 fps,
red in Series II through VI.) Comparisons of Series I and Series II erosion
(Arizona Road Dust, 650 fps, Tables VI and VII) reveal that erosion factors
significantly higher for the shorter, wider nozzle of Series I (i.e., about 3.5-
imes higher for the aluminum target, 2.5-2.7 times higher for the titanium
t, 3.0 times higher for the 17-7 PH target, and 2.8-2.9 times higher for the
S target). The differences in erosion factor are too great to attribute to a
concentration effect alone (Series I, 80 mg/ft^3 versus Series II, 40 mg/ft^3).
efore, the nozzle geometry itself must play a major role in determining the
iency of the erosion process. One possible reason for this change in efficiency
lieved to be related to the velocity profile of the jet; the smaller diameter,
r nozzle of Series II caused a somewhat sharper velocity profile than that of
s I (see Figure 56). The sharper profile means that a larger fraction of the
ined dust particles are concentrated or segregated nearer the jet center line
ak velocity, while there is a more uniform dust concentration within the jet
the shorter nozzles. Curiously, the jet from the smaller diameter (1/4-inch
) nozzle remained remarkably well collimated, in spite of the sharper velocity
le, as judged by the erosion patterns on target specimens at all impingement
s. In contrast, the jet from the shorter and wider (3/8-inch I. D.) nozzle

TABLE XI. SURVEY OF DUST CONCENTRATION EFFECT UPON EROSION FACTOR (SERIES II)

Target Alloy	Impingement Angle (deg)	Dust Concentration (mg/ft^3)	Erosion Factor (ϵ) (mg/gm)	Percentage Increase
2024 Al	37.5	40	1.19	55
	"	25	1.85	
	60.0	40	0.65	14
	"	25	0.74	
Ti-6Al-4V	37.5	40	1.06	12
	"	25	1.19	
	60.0	40	0.59	41
	"	25	0.83	
410 SS	37.5	40	1.02	19
	"	25	1.21	
	60.0	40	0.57	44
	"	25	0.82	
17-7 PH	37.5	40	1.02	29
	"	25	1.32	
	60.0	40	0.74	11
	"	25	0.82	

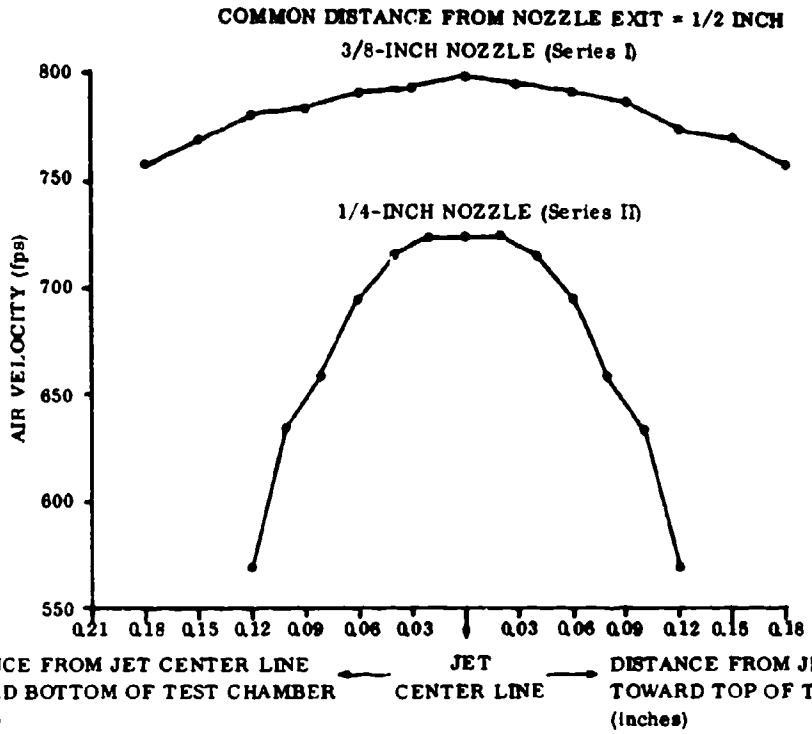

Figure 56. Carrier-Gas Velocity Profiles of the Air Jets Used in Series I and Series II Tests.

showed notable divergence, with a measured half-angle of 6-1/2 degrees. Variation of effective impingement angle with the degree of divergence seems the most likely cause of variable erosion efficiency. However, these aspects were deemed too complex for the current program to cover. Inasmuch as the same (Series II) nozzle was used in all subsequent test series, no other problems in data comparison were encountered.

Collection and Examination of Erosion Products and Spent Test Dusts

Attempts were made to collect spent test dusts and erosion products with a woven fiberglass filter cloth (1.0-micron opening), representing every test condition in Series II. With the exception of the extremely fine, metallic-gray powders (0.1-1.0-micron diameter) adhering to the target surfaces and chamber environs following every test, there was no visible evidence of eroded target metal of any size collected on the filter cloth. The fine metallic-gray powders, however, were observed for all test conditions but were particularly prevalent following tests with helium-air. It is speculated that these metal-gray powders are solidified droplets of the target metal surface, splattered in a molten or semimolten state by dust

particles colliding with the target (corner impacts) and producing sufficiently high local temperatures to cause a metal spray to develop (see "Study of Erosion Phenomena and Synthesis of Erosion Models" page 211). More of the metal-gray powders are evident in the helium-air environment than in air, probably because fewer of them totally oxidize while still hot, in the less reactive helium-air mix. The metal-gray powders collected from each target material (helium-air environment) were analyzed by electron diffraction technique and examined by transmission electron microscopy.

Arizona Road Dust particles (43-74-micron) all were examined before and after erosion testing for every test condition of Series II. The dust after testing at 650 fps appeared the same visually (30X) as the untested dust, in terms of mineral types, particle morphology, size distribution, and acuteness of corners. There was no apparent evidence of corner or edge rounding or of significant fragmentation of dust particles to smaller sizes at 650 fps. When placed on a black paper background, the spent dust showed a small quantity of fine silica flakes (<<50-micron), which may represent edge and corner materials chipped off during impact. However, similar flakes were noted in untested dust, so the origin of the fines is not clear. The untested dust (43-74-micron) contains 3.50 percent by weight fines or sizes less than 43 microns.

The dust after testing at 1100 fps (RT and 700°F) showed considerable visual evidence of fragmentation. Very few particles of maximum size (74-micron) remained, and the average or typical particle size shifted from about 50-60-micron down to about 25-35-micron, by visual estimate. This phenomenon of dust fragmentation was noted also by G. P. Tilley and W. Sage in England (Ref. 24). In the English work, fragmentation of silica test dust was observed down to ≈420 fps particle velocity; so that apparently the type and origin of test dust selected and its intrinsic structural defects have a bearing on the threshold velocity for appreciable fragmentation to occur.

EFFECTS OF VARYING PARTICLE ENERGY, VELOCITY, AND SIZE (SERIES III)

The primary objective of Test Series III was to establish the effects upon erosion factor (efficiency) and erosion mechanism of the dust kinetic energy level ($\propto Mu^2$). The influence of particle energy was determined at the terminal service temperatures (RT and 700°F), and for different sizes (masses) and species of test dusts. The principal experimental variable then was particle kinetic energy, with secondary variables of test temperature, particle mass and size, particle velocity, and dust variety.

Dust Particle Size	Dust Variety	Particle Velocity
0-43μ	Laterite (Pleiku,	$\approx$500 fps to $\approx$900 fps
43-74μ	Vietnam) and	(3 levels)
74-147μ	Arizona Road Dust	
147-208μ		

rticle energy parameter employed was $V_p u^2$, the product of the median-size e volume (V_p) times the square of the velocity of the median-size particle, u. tiplying this energy parameter by the dust density, all varieties of dust can pared on an equivalent energy scale.

ite room-temperature tests were carried out for each condition, employing a Road Dust or laterite in the four different particle size fractions. The of the test dust was held constant at 5.40 grams per test.

iginal intent was to test all dust fractions at three different particle velocities carrier gas; namely, 488, 670, and 925 fps. The two lower velocities were d with little difficulty. However, it was determined experimentally that the rrier-gas velocities (1000-1060 fps) required to accelerate all but the finest action to 925 fps were not attainable in the 10-foot by 1/4-inch diameter ation nozzle because of choking effects. A compromise solution adopted test all fractions at the highest carrier-gas velocity attainable (950 fps); ble XII.

her improve the understanding of the erosion mechanism, the erosion data in III were tabulated in terms of both standard erosion factors (ϵ and ϵ_V) as well single particle parameters, namely, (E) the average erosion weight loss per particle impact and (E_V) the average erosion volume loss per single particle .

ϵ (Weight Erosion Factor) = erosion weight loss (mg) per gram of dust impacted

ϵ_V (Volume Erosion Factor) = erosion volume loss ($cm^3 \times 10^{-3}$) per gram of dust impacted

E (Single Particle Parameter; Weight) = average target weight loss per single particle impact ($mg \times 10^{-8}$)

E_V (Single Particle Parameter; Volume) = average target volume loss per single particle impact ($cm^3 \times 10^{-11}$)

TABLE XII. SERIES III TEST FORMAT (PART I) ARIZONA ROAD DUST SUB-SERIES (α = 37.5 and 60 deg; N = 5.40 gm)

Temperature (° F)	Particle Size (μ)	Range, Estimated Particle Velocity (fps)	Particle Velocity, Median Particle Size (fps)	Carrier-Gas (Air) Velocity (fps)
RT	0-43	475/500	488	500
		650/685	670	685
		900/950	925	950
	43-74	475/500	488	525
		650/690	670	725
		860/900	880	950
	74-147	475/500	488	570
		650/690	670	760
		795/865	830	950
	147-208	475/500	488	605
		650/695	670	835
		715/795	755	950

Erosion factor (ϵ) is a gross or bulk engineering measure of the erosion efficiency assignat to a gram of test dust. Inasmuch as it does not directly take into account the number of particles involved in erosion, or their individual size and mass, it is not a very sensitive index to the erosion mechanism. Figure 57 shows that the number of cubic quartz particles in a gram of quartz dust ranges through 4 orders of magnitude, while the mean particle size (range of 10 to 160 microns) varies through just 1-1/2 orders of magnitude. Similarly, the volume (mass) and surface area of a single quartz particle progress through 3 to 4 orders of magnitude over the same range of particle size (Figure 58).

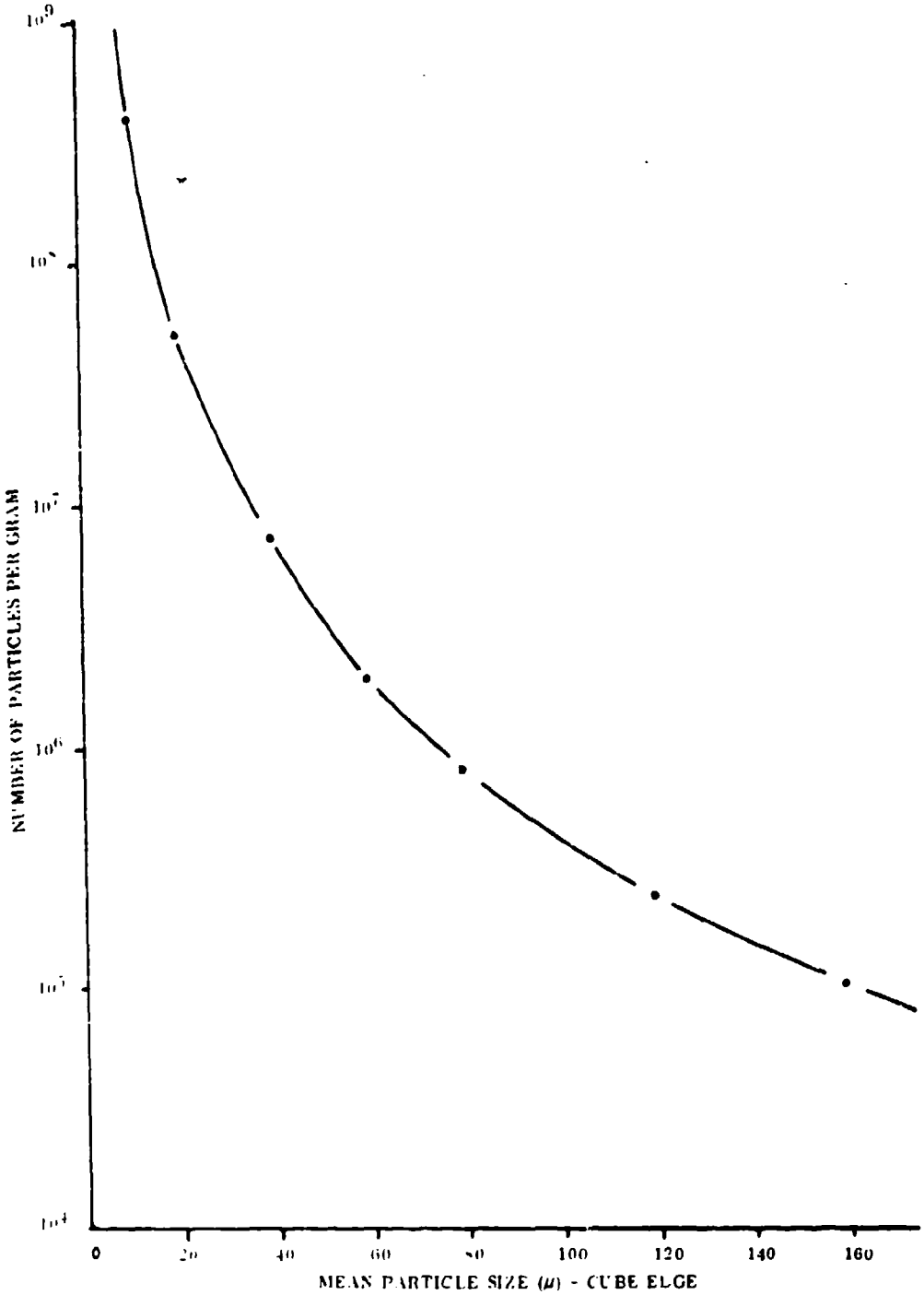

Figure 57. Number of Particles per Gram of Quartz Versus Particle Size (Cubic Particles of Quartz).

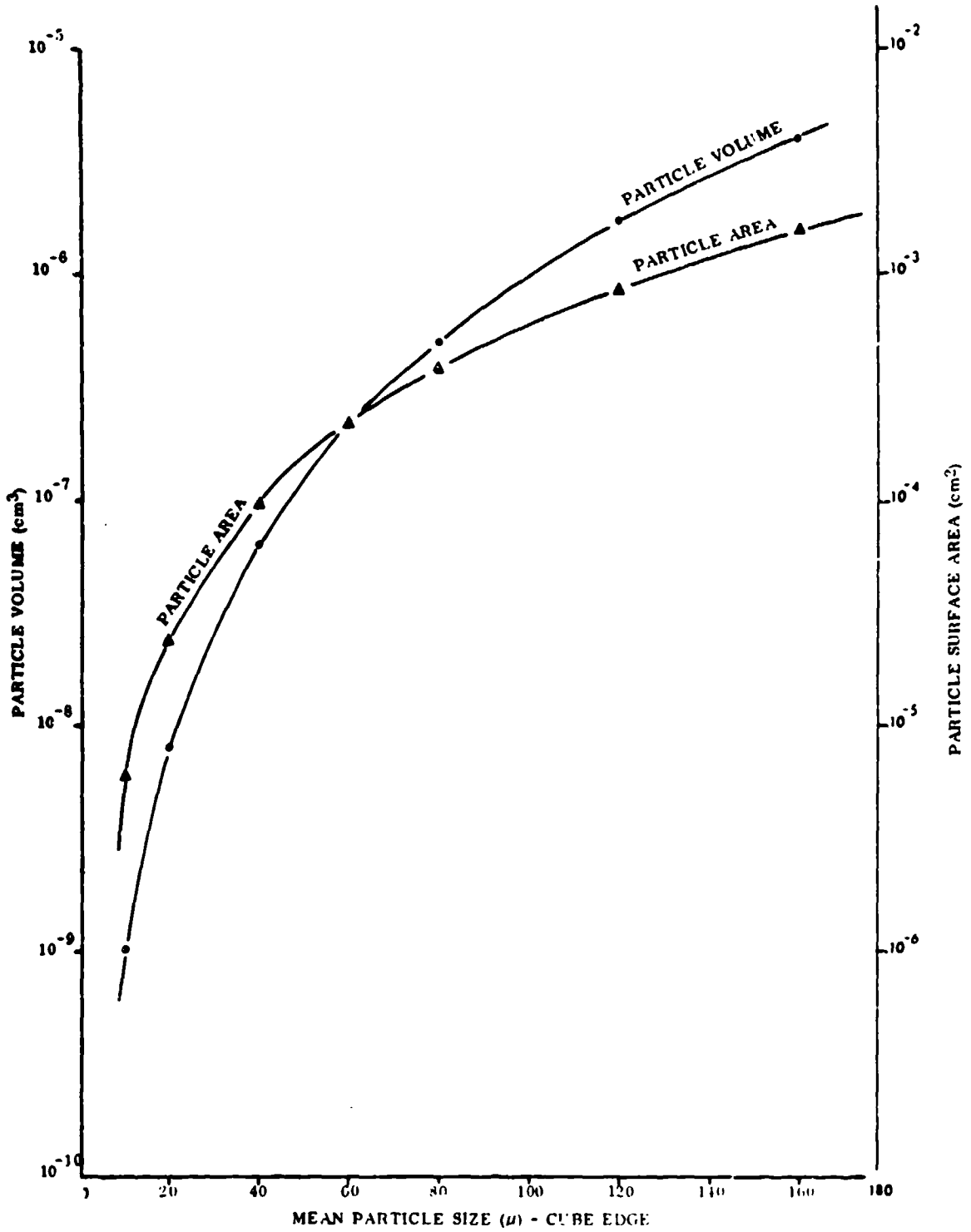

Figure 58. Particle Volume and Particle Surface Area Versus Particle Size (Cubic Particles of Quartz).

The discrete event (integral unit) causing erosion and constituting the mechanism is the collision of a single particle with the target, repeated over and over again millions or billions of times. Therefore, the average erosion loss per individual particle, when plotted against particle mass, particle energy or velocity, etc., should yield a better understanding of what each individual particle is doing mechanistically to the target surface under varying test conditions.

Erosion test results have been tabulated for all four target materials (2024 aluminum alloy, Table XIII; Ti-6Al-4V alloy, Table XIV; 410 stainless steel, Table XV; and 17-7 PH stainless steel, Table XVI). The first plots were made of volume erosion factor (ϵ_V) versus median-particle volume (V_p), typified by Figure 59 for the titanium alloy target. These curves show very little systematic variation in erosion factor, even though single particle volume varies through 3 orders of magnitude. A much more sensitive parameter was found to be E_V, the average target volume loss per single particle impact. Log-log plots of E_V versus V_p yielded essentially straightline relationships for almost every target material and particle velocity combination tested (see Figures 60 through 67). The slopes of the curves for all velocities proved to be 1.0 ± 0.1, suggesting a general equation of the type

$$E_V = K_u V_p^{(1.0 \pm 0.1)} \tag{8}$$

where K_u = system constant including velocity = $K\rho u^m$

This proportional erosion volume (mass) to particle volume (mass) relationship is reasonable, inasmuch as the integral unit of the erosion mechanism is the impact of a single particle with the target, which (on the basis of statistical averaging) generates a predictable volume of erosion product, E_V. A more basic equation that considers the kinetic energy of the particle (for mechanism activation) is

$$E_V = MKu^m = K\rho V_p^n u^m = K_M u^{2.0} \tag{9}$$

where n is assumed to be 1.0 and m is 2.0; and where

K = basic system constant

K_M = system constant including particle mass ($K_M = K\rho V_p = KM$)

M = median particle mass ($M = \rho V_p$)

ρ = dust particle density

TABLE XIII. COMPILATION OF SERIES III TEST DATA (PART I; 2024 Al Target)

Target Material	Particle Dia. (in.)	Carrier Gas Velocity (ft/s)	Median Particle Velocity (ft/s)	Range of Particle Velocity (ft/s)	Impingement Angle (deg)	Test Data Target Weight Loss (mg)	Average Target Weight Loss (mg)	Average Target Volume Loss ($cm^3 \times 10^{-4}$)	Weight Erosion Factor (mg/gm)	Volume Erosion Factor ($cm^3/gm \times 10^{-2}$)	(E) Average Target Weight Loss per Single Particle Impact* ($mg \times 10^{-3}$)	(Ey) Average Target Volume Loss per Single Particle Impact* ($cm^3 \times 10^{-7}$)	Ratio $\left(\frac{E}{E_0}\right)$	Expression for Velocity Ratio $\left(\frac{v}{v_0}\right)^n$	Expression for Velocity Ratio $\left(\frac{v}{v_0}\right)^n$
2024-T3 Al (Anodized)	0.125	400 (RT)	v_0	175/500	15	1.6	1.7	0.62	0.32	0.12	0.86	0.32	(1.0)	-	-
					30	1.1	1.1	0.40	0.20	0.074	0.56	0.20		-	
	0.125	600 (RT)	v_0	0/0/0	15	1.6	1.5	1.1	0.67	0.23	1.8	0.66	(1.5)	2.25	-
					30	2.6	2.5	0.92	0.46	0.17	1.3	0.46		2.63	
	0.1	700 (RT)	v_0	700/0	15	3.1	3.2	1.5	0.74	0.29	2.3	0.76	(2.1)	3.13	0.13
					30	2.0	2.0	0.71	0.37	0.14	1.0	0.37		0.94	0.0044
	0.1	1000 (Low T)	1000	-	15	7.8	7.9	2.9	1.5	0.58	4.0	1.4			

* Assuming the particle mass is equally distributed among the solid particle impacts (i.e., all of the 0.125-in. particles impact the target with the same energy).

Common Test Conditions

Arizona Road Dust; N = 5.40 gm
Dust Concentration: 40.0 mg/ft^3 (Nozzle)
Carrier Gas: Compressed Air

Carrier-Gas True Temperature: RT or 700°F
Nozzle Dimensions: 1/4-inch I.D. x 10-ft length

TABLE XIII – Continued

Target Material	Particle Size (μm)	Carrier Gas Velocity (fps)	Medium Particle Velocity (fps)	Range – Estimated Particle Velocity (fps)	Impingement Angle (deg)	Test Data Target Weight Loss (mg)	Average Target Weight Loss (mg)	Average Target Volume Loss ($cm^3 \times 10^{-3}$)	Weight Erosion Factor (mg/gm)	Volume Erosion Factor E_v ($cm^3 \times 10^{-3}$/gm)	(E) Average Target Weight Loss Per Single Particle Impact* (mg $\times 10^{-3}$)	(E_v) Average Target Volume Loss Per Single Particle Impact* ($cm^3 \times 10^{-3}$)	Ratio $\frac{E_{v_2}}{E_{v_1}}$	Exponent (n) of Velocity Ratio $\left(\frac{u_2}{u_1}\right)^n$	Exponent (n) of Velocity Ratio $\left(\frac{u_2}{u_1}\right)^n$
2024-T3 Al (Unabraded	11-74	725 (RT)	u_1 650	675/775	37.5	2.1	2.1	0.77	0.38	0.14	29	11		---	---
						2.0							(2.9)		
					60	1.1	1.2	0.48	0.20	0.074	15	5.1		---	---
						1.4									
	11-74	725 (RT)	u_2 970	870/950	37.5	3.9	3.8	1.4	0.70	0.26	52	19		1.44	---
						3.7							(1.3)		
					60	2.7	2.7	0.99	0.50	0.19	37	14		2.46	---
						2.6									
	11-74	725 (RT)	u_3 1400	1250/1500	37.5	5.4									
						5.0	5.4	2.0	1.0	0.37	74	29		1.43	1.38
					60	5.6							(1.5)		
						5.4	5.5	2.1	0.65	0.24	40	15		1.37	1.32
	11-74	1200 (Cold*)	1100	-----	37.5	10.8	11.2	4.1	2.1	0.76	150	56			
						12.3									

* Assumed to be predominantly quartz composition with some particles of quartz (50% of the 37 μm, with the remainder about the same as particle size

TABLE XIII - Continued

Target Material	Particle Size (μ)	Carrier Gas Velocity (fps)	Median Particle Velocity (fps)	Range, Estimated Particle Velocity (fps)	Impingement Angle (deg)	Test Data: Target Weight Loss (mg)	Average Target Weight Loss (mg)	Average Target Volume Loss ($cm^3 \times 10^{-3}$)	Weight Erosion Factor, E (mg/gm)	Volume Erosion Factor, ϵ_v ($cm^3 \times 10^{-3}$/gm)	Average Target Weight Loss Per Single Particle Impact* (mg $\times 10^{-6}$)	Average Target Volume Loss Per Single Particle Impact* ($cm^3 \times 10^{-12}$)	Ratio, $\frac{d_{37.5°}}{d_{60°}}$	Exponent (n) of Velocity Ratio: $\left(\frac{v_1}{v_2}\right)^n$ or $\left(\frac{v_1}{v_2}\right)^n$	Exponent (n) of Velocity Ratio: $\left(\frac{v_1}{v_2}\right)^n$
2024 Al (Annealed)	74-147	570 (RT)	v_1 = 488	675/500	37.5	1.9 1.9	1.9	0.69	0.38	0.13	170	61	(2.1)	---	---
					60	0.9 0.9	0.9	0.33	0.17	0.062	80	29		---	---
	74-147	700 (RT)	v_2 = 670	850/600	37.5	3.7 3.7	3.7	1.4	0.69	0.26	330	130	(1.9)	2.12	---
					60	2.4 2.5	2.5	0.91	0.48	0.17	230	81		2.25	---
	74-147	950 (RT)	v_3 = 830	705/865	37.5	4.6 4.4	4.6	1.7	0.65	0.22	410	150	(1.9)	1.66	1.66
					60	2.6 2.6	2.4	0.88	0.45	0.16	210	78		1.65	(-)0.190
	74-147	1200 (700°F)	1060	---	37.5	9.9 10.7	10.3	3.8	1.8	0.70	950	360			

* Assuming the predominant erosive components are cubic particles of quartz (~2.6 gm/cc or 1.75 gm), with edge dimensions equivalent to mean particle size

TABLE XIII – Continued

Target Material	Particle Size (μm)	Carrier Gas Velocity (fps)	Median Particle Velocity (fps)	Range, Estimated Particle Velocity (fps)	Impingement Angle (deg)	Test Data: Target Weight Loss (mg)	Average Target Weight Loss (mg)	Average Target Volume Loss ($cm^3 \times 10^{-3}$)	Weight Erosion Factor, ϵ (mg/gm)	Volume Erosion Factor, ϵ_v ($cm^3 \times 10^{-3}$/gm)	Average Target Weight Loss Per Single Particle Impact* (mg $\times 10^{-6}$)	Average Target Volume Loss Per Single Particle Impact* ($cm^3 \times 10^{-11}$)	Ratio, $\frac{\epsilon_{37.5°}}{\epsilon_{60°}}$	Exponent (n) of Velocity Ratio: $\left(\frac{u_2}{u_1}\right)^n$ or $\left(\frac{u_3}{u_1}\right)^n$	Exponent (n) of Velocity Ratio: $\left(\frac{u_3}{u_2}\right)^n$
2024 Al (Annealed)	147-208	605 (RT)	u_1 488	475/500	37.5	1.9	1.9	0.69	0.35	0.13	670	240	(1.6)	---	---
						1.9									
					60	1.0	1.0	0.37	0.19	0.069	350	130		---	---
						0.9									
	147-208	835 (RT)	u_2 670	650/695	37.5	3.9	3.9	1.4	0.72	0.26	1700	650	(2.8)	2.23	---
						3.8									---
					60	1.3	1.4	0.51	0.26	0.094	450	180		1.14	---
						1.4									

	147-208	950 (RT)	u_3 755	715/795	37.5	4.6	4.4	1.6	0.82	0.30	1800	680		1.92	1.68
						4.2									
					60	2.6	2.4	0.88	0.44	0.16	850	310		2.00	4.79
						2.2									
	147-208	1200 (700°F)	980	----	37.5	9.0	9.2	3.4	1.7	0.63	3230	1200			
						9.4									

* Assuming the predominant erosive components are cubic particles of quartz (ρ=2.65 gm/cc or 3.78 gm), with edge dimensions equivalent to mean particle size.

TABLE XIV. COMPILATION OF SERIES III TEST DATA (PART I; Ti-6Al-4V Target)

Target Material	Projectile Specific Gravity	Impact Velocity (fps)	Median Particle Velocity (fps)	Range of Particle Velocity (fps)	Impingement Angle (deg)	Test Data Target Weight Loss (mg)	Average Target Weight Loss (mg)	Average Target Volume Loss ($cm^3 \times 10^{-3}$)	Weight Erosion Factor, ϵ_w (mg/gm)	Volume Erosion Factor, ϵ_v ($cm^3 \times 10^{-7}$/gm)	Average Target Weight Loss Per Single Particle Impact* (mg $\times 10^{-3}$)	Average Target Volume Loss Per Single Particle Impact* ($cm^3 \times 10^{-11}$)	Ratio $\left(\frac{\epsilon_v}{\epsilon_w}\right)$	Exponent (n) of Velocity Ratio $\left(\frac{v}{v_1}\right)^n$	Exponent (n) of Velocity Ratio $\left(\frac{v}{v_1}\right)^n$
Ti-6Al-4V (Annealed)	4.43	500 (RT)	v_1	175/500	37.5	2.0	2.1	0.48	0.38	0.069	1.1	0.24	(1.6)	---	---
						2.1									
					60	1.2	1.3	0.29	0.24	0.054	0.66	0.15		---	---
						1.3									
	4.43	650 (RT)	v_1	650/650	37.5	1.6	3.7	0.84	0.69	0.16	1.9	0.43	(1.5)	1.92	---
						3.8									
					60	2.7	2.8	0.64	0.52	0.12	1.4	0.31		2.46	---
						2.8									
	4.43	950 (RT)	v_1	950/950	37.5	6.0									
						6.0	5.1	1.2	0.94	0.22	2.6	0.58		1.39	0.36
						5.2									
						4.8							(1.2)		
					60	4.4									
						4.0	4.1	0.93	0.76	0.17	2.1	0.47		1.77	1.15
						2.6									
						5.4									
	4.43	1200 (700°F)	1165	----	37.5	5.5	5.7	1.3	1.1	0.24	2.9	0.66			
						5.9									

* Assuming the predominant erosive components are cubic particles of quartz (ρ_p=2.75 gm/cc), with edge dimensions equivalent to mean particle size

TABLE XIV – Continued

Target Material	Particle Size (μm)	Carrier Gas Velocity (fps)	Median Particle Velocity (fps)	Range, Estimated Particle Velocity (fps)	Impingement Angle (deg)	Test Data: Target Weight Loss (mg)	Average Target Weight Loss (mg)	Average Target Volume Loss ($cm^3 \times 10^{-3}$)	Weight Erosion Factor, ϵ (mg/gm)	Volume Erosion Factor, ϵ_v ($cm^3 \times 10^{-3}$/gm)	Average Target Weight Loss Per Single Particle Impact* (mg $\times 10^{-5}$)	Average Target Volume Loss Per Single Particle Impact* ($cm^3 \times 10^{-11}$)	Ratio $\frac{\epsilon_v(\alpha)}{\epsilon_v(90°)}$	Exponent (x) of Velocity Ratio $\left(\frac{v_2}{v_1}\right)^x$ or $\left(\frac{v_{n2}}{v_{n1}}\right)^x$	Exponent (x) of Velocity Ratio $\left(\frac{v_3}{v_2}\right)^x$
Ti-6Al-4V (Annealed)	43-74	525 (RT)	v_1 498	475/500	37.5	2.3 2.2	2.3	0.52	0.43	0.086	32	7.1	(1.5)	---	---
					60	1.4 1.5	1.5	0.34	0.28	0.083	21	4.7		---	---
	43-71	725 (RT)	v_2 670	650/700	37.5	3.9 3.9	3.9	0.88	0.72	0.16	53	12	(1.1)	1.49	---
					60	3.6 3.2	3.4	0.77	0.63	0.14	47	11		2.60	---
	43-74	950 (RT)	v_3 880	850/900	37.5	7.2 6.6	6.9	1.6	1.3	0.30	95	22	(1.3)	1.87	2.12
					60	5.0 5.6	5.3	1.2	0.98	0.22	73	16		2.15	1.65
	43-74	1500 (700°F)	1100	----	37.5	8.3 8.1	8.2	1.9	1.5	0.35	110	26			

* Assuming the predominant erosive components are cubic particles of quartz (ρ = 2.65 gm/cc, with edge dimensions equivalent to mean particle size

TABLE XIV - Continued

Target Material	Particle Size (μ)	Carrier Gas Velocity (fps)	Median Particle Velocity (fps)	Range, Estimated Particle Velocity (fps)	Impingement Angle (deg)	Test Data, Target Weight Loss (mg)	Average Target Weight Loss (mg)	Average Target Volume Loss ($cm^3 \times 10^{-3}$)	Weight Erosion Factor, ϵ (mg/gm)	Volume Erosion Factor, ϵ_v ($cm^3 \times 10^{-3}$/gm)	Average Target Weight Loss Per Single Particle Impact* (mg $\times 10^{-6}$)	Average Target Volume Loss Per Single Particle Impact* ($cm^3 \times 10^{-11}$)	Ratio $\frac{\epsilon_{37.5°}}{\epsilon_{60°}}$	Exponent (n) of Velocity Ratio $\left(\frac{u_2}{u_1}\right)^n$ or $\left(\frac{u_1}{u_2}\right)^n$	Exponent (n) of Velocity Ratio $\left(\frac{u_3}{u_2}\right)^n$
Ti-6Al-4V (Annealed)	74-147	570 (RT)	u_1 = 488	475/500	37.5	2.8 2.3	2.4	0.56	0.44	0.10	$2\bar{1}0$	40	(2.3)	---	---
					60	1.8 1.9	1.9	0.43	0.35	0.080	$1\bar{7}0$	30		---	---
	74-147	760 (RT)	u_2 670	650/690	37.5	4.3 4.3	4.3	0.97	0.80	0.18	$3\bar{8}0$	6C	(1.3)	1.65	---
					60	3.5 3.6	3.6	0.81	0.67	0.15	$2\bar{8}0$	72		2.04	---
	74-147	950 (RT)	u_3 930	795/865	37.5	5.8 6.0	5.8	1.3	1.1	0.24	$3\bar{8}0$	$1\bar{3}0$	(2.1)	1.66	1.90
					60	5.6 5.4	5.5	1.2	1.0	0.22	$4\bar{8}0$	$1\bar{1}0$		2.00	1.90
	74-147	1290 (700°F)	1054	----	37.5	7.8 8.0	7.9	1.8	1.5	0.33	$7\bar{8}0$	$1\bar{8}0$			

* Assuming the predominant erosive components are cubic particles of quartz (2.65 wt or 3.74 gm), with edge dimensions equivalent to mean particle size

TABLE XIV – Continued

Target Material	Particle Size (μ)	Carrier Gas Velocity (fps)	Median Particle Velocity (fps)	Range, Estimated Particle Velocity (fps)	Impingement Angle (deg)	Test Data, Target Weight Loss (mg)	Average Target Weight Loss (mg)	Average Target Volume Loss ($cm^3 \times 10^{-3}$)	Weight Erosion Factor, ϵ (mg/gm)	Volume Erosion Factor, ϵ_v ($cm^3 \times 10^{-3}$/gm)	Average Target Weight Loss Per Single Particle Impact* (mg $\times 10^{-6}$)	Average Target Volume Loss Per Single Particle Impact* ($cm^3 \times 10^{-12}$)	Ratio, $\frac{\epsilon_{37.5°}}{\epsilon_{60°}}$	Exponent (n) of Velocity Ratio, $\left(\frac{v_2}{v_1}\right)^n$ or $\left(\frac{v_3}{v_1}\right)^n$	Exponent (n) of Velocity Ratio, $\left(\frac{v_3}{v_2}\right)^n$
Ti-6Al-4V (Annealed)	147-208	605 (RT)	v_1 488	475/500	37.5	2.4 2.4	2.4	0.54	0.44	0.10	850	190	(1.2)	---	---
					60	2.0 2.0	2.0	0.45	0.37	0.083	700	160		---	---
	147-208	835 (RT)	v_2 670	650/695	37.5	4.0 4.1	4.1	0.93	0.76	0.17	1400	330	(1.4)	1.67	---
					60	2.8 3.0	2.9	0.66	0.54	0.12	1000	230		1.16	---
	147-208	950 (RT)	v_3 755	715/795	37.5	5.8 6.0	5.9	1.3	1.1	0.24	2100	484	(1.2)	2.08	3.23
					60	4.8 5.4	5.1	1.2	0.94	0.22	1800	420		2.14	5.48
	147-208	1200 (70°F)	960	----	37.5	7.2 7.8	7.5	1.7	1.4	0.32	2600	600			

* Assuming the predominant erosive components are cubic particles of quartz (specific gravity = 2.65 gm/cm³), with edge dimensions equivalent to mean particle size.

TABLE XV. COMPILATION OF SERIES III TEST DATA (PART I; 410 SS Target)

Target Material	Particle Size (μ)	Carrier Gas Velocity (fps)	Median Particle Velocity (u_1) (fps)	Range, Estimated Particle Velocity (fps)	Impingement Angle (deg)	Test Data, Target Weight Loss (mg)	Average Target Weight Loss (mg)	Average Target Volume Loss ($cm^3 \times 10^{-3}$)	Weight Erosion Factor, ϵ (mg/gm)	Volume Erosion Factor, ϵ_v ($cm^3 \times 10^{-3}$/gm)	Average Target Weight Loss Per Single Particle Impact* (mg $\times 10^{-5}$)	Average Target Volume Loss per Single Particle Impact* ($cm^3 \times 10^{-11}$)	Ratio $\frac{\epsilon_v}{\epsilon}$ (cm^3/gm)	Exponent (n) of Velocity Ratio $\left(\frac{u_2}{u_1}\right)^n$ or $\left(\frac{u_1}{u_2}\right)^n$	Exponent (n) of Velocity Ratio $\left(\frac{u_2}{u_1}\right)^n$
410 SS (Annealed)	0-44	500 (RT)	u_1 195	475/500	37.5	1.8 2.0	1.9	0.24	0.35	0.045	0.97	0.12		---	---
					60	1.2 1.3	1.3	0.17	0.24	0.032	0.66	0.087	(1.5)	---	---
	0-44	500 (RT)	u_1 470	450/485	37.5	3.9 4.0	3.9	0.50	0.72	0.093	2.0	0.25	(1.5)	2.29	---
					60	2.7 2.7	2.7	0.35	0.50	0.065	1.4	0.19		2.42	---
	0-44	950 (RT)	u_1 925	900/950	37.5	6.8 5.0 5.6 4.4	5.5	0.70	1.0	0.13	2.8	0.36	(1.5)	1.67	1.95
					60	4.2 3.0 3.2 4.4	3.7	0.47	0.69	0.087	1.9	0.24		1.68	0.96
	0-44	1500 (700°F)	1195	----	37.5	8.0 6.1	7.1	0.91	1.3	0.17	3.6	0.46			

* Assuming the particulate erosive component of carbon particles and quartz (d_{50} = about 0.0 gm), with like dimensions, equivalent to mean particle size

TABLE XV - Continued

Target Material	Particle Size (μm)	Carrier Gas Velocity (fps)	Median Particle Velocity (fps)	Range, Estimated Particle Velocity (fps)	Impingement Angle (deg)	Test Data Target Weight Loss (mg)	Average Target Weight Loss (mg)	Average Target Volume Loss ($cm^3 \times 10^{-3}$)	Weight Erosion Factor, ϵ (mg/gm)	Volume Erosion Factor, ϵ_v ($cm^3 \times 10^{-3}$/gm)	Average Target Weight Loss Per Single Particle Impact* ($mg \times 10^{-5}$)	Average Target Volume Loss Per Single Particle Impact* ($\mu m^3 \times 10^{-11}$)	Ratio $\frac{\epsilon_{v_1}}{\epsilon_{v_2}}$	Exponent (n) of Velocity Ratio $\left(\frac{v_1}{v_2}\right)^n$ $= \left(\frac{v_1}{v_3}\right)^n$	Exponent (n) of Velocity Ratio $\left(\frac{v_1}{v_2}\right)^n$
410 SS (Annealed)	53-74	525 (RT)	v_1 694	675/500	37.5	2.2 2.2	2.2	0.28	0.41	0.052	30	3.8	(1.3)	---	---
					60	1.5 1.5	1.5	0.19	0.28	0.035	21	2.6		---	---
	53-74	725 (RT)	v_2 670	650/690	37.5	4.2 4.2	4.2	0.54	0.78	0.10	58	7.4	(1.2)	2.86	---
					60	3.6 3.6	3.6	0.46	0.67	0.085	49	6.3		2.78	---
	53-74	950 (RT)	v_3 940	910/960	37.5	6.0 5.4	6.1	0.78	1.1	0.14	84	11	(1.3)	1.73	1.36
					60	5.2 5.4	5.3	0.68	0.96	0.12	73	9.3		2.15	1.43
	53-74	1200 (700°)	1190	----	37.5	7.0 7.5	7.3	0.93	1.4	0.17	100	13			

* Assuming the predominant erosive components are cubic particles of quartz (ρ 2.64 or 2.75 g/cm), with edge dimensions equivalent to mean particle size.

TABLE XV – Continued

Target Material	Particle Size (μ)	Carrier Gas Velocity (ft/s)	Incident Particle Velocity (ft/s)	Impinging Particle Velocity (ft/s)	Impingement Angle (deg)	Test Duration, Target Weight Loss (mg)	Average Target Weight Loss (mg)	Average Target Volume Loss ($cm^3 \times 10^{-3}$)	Weight Erosion Factor, E_w (mg/gm)	Volume Erosion Factor, E_v ($mm^3 \times 10^{-3}$/gm)	Average Target Weight Loss Per Single Particle Impact* (mg $\times 10^{-9}$)	Average Target Volume Loss Per Single Particle Impact* ($mm^3 \times 10^{-11}$)	Ratio $\frac{d_{30}}{d_{50}}$ at θ_{opt}	Exponent (n) of Velocity Ratio $\left(\frac{v_2}{v_1}\right)^n = \left(\frac{a_2}{a_1}\right)^n$	Exponent (n) of Velocity Ratio $\left(\frac{v_2}{v_1}\right)^n$
410 SS (Annealed)	74-147	530 (RT)	v_1 600	600/500	37.5	2.3 2.4	2.4	0.31	0.44	0.057	216	27	(0.3)	---	---
					60	1.9 1.9	1.9	0.44	0.35	0.044	176	22		---	---
	74-147	780 (RT)	v_2 670	670/580	37.5	4.4 4.5	4.5	0.59	0.83	0.11	280	34	(0.3)	2.30	---
					60	3.7 3.7	3.7	0.47	0.68	0.087	280	42		2.12	---
	74-147	950 (RT)	v_3 830	795/685	37.5	6.4 6.4	6.4	0.82	1.2	0.15	570	73	(0.3)	1.66	1.63
					60	5.2 5.4	5.3	0.68	0.96	0.13	470	60		1.93	1.67
	74-147	1200 (700°F)	1050	---	37.5	8.3 8.3	8.3	1.1	1.5	0.20	760	98			

* Assuming the predominant erosive components are cubic particles of quartz ($\rho = 2.65$ gm/cc), with edge dimensions equivalent to mean particle size.

TABLE XV - Continued

Target Material	Particle Size (μ)	Carrier Gas Velocity (fps)	Median Particle Velocity (fps)	Range, Estimated Particle Velocity (fps)	Impingement Angle (deg)	Test Data, Target Weight Loss (mg)	Average Target Weight Loss (mg)	Average Target Volume Loss ($cm^3 \times 10^{-3}$)	Weight Erosion Factor, ϵ (mg/gm)	Volume Erosion Factor, ϵ_v ($cm^3 \times 10^{-3}$/gm)	Average Target Weight Loss Per Single Particle Impact* ($g \times 10^{-9}$)	Average Target Volume Loss Per Single Particle Impact* ($cm^3 \times 10^{-12}$)	Ratio, $\frac{\epsilon_{\alpha}}{\epsilon_{60^\circ}}$	Exponent (n) of Velocity Ratio, $\left(\frac{u_2}{u_1}\right)^n$ or $\left(\frac{u_3}{u_1}\right)^n$	Exponent (n) of Velocity Ratio $\left(\frac{u_3}{u_2}\right)^n$
410 SS (Annealed)	147-208	605 (RT)	u_1 490	475/505	37.5	2.4 2.4	2.4	0.31	0.44	0.057	650	110	(1.3)	---	---
					60	2.0 2.1	2.1	0.27	0.39	0.050	740	95		---	---
	147-208	835 (RT)	u_2 670	650/695	37.5	6.1 6.3	6.2	0.34	0.78	0.10	1500	190	(1.4)	1.74	---
					50	3.0 2.9	3.0	0.38	0.56	0.070	1100	130		1.11	---
	147-208	950 (RT)	u_3 755	715/795	37.5	5.8 6.0	5.9	0.76	1.1	0.14	2100	270	(1.2)	2.06	3.04
					60	4.8 5.0	4.9	0.63	0.91	0.12	1700	220		1.93	4.33
	147-208	1200 (700° F)	960	---	37.5	7.4 7.9	7.7	0.99	1.4	0.18	2700	350			

* Assuming the predominant erosive components are cubic particles of quartz (ρ=70$^{\#}$ or 3.78 gm), with edge dimensions equivalent to mean particle size

TABLE XVI. COMPILATION OF SERIES III TEST DATA (PART I; 17-7 PH Target)

Target Material	Particle Size (μ)	Carrier Gas Velocity (fps)	Median Particle Velocity (fps)	Range, Estimated Particle Velocity (fps)	Impingement Angle (deg)	Test Data, Target Weight Loss (mg)	Average Target Weight Loss (mg)	Average Target Volume Loss ($cm^3 \times 10^{-3}$)	Weight Erosion Factor, ϵ (mg/gm)	Volume Erosion Factor, ϵ_v ($cm^3 \times 10^{-7}$/gm)	Average Target Weight Loss Per Single Particle Impact* (mg $\times 10^{-6}$)	Average Target Volume Loss Per Single Particle Impact* ($cm^3 \times 10^{-11}$)	Ratio $\epsilon_{37.5°}/\epsilon_{60°}$	Exponent (x) of Velocity Ratio $\left(\frac{u_2}{u_1}\right)^x$ or $\left(\frac{u_3}{u_1}\right)^x$	Exponent (x) of Velocity Ratio $\left(\frac{u_3}{u_2}\right)^x$
17-7 PH (Annealed)	0-11	500 (RT)	u_1 385	475/500	37.5	2.0	2.1	0.28	0.39	0.052	1.1	0.14		---	---
						2.1							(1.6)		
					60	1.4	1.3	0.17	0.24	0.032	0.66	0.087		---	---
						1.2									
	0-11	645 (RT)	u_2 670	650/695	37.5	3.9	3.9	0.52	0.72	0.096	2.0	0.26		1.96	---
						3.9							(1.3)		
					60	2.8	2.9	0.39	0.54	0.072	1.5	0.20		2.58	---
						2.9									
	0-11	900 (RT)	u_3 925	900/950	37.5	3.8									
						1.2	5.5	0.73	1.0	0.14	2.8	0.37		1.51	1.05
						5.2							(2.3)		
						5.9									
					60	4.4									
						4.6	4.3	0.57	0.80	0.11	2.2	0.29		1.88	1.19
						3.9									
						4.4									
	0-11	1200 (700° F)	1165	---	37.5	7.4	7.8	1.0	1.4	0.19	3.9	0.51			
						8.1									

* Assuming the predominant erosive component to be quartz particles of quartz (ρ = 2.65 gm/cm^3) with edge dimensions equivalent to the particle size.

TABLE XVI - Continued

Target Material*	Particle Size (μ)	Gas Velocity (fps)	Median Particle Velocity (fps)	Range, Estimated Particle Velocity (fps)	Impingement Angle (deg)	Test Data, Target Weight Loss (mg)	Average Target Weight Loss (mg)	Average Target Volume Loss ($cm^3 \times 10^{-3}$)	Weight Erosion Factor, ε (mg/gm)	Volume Erosion Factor, ϵ_v ($cm^3 \times 10^{-3}$/gm)	Average Target Weight Loss Per Single Particle Impact* (mg $\times 10^{-6}$)	Average Target Volume Loss Per Single Particle Impact* ($cm^3 \times 10^{-11}$)	Ratio $\frac{\epsilon_{90°}}{\epsilon_{60°}}$	Exponent (n) of Velocity Ratio $\left(\frac{u_2}{u_1}\right)^n$ = ... $\left(\frac{u_2}{u_1}\right)^n$	Exponent (n) of Velocity Ratio $\left(\frac{u_3}{u_2}\right)^n$
17-7 PH (Annealed)	43-74	[illegible] (RT)	u_1 [illegible]	475/500	37.5	2.3 2.4	2.4	0.32	0.44	0.059	33	4.4	(1.6)	---	---
					60	1.4 1.5	1.5	0.20	0.20	0.027	21	2.7		---	---
	43-74	725 (RT)	u_2 670	650/690	37.5	4.2 4.3	4.3	0.57	0.80	0.11	50	7.0	(1.2)	1.85	---
					60	3.8 3.7	3.7	0.49	0.69	0.093	51	6.7		2.06	---
	43-74	950 (RT)	u_3 880	860/900	37.5	8.4 7.8	8.0	1.1	1.5	0.20	110	15	(1.4)	2.05	2.30
					60	5.6 5.8	5.7	0.78	1.1	0.14	78	10		2.27	1.60
	43-74	1500 (700°F)	1100	----	37.5	8.9 9.5	9.2	1.3	1.7	0.22	120	17			

* Assuming the predominant erosive components are cubic particles of quartz (≈70% wt or 3.78 gm), with edge dimensions equivalent to mean particle size.

TABLE XVI - Continued

Target Material	Particle Size (μ)	Carrier Gas Velocity (fps)	Median Particle Velocity (fps)	Range, Estimated Particle Velocity (fps)	Impingement Angle (deg)	Test Data, Target Weight Loss (mg)	Average Target Weight Loss (mg)	Average Target Volume Loss ($cm^3 \times 10^{-3}$)	Weight Erosion Factor, ϵ (mg/gm)	Volume Erosion Factor, ϵ_v ($cm^3 \times 10^{-3}$/gm)	Average Target Weight Loss Per Single Particle Impact* (mg $\times 10^{-6}$)	Average Target Volume Loss Per Single Particle Impact* ($cm^3 \times 10^{-11}$)	Ratio $\epsilon_{37.5°}/\epsilon_{60°}$	Exponent (n) of Velocity Ratio $\left(\frac{u_2}{u_1}\right)^n$ or $\left(\frac{u_3}{u_1}\right)^n$	Exponent (n) of Velocity Ratio $\left(\frac{u_3}{u_2}\right)^n$
17-7 PH (Annealed)	74-147	570 (RT)	u_1 488	475/500	37.5	2.3 2.4	2.4	0.32	0.44	0.060	$2\bar{1}0$	28	(1.3)	---	---
					60	1.9 1.9	1.9	0.25	0.35	0.048	$1\bar{7}0$	22		---	---
	74-147	760 (RT)	u_2 670	650/690	37.5	4.6 4.6	4.6	0.61	0.85	0.11	$4\bar{1}0$	54	(1.2)	2.17	---
					60	3.9 3.9	3.9	0.53	0.72	0.098	$3\bar{4}0$	46		2.28	---
	74-147	950 (RT)	u_3 930	795/865	37.5	5.6 7.0	6.3	0.86	1.2	0.16	$5\bar{6}0$	76.	(1.1)	1.82	1.47
					60	5.8 5.8	5.8	0.77	1.1	0.14	$5\bar{1}c$	68		2.10	1.96
	74-147	1300 (700°F)	1050	----	37.5	9.1 9.2	9.2	1.2	1.7	0.22	$8\bar{2}0$	$1\bar{1}0$			

* Assuming the predominant erosive components are cubic particles of quartz (ρ=2.65 gm/cc or 3.74 gm), with edge dimensions equivalent to mean particle size.

TABLE XVI - Continued

Target Material	Particle Size (μm)	Carrier Gas Velocity (fps)	Median Particle Velocity (fps)	Range, Estimated Particle Velocity (fps)	Impingement Angle (deg)	Test Data, Target Weight Loss (mg)	Average Target Weight Loss (mg)	Average Target Volume Loss ($cm^3 \times 10^{-3}$)	Weight Erosion Factor, ϵ (mg/gm)	Volume Erosion Factor, ϵ_v ($cm^3 \times 10^{-3}$/gm)	Average Target Weight Loss Per Single Particle Impact* (mg $\times 10^{-6}$)	Average Target Volume Loss Per Single Particle Impact* ($cm^3 \times 10^{-11}$)	Ratio $\frac{\epsilon_{37.5°}}{\epsilon_{60°}}$	Exponent (n) of Velocity Ratio $\left(\frac{u_2}{u_1}\right)^n$ or $\left(\frac{u_3}{u_1}\right)^n$	Exponent (n) of Velocity Ratio $\left(\frac{u_3}{u_2}\right)^n$
17-7 PH (Annealed)	147-208	605 (RT)	u_1 488	175/580	37.5	2.4 2.5	2.5	0.33	0.46	0.061	880	120	(1.2)	---	---
					60	2.2 2.0	2.1	0.28	0.38	0.052	740	99		---	---
	147-208	915 (RT)	u_2 670	650/695	37.5	4.2 4.2	4.2	0.56	0.78	0.10	1500	200	(1.3)	1.61	---
					60	3.2 3.3	3.3	0.44	0.61	0.082	1200	160		1.40	---
	147-208	950 (RT)	u_3 755	715/795	37.5	6.0 6.2	6.1	0.81	1.1	0.15	2200.	290.	(1.2)	2.04	3.29
					60	5.2 5.0	5.1	0.68	0.94	0.13	1800	240		2.03	3.88
	147-208	1200 (700°F)	960	----	37.5	8.8 9.3	9.1	1.2	1.7	0.22	3200	420			

* Assuming the predominant erosive components are cubic particles of quartz (density = 2.65 gm), with edge dimensions equivalent to mean particle size.

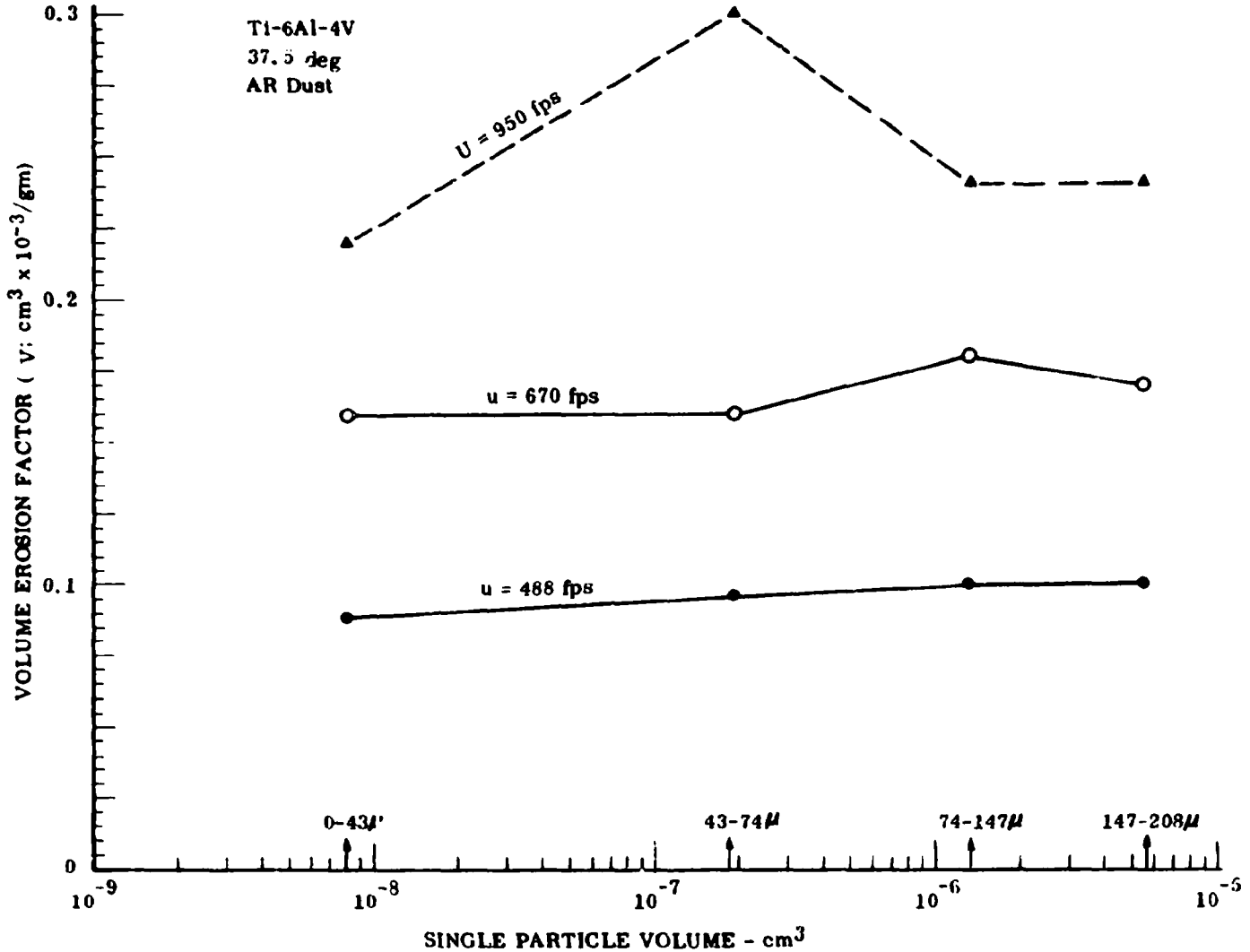

Figure 59. Volume Erosion Factor (ϵ_v) Versus Single Particle Volume (V_p).

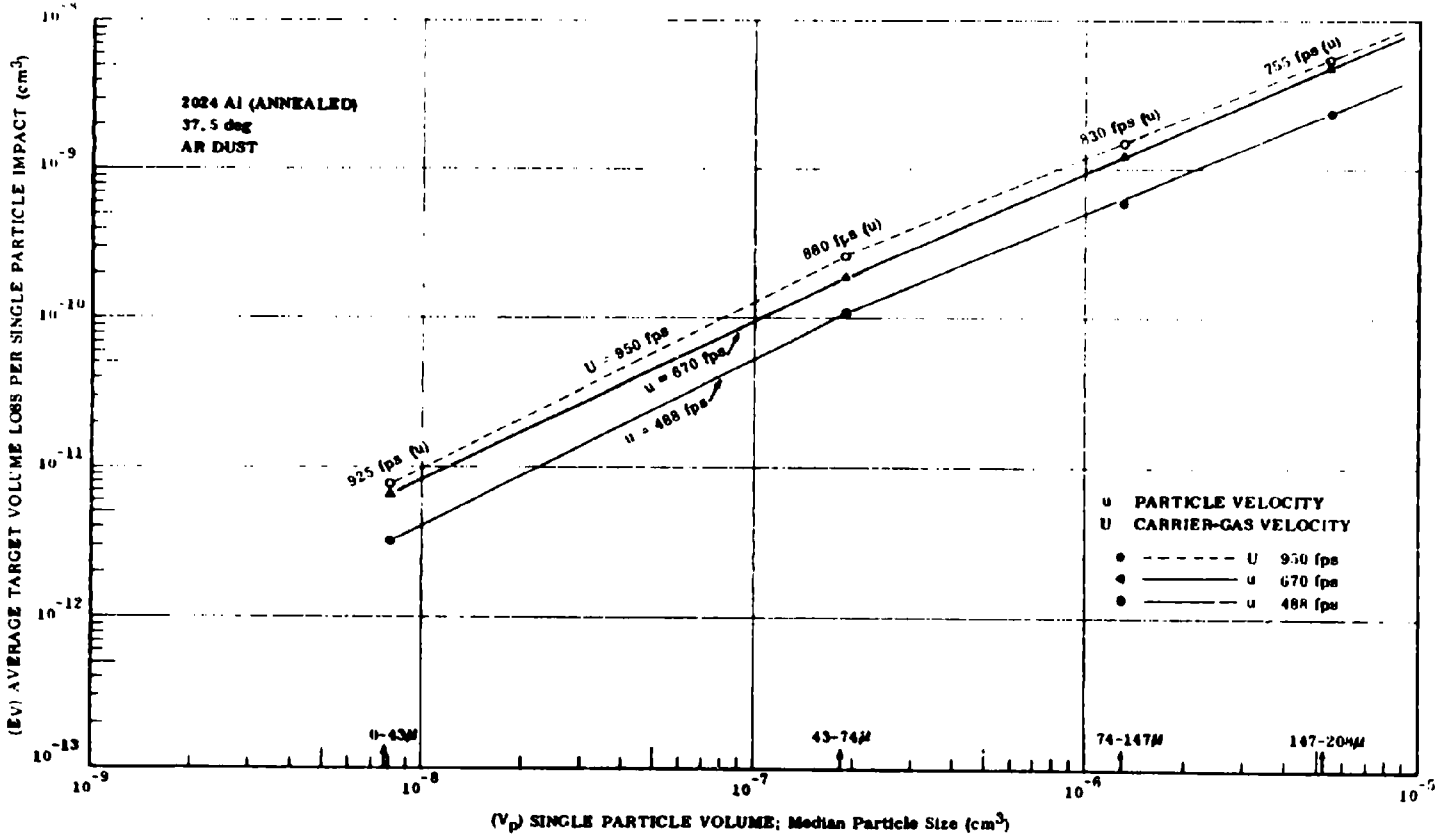

Figure 60. Average Target Volume Loss per Single Particle Impact (E_V) Versus Single Particle Volume (V_p).

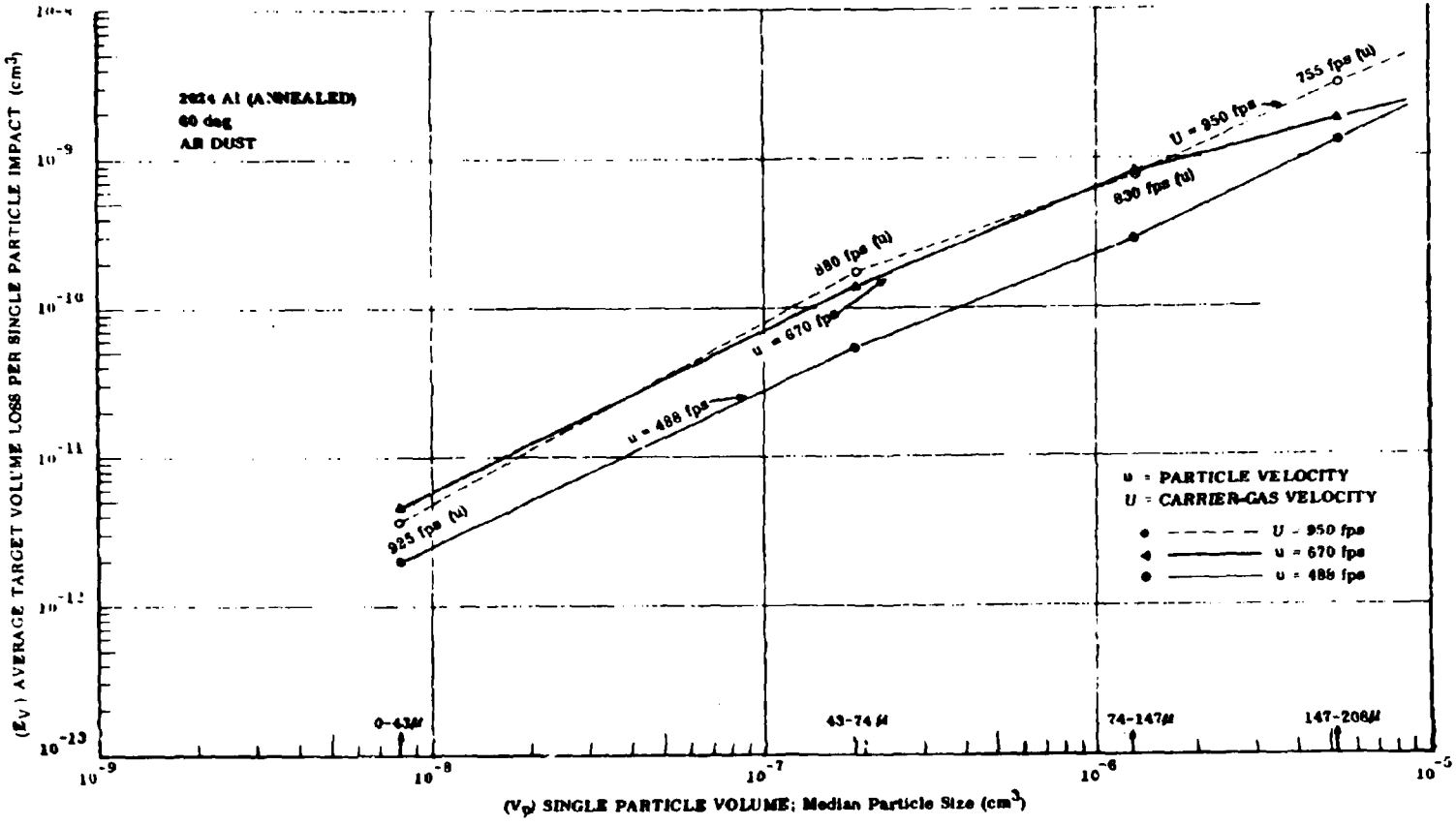

Figure 61. Average Target Volume Loss per Single Particle Impact (E_V) Versus Single Particle Volume (V_p).

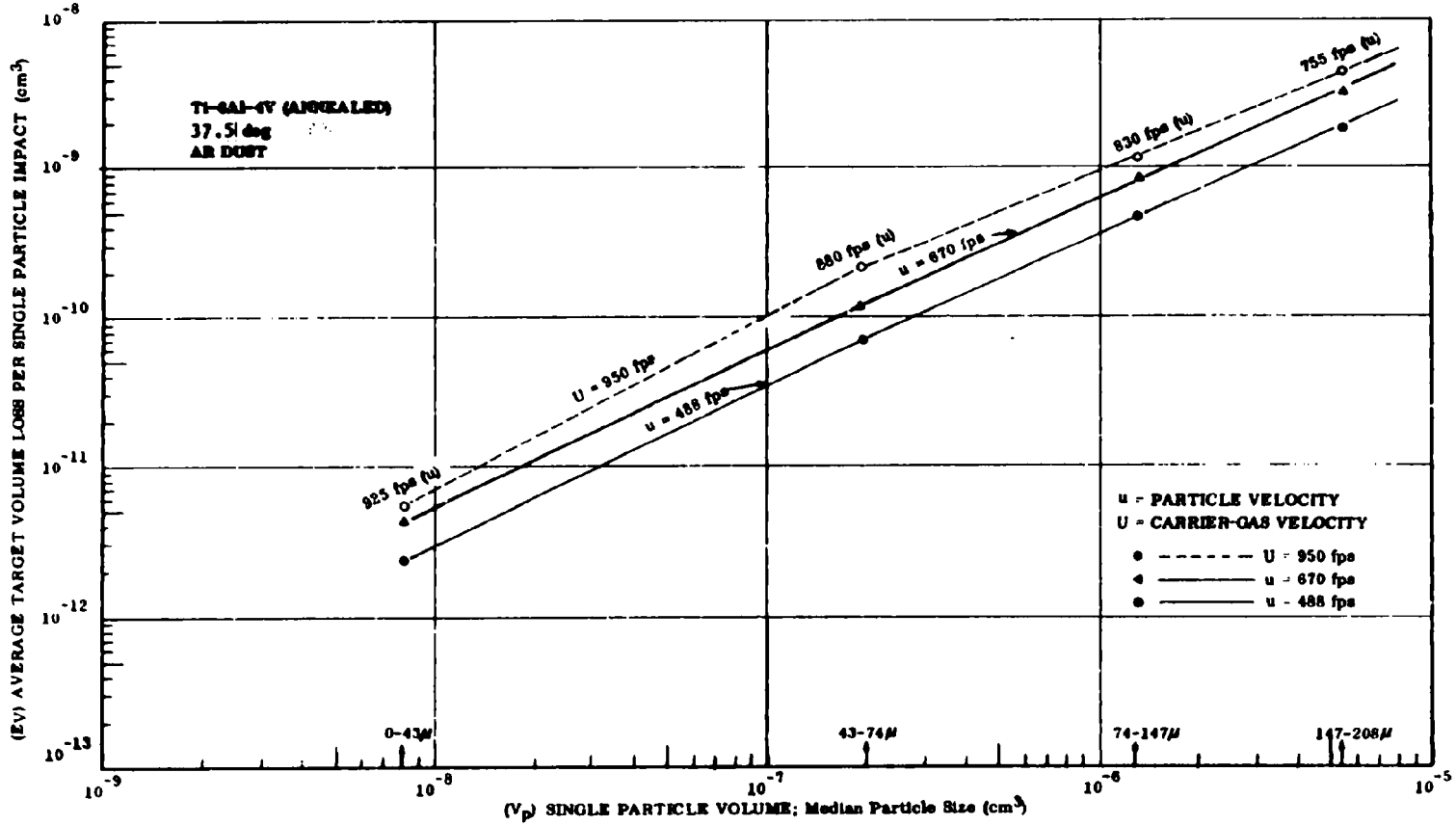

Figure 62. Average Target Volume Loss per Single Particle Impact (Ev) Versus Single Particle Volume (V_p).

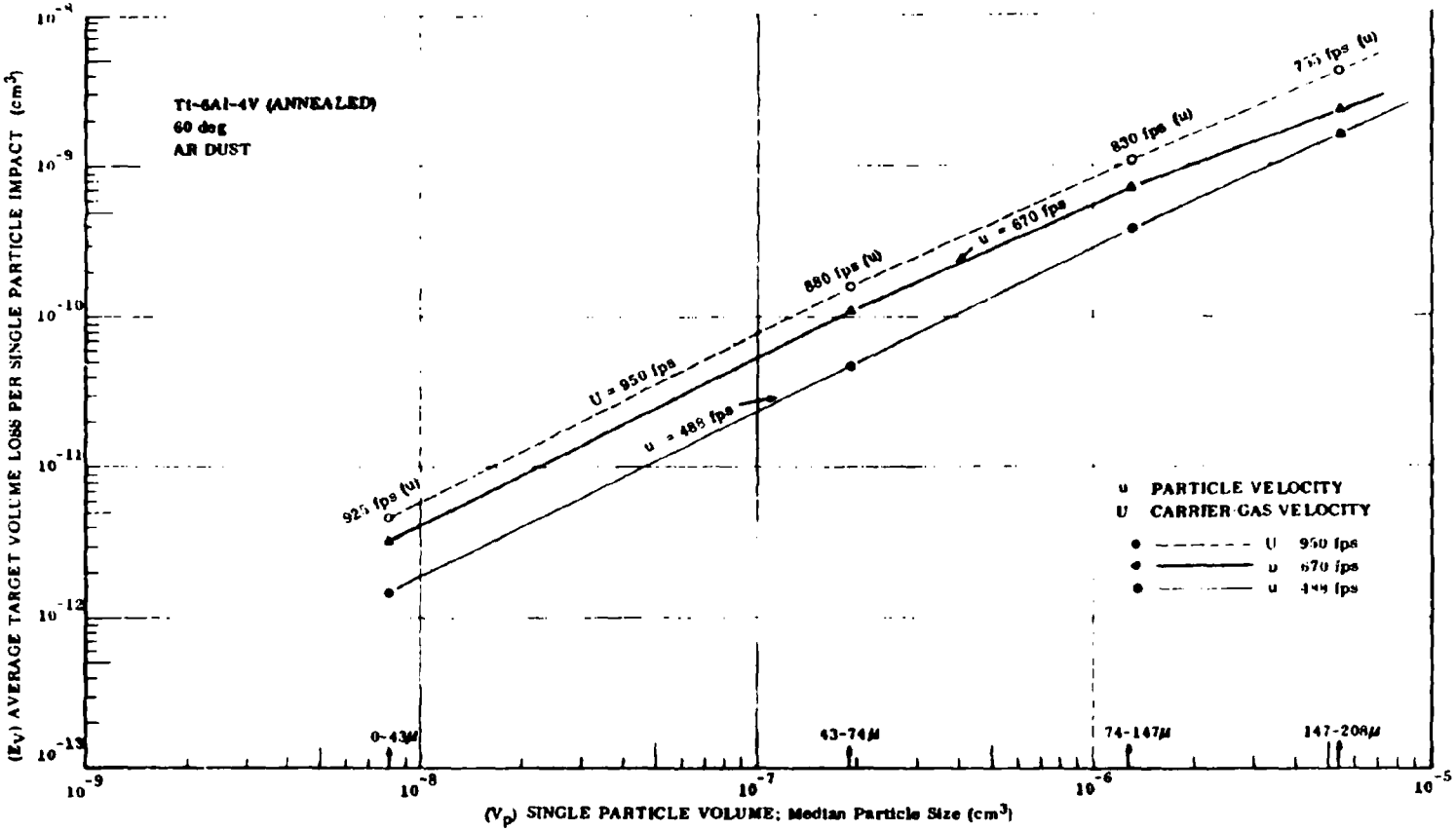

Figure 63. **Average Target Volume Loss per Single Particle Impact (E_V) Versus Single Particle Volume (V_p).**

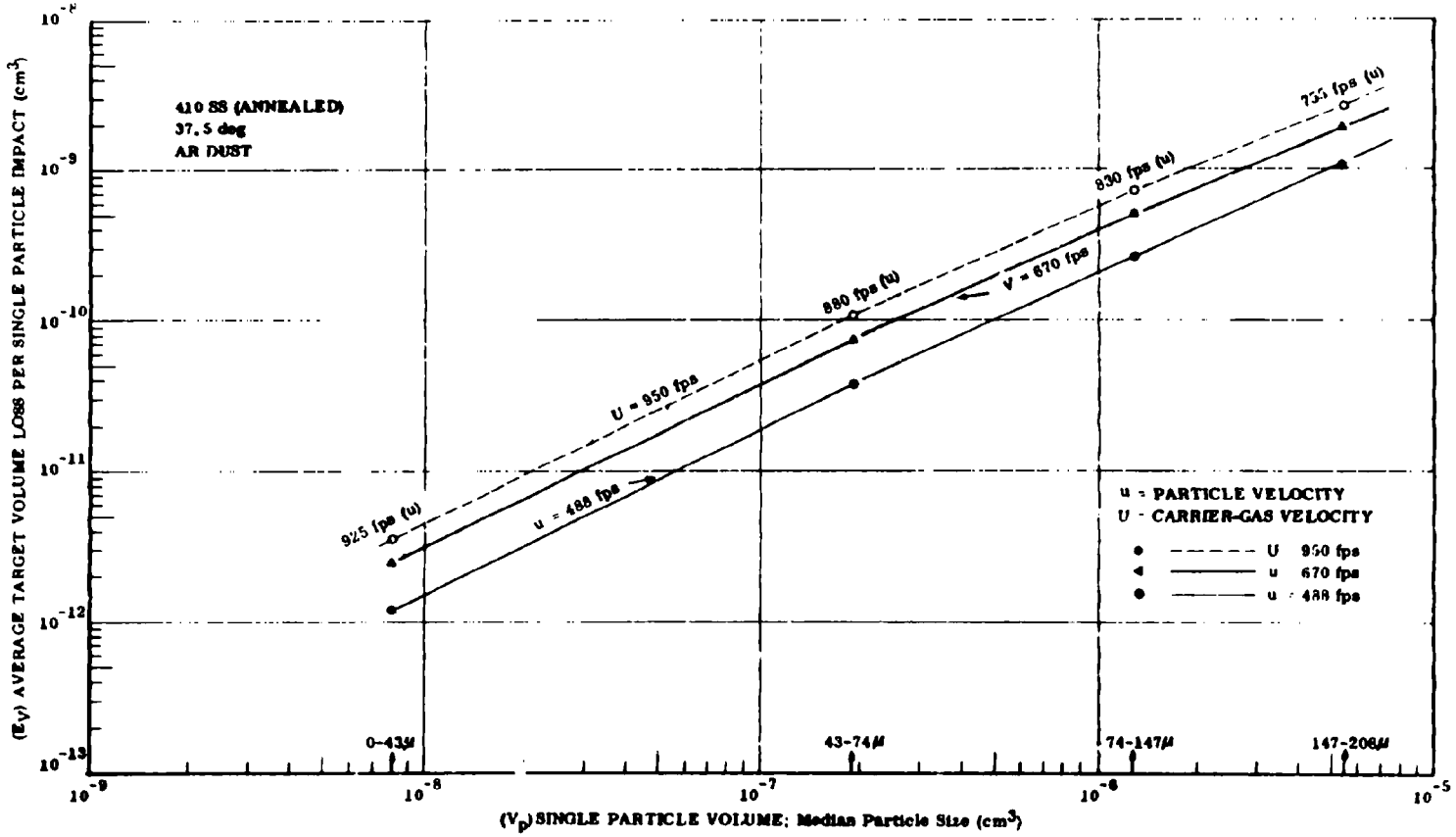

Figure 64. Average Volume Loss per Single Particle Impact (E_V) Versus Particle Volume (V_p).

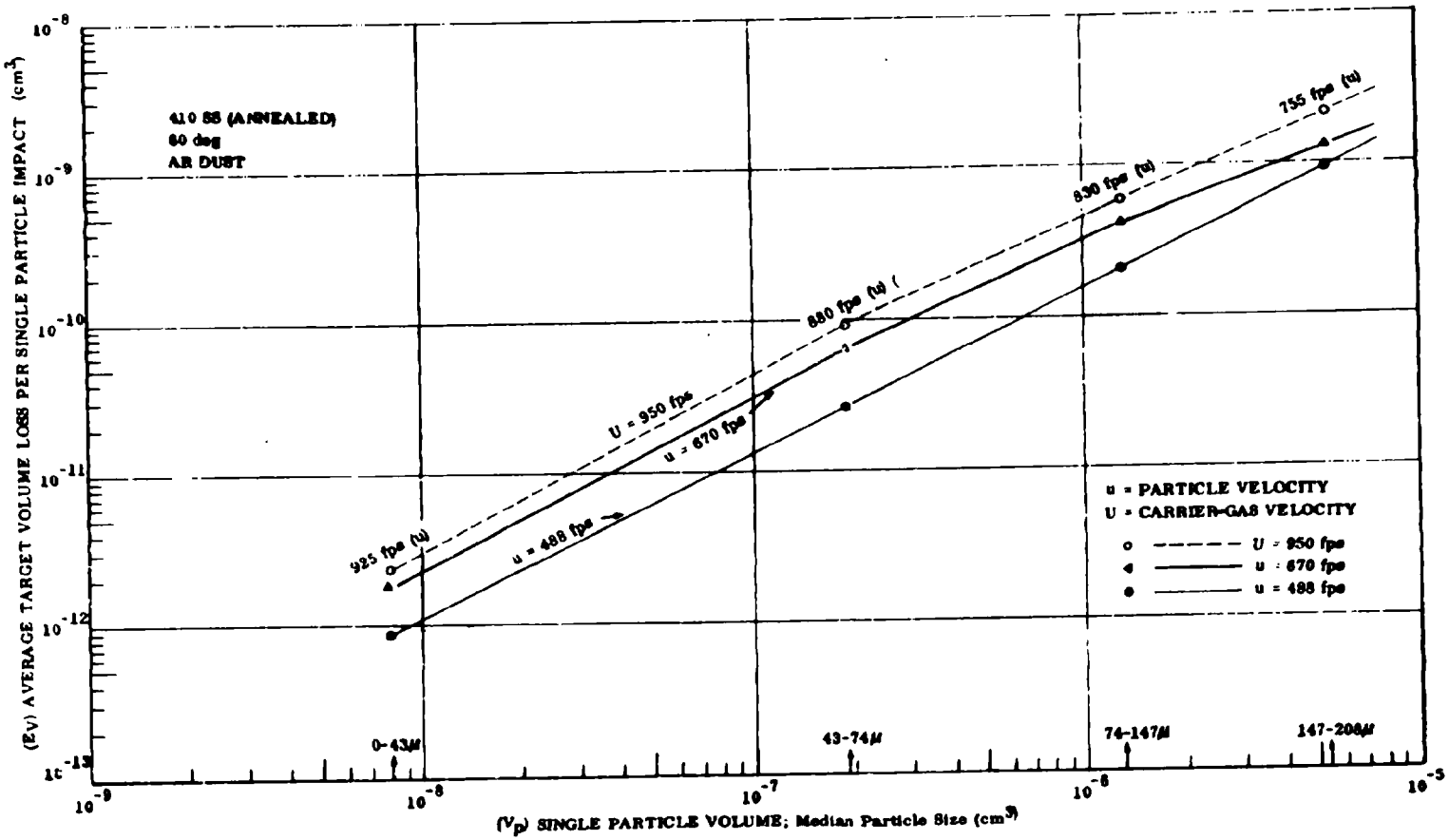

Figure 65. Average Target Volume Loss per Single Particle Impact (E_V) Versus Single Particle Volume (V_p).

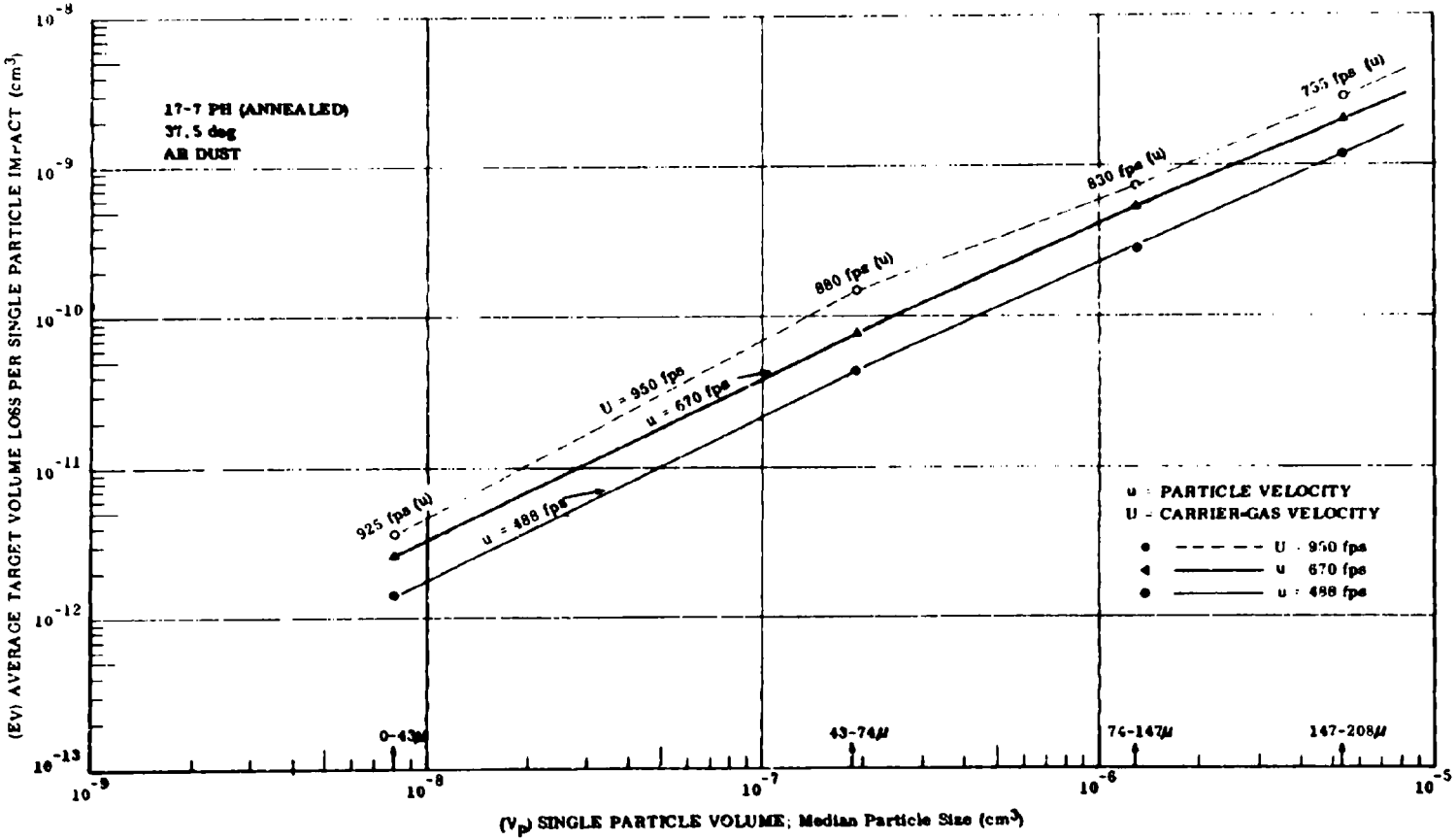

Figure 66. Average Target Volume Loss per Single Particle Impact (E_V) Versus Single Particle Volume (V_p).

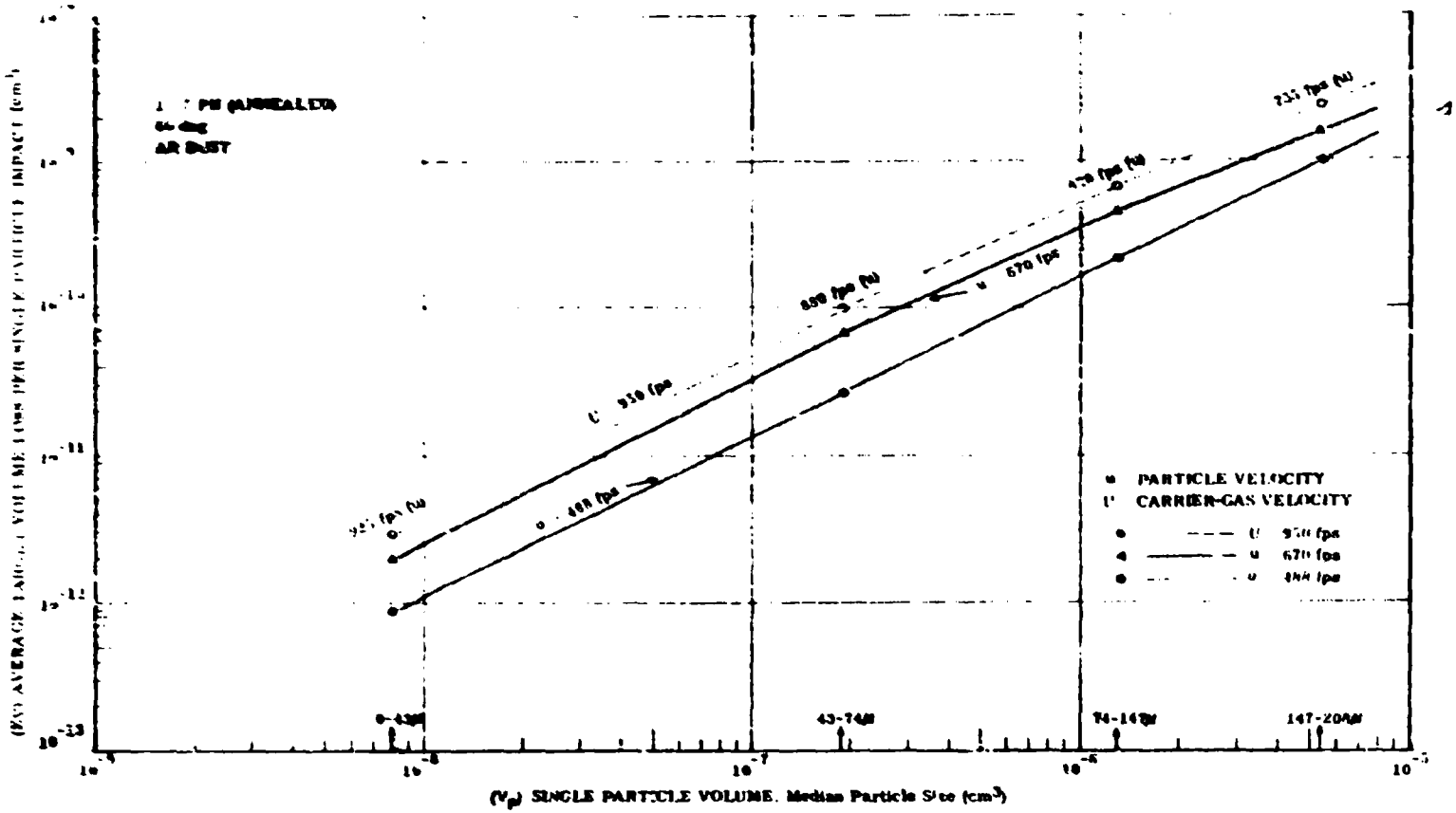

Figure 67. Average Target Volume Loss per Single Particle Impact (Ev) Versus Single Particle Volume (V_p).

As an initial test of the validity of the energy-based equation (8), plots were drawn of E_V versus u (particle velocity), and then analyzed as follows (using the Ti-6Al-4V target and 37.5-degree impingement angle as a typical example, Figure 68):

Particle Size (μ)	Measured Slope (m)	K_M (1, 2, 3, 4)	$n_{1,2}$; $n_{1,3}$; $n_{1,4}$ Derived from the typical equation $\frac{K_{M_2}}{K_{M_1}} = \left(\frac{V_{p_2}}{V_{p_1}}\right)^{n_{1,2}}$
0-43 (subscript 1)	1.66	$K_{M_1} = 8.47 \times 10^{-17}$	----
43-74 (subscript 2)	1.75	$K_{M_2} = 1.46 \times 10^{-15}$	$n_{1,2} = 0.897$
74-147 (subscript 3)	1.68	$K_{M_3} = 1.55 \times 10^{-14}$	$n_{1,3} = 1.02$
147-208 (subscript 4)	1.89	$K_{M_4} = 1.60 \times 10^{-14}$	$n_{1,4} = 0.804$
Average Value	1.75	--------	0.907

Based upon this preliminary analysis, the equation for the relationship of E_V and particle energy might be written

$$E_V = K\rho\,(V_p u^2)^{0.9}. \qquad (10)$$

The reasonably good reproducibility of the velocity exponent, m, in the analysis above contrasts markedly with the wide and apparently random scatter of the velocity exponent ratios listed in Tables IX, XIII, XIV, XV, and XVI. In these tables the ratio of erosion factors represented by individual data points (for varying particle velocity, but constant particle size and incidence angle) is equated to the corresponding ratio of particle velocities raised to a power, x. The exponent, x, ranges more or less randomly between (-) 0.68 and + 5.48 (Series III data). The problem in not defining a more reproducible exponent by this two-point method undoubtedly arises from taking too restricted a view of available data. Each ratio selected comes from within a rather narrow range of particle energies, relative to the total range of particle energies tested. Moreover, each data point is the average of duplicate testing only; whereas data from 24 tests is available for each

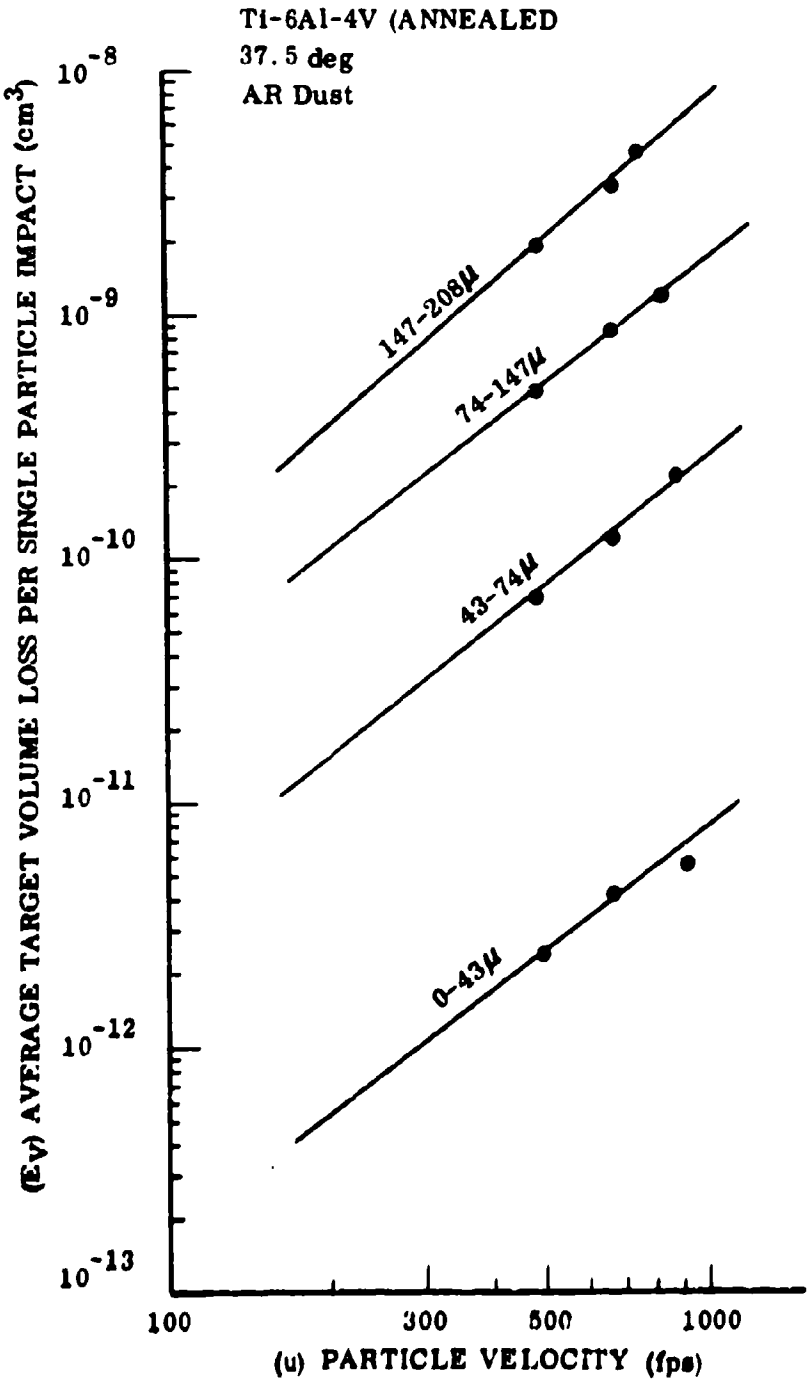

Figure 68. Average Target Volume Loss per Single Particle Impact (Ev) Versus Particle Velocity (u).

target material and impingement angle combination by grouping all velocities and particle sizes together. To obtain better data averaging, log-log plots of E_V versus $V_p u^2$ ($\propto Mu^2$) were drawn using all available data (RT) for each target-angle combination (see Figures 69 through 76). The correlations between E_V and $V_p u^2$ for all combinations of test variables proved remarkably good and very similar, as demonstrated by the linearity of the curves and by the calculated values for $K\rho$ and the exponent, y (equation (11)), derived from analysis of the curves, using the relation

$$E_V = K\rho\,(V_p u^2)^y \qquad (11)$$

Target Alloy	Impingement Angle (deg)	$K\rho = \frac{K_M}{V_p}$	y
2024 Al	37.5	2.0×10^{-9}	1.04
	60	1.1×10^{-9}	1.00
Ti-6Al-4V	37.5	1.5×10^{-9}	0.99
	60	1.2×10^{-9}	1.08
410 SS	37.5	9.0×10^{-10}	1.06
	60	7.0×10^{-10}	1.10
17-7 PH	37.5	9.6×10^{-10}	1.07
	60	7.5×10^{-10}	1.10

The close similarity of the erosion responses for all targets is evident when all curves are plotted together (Figure 77). The advantage in using all available data in a single plot to clarify relationships is well illustrated by these curves of E_V versus $V_p u^2$. The 37.5- and 60-degree curves of best fit for each target alloy show no indication of crossover with varying particle energy or gas temperature, although the average curves are so close (data bands do overlap) that the possibility of convergence and crossover cannot be ruled out for specific experimental situations.

The correlations among the test variables expressed by equation (11) are sufficiently accurate to be made into nomographs relating V_p, u, and E_V. The nomographs for each target alloy and impingement angle combination tested are given in Figures 78 through 85; they should prove useful to the design or applications engineer to predict actual and relative erosion damage to specific blade materials.

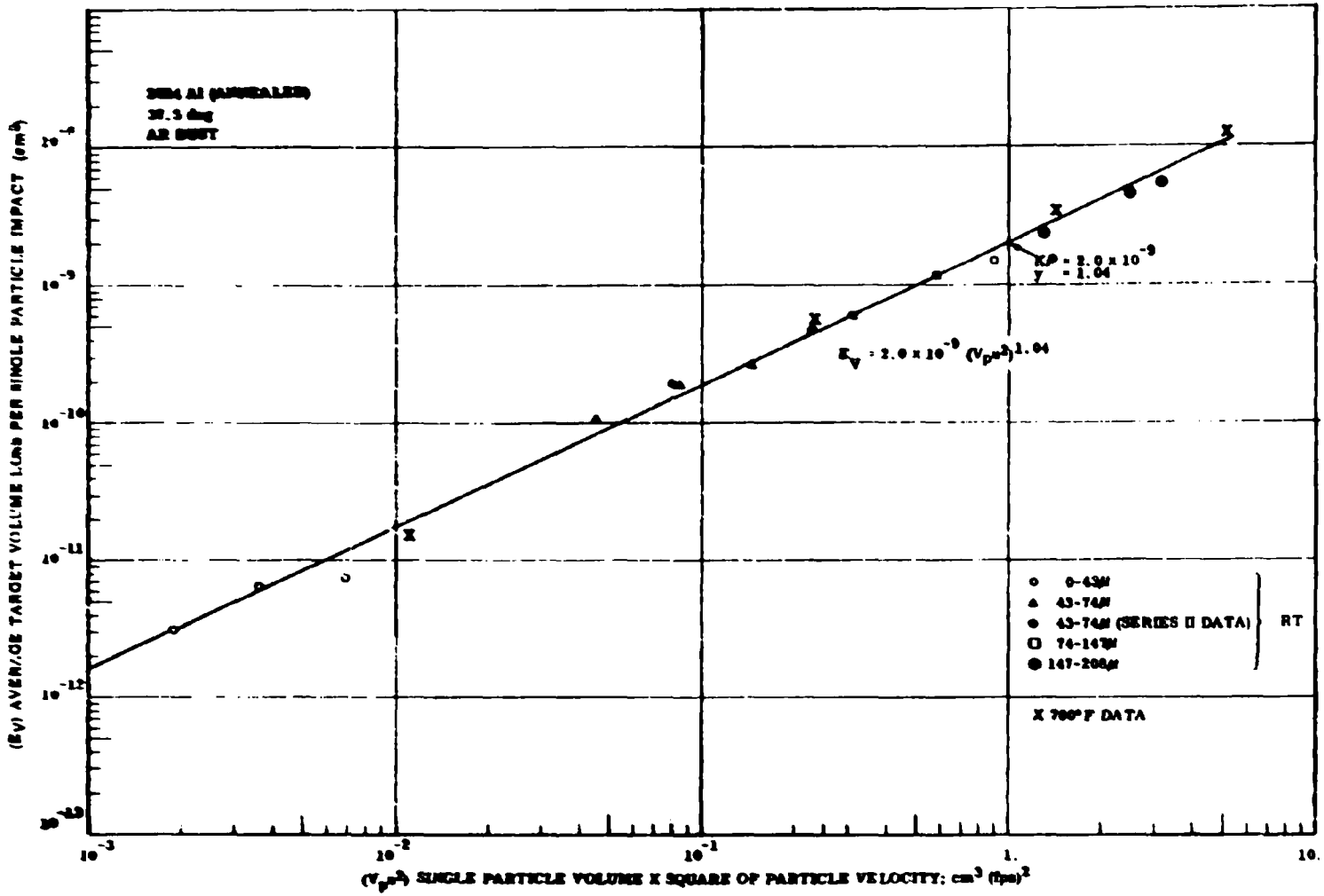

(Ev) AVERAGE TARGET VOLUME LOSS PER SINGLE PARTICLE IMPACT (cm^3)

($V_p\mu^2$) SINGLE PARTICLE VOLUME X SQUARE OF PARTICLE VELOCITY: cm^3 $(fps)^2$

Figure 69. Average Target Volume Loss per Single Particle Impact (Ev) Versus $V_p\mu^2$.

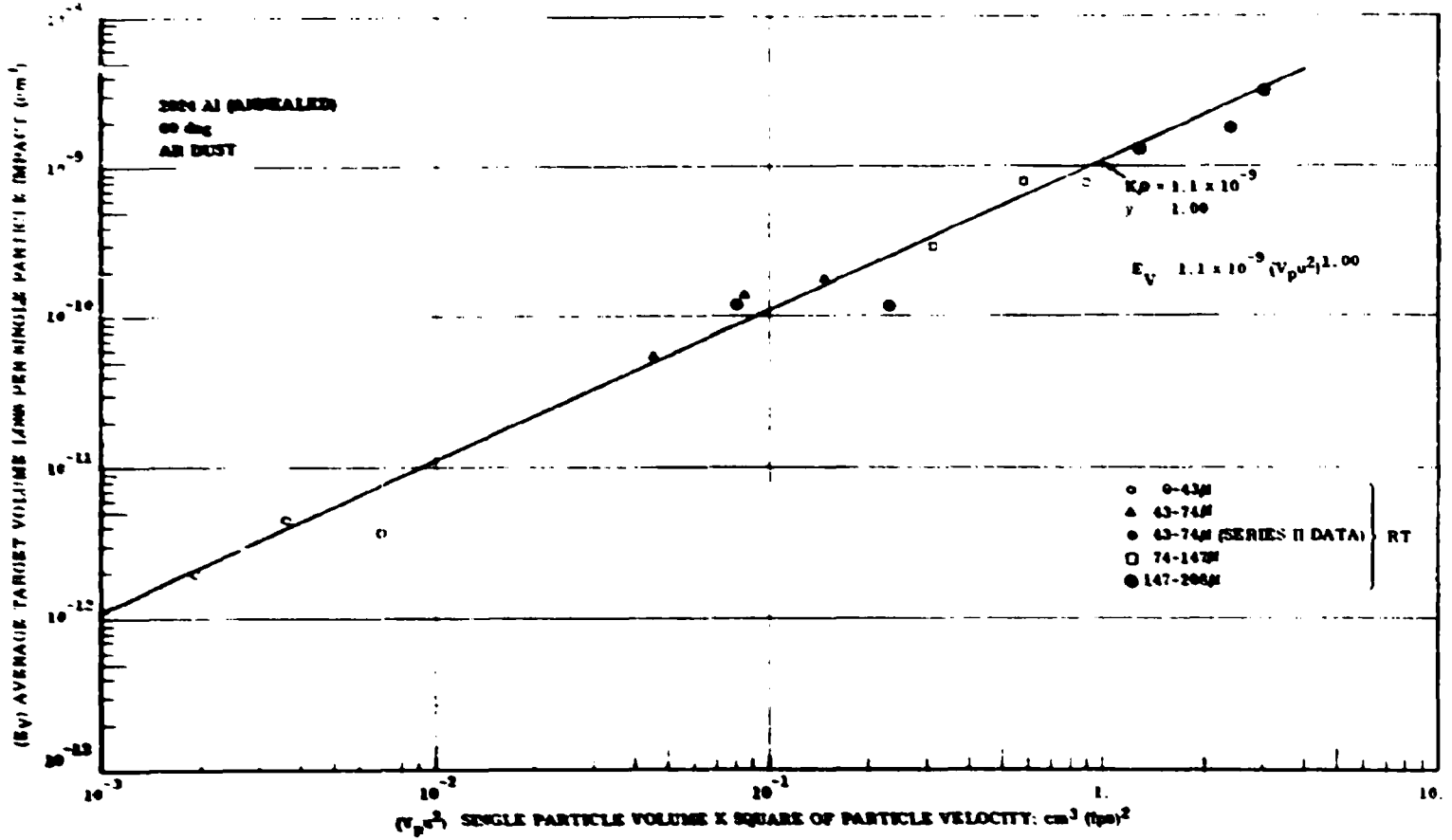

Figure 70. Average Target Volume Loss per Single Particle Impact (E_V) Versus ($V_p u^2$).

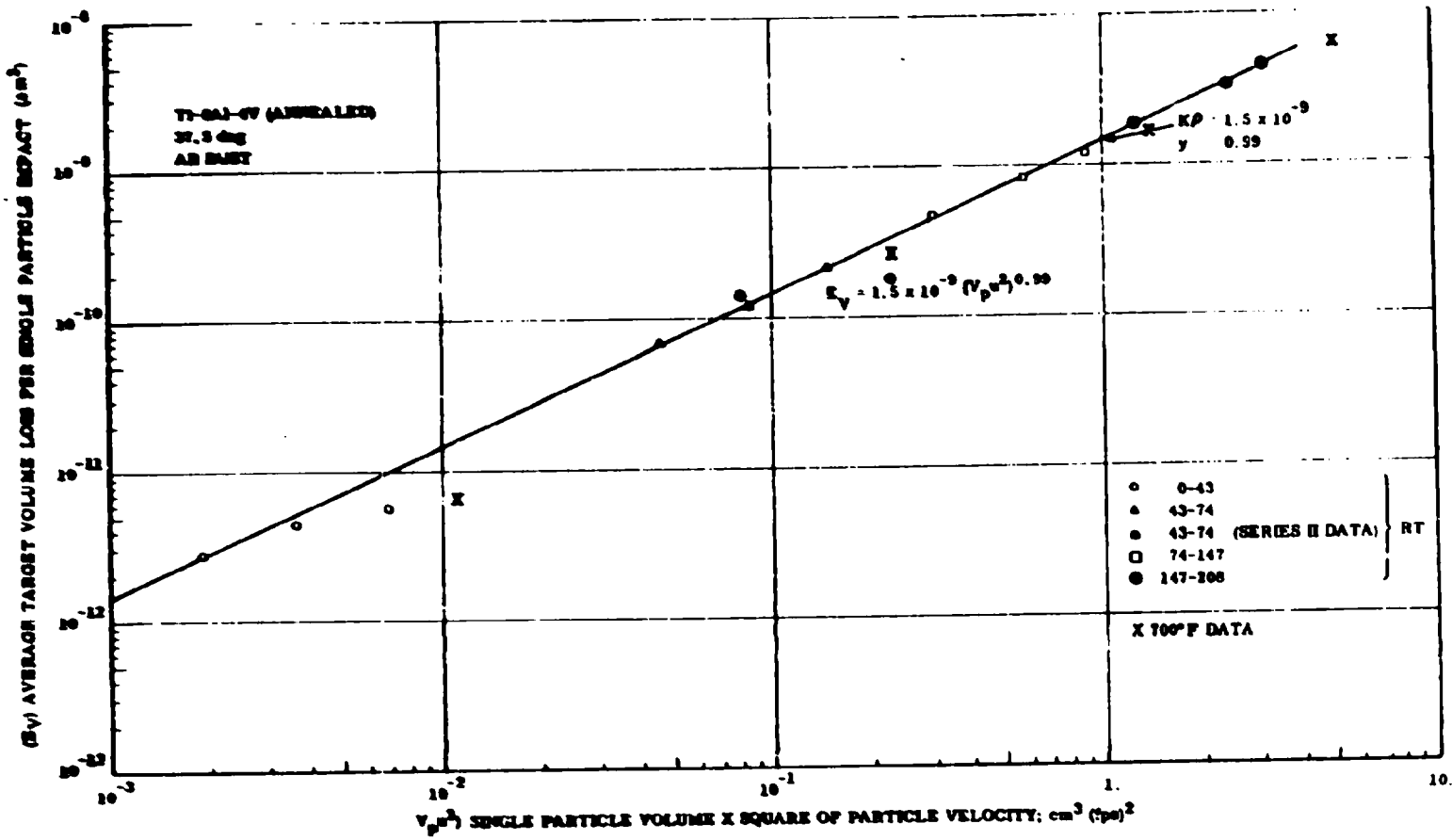

Figure 71. Average Target Volume Loss per Single Particle Impact (Ev) Versus ($V_p u^2$).

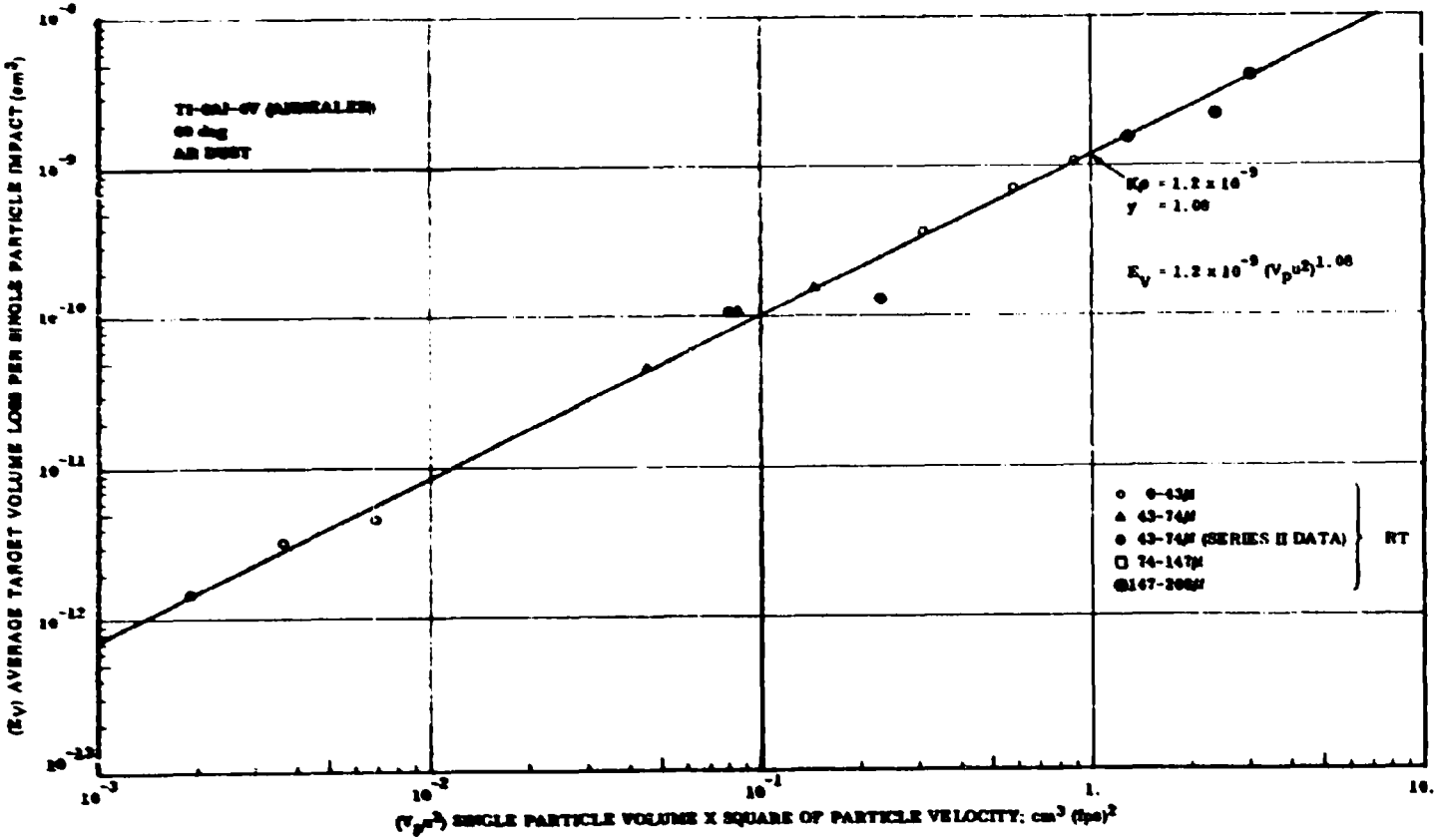

Figure 72. Average Target Volume Loss per Single Particle Impact (E_V) Versus ($V_p u^2$).

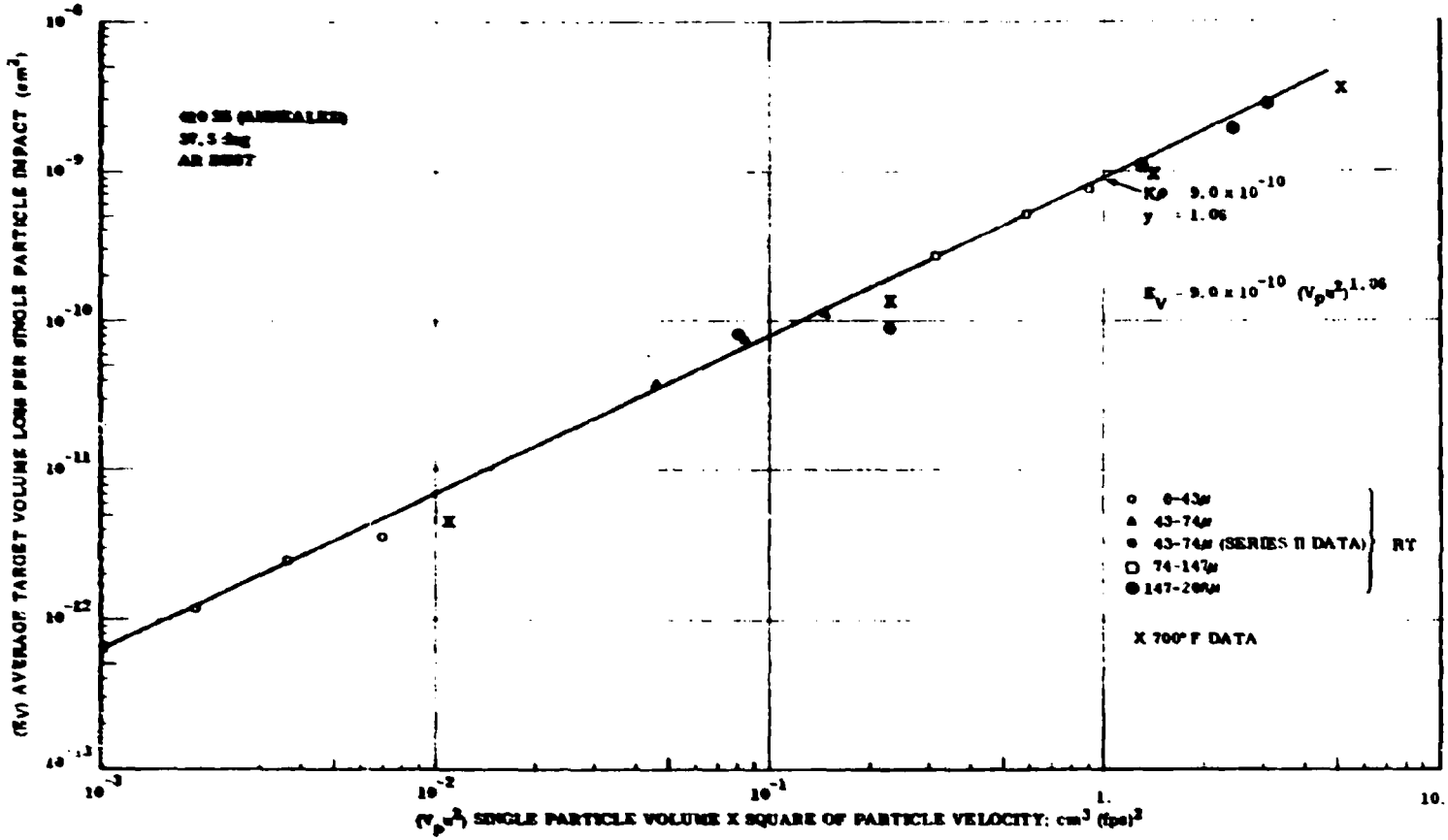

Figure 73. Average Target Volume Loss per Single Particle Impact (E_V) Versus (V_pU^2).

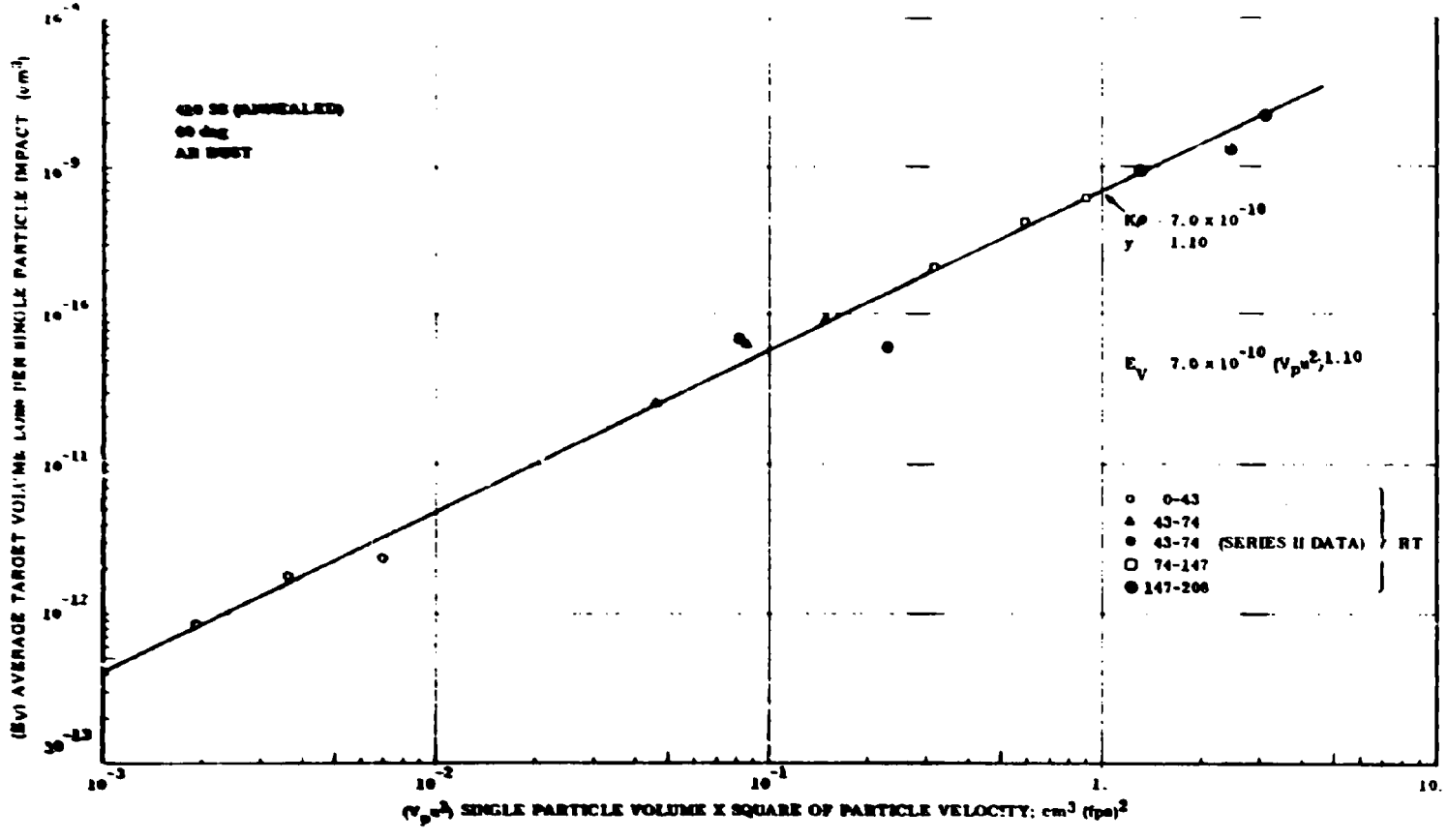

Figure 74. Average Target Volume Loss per Single Particle Impact (E_V) Versus ($V_p u^2$).

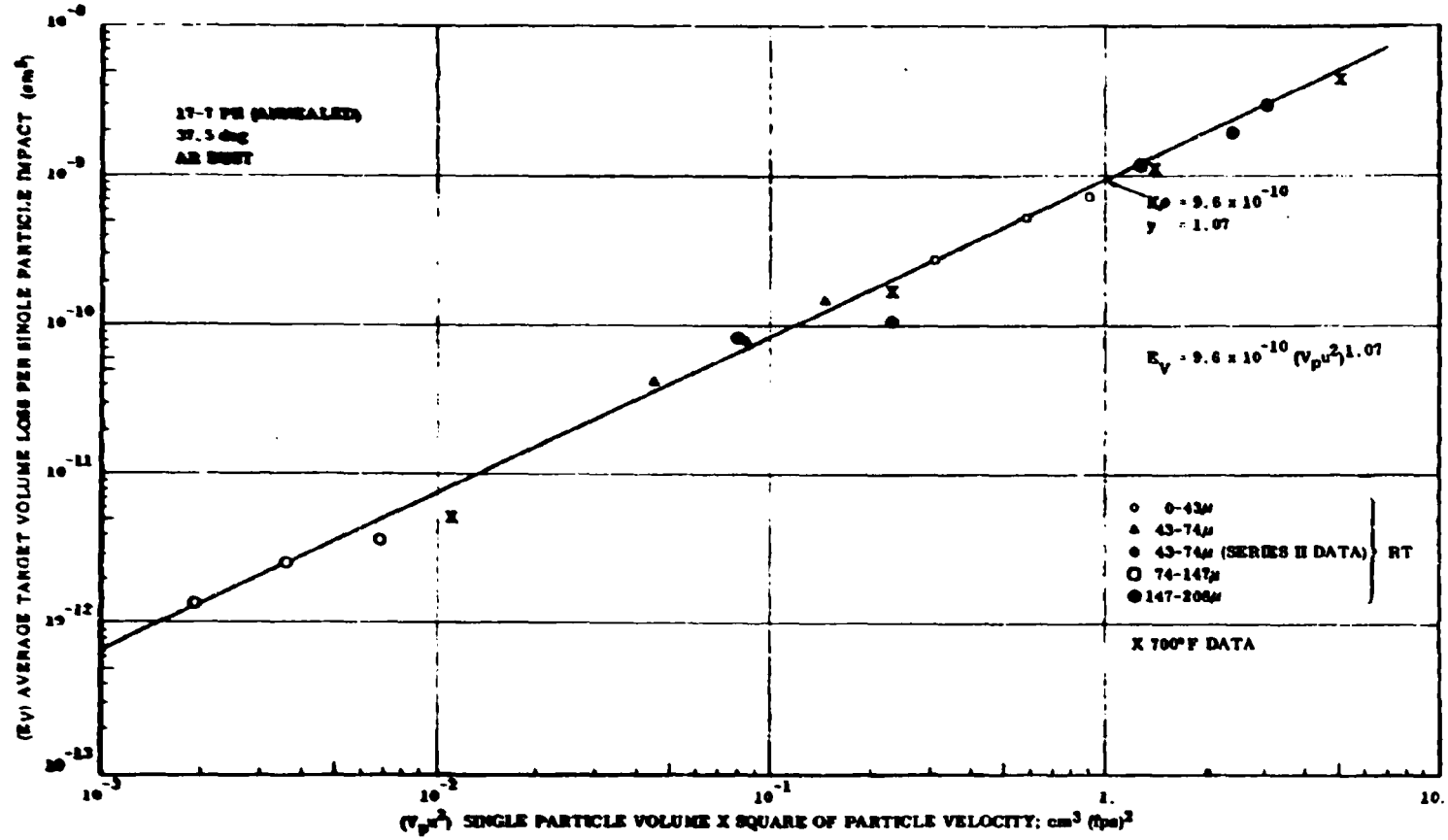

Figure 75. Average Target Volume Loss per Single Particle Impact (E_V) Versus ($V_p u^2$).

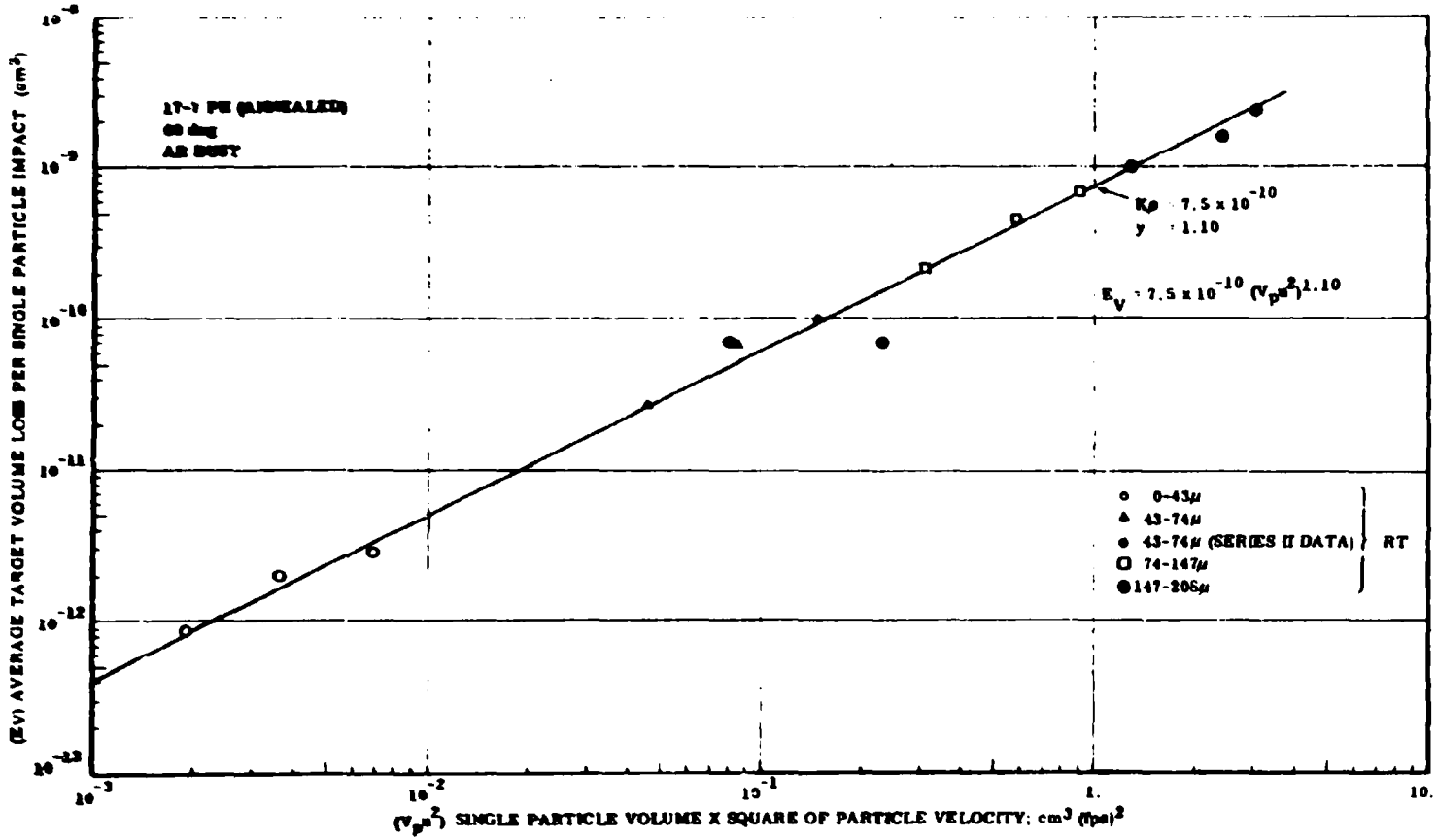

Figure 76. Average Target Volume Loss per Single Particle Impact (EV) Versus $(V_p u^2)$.

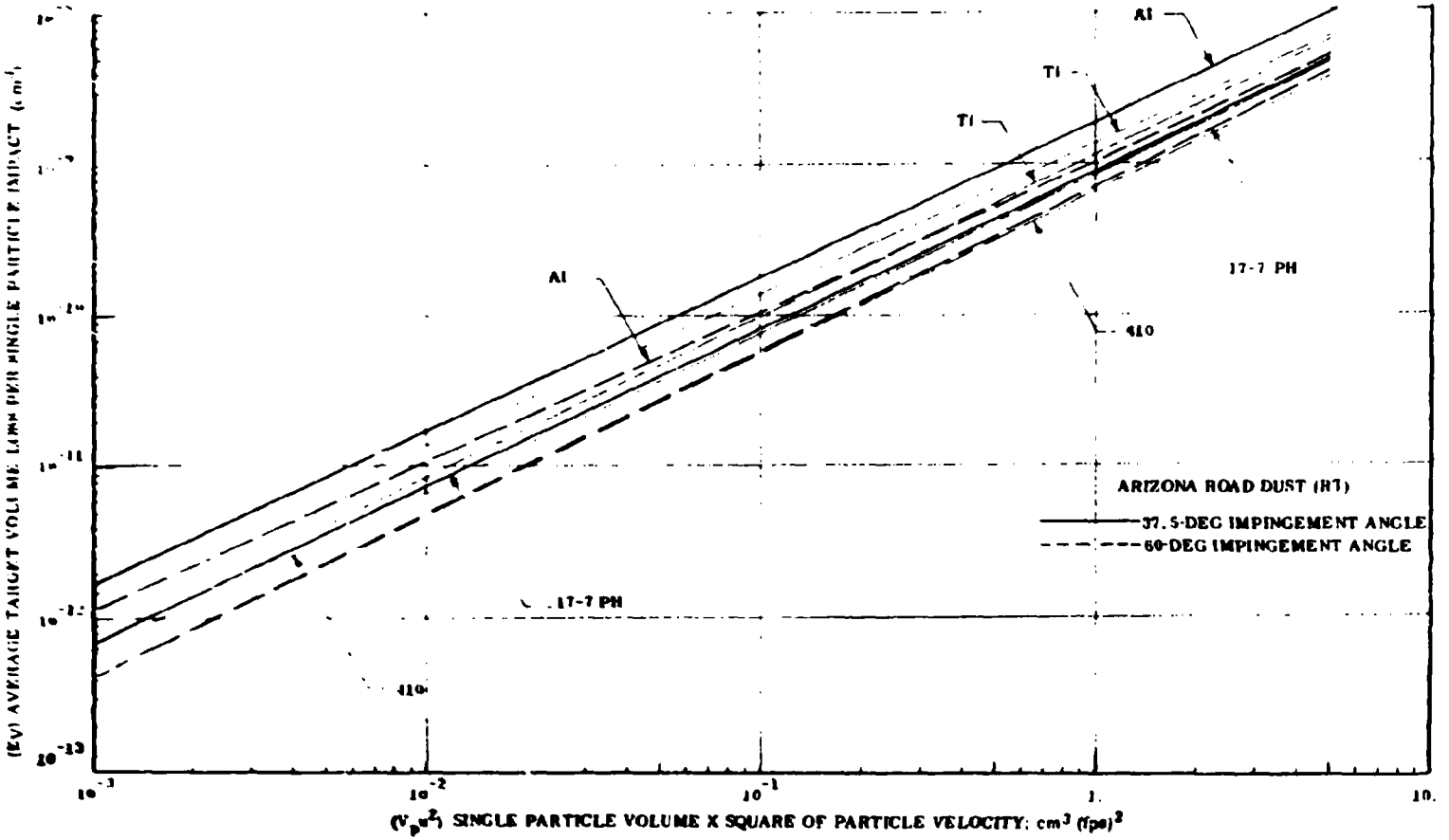

Figure 77. Plots of Ev Versus $V_p u^2$ for all Target Material and Impingement Angle Combinations.

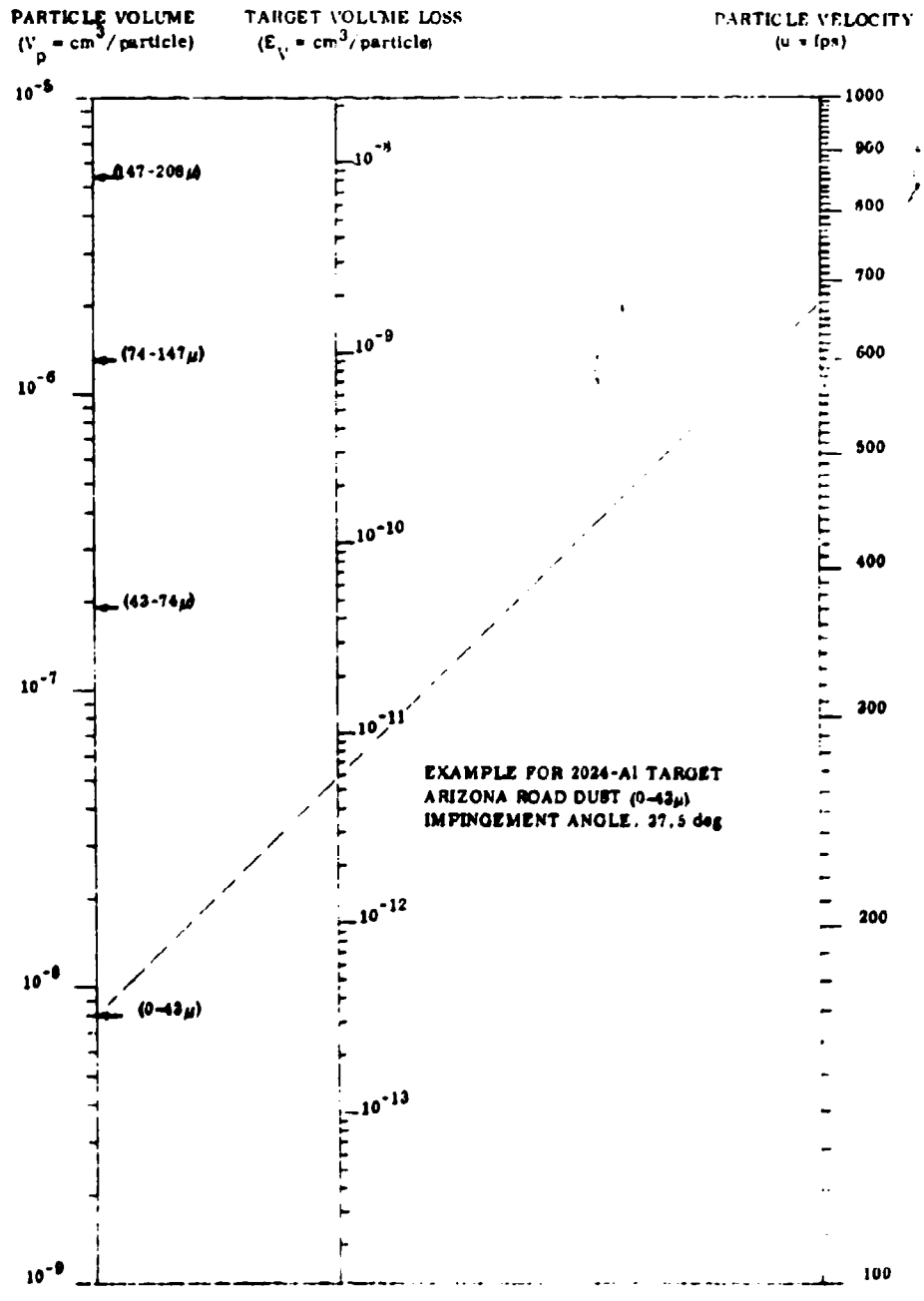

Figure 78. Nomograph Relating V_p, u, and E_V for the 2024 Al Target.

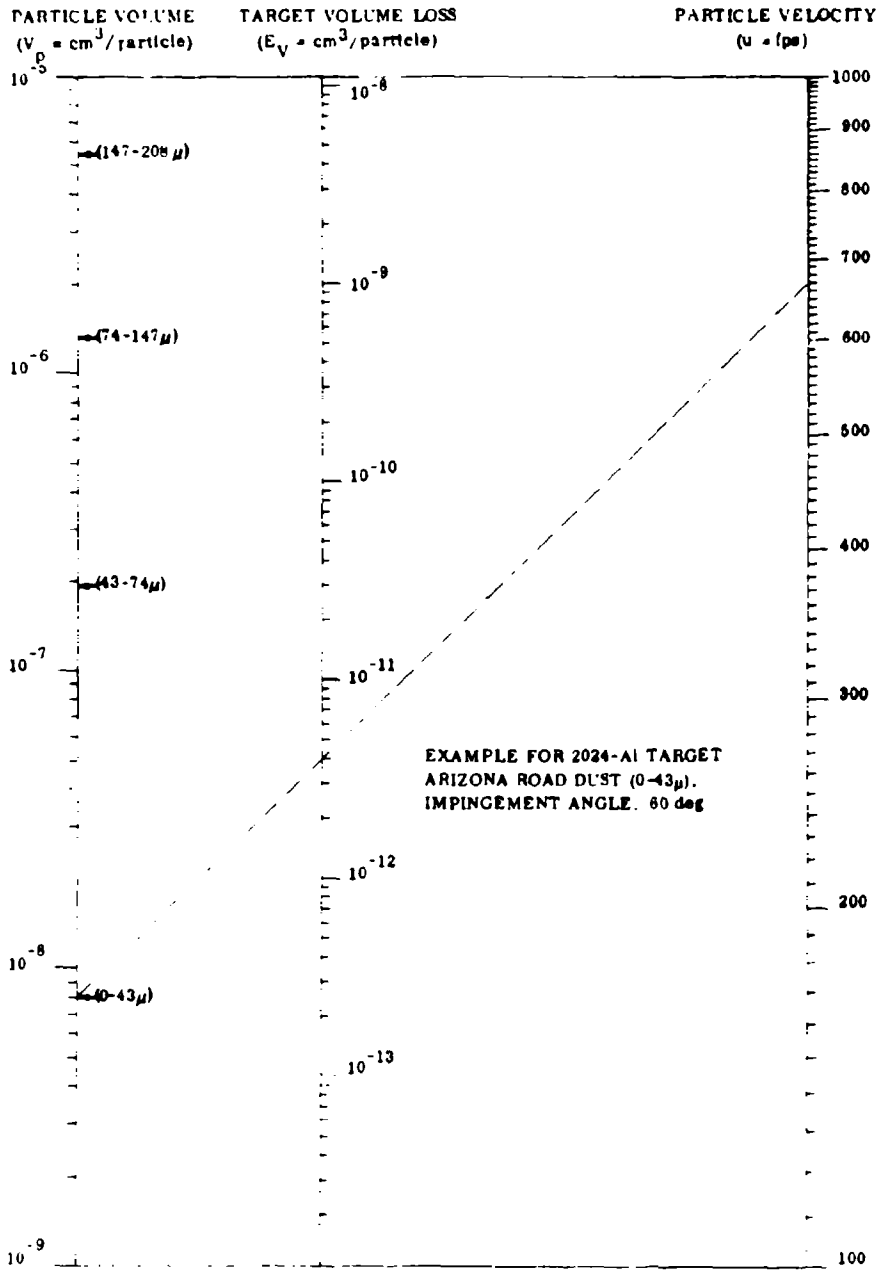

Figure 79. Nomograph Relating V_p, u, and E_V for the 2024 Al Target.

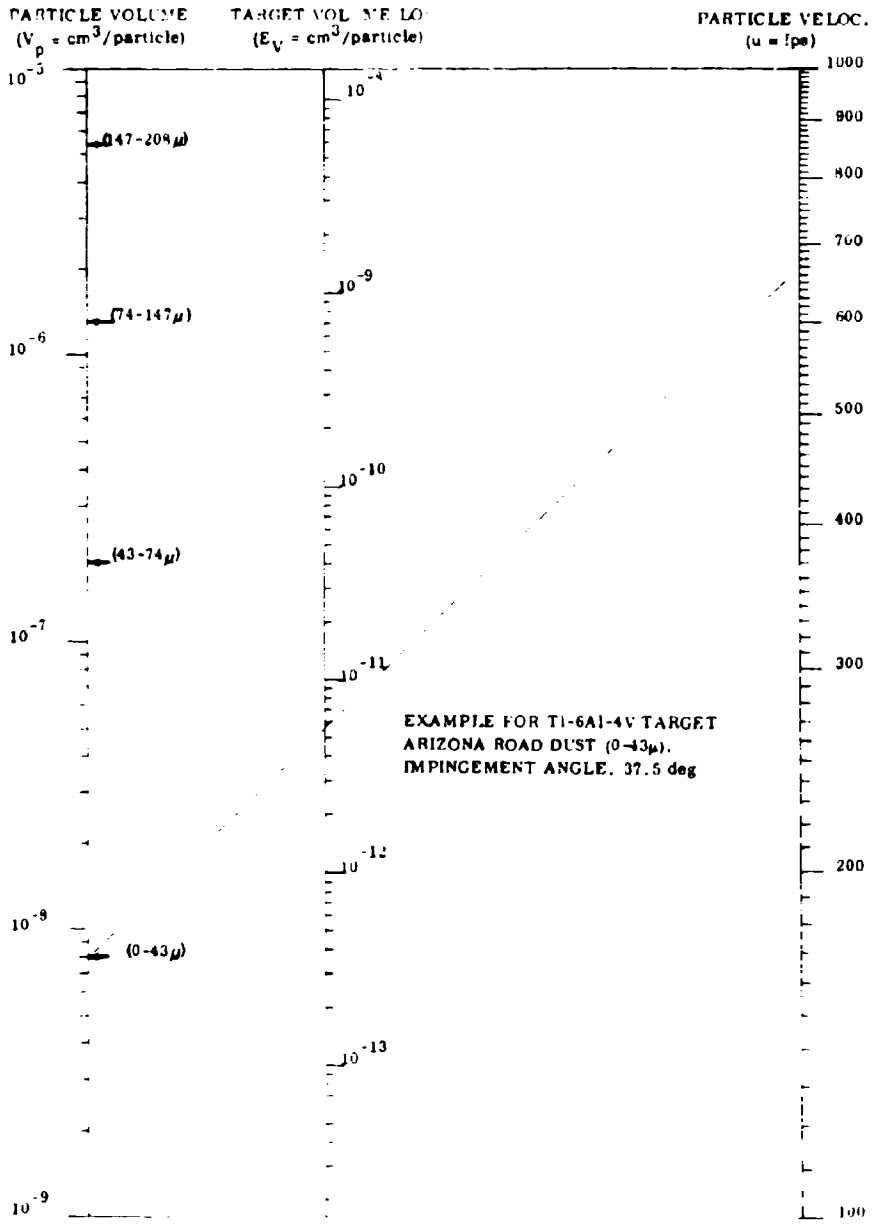

Figure 80. Nomograph Relating V_p, u, and Ev for the Ti-6Al-4V Target.

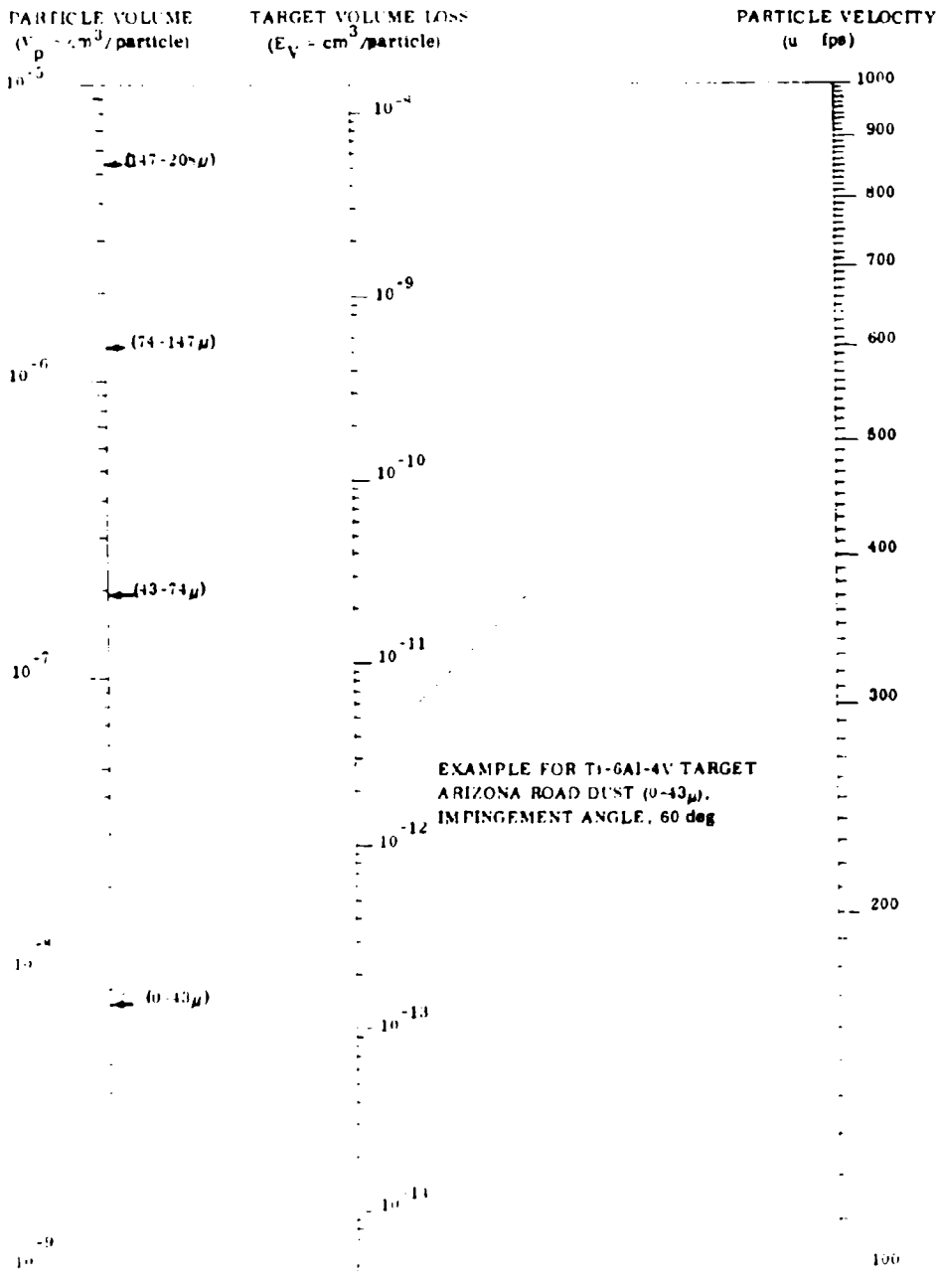

Figure 81. Nomograph Relating V_p, u, and E_V for the Ti-6Al-4V Target.

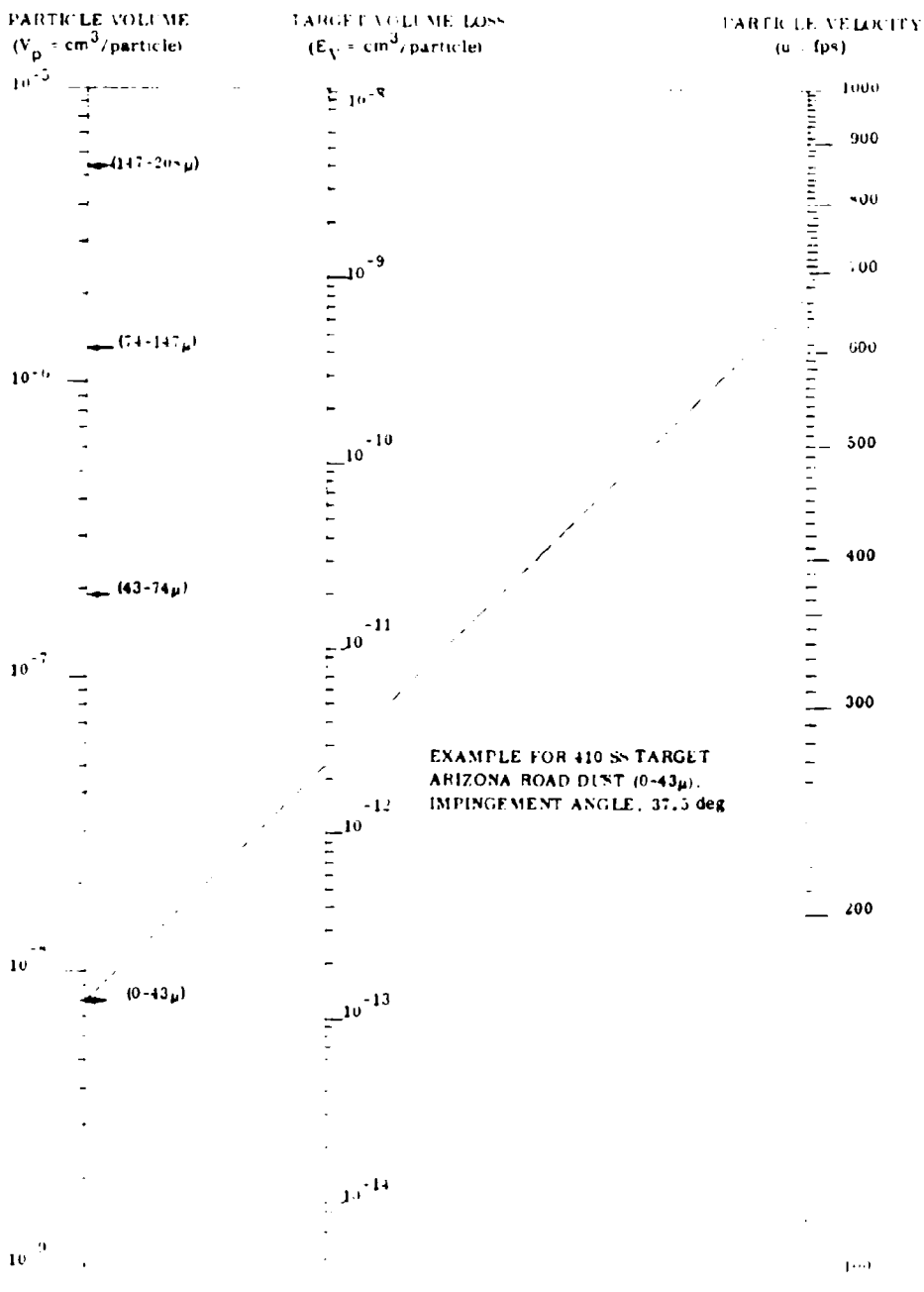

Figure 82. Nomograph Relating V_p, u, and E_V for the 410 SS Target.

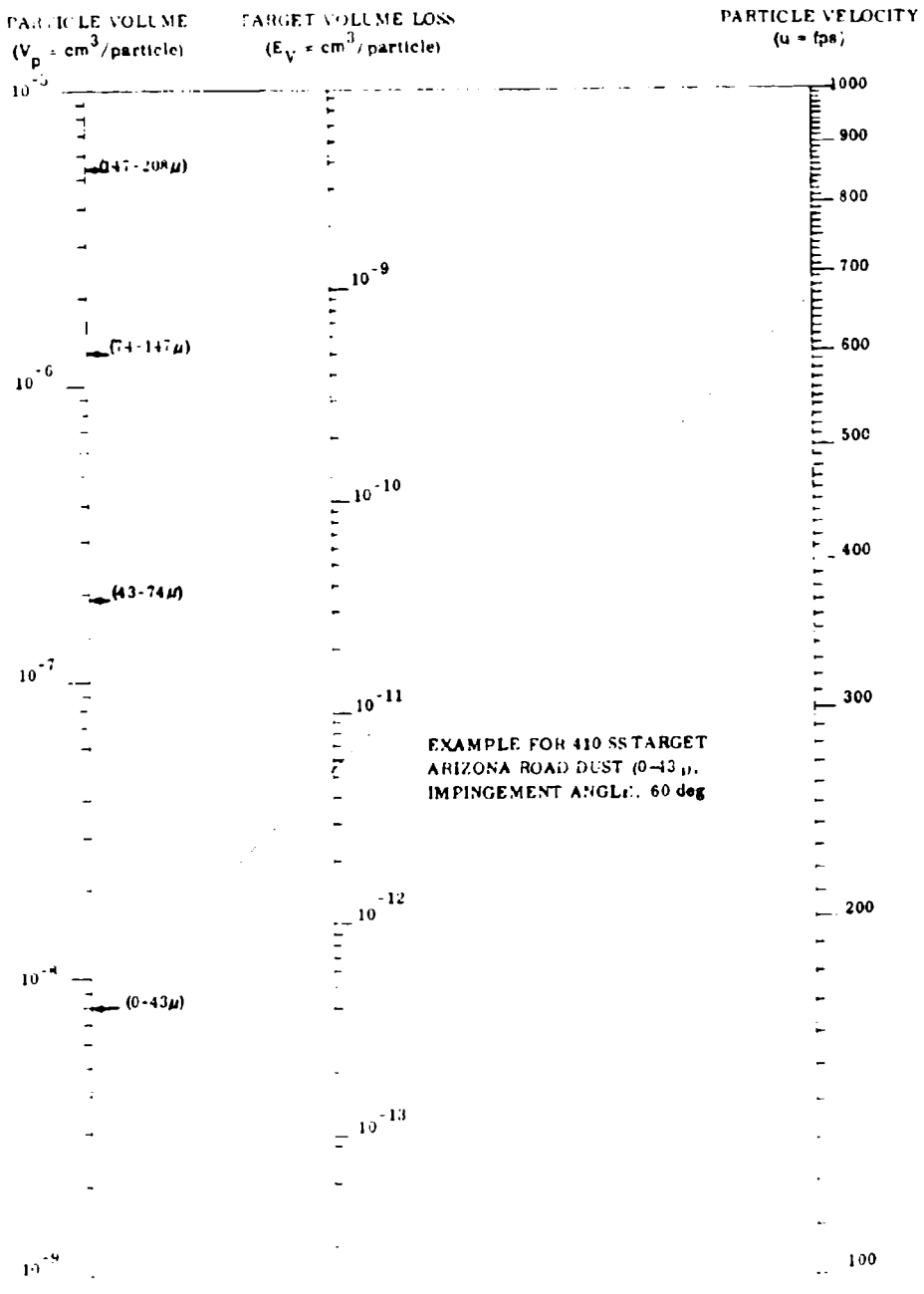

Figure 83. Nomograph Relating V_p, u, and E_V for the 410 SS Target.

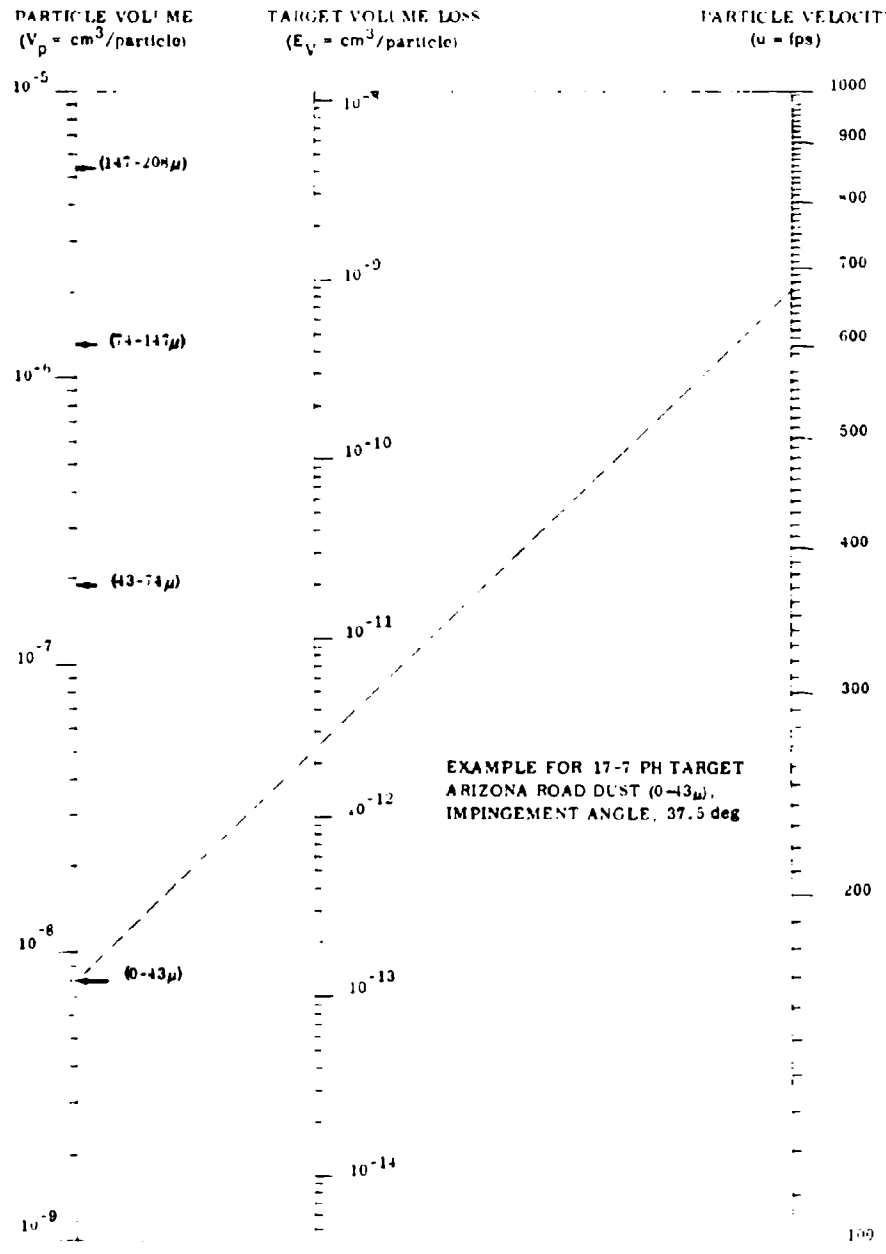

Figure 84. Nomograph Relating V_p, u, and E_V for the 17-7 PH Target.

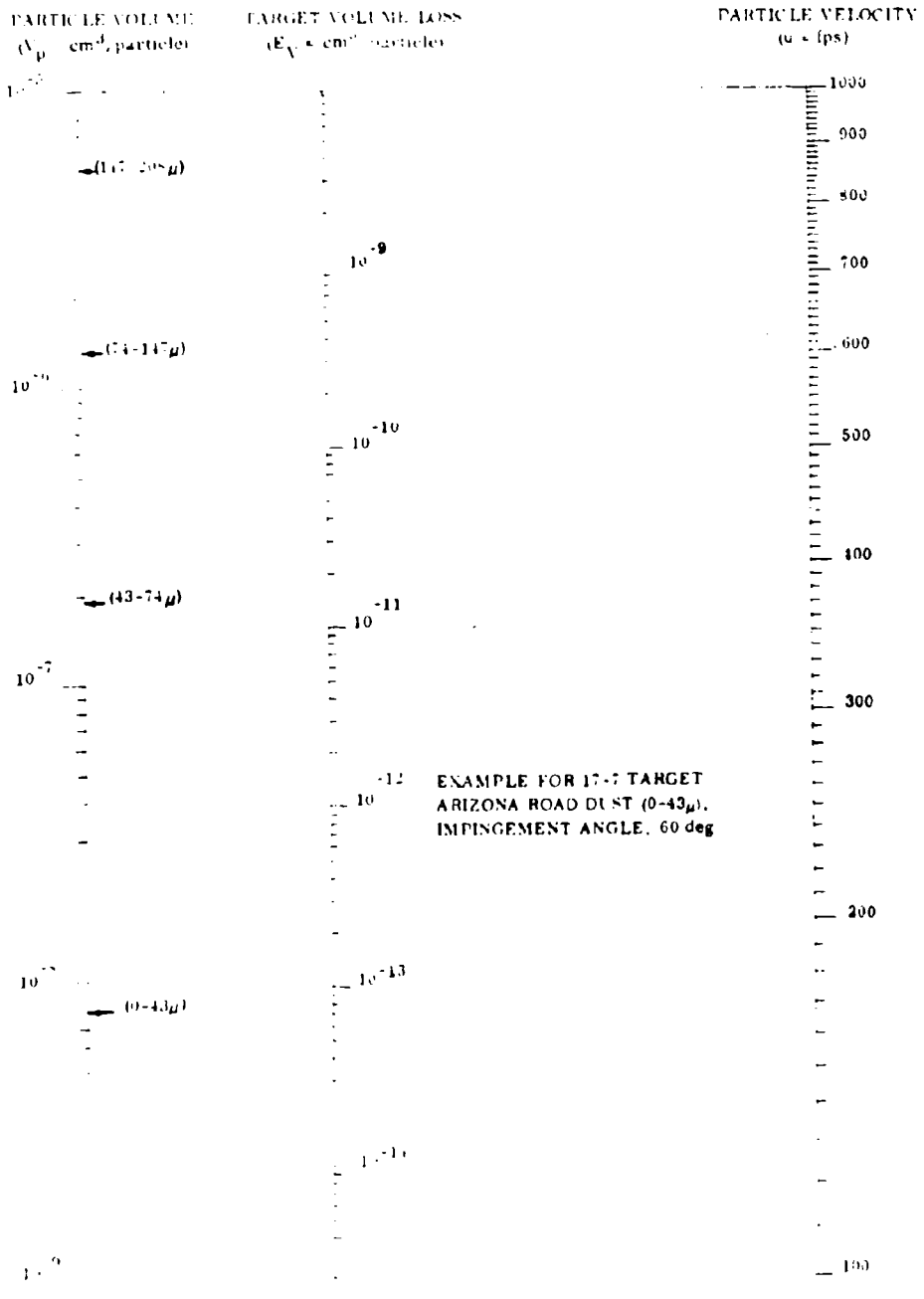

Figure 85. Nomograph Relating V_p, u, and E_V for the 17-7 PH Target.

It is apparent that erosion loss per particle is proportional to each particle's kinetic energy for all the particle sizes (range of ≈10-200-microns), impingement angles (37.5 and 60 degrees) and target alloys evaluated. This is remarkable, especially when considering that particle volume and mass range through 3 orders of magnitude and particle energy ranges through nearly 4 orders of magnitude. No evidence of an erosion threshold at the lower particle energies or particle sizes was discerned; so that even lower velocities and/or particle sizes were found to be necessary to study this phenomenon in subsequent testing.

Data points from Series II work (43-74-micron particle size) have been superimposed on the curves of E_V versus $V_p u^2$ (Figures 69 through 76). Although all the Series II data conform reasonably well to the average curves, the lower velocity points tend to fall above the line, while the higher velocity points tend to fall below the line. The lower slope of the line drawn through these two points for every target explains why the velocity exponent ratios (x) calculated in Series II work all were less than 2.0.

Data points for the 700° F erosion tests also were plotted with the room-temperature data in Figures 69 through 76 (37.5-degree impingment). It is evident that the slopes of lines drawn through the 700° F points are essentially the same as those for the room-temperature data, confirming the velocity-squared relation to erosion at 700° F. With the exception of the aluminum alloy target, the curves of best fit for 700° F lie slightly below the RT curves, indicating somewhat decreased erosion losses with increasing temperature. This supports the trend with temperature variation previously noted in Series II.

Most natural-occurring dusts (e.g., Arizona Road Dust and beach sands) owe their erosiveness to a high silica (SiO_2) content, usually ≥50 weight percent (Ref. 24). An apparent exception was the lateritic soil from Vietnam, which has been reputed to be very damaging to helicopter turbines. A sample of laterite soil from Pleiku, Vietnam. was tested in Series III to determine the influence of particle mass, size, and energy on erosion characteristics for a low-silica dust. The red-brown Pleiku soil has been analyzed, and it is comprised of 80-90 percent clay minerals (principally hydrous oxides and silicates of aluminum and iron), with the balance predominantly quartz (SiO_2) and feldspars. The clay minerals of the laterite occur in the form of aggregate particles, ≈30-500 microns, each aggregate made up of collodial-size constituent particles. After decontamination by baking for 24 hours at 400° F, samples of Pleiku laterite for Series III testing were readily classified by a dry sieving method at Solar into particle-size fractions equivalent to those employed for the Airzona Road Dust classification:

Particle Size Range (μ)	Sieve Sets
-43	-325 mesh
-74/+43	-200 mesh/+325 mesh
-147/+74	-100 mesh/+200 mesh
-208/+147	- 65 mesh/+100 mesh

Even after oven baking at 400°F, the two finer fractions of laterite soil showed a marked tendency toward caking and bridging under light pressure, and were impossible to meter into the erosion tester using the Giannini powder feeder. Much better results were obtained using the gravity feeder developed at Solar (Appendix III). Preliminary room-temperature erosion testing with the finest fraction (-43 micron) showed an interesting tendency for the laterite dust to stick to the target erosion surfaces, apparently protecting the targets from measurable erosion damage.

Density determinations made upon various fractions of Pleiku laterite resulted in very uniform densities, as might be expected for aggregates made up of common (collodial) constituents. Curiously, the density for Pleiku laterite also proved to be similar to the measured density for Arizona Road Dust. A standard pycnometric method was employed.

Fraction	Density (, m./cc)
Pleiku laterite (0-43μ)	2.39
Pleiku laterite (43-74μ)	2.42
Pleiku laterite (74-147μ)	2.44
Pleiku laterite (147-208μ)	2.40
Arizona Road Dust (Coarse)	2.41

The essentially identical densities enabled a direct comparison of the relative erosion potentials of Pleiku laterite versus Arizona Road Dust, at equivalent particle velocities and particle energy levels. Room-temperature erosion testing in triplicate was initiated with laterite test dust, following the initial format previously employed for Arizona Road Dust (see Table XVII). It was soon apparent that, at low and intermediate particle velocities of 488 and 670 fps, the 0-43μ, 43-74μ, and 74-147μ fractions of laterite soil were causing no measurable erosion on any of the program target materials (Table XVIII). This was true for both 37.5- and 60-degree incidence angles. Examination of the target surfaces showed that all were covered with a thin, adherent film of laterite dust, possibly adequate to function as a protective layer and prohibit erosion losses. However, polymeric material targets

TABLE XVII. SERIES III TEST FORMAT (PART I)

PLEIKU LATERITE SUBSERIES (α = 37.5° and 60°; N = 5.40 gm)

Temperature (° F)	Particle Size (μ)	Range, Estimated Particle Velocity (fps)	Particle Velocity, Median Particle Size (fps)	Carrier-Gas (Air) Velocity (fps)
RT	0-43	475/500	488	500
		650/685	670	685
		900/950	925	950
	43-74	475/500	488	525
		650/690	670	725
		860/900	880	950
	74-147	475/500	488	570
		650/690	670	760
		795/865	830	950
	147-208	475/500	488	605
		650/695	670	835
		715/795	755	950

frequently behave similarly, simultaneously picking up dust as well as suffering erosion losses at the target surface, so that a net erosion loss becomes evident only after considerable sequential testing of the same target, by measuring cumulative weight changes. It was decided to carry out 10 sequential erosion tests on both an aluminum alloy target and a 410 stainless steel target at the highest programmed particle velocity (830 fps for 74-147μ particles) for a total dust impingement weight of 54.0 grams per specimen. The next to largest aggregate size (74-147μ) was selected to minimize the probability that the collodial size constituents, making up each aggregate particle, would be diverted from the target surface by carrier-gas streamlines prior to impact. The test results are shown in Figure 86. After bombardment with laterite in the thermally decontaminated condition

TABLE XVIII. RESULTS OF RT EROSION TESTS WITH PLEIKU LATERITE

Target Alloy	Average Particle Velocity, m/s	Mean Particle Velocity, m/s	Impingement Angle, °	Mass Loss, mg	Erosion Weight Change, mg
2024-T3	244	244	90	1	
7075-T6					
410 SS					
17-7 PH	0	0		0	
2024-T3	244			1	
7075-T6					
410 SS					1
17-7 PH	0	0		0	
2024-T3	244	244		1	1
7075-T6					
410 SS					
17-7 PH	0	0		0	
2024-T3	244	244		1	1
7075-T6					
410 SS					
17-7 PH	0	0		0	
2024-T3	244	244		1	
7075-T6					
410 SS					
17-7 PH	0	0		0	

(24 hours at 400°F, in air) as in previous tests, both the aluminum and stainless steel targets rapidly picked up initial films of test dust (1.0 mg and 1.5 mg, respectively) and then stabilized at constant dust film weights (0.9 mg and 1.3 mg, respectively) after the second or third erosion test. The dust films appeared to be continuous on visual examination (30X), and were rather tenacious, based on a simple fingernail scratch test. Because the film was more readily removed with acetone than distilled water, it was reasoned that an organic constituent in the jungle soil might be acting as a binder and adhesive agent. To check this possibility, a sample of laterite was baked in 750°F air for 2 hours prior to erosion testing. This bake resulted in an ≈10 percent weight loss, about half of which was a permanent loss, presumably the distillation or burning of organic material. (The half that was restored in about 1-2 days of RT aging was assumed to be water of hydration.)

Sequential erosion testing of the aluminum alloy with the laterite baked at 750°F (the highest temperature likely to be encountered in a turbine compressor) yielded practically the same result as with decontaminated laterite; i.e., no indication of erosion losses (Figure 86). However, this test demonstrated that the lack of erosion is probably due to the low inherent erosiveness of the laterite under the test conditions cited, rather than to a protective film, inasmuch as no continuous films were formed with laterite baked at 750°F. (Instead of films, discontinuous patches of lightly adherent, powderly occlusions were noted.) It should be mentioned that examination of spent dust (during and after testing) revealed that all laterite aggregates disintegrate on impacting the target, forming a dense cloud of very fine constituent particles in the test chamber.

It was not clear why the laterite in Series III tests seemed innocuous, while the laterite ingested into compressors in Vietnam was reported to be quite erosive. The low erosiveness of Pleiku laterite might have been predicted from its low quartz content (≈5-10%). However, electron microscopic examination of Pleiku laterite and the red-brown laterite dust collected from erosion-damaged turbines (Vietnam) indicated that the two laterites are identical in appearance and makeup. It was thought that the submicron-size constituent particles in laterite might require a high energy level to activate an erosion mechanism, and that the low-to-intermediate particle velocities tested to this point could be below the threshold level for erosion. To check this possibility, additional sequential tests with laterite in air carrier gas were conducted at higher particle velocities (1050 and 1100 fps) and at elevated temperature (700°F) (see Table XIX). The common result with both 43-74-micron and 74-147-micron fractions (750°F, bake) was appreciably increased dust film formation on all target surfaces, particularly 410 stainless steel. In spite of the heavy surface films, the targets themselves exhibited visible evidence of surface deformation (roughening), appearing to have been sand-blasted. However, there was no target material removal from any specimen even at these high particle velocities (1050 and 1100 fps), sensed either by target weight change or by micrometer measurements of thickness change (after removal of the dust films).

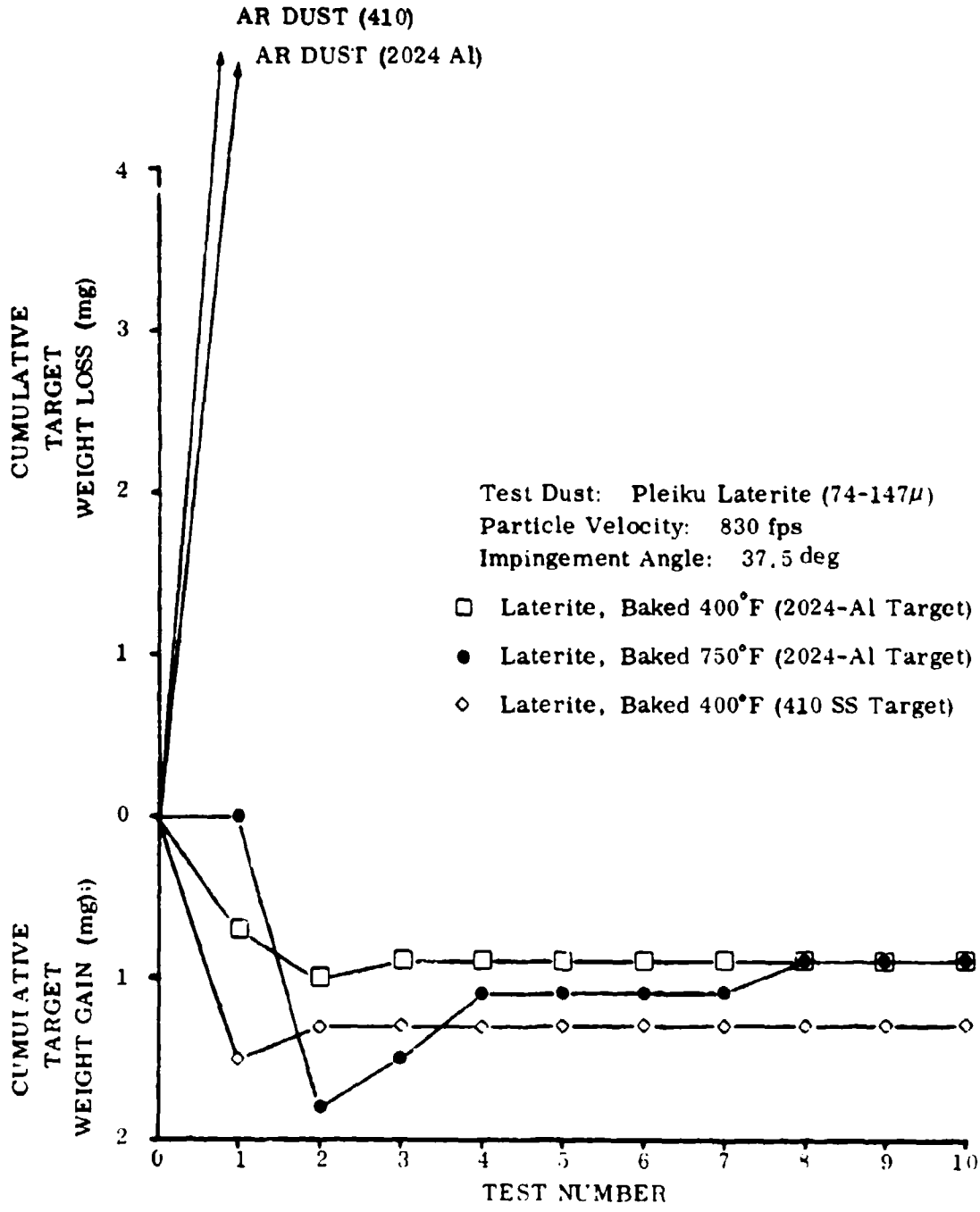

Figure 86. Cumulative Target Weight Changes Following Erosion Tests (RT) With Pleiku Laterite.

TABLE XIX. RESULTS OF 700°F EROSION TESTS WITH PLEIKU LATERITE

Target Alloy	Aggregate Particle Size (μ)	Median Particle Velocity (fps)	Impingement Angle (deg)	Dust Concentration (Nozzle) (mg/ft^3)	Target Weight Change (mg); Same Specimen and Target Area	
					Per Individual Test	Cumulative
2024 Al (Annealed)	43-74	1100	37.5	40	+ 1.7	+ 1.7
					- 0.8	+ 0.9
					+ 2.8	+ 3.7
					+ 3.3	+ 7.0
					+ 3.1	+ 10.1
					- 1.5	+ 8.6
					- 1.5	+ 7.1
					- 2.3	+ 4.8
					+ 4.1	+ 8.9
					- 0.3	+ 8.6
410 SS (Annealed)					+ 4.3	+ 4.3
					+ 14.0	+ 18.3
2024 Al (Annealed)	74-147	1050			+ 1.1	+ 1.1
					+ 2.6	+ 3.7
410 SS (Annealed)					+ 8.3	+ 8.3
					- 8.7	+ 17.0

The most likely explanation for this situation is that laterite was mistakenly identified as the erosive species. That is, the ubiquitous red-brown laterite dust in Vietnam is ingested into virtually all engines, and because of its strong fouling tendency, leaves a visible trace on compressor blades and vanes. However, this is only evidence that laterite is ingested, not that it is an erosive species. Quite probably, another ingested dust or soil species, not leaving a visible trace, is responsible for the erosion problem.

THE EROSION THRESHOLD STUDY

The objective of this study was to search for and identify specific levels of particle energy ($\propto V_p u^2$) and/or particle mass ($\propto V_p$) above which the erosion mechanism produces erosion at a predictable level and below which the erosion mechanism ceases to function. It was reasoned that the phenomenological study and comparison of erosion surfaces obtained from either side of the threshold values of particle mass

and/or energy should be valuable in constructing a more complete model of the erosion mechanism. Although the concept of an erosion threshold seemed plausible because of the clear relationship between E_V and particle energy ($\propto V_p u^2$) developed in Test Series III, the actual existence of these thresholds had yet to be proven. Previous work over the usual range of $V_p u^2$ encountered in the main experimental program (namely, $\approx 3.0 \times 10^0$ to 2.0×10^{-3} cm^3 $(fps)^2$) failed to uncover any sign of an erosion threshold. The basic test plan employed in the subject study was to conduct standard RT erosion tests in triplicate with the four different particle sizes of Arizona Road Dust (d = 0-43-micron, 43-74-micron, 74-147-micron, 147-208-micron; N = 5.40 grams; impingement angle of 37.5-degrees) and two target materials (410 SS and 2024 Al), with progressively slower particle velocities, to eventually obtain values of $V_p u^2$ about 1-1/2 to 2 orders of magnitude lower (for each particle size) than in prior testing (see Table XX). Assuming that the nearly equiaxed dust grains (predominantly silica) are actually cubic particles, the single-particle volumes (V_p) for median-size particles in each fraction are 8.0×10^{-9} cm^3, 1.9×10^{-7} cm^3, 1.3×10^{-6} cm^3, and 5.4×10^{-6} cm^3, respectively.

The erosion threshold study also provided considerable additional data with which to check the E_V (volume erosion loss per particle) versus $V_p u^2$ ($\propto$kinetic energy per particle) relation developed in Series III. The 410 SS target was investigated first. Although all of the erosion data taken together (E_V versus $V_p u^2$; see Figure 87) produces a rather narrow band which conforms well to the original relation described in Series III, namely

$$E_V = K\rho(V_p u^2)^{1.0}, \qquad (12)$$

the curve for each particle size range is distinctly separate within the data band (Figure 87). In other words, the value of E_V for the 410 SS target appears to be determined not only by the level of particle energy, but by the particle size as well. The larger particles possess somewhat higher erosive potential at equivalent energy levels than the smaller particles. Because the constant particle size curves (comprising a family of four) are all parallel, the ratios of their erosion losses remain constant at any given level of particle energy. For example, the curves indicate that, at equivalent particle energies, the heaviest particle (147-208-micron) will erode $\approx$1.6 times more than the 74-147-micron particle, $\approx$2.8 times more than the 43-74-micron particle, and $\approx$4.6 times more than the finest particle 0-43-micron. A good test confirmation of the first two ratios can be obtained at a $V_p u^2$ value of 1.8×10^{-1} (cm^3 fps^2); see Table XX.

For the 410 SS target, it was calculated that the average volume erosion loss per single particle impact (E_V) is reduced systematically with both decreasing particle energy ($\propto V_p u^2$) and/or particle size (d) according to the relation

TABLE XX. TEST PARAMETERS, EROSION THRESHOLD STUDY (RT Air)

Dust Variety	Particle Size (μ)	Impingement Angle (degrees)	Dust Concentration (mg /ft^3)	Test Period (sec)	Carrier-Gas Velocity (fps)	Median-Particle Velocity (fps)	Particle Energy Parameter $V_p u^2$ (cm^3 fps^2)	E_V (cm^3-particle of SiO_2) 410 SS	E_V (cm^3-particle of SiO_2) 2024-Al
AR Dust (70% SiO_2)	0-43	37.5	40	1000	420	415	1.4×10^{-3}	8.9×10^{-13}	2.0×10^{-12}
				1340	320	320	8.2×10^{-4}	6.0×10^{-13}	1.1×10^{-12}
				1870	245	245	4.8×10^{-4}	2.0×10^{-13}	3.7×10^{-13}
				2540	178	178	2.5×10^{-4}	1.3×10^{-13}	1.9×10^{-13}
				3700.	110	110	9.7×10^{-5}	0.0	0.0
AR Dust (70% SiO_2)	43-74	37.5	40	1340	320	305	1.8×10^{-2}	1.5×10^{-11}	3.5×10^{-11}
				2350	185	182	6.3×10^{-3}	5.9×10^{-12}	9.9×10^{-12}
				3700	110	110	2.3×10^{-3}	3.0×10^{-12}	5.0×10^{-12}
AR Dust (70% SiO_2)	74-147	37.5	40	1000	420	370	1.8×10^{-1}	1.9×10^{-10}	3.9×10^{-10}
				1710	260	233	7.1×10^{-2}	5.4×10^{-11}	1.3×10^{-10}
				3370	125	117	1.8×10^{-2}	2.7×10^{-11}	3.2×10^{-11}
AR Dust (70% SiO_2)	147-208	37.5	40	788	550	443	1.1×10^{0}	1.5×10^{-9}	3.5×10^{-9}
				1175	365	296	4.7×10^{-1}	6.9×10^{-10}	1.6×10^{-9}
				1920	220	180	1.8×10^{-1}	3.1×10^{-10}	5.2×10^{-10}
				2540	178	148	1.2×10^{-1}	9.4×10^{-11}	2.6×10^{-10}
				3700	110	95	4.9×10^{-2}	2.3×10^{-11}	1.1×10^{-10}
MS-30 (100% SiO_2)	9.5	37.5	40	788	540	540	2.5×10^{-4}	1.2×10^{-13}	2.6×10^{-13}
				1340	320	320	8.6×10^{-5}	3.5×10^{-14}	4.6×10^{-14}
				2540	178	178	2.7×10^{-5}	1.1×10^{-14}	3.2×10^{-14}
				3700	110	110	1.0×10^{-5}	6.3×10^{-15}	0.0
MS-15 (100% SiO_2)	4.5	37.5	40	410	950	950	9.0×10^{-5}	3.7×10^{-14}	6.9×10^{-14}
				788	550	550	3.0×10^{-5}	9.0×10^{-15}	2.3×10^{-14}
				2540	178	178	3.2×10^{-6}	3.2×10^{-16}	4.5×10^{-16}
				3700	110	110	1.2×10^{-6}	1.6×10^{-16}	0.0
MS-10 (100% SiO_2)	3.1	37.5	40	788	550	550	1.1×10^{-5}	4.1×10^{-15}	9.6×10^{-15}
				1340	320	320	3.6×10^{-6}	5.3×10^{-16}	1.9×10^{-15}
				2540	178	178	1.1×10^{-6}	6.7×10^{-17}	1.9×10^{-16}
				3700	110	110	4.2×10^{-7}	0.0	0.0
MS-5 (100% SiO_2)	1.3	37.5	40	788	550	550	6.0×10^{-7}	6.3×10^{-17}	3.0×10^{-16}
				1340	320	320	2.1×10^{-7}	1.6×10^{-17}	4.6×10^{-17}
				2540	178	178	6.4×10^{-8}	0.0	0.0

$$E_V = K_d (d)^q (V_p u^2)^y = 2.3 \times 10^{-8} (d)^{.73} (V_p u^2)^{.84} \qquad (13)$$

where $K_d = K/d^q$ = system constant excluding the particle size effect

d = dust particle edge dimension (cm); median particle size

V_p = single particle volume (cm^3); median particle size

u = particle velocity (fps); median particle size

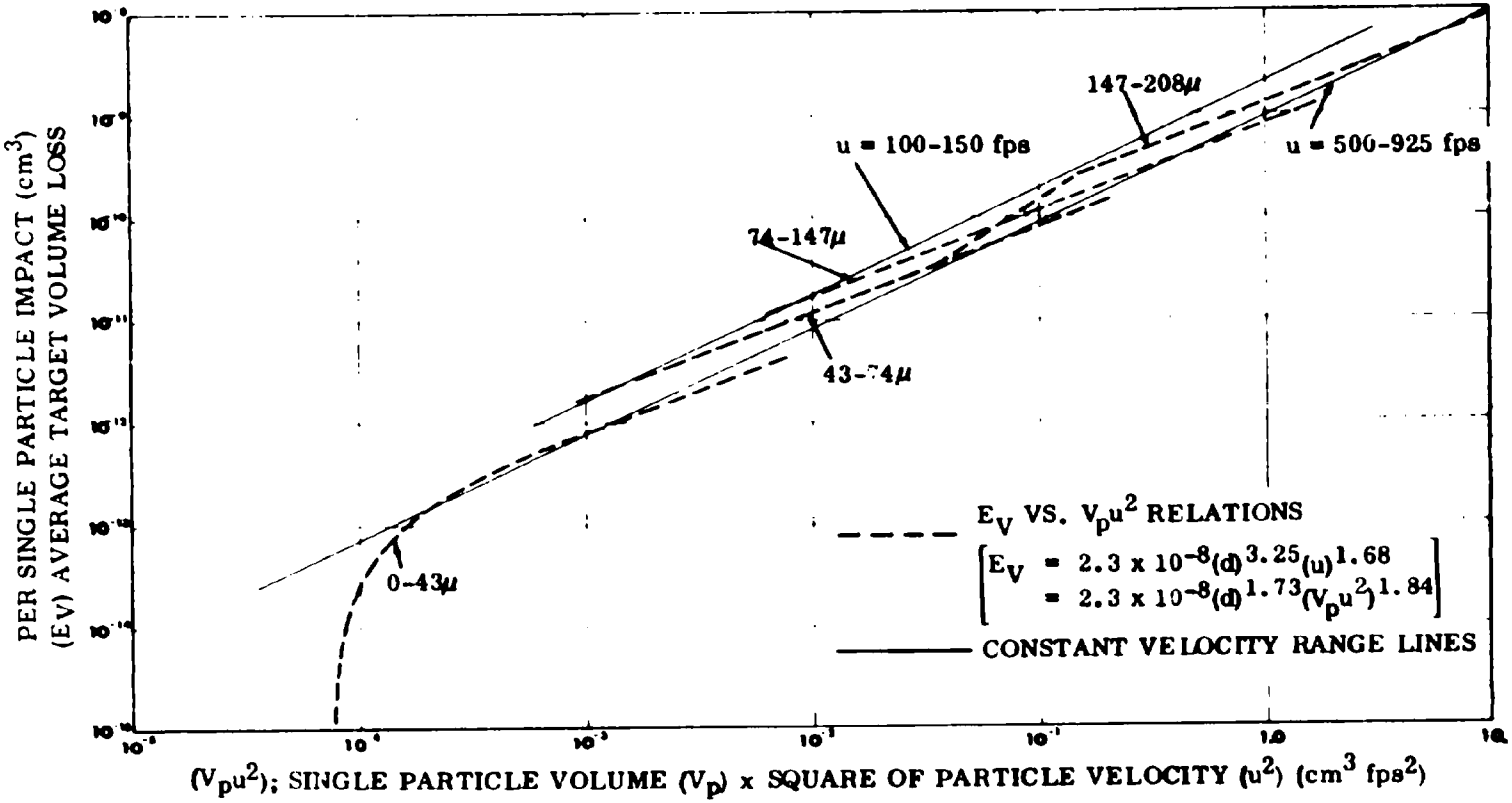

Figure 87. Plot of E_V Versus V_pu^2 for Different Particle Sizes of Arizona Road Dust: 410 SS Target (37.5 Degrees).

Inasmuch as V_p is equal to d^3 (assuming cubic particles), equation (13) can be rewritten as

$$E_V = 2.3 \times 10^{-8} (d)^{3.25} (u)^{1.68} \qquad (14)$$

Another expression that correctly predicts E_V as a function of d, V_p, and u is based on the first two terms of a Taylor Series:

$$\begin{aligned} E_V &= (K_1 + K_2 d)(V_p u^2)^y \\ &= (1.2 \times 10^{-10} + 6.3 \times 10^{-8} d)(V_p u^2)^{0.84} \end{aligned} \qquad (15)$$

where K_1 and K_2 are system constants.

The dependency of E_V on particle size variation (other than its normal involvement as $d^2 = V_p$ in setting the kinetic energy level) was not anticipated from the earlier E_V versus $V_p u^2$ curves that resulted in equation (12). However, it seems likely that (for the 410 SS target) equation (12) actually represents a family of "iso-velocity" curves that intersect the family of constant-particle size curves shown in Figure 87; the intersection points indicate the erosion due to a given particle velocity or narrow range of velocities. This situation became evident when the lower limit of particle velocity was extended to ≈100 fps. Equation (12) can be used to predict erosion levels properly, so long as the system constant, K, is fitted to the specific particle velocity range in question.

For the 410 SS (37.5 degree) example,

Velocity Range (fps)	$K\rho$	y (exponent of $V_p u^2$)
500-925 (Series III)	9.0×10^{-10}	1.06
200-400	1.4×10^{-9}	1.06
100-150	2.0×10^{-9}	1.06

As regards best curve fitting, however, equations (13) and (14) appear better suited for the data produced in the erosion threshold study for 410 SS, because they predict the combined effects of both variable particle size and variable particle energy. A comparison of the exponents for the variables, d,($V_p = d^3$), and u in equations (13) and (14) indicates that equation (14) significantly overrates the influence of the

particle size variable ($d^{3.25}$ instead of $d^{3.0}$) and underrates the influence of the velocity component ($u^{1.68}$ instead of $u^{2.0}$). "Overrating" and "underrating" refer to the arbitrarily selected parameter, $V_p u^2$ ($\propto$particle kinetic energy). For the 2024-Al target, the new data generated within the erosion threshold study did not show any discernible tendency to stratify for the different particle sizes (E_V versus $V_p u^2$; Figure 88). Instead, all of the data, new and old, is best defined by equation (12). The curve of best fit is still the same as given for the original Series III data, except for the value of $K\rho$ (2.5×10^{-9}, instead of 2.0×10^{-9}).

$$E_V = 2.5 \times 10^{-9} (V_p u^2)^{1.04} \qquad (16)$$

All erosion data fit well within a narrow band, formed by varying the $K\rho$ value (equation (12)) between limits of 4.0×10^{-9} and 1.4×10^{-9} (Figure 88). Obviously, the particle size (mass) and particle velocity influences vary somewhat from target to target. Even so, the correlations between E_V and particle kinetic energy ($\propto V_p u^2$) over five orders of magnitude are remarkably good for both the aluminum-alloy and 410 SS targets. The scatter bands for the erosion data (Figures 87 and 88) could undoubtedly be narrowed by switching to more chemically homogeneous test dusts and restricting the range of particle sizes in a given test dust sample (e.g., from 43-74-micron to 55-60-micron). This would enable a more accurate estimate of the average or effective number of particle impacts per test (for E_V calculation), as well as provide a more physically homogeneous test dust with better reproducibility of average particle size, the actual number of particle impacts from test to test, and average particle velocity. For example, N = 5.40 grams of 43-74-micron Arizona Road Dust might contain as many as 2.3×10^7 silica particles, if all were 43-micron, or as few as 3.8×10^6 silica particles, if all were 74-micron. For the E_V calculation, the number of particles used is that corresponding to a uniform sample of the median-particle size (58-micron), or 7.2×10^6 particles.

It should be emphasized that equations (12), (13), (14), (15), and (16) are valid only at energy levels above the threshold energy for activation of the erosion mechanism for the particle size and variety in question. Of perhaps most importance to the mechanism study, erosion thresholds (re: particle energy) were identified for both the 410 SS and the 2024 Al alloy targets (see Figures 87 and 88). For the smallest particle size (0-43-micron), no cumulative erosion losses were recorded for either the 410 SS or the aluminum alloy target followi. 23 and 13 cumulative erosion tests (respectively) at a $V_p u^2$ level of 9.7×10^{-5} (cm^3 fps^2) (see Table XX). This sub-threshold level of $V_p u^2$ corresponds to a particle velocity (u) of 110 fps. At $V_p u^2$ = 2.5×10^{-4} (cm^3 fps^2) and u = 178 fps, erosion resumed at a predictable level for both target alloys. No erosion thresholds were detected for the larger size particles, although a noticeable drop in E_V did occur for the 147-208-micron particles (410 SS target only) at particle velocities below 180 fps (Figure 87).

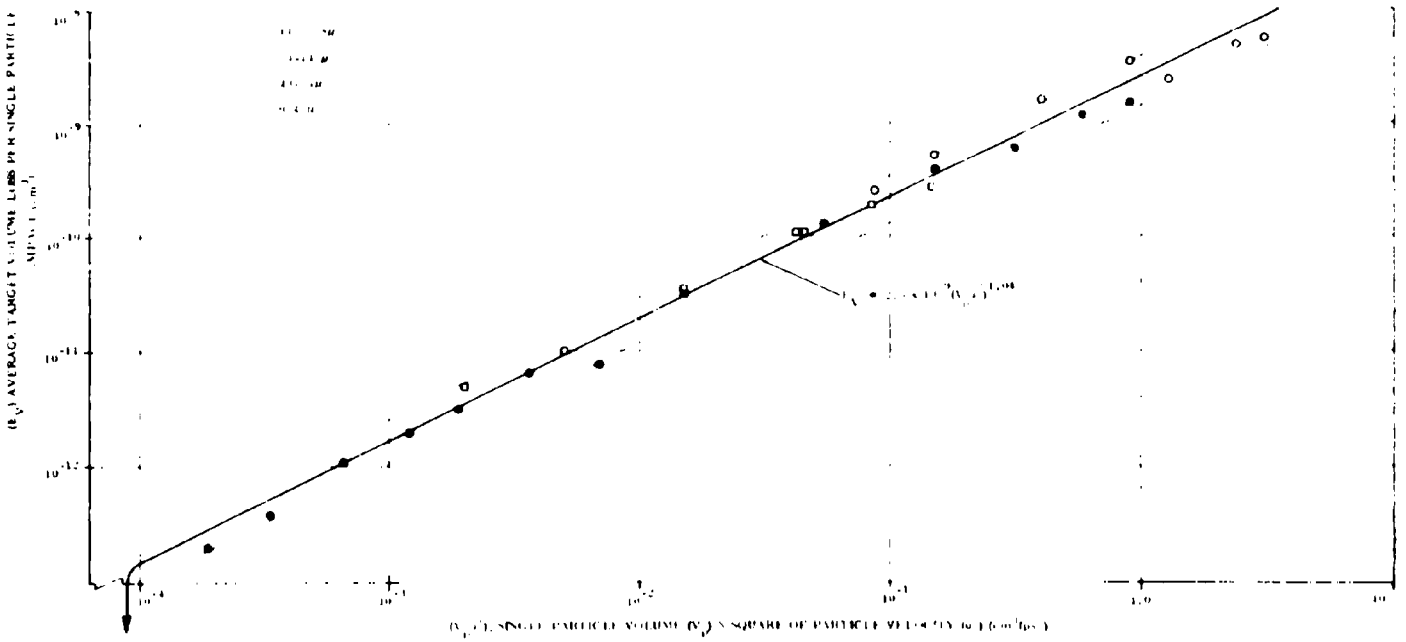

Figure 88. Plot of E_V Versus $V_p u^2$ for Different Particle Sizes of Arizona Road Dust: 2024 Al Target (37.5 Degrees).

The large number of tests run on single specimens resulting in no cumulative erosion losses confirm that erosion thresholds exist with regard to particle energy. The actual thresholds for 410 SS and 2024 Al targets and 0-43-micron Arizona Road Dust occur somewhere between $V_p u^2$ levels of 9.7×10^{-5} and 2.5×10^{-4} (cm^3 fps^2). Visual and electron microscopy examination of the subject erosion surfaces formed just above and just below the erosion thresholds indicates that both experience considerable surface deformation (surface metal movement). This is corroborative evidence that the process of erosion (surface removal) is distinct from that of surface deformation.

It is interesting that erosion losses for the 410 SS target (147-208-micron particles) at $V_p u^2 < 1.8 \times 10^{-1}$ (cm^3 fps^2) (range of u = 95-108 fps) drop somewhat below the levels predicted by equation (14), which may indicate the existence of an erosion threshold for the largest particle size at a particle velocity not too far below u = 95 fps (see Table XX). Erosion thresholds were not detected for the two intermediate particle sizes down to u = 100-117 fps, although it still seems reasonable that thresholds could exist for these particle sizes not too far below 100 fps. Difficulty in accurately measuring the low carrier-gas pressures associated with $u \ll 100$ fps prevented the continuation of the threshold search to even lower particle velocities.

The erosion threshold study was concluded with an investigation of the particle-size effect. The objective was to search for thresholds of erosion related to diminishing particle size, analogous to the particle-energy thresholds already defined.

Very fine silica sand in four different particle sizes was obtained from the Pennsylvania Glass Sand Corporation for this study. The median particle sizes are as follows: MS-30, 9.5-micron; MS-15, 4.5-micron; MS-10, 3.1-micron; and MS-5, 1.3-micron. The results of erosion testing targets of 410 SS and 2024 Al alloys (37.5 degrees) with these fine silica particles are given in Table XX. Plots of these new data (E_V versus $V_p u^2$), which encompass particle kinetic energy levels 3-4 orders of magnitude lower than the lowest levels in prior testing, indicate continued conformance (above the erosion thresholds) to previously determined erosion loss/particle energy relationships (see Figures 89 and 90). As in Series III work, E_V signifies erosion loss per individual silica particle impact. Erosion thresholds were observed for all four particle sizes (2024 Al target) and for two particle sizes (410 SS target) at the particle velocity and particle energy levels listed below.

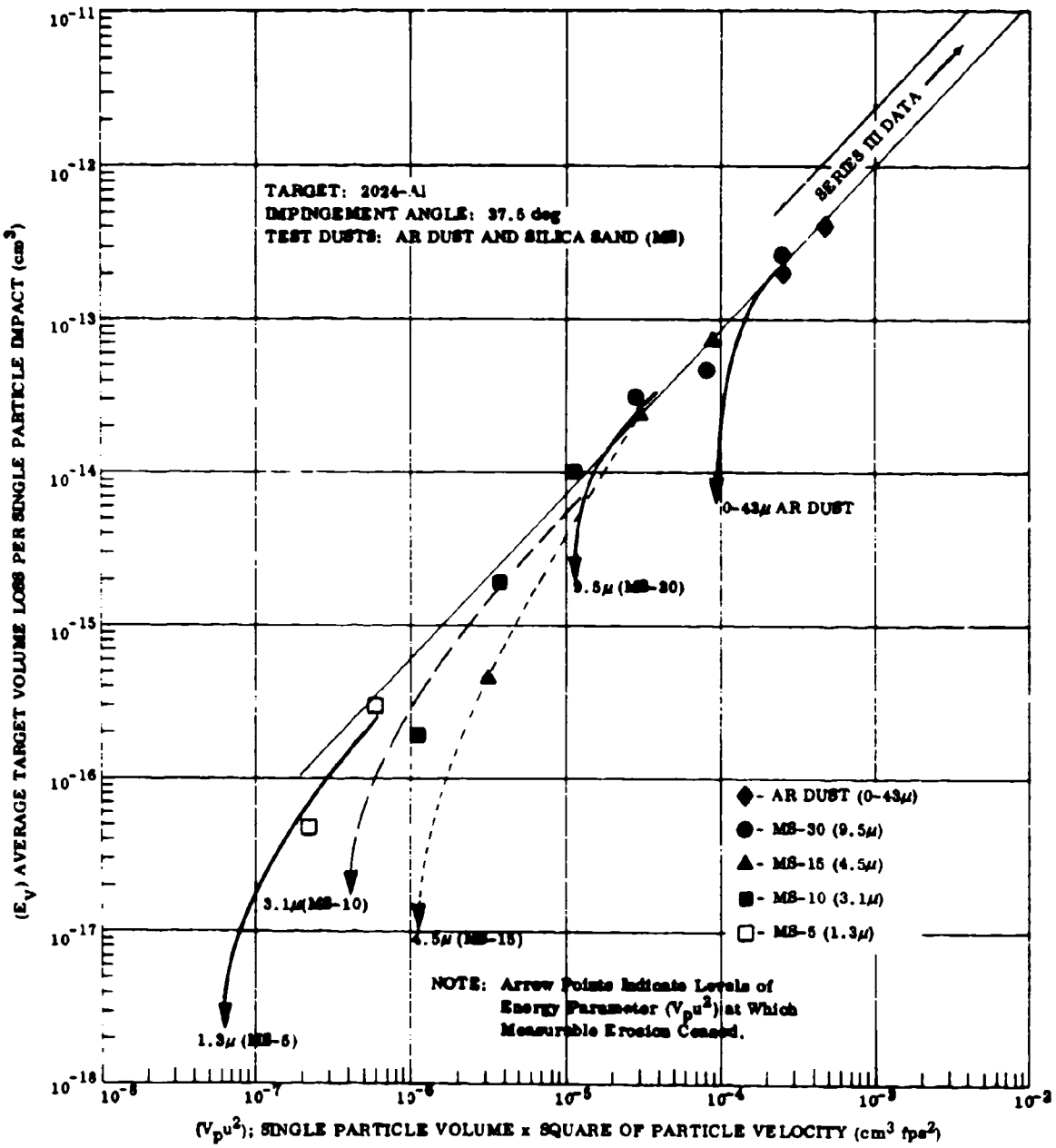

Figure 89. Plot of E_V Versus $V_p u^2$ Showing Erosion Thresholds.

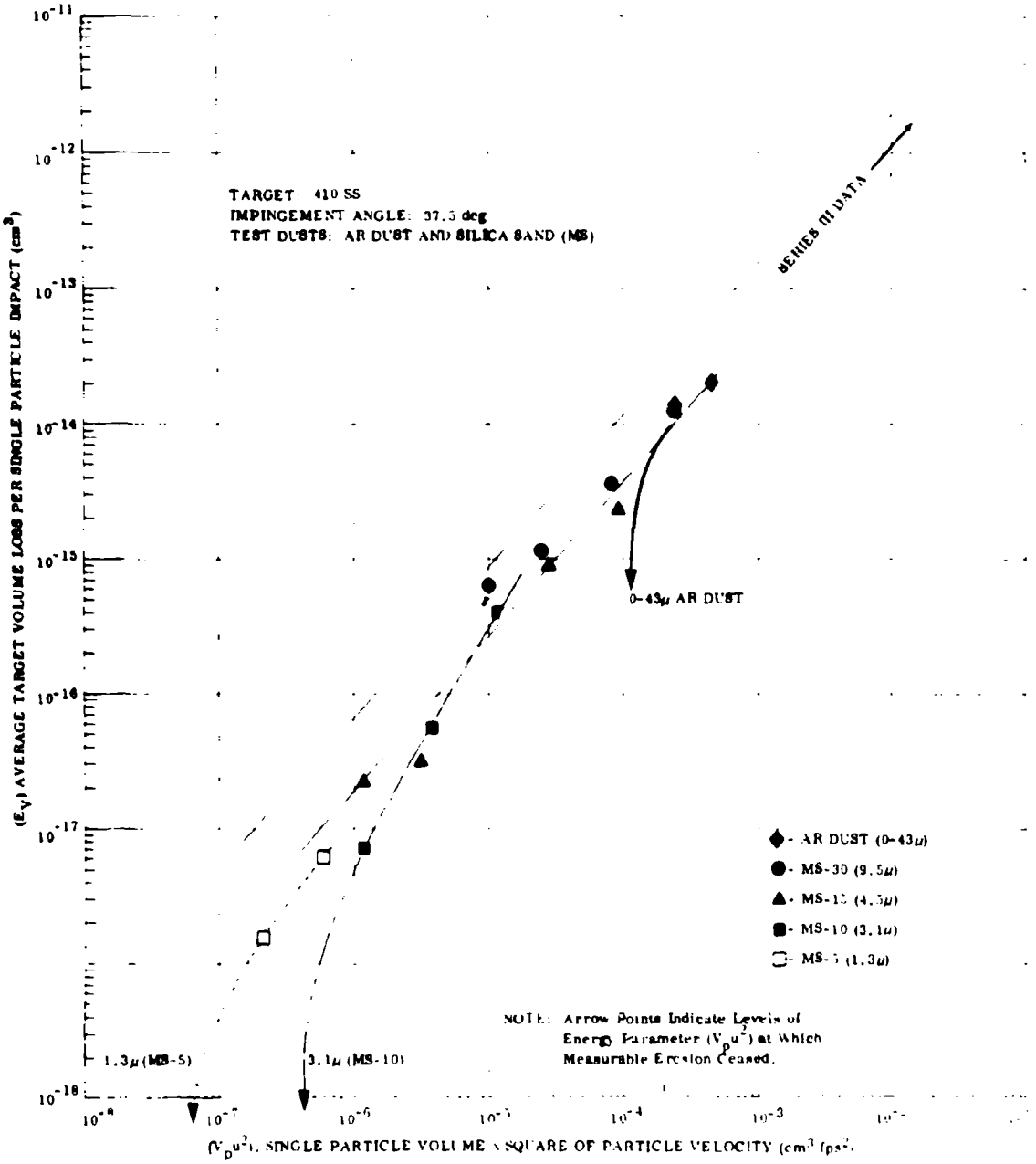

Figure 90. Plot of E_V Versus $V_p u^2$ Showing Erosion Thresholds.

Median Particle Size (u)	Target Material	Erosion Threshold: Particle Velocity (fps)	Erosion Threshold: Particle Energy Parameter ($cm^3\ fps^2$)
20 (AR Dust)	410 SS	between 110 and 178	between 9.7×10^{-5} and 2.5×10^{-4}
	2024 Al	" " "	" " "
9.5 (MS-30)	410 SS	------	------
	2024 Al	between 110 and 178	between 1.0×10^{-5} and 2.7×10^{-5}
4.5 (MS-15)	410 SS	------	------
	2024 Al	between 110 and 178	between 1.2×10^{-6} and 3.2×10^{-6}
3.1 (MS-10)	410 SS	between 110 and 178	between 4.2×10^{-7} and 1.1×10^{-6}
	2024 Al	" " "	" " "
1.3 (MS-5)	410 SS	between 178 and 320	between 6.4×10^{-8} and 2.1×10^{-7}
	2024 Al	" " "	" " "

It is obvious that each particle size has its own cutoff or threshold level of velocity (and energy), below which erosion either drops to zero or falls at least one order of magnitude below that predicted from the Ev versus $V_p u^2$ plots. It is interesting that even the tiny 1.3-micron and 3.1 micron particles have considerable ability to erode above their threshold energy levels; hence, there is no evidence to support the idea of a particle-size threshold (below which size no erosion occurs) at least down to the 1.3-micron size. The predictable erosiveness of the tiny particles therefore is an important factor to consider in designing air intake filters and dust separators for gas turbine protection. It is remarkable that the tiny particles are measurably erosive, because strike efficiencies for silica particles ≤5-micron can be of the order of only 40-50 percent. Strike efficiency is the percentage of incoming particles that break through the boundary layer at the target surface and actually strike the specimen, the balance being deflected by airstream lines.

The bulk erosion efficiencies of the smaller particles, as gaged by volume erosion factor, are somewhat less than for the larger particle sizes. This phenomenon has been noted by many previous researchers, and is commonly termed the "particle-size effect". (See Figures 91 and 92 and Table XXI, where volume erosion factors for all particle sizes from 1.3-micron to 147-208-micron are listed for a common particle velocity of 488 fps as an example.) Erosion factor is reduced systematically with decreasing particle size for both the 410 SS and 2024 Al targets (Figures 91 and 92). This reduction in apparent erosion efficiency (by about one order of magnitude over the particle size range studied) may be due to progressive reduction in strike efficiency with decreasing particle size and/or to increasing tendencies for particle clustering and sticking, also with decreasing particle size.

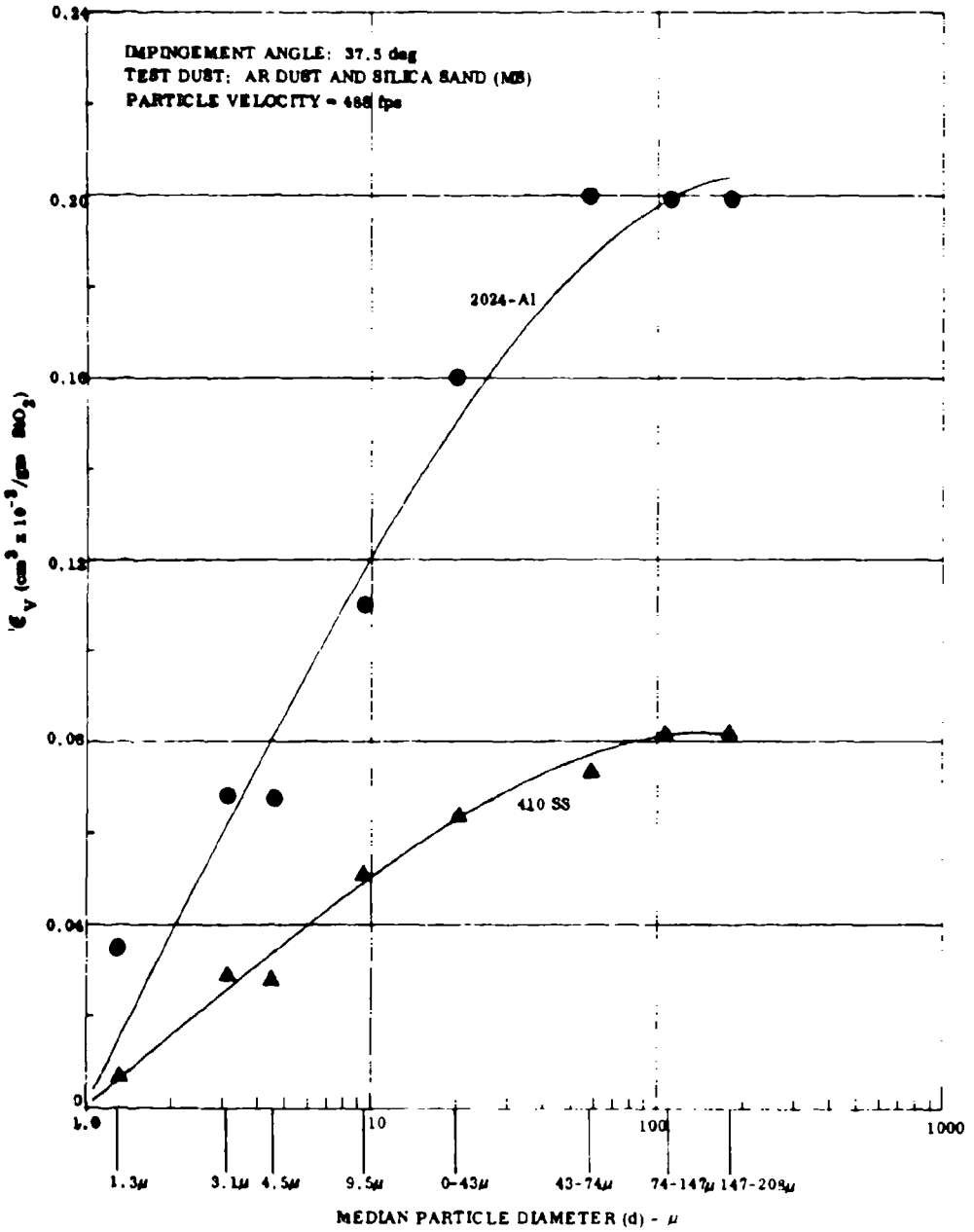

Figure 91. Variation in Volume Erosion Factor (ϵ_V) With Median-Particle Diameter (d).

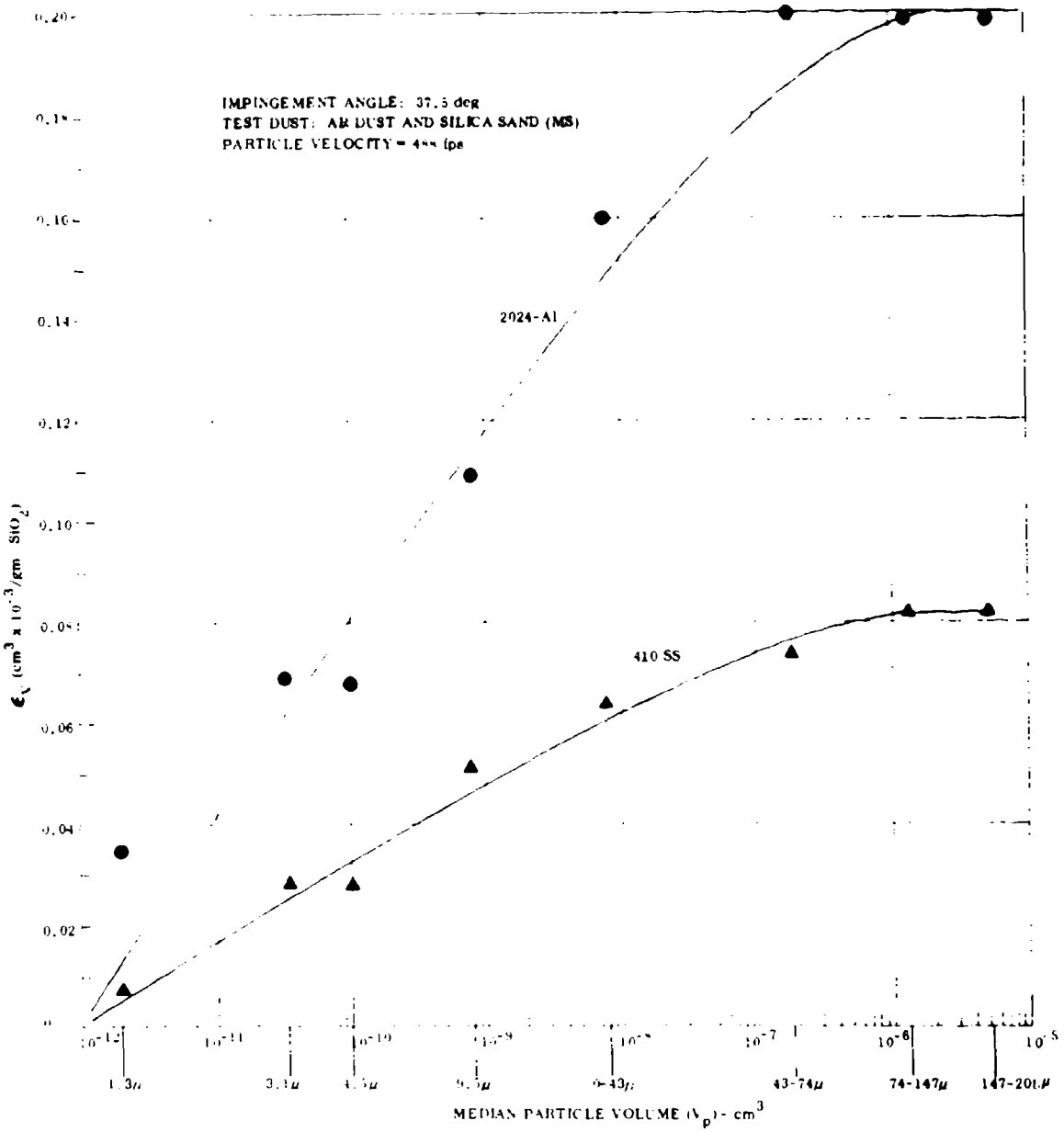

Figure 92. Variation in Volume Erosion Factor (ϵ_V) With Median-Particle Volume (V_p).

TABLE XXI. VARIATION IN VOLUME EROSION FACTOR (ϵ_V) WITH SILICA PARTICLE SIZE

(u = 488 fps; α = 37.5 deg)

Dust Variety	Particle Size (μ)	ϵ_V ($cm^3 \times 10^{-3}$/gm dust)		ϵ_V ($cm^3 \times 10^{-3}$/gm SiO_2)	
		410 SS	2024 Al	410 SS	2024 Al
AR Dust	147-208	0.057	0.13	0.082	0.19
" "	74-147	0.057	0.13	0.082	0.19
" "	43-74	0.052	0.14	0.074	0.20
" "	0-43	0.045	0.11	0.064	0.16
MS-30	9.5	0.051	0.11	0.051	0.11
MS-15	4.5	0.028	0.068	0.028	0.068
MS-10	3.1	0.029	0.069	0.029	0.069
MS-5	1.3	0.0073	0.035	0.0073	0.035

A plot of the threshold values of the particle energy parameter versus corresponding particle volume (Figure 93) indicates that the threshold energy value is almost directly proportional to the particle volume (or mass).

Therefore, for given target and dust varieties, the particle velocity at the erosion threshold (u_{th}) should and does occur at about the same level, regardless of particle size or volume (about 110 fps, wherever an erosion threshold exists). The single exception is for the smallest, 1.3-micron, particles. The higher threshold velocity here ($\approx$178 fps) could be due to reduced strike efficiency and/or particle clustering and sticking phenomena.

EFFECTS OF VARYING DUST CONCENTRATION (TEST SERIES IV)

Test Series IV is designed to evaluate the influence of varying dust concentration in the carrier gas upon the efficiency of erosion. Dust concentration is measured and compared in terms of:

C = Weight of dust (mg) per unit volume (ft^3) of compressed carrier gas at the nozzle exit.

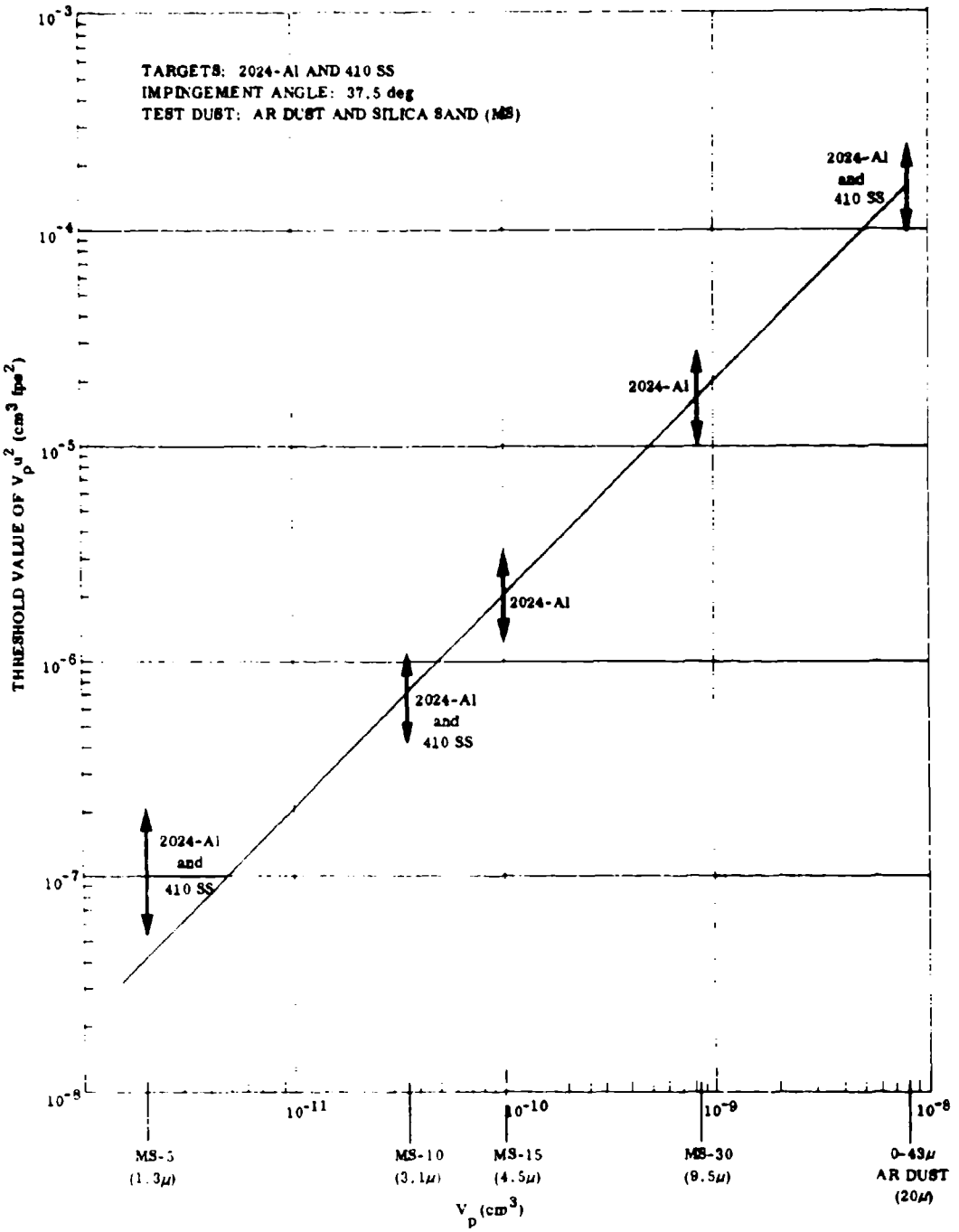

Figure 93. Variation in the Threshold Value of $V_p u^2$ With Median-Particle Volume (V_p).

C_{std} = Weight of dust (mg) per unit volume (ft^3) of ambient air (80°F, 1 atmosphere pressure).

C_A = Weight of dust (mg) striking a unit area of target surface (ft^2) normal to the carrier-gas flow per unit time (sec).

C_B = Total number of dust particles striking a unit area of target surface (ft^2) normal to the carrier-gas flow per unit time (sec).

$C_A \propto C_B \propto$ (C x Carrier-Gas Velocity, U)

Target losses are measured and compared in terms described for Test Series III. In prior work on this program, the concentration of dust in the carrier gas appeared to be a significant factor in determining the efficiency of the erosion process. The common method of reporting dust concentration (C), which has direct significance to the mechanism study, is in terms of the weight of dust (mg) contained in a cubic foot of the compressed carrier gas at the nozzle exit. Thus, for a given dust variety and dust particle size, the spatial array or geometric concentration of dust particles (in terms of particles/ft^3 or mg/ft^3) and the effective interparticle spacing or separation in the carrier gas remains the same for constant dust concentration, regardless of differences in particle velocity and/or temperature (and corresponding changes in carrier-gas compression and density). Another kind of dust concentration, namely, the number of milligrams of dust (C_A) or the number of dust particles (C_B) striking a unit area of target surface normal to carrier gas flow per unit time, is proportional to the reported dust concentration (in mg/ft^3 or particles/ft^3) times the carrier-gas velocity (ft/sec) or the volume flow of carrier gas passing through the nozzle exit per unit time (ft^3/sec). The current method of determining carrier-gas volume flow is to multiply mean carrier-gas velocity, measured with a Pitot tube about 1/4 inch inside the nozzle throat, times the nozzle area. This volume flow is used to determine the metering rate for the test dust. The coefficient of discharge for the nozzle is assumed to be ≈1.00.

It is believed that the described methods of reporting dust concentration are most meaningful for the subject Test Series IV, which is designed specifically to study the effect of dust concentration upon dust erosion and erosion mechanism. However, some thought also was given to reporting effective dust concentration in the ambient air, prior to ingestion. This dust concentration in the ambient air (C_{std}) or air at standard temperature (T_1) and pressure (P_1) has considerable engineering significance. A good approximation of the marked increase in dust concentration due to carrier-gas compression in the turbine compressor (at P_2, T_2) can be obtained using the $PV_g = nRT$ relation; i.e.,

$$\frac{P_1 V_{g_1}}{T_1} = \frac{P_2 V_{g_2}}{T_2} .$$

See Tables XXII and XXIII.

Dust concentration effects were investigated using 0-43-micron and 43-74-micron Arizona Road Dust at particle velocities (RT) of 488 and 925 fps and 488 and 880 fps (respectively), against targets of 410 SS and 2024 Al alloy. Four levels of dust concentration in the compressed air carrier gas (nozzle) were programmed: C = 40, 80, 200, and 800 mg/ft^3. Converted to ambient (STP) conditions, these concentrations cover the range C_{std} = 4.2-190 mg/ft^3 (see Table XXII). This range corresponds well to the normal limits encountered in service. Additional erosion tests at similar dust concentrations were conducted at 700° F true temperature with air carrier gas at particle velocities of 650 and 1100 fps (43-74-micron) and 700 and 1170 fps (0-43-micron) (see Table XXIII). Three tests were conducted in each condition. Average erosion data are plotted for both particle sizes and both target alloys in terms of E_V (target volume loss per single particle impact) versus the dust concentration parameter, C_B (Figures 94 through 97). The dust concentration, C (mg/ft^3), is also noted on each plot.

It is evident from the data plots that erosion efficiency does not vary in any consistent or predictable way with dust concentration, even though dust concentration ranges through nearly two orders of magnitude for each situation examined. In most instances where an apparent trend was observed, erosion losses were slightly greater for the intermediate or higher dust concentrations, just the opposite of the predominant trend in prior work which indicated that the lower dust concentrations were more erosive. The variation in erosion efficiency observed is probably due only to the normal and random data scatter associated with a heterogeneous dust. The variations in E_V values recorded here are no greater (and usually far less) than those obtained in Series III work where the dust concentration was held constant at C = 40 mg/ft^3 (compare Figures 94 through 97 with Figures 70 through 74).

It is reasonable that a dust concentration effect, if one exists, should be minimal. This is because the probability of interparticle collision at the target/carrier-gas interface for a uniformly distributed dust suspension is so low (typically $\leq 0.5\%$; see Appendix V). If a dust concentration effect is exhibited on occasion, it is likely caused by clumping or clustering of dust particles (i.e., an uneven spatial distribution in the carrier-gas stream). Somewhat reduced erosiveness then would be logical, due to physical shielding of the target by the front-running (vanguard) particles. The occasional occurrence of clumping and/or clustering of dust particles in the feed line has been observed, most often at the higher feed rates (heaviest dust concentrations) and for the finer dust particles.

TABLE XXII. COMPILATION OF SERIES IV TEST DATA

Test Temperature: RT
Impingement Angle: 37.5 deg

N = 5.40 gm, Arizona Road Dust
= 3.78 gm, Constituent Silica Particles

Particle Size (μ)	Particle Material	Dust Concentration C_N (mg/ft³)	Dust Concentration C_V (mg ft²/sec)	Dust Concentration C_{II} (particles/ft²/sec)	Carrier Gas Velocity (ft/sec)	Dust Particle Velocity, Median-Particle Size (ft/sec)	Test Time (sec)	ϵ (mg/gm)	ϵ_V (cm³ x 10⁻³/gm)	F (mg x 10⁻⁸)	E_V (cm³ x 10⁻¹¹)	Average Target Weight Loss (mg)
10-21	1100-H	10	9.1	2.1×10^8	2.8×10^7	525	488	745	0.41	0.052	30	3.9	2.2
		20	17	3.9×10^8	5.7×10^7			373	0.63	0.080	47	5.9	3.4
		100	43	1.1×10^9	1.4×10^8			149	0.61	0.078	45	5.8	3.3
		500	170	4.3×10^9	5.7×10^8			37	0.56	0.071	42	5.3	3.0
		10	9.2	1.9×10^8	5.2×10^7	950	880	410	1.1	0.14	84	11	6.1
		20	9.1	7.5×10^8	1.0×10^8			205	1.4	0.18	110	14	7.8
		100	21	1.9×10^9	2.6×10^8			82	1.5	0.19	110	14	8.2
		500	94	7.5×10^9	1.0×10^9			21	1.5	0.19	110	14	8.0
10-21	1100-H-XII	10	9.1	2.1×10^8	2.8×10^7	525	488	745	0.39	0.14	29	11	2.1
		20	17	3.9×10^8	5.7×10^7			373	0.45	0.16	33	12	2.4
		100	43	1.1×10^9	1.4×10^8			149	0.45	0.16	33	12	2.4
		500	170	4.3×10^9	5.7×10^8			37	0.46	0.16	34	13	2.5
		10	9.2	1.9×10^8	5.2×10^7	950	880	410	1.0	0.35	77	27	5.4
		20	9.1	7.5×10^8	1.0×10^8			205	1.4	0.50	100	39	7.7
		100	21	1.9×10^9	2.6×10^8			82	1.4	0.50	110	39	7.7
		500	94	7.5×10^9	1.0×10^9			21	1.3	0.48	99	37	7.2
1-3	1100	10	9.1	2.0×10^8	7.4×10^8	500	488	785	0.35	0.045	0.98	0.12	1.9
		20	19	4.0×10^8	1.5×10^9			393	0.33	0.043	0.93	0.12	1.8
		100	37	1.0×10^9	3.7×10^9			157	0.33	0.043	0.93	0.12	1.8
		500	190	4.0×10^9	1.5×10^{10}			39	0.30	0.038	0.83	0.10	1.6
		10	9.2	1.9×10^8	1.4×10^9	950	925	410	1.0	0.13	2.8	0.36	5.5
		20	9.1	7.5×10^8	2.8×10^9			205	1.0	0.13	2.9	0.36	5.6
		100	21	1.9×10^9	7.1×10^9			82	1.1	0.14	3.0	0.38	5.9
		500	94	7.5×10^9	2.8×10^{10}			21	1.1	0.14	2.9	0.37	5.7
1-3	1100-H-XII	10	9.4	2.0×10^8	7.4×10^8	500	488	785	0.32	0.11	0.88	0.31	1.7
		20	19	4.0×10^8	1.5×10^9			393	0.28	0.099	0.77	0.27	1.5
		100	37	1.0×10^9	3.7×10^9			157	0.26	0.092	0.72	0.26	1.4
		500	190	4.0×10^9	1.5×10^{10}			39	0.28	0.099	0.77	0.27	1.5
		10	9.2	1.9×10^8	1.4×10^9	950	925	410	0.78	0.28	2.2	0.77	4.2
		20	9.1	7.5×10^8	2.8×10^9			205	0.98	0.35	2.7	0.97	5.3
		100	21	1.9×10^9	7.1×10^9			82	0.93	0.33	2.6	0.91	5.0
		500	94	7.5×10^9	2.8×10^{10}			21	0.87	0.31	2.4	0.86	4.7

TABLE XXIII. COMPILATION OF SERIES IV TEST DATA

Test Temperature: 700°F
Impingement Angle: 37.5 deg

N = 5.40 gm, Arizona Road Dust
= 3.78 gm, Constituent Silica Particles

Particle Size (μ)	Target Material	Dust Concentration C (mg/ft³)	Dust Concentration C_{sol} (mg/ft³)	C_A (mg/ft²/sec)	C_B (particles/ft²/sec)	Carrier-Gas Velocity (ft/sec)	Dust Particle Velocity, Median-Particle Size (ft/sec)	Test Time (sec)	ϵ (mg/gm)	ϵ_V ($cm^3 \times 10^{-3}$/gm)	E (mg × 10^6)	E_V ($m^3 \times 10^{-4}$)	Average Target Weight Loss (mg)
43-74	410 SS	40	~ 22	2.9×10^4	3.9×10^7	725	650	534	0.59	0.075	44	5.6	4.2
		40	~ 65	6.0×10^4	8.0×10^7			267	0.57	0.073	43	5.4	3.1
		200	~ 110	1.5×10^5	2.0×10^8			107	0.47	0.085	49	6.3	3.6
		400	~ 450	6.0×10^5	8.0×10^8			27	0.63	0.080	47	5.9	3.4
		40	~ 13	4.9×10^4	6.5×10^7	1200	1100	325	1.5	0.19	110	14	4.6
		40	26	9.8×10^4	1.3×10^8			163	1.5	0.19	110	14	8.1
		200	65	2.5×10^5	3.2×10^8			65	1.4	0.18	100	11	7.6
		400	260	9.8×10^5	1.3×10^9			16	1.4	0.18	100	13	7.6
43-74	2024-Al	40	~ 22	2.9×10^4	3.9×10^7	725	650	534	0.85	0.30	63	23	4.6
		40	65	6.0×10^4	8.0×10^7			267	0.81	0.29	60	22	4.8
		200	110	1.5×10^5	2.0×10^8			107	0.91	0.29	60	22	6.4
		400	450	6.0×10^5	8.0×10^8			27	0.90	0.28	59	22	4.3
		40	13	4.9×10^4	6.5×10^7	1200	1100	325	2.0	0.71	150	56	11.0
		40	26	9.8×10^4	1.3×10^8			163	2.2	0.78	160	59	11.7
		200	65	2.5×10^5	3.2×10^8			65	2.2	0.78	160	59	11.7
		400	260	9.8×10^5	1.3×10^9			16	2.2	0.79	170	61	12.0
0-43	410 SS	40	22	2.9×10^4	1.1×10^9	725	700	534	0.44	0.056	1.2	0.16	2.4
		40	65	6.0×10^4	2.3×10^9			267	0.41	0.052	1.1	0.14	2.2
		200	110	1.5×10^5	5.4×10^9			107	0.41	0.052	1.1	0.14	2.2
		400	450	6.0×10^5	2.2×10^{10}			27	0.46	0.060	1.3	0.16	2.5
		40	13	4.9×10^4	1.8×10^9	1200	1170	325	1.1	0.14	3.0	0.38	5.4
		40	26	9.8×10^4	3.6×10^9			163	1.0	0.13	2.8	0.35	5.4
		200	65	2.5×10^5	8.9×10^9			65	1.1	0.14	2.9	0.37	5.7
		400	260	9.8×10^5	3.6×10^{10}			16	0.98	0.12	2.7	0.34	5.3
0-43	2024-Al	40	22	2.9×10^4	1.1×10^9	725	700	534	0.56	0.20	1.5	0.55	3.0
		40	65	6.0×10^4	2.3×10^9			267	0.57	0.20	1.6	0.57	3.1
		200	110	1.5×10^5	5.4×10^9			107	0.54	0.19	1.5	0.53	2.9
		400	450	6.0×10^5	2.2×10^{10}			27	0.52	0.18	1.4	0.51	2.8
		40	13	4.9×10^4	1.8×10^9	1200	1170	325	1.5	0.54	4.2	1.5	8.1
		40	26	9.8×10^4	3.6×10^9			163	1.6	0.57	4.4	1.6	8.6
		200	65	2.5×10^5	8.9×10^9			65	1.5	0.53	4.2	1.5	8.2
		400	260	9.8×10^5	3.6×10^{10}			16	1.6	0.57	4.5	1.6	8.8

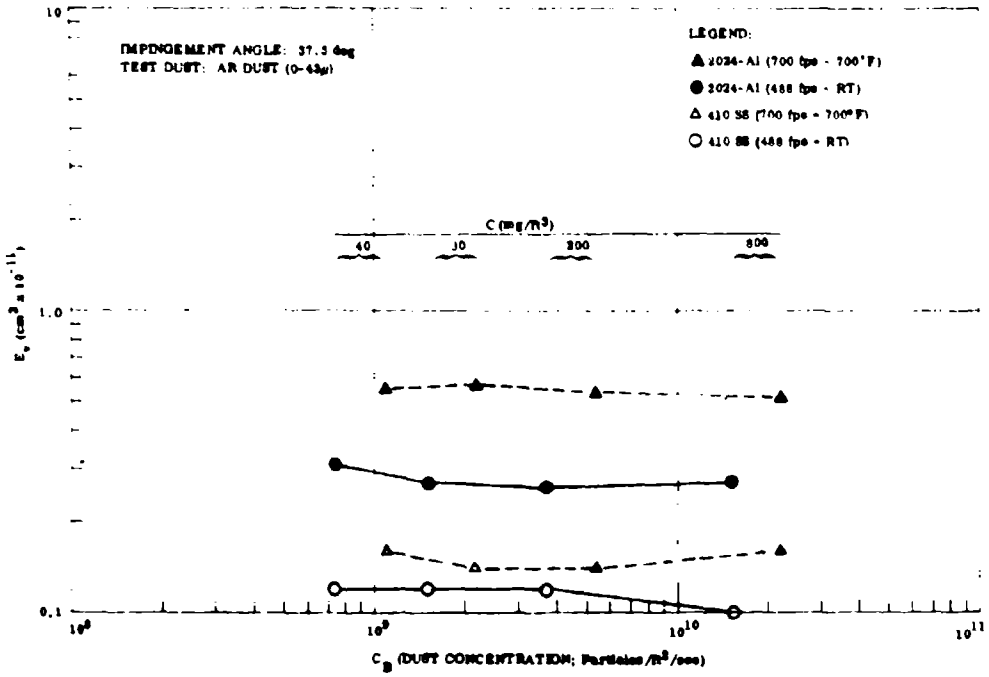

Figure 94. Plot of E_V Versus C_B (Dust Concentration).

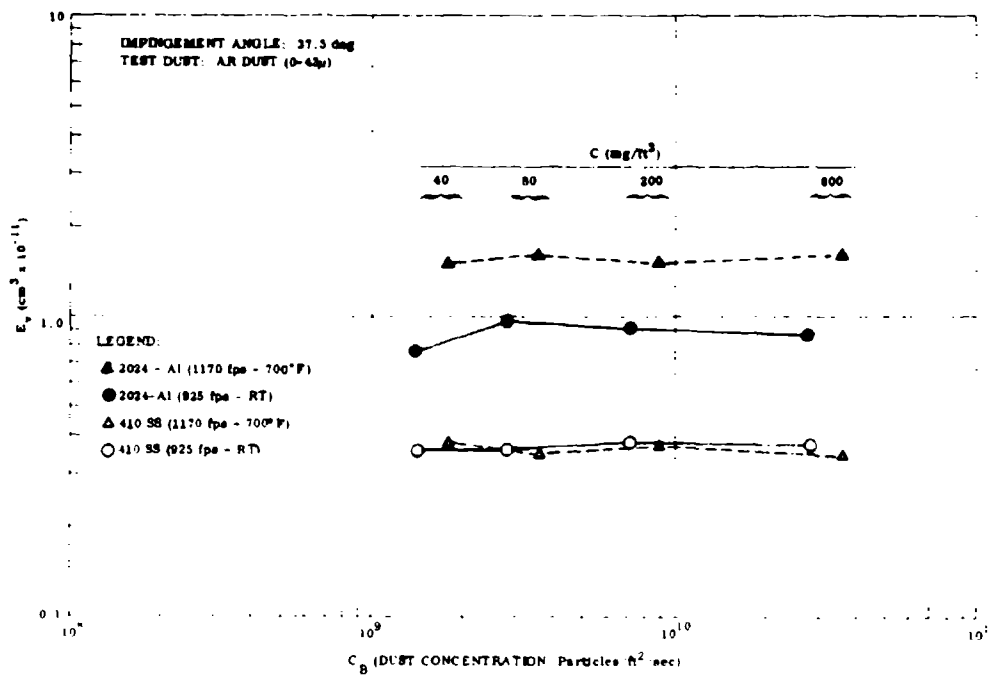

Figure 95. Plot of E_V Versus C_B (Dust Concentration).

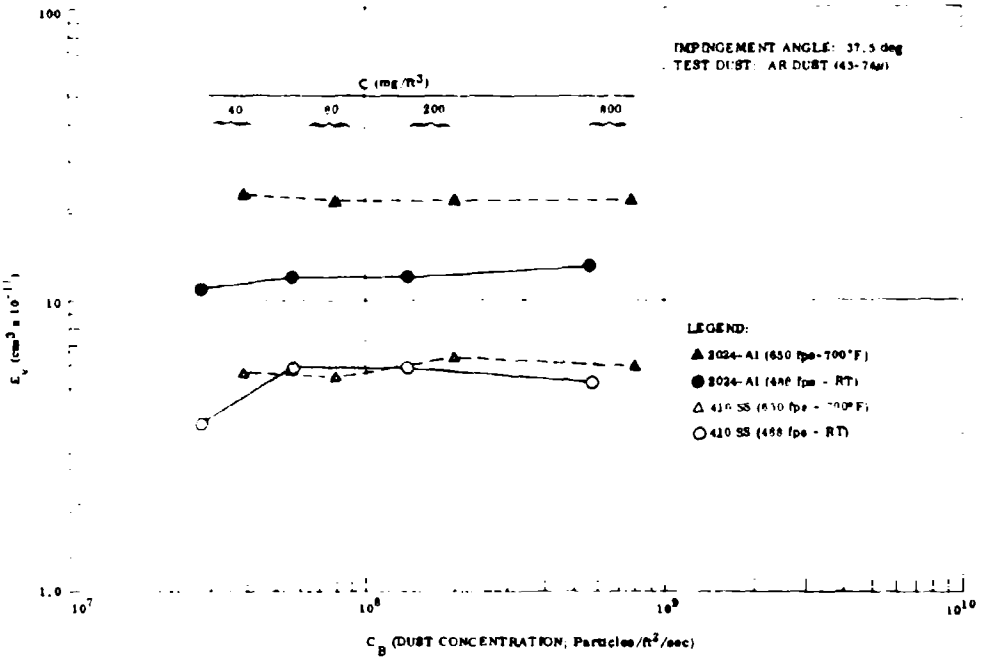

Figure 96. Plot of E_V Versus C_B (Dust Concentration).

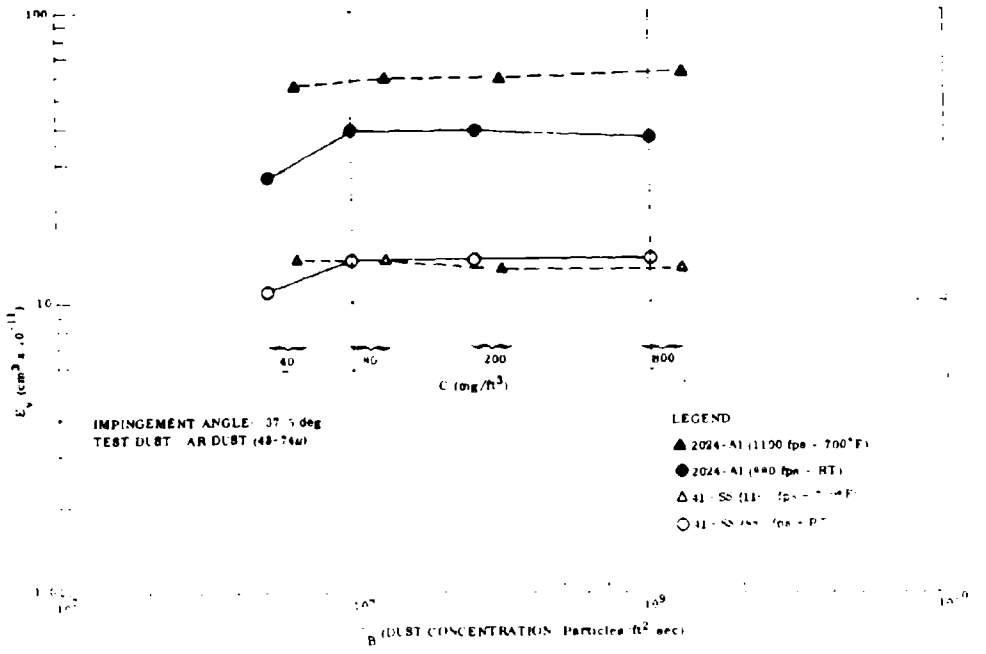

Figure 97. Plot of E_V Versus C_B (Dust Concentration).

Experience has also shown that the finer particles (≤20-micron) of all test dusts frequently tend to stick or clot on the target surface, a condition much more prevalent the finer the particle size. This temporary sticking of fine particles, even though brief, could effectively shield the target from subsequent impacts, inasmuch as the normal duration of particle/target contact and the average time interval separating successive particles are both on the order of microseconds. It seems reasonable then that uneven distributions of dust particles in the carrier-gas stream and on the target surface (following impact) are the most probable causes of the dust concentration effect, when observed. These same conditions could contribute to the "particle-size effect" as well, by virtue of the observed particle size dependence on particle clustering and sticking. Variation in "strike efficiency" with particle size is undoubtedly an additional factor in the "particle-size effect", discussed previously.

TARGET STRESS-STATE EFFECTS (TEST SERIES V)

The objective of this test series was to determine the possible influence of elastic tensile strain in the target metal upon erosion resistance. To simulate the erosion conditions and maximum levels of operational stress-strain in a typical compressor blade, exploratory erosion tests were carried out on all four program alloys (fully heat treated conditions) under applied tensile stresses corresponding to 60 percent of their respective RT yield strengths (0.2%) (see Table XXIV). Unstressed specimens were tested also for base-line data. Uniaxial tensile loads were applied to the standard-size erosion specimens through shear-pins at either specimen end, using a hydraulic jack. All tests were conducted with 43-74-micron Arizona Road Dust, at an intermediate particle velocity of 670 fps (RT). Dust concentration was held at the usual level of 40 mg/ft^3.

The application of tensile stress did not change the normal ductile erosion response of the target alloys, the erosion losses at 37.5 degrees impingement in all cases being higher than at 60 degrees. However, the stressed specimens (all 4 alloys) eroded slightly more than the unstressed, the change being of the order of 4 to 12 percent (Table XXIV). This minor increase in erosion was not felt to be sufficient to warrant additional testing at intermediate stress levels. Inasmuch as the stressed targets represent a higher energy situation than the unstressed, these erosion data are not inconsistent with previous results showing the direct relationship between particle energy and erosion level.

However, it is difficult to comprehend how the relatively small amount of potential energy stored (as elastic strain) in the target material removed per impact could be important in the ductile erosion mechanism, when this energy is contrasted to the much larger kinetic energy of each impacting particle. For example, the average kinetic energy of each 43-74-micron particle is on the order of 100 ergs or about 2.3×10^{-6} calories; whereas the potential (elastic) energy stored in the

TABLE XXIV. EROSION TEST RESULTS, TEST SERIES V (TARGET STRESS-STATE EFFECTS)

Target Material	Test Dust	Median-Particle Velocity (fps)	Impingement Angle (deg)	Average Target Weight Loss (mg)	Weight Erosion Factor, ε (mg/gm)	Tensile Stress Imposed On Target (psi)	Percent Increase In Erosion Loss, Due to Stress
2024-Al*	AR Dust (43-74μ)	670	37.5	5.3	0.98	0	---
			60	4.2	0.78	0	---
			37.5	5.9	1.1	30,000**	11
			60	4.5	0.83	"	7
Ti-6Al-4V*			37.5	5.5	1.0	0	---
			60	4.6	0.85	0	---
			37.5	6.0	1.1	93,000**	9
			60	5.0	0.93	"	9
410 SS*			37.5	6.0	1.1	0	---
			60	5.3	0.98	0	---
			37.5	6.6	1.2	72,000**	10
			60	5.5	1.0	"	4
17-7 PH*			37.5	6.5	1.2	0	---
			60	5.7	1.1	0	---
			37.5	7.2	1.3	110,000**	11
			60	6.4	1.2	"	12

* Fully Heat Treated Condition
** 60% of 0.2% Yield Strength

average target material removed per single particle impact is only about 3.0×10^{-11} calories. Being some 5 orders less in magnitude, the energy contribution of the strained target lattice should be negligible. Whatever the true situation, the influence of target stress-state in the ductile erosion mechanism appears to be very minor.

EFFECT OF OXYGEN CONCENTRATION IN THE CARRIER GAS (TEST SERIES VI)

The objectives of this test series were to assess the possible importance of oxidation to the erosion mechanism and the influence of varying the carrier-gas composition. Dust erosion testing in England (Ref. 23 and 24) using an evacuated test chamber (pressure of 1.0×10^{-3} Torr) has yielded erosion factors as high or somewhat higher than the subject Solar testing in air atomsphere. (Similar test dusts and stainless steel targets were employed.) This suggested that an oxygen-containing

environment and target oxidation, per se, are not essential prerequisites to obtaining erosion. Moreover, in Test Series II it was noted that high velocity (1100 fps) erosion tests conducted at RT with a helium-air mixture (≈13% O_2) normally generated similar or somewhat higher erosion rates than equivalent velocity tests in air (20% O_2); this was in spite of the fact that the air tests were carried out at 700°F where target oxidation (if it were occurring and influential) would be more rapid and self-supporting (Table XXV). On the strength of these inferences, it was decided to conduct equivalent particle-velocity erosion tests with air carrier-gas as well as with inert (oxygen-free) carrier-gases to directly compare dust erosion in potentially oxidizing versus inert environments. Pure helium and pure argon (welding grade) were used for the inert carrier gases, the nozzle jets effectively shielding the target erosion surfaces as in inert-gas welding.

The first series of tests was conducted with 43-74-micron Arizona Road Dust at a common particle velocity of 1100 fps (air carrier gas at 700°F true temperature; pure helium carrier gas at room temperature). The second series was conducted at an intermediate particle velocity of 670 fps, using air, pure helium, and pure argon carrier gases, all at RT. All four program alloys were tested at both 37.5- and 60-degree impingement angles (see Table XXV). Tests were in duplicate.

In the first series at 1100 fps, erosion losses on all targets increased dramatically in the pure helium environment anywhere from 117 to 222 percent, depending upon the target alloy and impingement angle (Table XXV). In the second series at 670 fps, erosion losses with helium carrier gas again were invariably higher than with air, but by lesser percentages (10-43%, depending upon the target alloy and impingement angle). The trend with argon carrier gas at 670 fps was the same, but again the percentage increases over air carrier gas were somewhat lower (0-26%).

The significant influence of the carrier gas on erosion loss is proof that the nature of the carrier gas is as much involved with erosion mechanics as dust particle characteristics and target material properties. This is evident also in the different appearance of surface ripples formed on the erosion surfaces with the different carrier gases. The ripples formed with helium (670 fps) are much deeper and better defined than those made using argon or air. One can only speculate as to the specific function of the carrier gas in the erosion mechanism. It may be the variable quenching (heat absorption) abilities of the different gases, particularly if redeposition of (sprayed) molten erosion products is an important factor in determining net erosion losses. That is, molten droplets of eroded target metal which are quenched rapidly (as with helium) and caused to solidify while suspended in the carrier gas may have negligible opportunity to redeposit on the target surface. On the other hand, metal droplets suspended in air or argon carrier gases should not be quenched as rapidly as with helium, and may have increased opportunity to redeposit on (and be bonded to) the target surface while in the liquid state, thereby effectively reducing the net

TABLE XXV. COMPILATION OF SERIES VI TEST DATA

Target Material	True Gas Temperature (°F)	Carrier Gas Composition	Impingement Angle (deg)	Median-Particle Velocity (fps)	Weight Erosion Factor, ϵ (mg/gm)	Percent Change Over Air Carrier Gas	Volume Erosion Factor, ϵ_V ($cm^3 \times 10^{-3}/gm$)	E_V ($cm^3 \times 10^{-11}$)
2024 Al	700	Compressed Air	37.5	1100	1.2	--	0.43	33
(Annealed)		(20% wt. O_2)	60		0.65	--	0.24	18
	RT	65% Air-35% He	37.5		1.4	--	0.51	39
		(13% wt. O_2)	60		0.45	--	0.16	12
		Pure Helium	37.5		2.6	117	0.95	72
		(0% wt. O_2)	60		1.5	130	0.55	41
		Compressed Air	37.5	670	0.70	--	0.26	19
		(20% wt. O_2)	60		0.50	--	0.18	14
		Pure Helium	37.5		1.0	43	0.37	28
		(0% wt. O_2)	60		0.63	26	0.23	17
		Pure Argon	37.5		0.78	11	0.29	22
		(0% wt. O_2)	60		0.52	4	0.19	14
Ti-6Al-4V	700	Compressed Air	37.5	1100	1.1	--	0.24	19
(Annealed)		(20% wt. O_2	60		0.59	--	0.14	10
	RT	65% Air-35% He	37.5		1.1	--	0.24	19
		(13% wt. O_2)	60		0.78	--	0.18	13
		Pure Helium	37.5		2.6	136	0.58	44
		(0% wt. O_2)	60		1.9	222	0.42	32
		Compressed Air	37.5	670	0.72	--	0.16	12
		(20% wt. O_2)	60		0.63	--	0.14	11
		Pure Helium	37.5		0.96	33	0.21	16
		(0% wt. O_2)	60		0.74	18	0.16	13
		Pure Argon	37.5		0.89	24	0.20	15
		(0% wt. O_2)	60		0.67	6	0.15	11

TABLE XXV - Continued

Target Material	True Gas Temperature (°F)	Carrier Gas Composition	Impingement Angle (deg)	Median-Particle Velocity (fps)	Weight Erosion Factor, ϵ (mg/gm)	Percent Change Over Air Carrier Gas	Volume Erosion Factor, ϵ_V ($cm^3 \times 10^{-3}$/gm)	E_V ($cm^3 \times 10^{-11}$)
410 SS	700	Compressed Air	37.5	1100	1.0	--	0.13	9.4
(Annealed)		(20% wt, O_2)	60		0.57	--	0.074	5.4
	RT	65% Air-35% He	37.5		0.85	--	0.12	8.0
		(13% wt, O_2)	60		0.63	--	0.083	6.1
		Pure Helium	37.5		2.5	150	0.32	24
		(0% wt, O_2)	60		1.8	218	0.23	17
		Compressed Air	37.5	670	0.78	--	0.10	7.4
		(25% wt, O_2	60		0.67	--	0.085	6.3
		Pure Helium	37.5		0.96	23	0.12	9.1
		(0% wt, O_2)	60		0.74	10	0.095	7.0
		Pure Argon	37.5		0.98	26	0.13	9.9
		(0% wt, O_2)	60		0.67	0	0.083	6.3
17-7 PH	700	Compressed Air	37.5	1100	1.0	--	0.13	9.7
(Annealed)		(20% wt, O_2)	60		0.74	--	0.095	7.2
	RT	65% Air-35% He	37.5		1.1	--	0.15	11
		(13% wt, O_2)	60		0.70	--	0.093	6.8
		Pure Helium	37.5		2.7	170	0.36	26
		(0% wt, O_2)	60		2.1	194	0.28	20
		Compressed Air	37.5	670	0.80	--	0.11	7.8
		(20% wt, O_2)	60		0.68	--	0.091	6.7
		Pure Helium	37.5		1.1	38	0.15	11
		(0% wt, O_2)	60		0.87	9	0.12	8.5
		Pure Argon	37.5		0.90	13	0.14	9.6
		(0% wt, O_2)	60		0.78	17	0.11	7.8

(measureable) erosion loss. (Helium is an appreciably better quenching medium than either argon or air.) Another possibility is that an inert carrier gas precludes the formation of refractory oxides on the erosion surface, thereby decreasing surface tension and surface viscosity and promoting liquid metal splattering. In any case, it is clear that an oxygen-free carrier gas tends to increase erosion at constant particle velocity and energy.

SUMMATION OF MECHANISM-RELATED FINDINGS: THE EROSION TEST PHASE

- For a given erosion system, erosion per particle is directly proportional to particle kinetic energy ($\propto Mu^2$). The apparent efficiency of available energy utilization by the erosion (target metal removal) process is a function of dust particle variety and impingement angle, but not of variable engineering strength, for a given target material. The efficacy of (particle) energy translation into the metal removal process remains constant over wide ranges of particle mass and particle energy.

- The erosion mechanism ceases to function for fine particles ($\leq$20-micron) below about 100-200 fps, the exact cutoff velocity depending upon particle variety, size, and target alloy. This erosion threshold suggests that a certain minimum particle energy is necessary to activate the erosion mechanism.

- Because of the insensitivity of the erosion process to marked changes in metallurgical structure and engineering strength (for a given target alloy), the implication is strong that target material properties not appreciably affected by heat treatment or cold work are controlling erosion. However, because widely different target materials (with regard to structure, chemical composition, strength, modulus, melting point, thermal diffusivity, density, etc.) experience nearly equivalent erosion losses, a complex parameter of material properties is indicated.

- The harder, denser, and more refractory Al_2O_3 dust proved significantly more erosive per gram and per particle than SiO_2-rich Arizona Road Dust (equivalent particle energies). Vietnamese laterite soil showed negligible erosion potential, probably because of its very low SiO_2 content. Apparently, to be troublesomely erosive, mineral dusts at least as hard and refractory as silica are required.

- Increasing the carrier-gas true temperature from RT to 700°1 results in variable changes (usually reductions) in erosion losses (changes not predictable on the basis of decreasing target flow strength with increasing temperature).

- Variation in the concentration of dust uniformly dispersed in the carrier-gas stream, over the range normally encountered in service, has negligible influence on erosion efficiency. In those occasional instances where a dust concentration effect is observed, it is believed to be due to target shielding resulting from uneven distribution (e.g., clumping or clustering) of dust particles in the carrier-gas stream and/or transient sticking (fouling, adhesion) of particles upon the target surface. Both of these particle behaviors have been observed in testing and become especially prevalent with the finer dust fractions. The "particle size effect" (i.e., reduced bulk erosion efficiency per gram of dust, with decreasing particle size) is also likely related to these same particle aggregation tendencies.

- Elastic tensile strain in the target alloy (60% of 0.2% yield strain) promotes slightly higher erosion losses than the unstrained condition. The potential energy stored in the strained target-metal lattice may contribute to the activation of the erosion mechanism.

- The use of inert, oxygen-free carrier gases tends to increase erosion losses significantly over otherwise similar erosion tests conducted with air carrier gas. It appears that surface oxidation is not a prerequisite for ductile erosion.

Just what reactions the particle energy activates on the target surface was not clear at this point. Fortunately, the companion electron microscopy study supplied the missing phenomenological information.

STUDY OF EROSION PHENOMENA AND SYNTHESIS OF EROSION MODELS

VARIETIES OF PARTICLE IMPACTS

In an attempt to gain further insight into the actual mechanics of erosion, the target surfaces from Test Series I and II were examined at high magnification using scanning electron microscopy and replication for standard electron microscopy.

Initially, observations were made on target surfaces from the long-duration erosion tests, each subjected to 12-70 million particle impacts. Assuming a micromachining process of erosion, it was anticipated that machining grooves, perhaps 5-20μ in length (oriented in the particle direction) and 1/5-1/10 as wide, would be found, along with tiny (unreleased) chips of approximately the same dimensions. None were found on any target surface, nor were metallic chips ever detected in the spent dust. The general appearance of all specimen surfaces is that of very intensive surface flow and severe plastic deformation as typified by Figure 98. Not only was there a complete absence of micromachining evidence, but there appeared to be little if any readily distinguishable differences among the structures of the eroded surfaces for the different target alloys and impingement angles (constant particle velocities and varieties).

Although the erosion surfaces had obviously been exposed to many millions of superimposed particle impacts, so that the effect of a single impact was impossible to ascertain, one important feature was common to all specimens. This was that the erosion surfaces had been altered to a high degree of plasticity by the multiple particle impacts, and certain portions actually appeared to have been molten. The melting phenomenon apparently was very localized and restricted to the immediate surface layer in direct contact with the particles, inasmuch as no visible evidence of bulk melting (i.e., $>1\mu$ below the surface) was obtained metallographically. It was recognized that the surface melting phenomenon might have an important connection with the true erosion mechanism, especially since erosion loss and target melting point can be related, empirically at least for pure elemental targets which melt $\geq 1200°$ F. (See Figure 99, where erosion data supplied by Prof. Finnie has been plotted versus absolute melting temperature.) It was also realized at this point that the large number of particle impacts superimposed on the specimen surface ($\approx$70 million per test, in Series I) was effectively obliterating individual particle effects. For example, it was not clear whether the localized surface melting was the end result of the incessant bombardment of many particles, or whether local melting occurred for each particle impact.

In order to differentiate between the individual particle events, a special set of erosion tests (at 20, 37.5, 60 and 90 degrees) was conducted under conditions

Target: 2024-Al (Annealed)
Test Dust: AR Dust, 43-74μ
Velocity (u): 650 fps
Impingement Angle: 60 deg
Temperature: RT
Magnification: 2400X

Figure 98. Target Surface After 70-Million Particle Impacts.

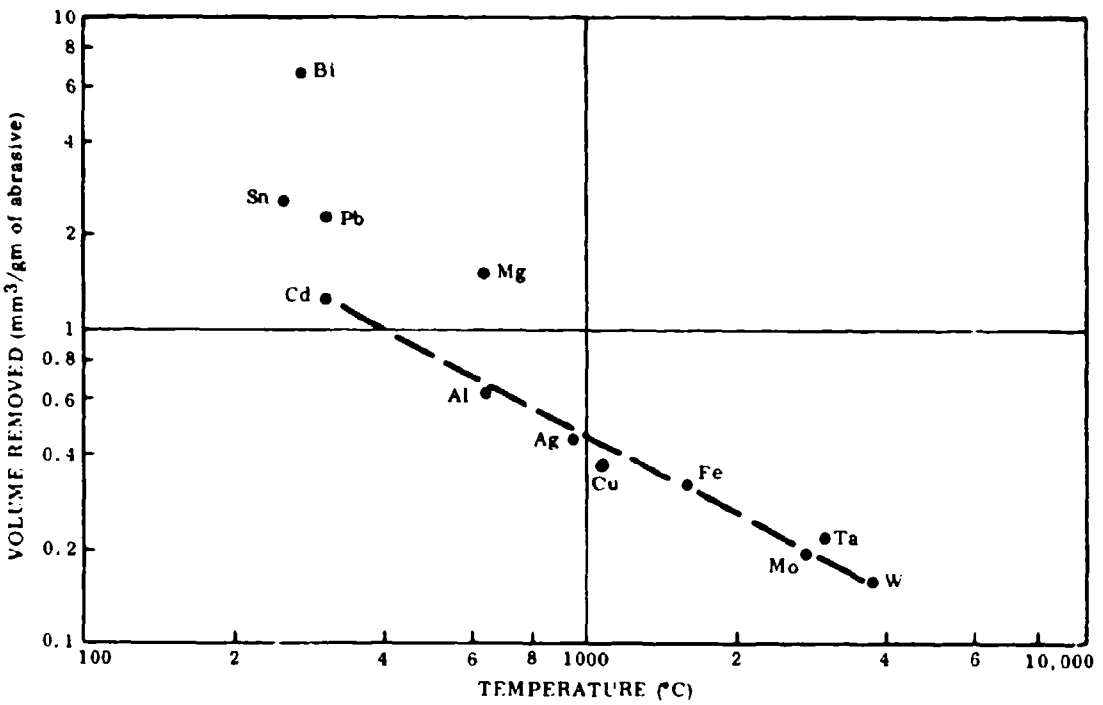

Figure 99. Volume Removal Versus Melting Temperature for Metals Eroded at α = 20 Degrees and Velocity of 450 fps.

identical to Series I and Series II, except that the number of particle impacts was limited to 10,000 per specimen. To insure that the features of surface structure seen by electron microscopy were only a function of test particle impact, and not preexisting roughness, each test coupon was carefully polished with 1.0μ Al_2O_3 powder prior to erosion testing.

It was found that the type of impression an incoming particle (of given size and velocity) makes on the target surface, and the resulting plastic deformation, are very dependent on the configuration and orientation of the leading surface of the particle and much less dependent on target material, heat treat condition, carrier-gas temperature, or angle of impingement. Three different categories of impact impressions were noted. When the particle is oriented such that a flat face (Type I) or an edge (Type II) strikes the surface, very little damage is done to the target surface. An example of both situations is shown in Figure 100. The impact traces are shallow, and very little plastic deformation or heating of the matrix are indicated. The negligible shift in adjacent polishing marks is also an indication of the very minor amount of secondary plastic deformation resulting from such a particle impact. A particle experiencing either of these two types of impact tends to slide or tumble across the target surface, retaining nearly all of its original kinetic energy. However, when a particle corner strikes the target surface (Type III), the particle is effectively snagged and rapidly decelerated, causing considerable surface and subsurface deformation of the target to occur, as shown in Figure 101. The snagged particle has not only gouged a crater in the surface (region A), but has pushed up a ridge of metal in front of the crater (region B). These exposed ridges might be more vulnerable to erosion during subsequent collisions than the adjacent flat surfaces; however, no evidence of actual material removal due to gouging or cratering was seen, i.e., the volume of the ridge was always comparable with the volume of the crater. (The ridge is not a chip, but is firmly attached to the target.) An interesting feature typical of the corner-oriented impact is the compression of the otherwise undisturbed target metal in front of the crater ridge, as evidenced by the movement of the background polishing marks (see Figure 102). This is an indication of the greater magnitude of material deformed and energy absorbed in the corner-oriented impact.

A further characteristic of the corner-oriented collision is the microsmearing effect in the grooved portion of the trace, which is not present on the face or edge-oriented collisions. This is shown graphically in region A, Figure 103. The microsmearing phenomenon, evident for all target alloys and heat-treat conditions, indicates extreme plasticity and thus the presence of localized temperatures approaching or exceeding the melting point of the target. For reasons to be explained later, the corner-oriented collision is believed to be primarily responsible for target material removal (erosion).

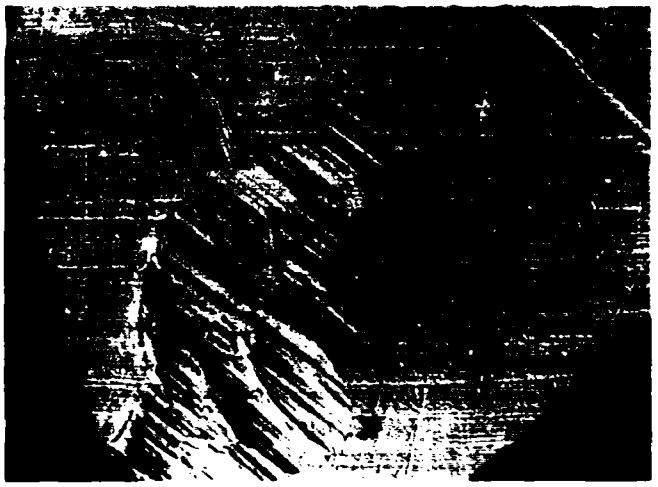

Target: 410 SS (Service Heat Treatment)
Test Dust: AR Dust, 43-74μ
Velocity (u): 650 fps
Impingement Angle: 20 deg
Temperature: RT
Magnification: 2400X

Figure 100. Face-Oriented (A) and Edge-Oriented (B) Particle Impacts.

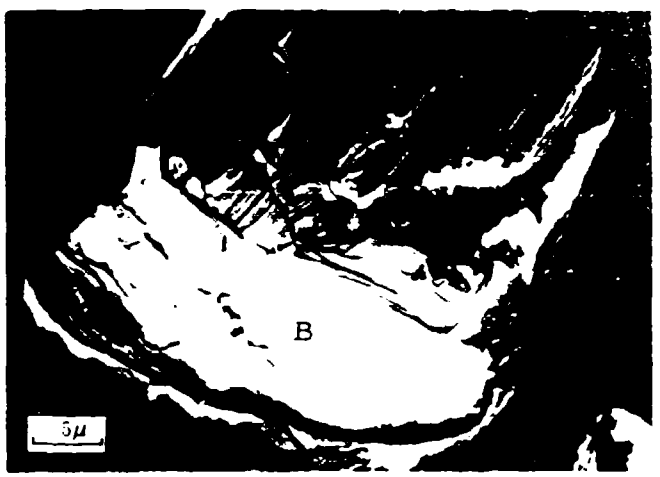

Target: 410 SS (Annealed)
Test Dust: Al_2O_3, 50μ
Velocity (u): 500 fps
Impingement Angle: 30 deg
Temperature: RT
Magnification: 2400X
(A) Impact Crater
(B) Ridge, Crater Rim

Figure 101. Impact Crater Formed by Corner-Oriented Particle Impact. (Arrow Indicates Particle Direction.)

Target: 410 SS (Annealed)
Test Dust: AR Dust, 43-74μ
Velocity (u): 650 fps
Impingement Angle: 30 deg
Temperature: RT
Magnification: 2400X

Figure 102. Impact Craters Formed by Corner-Oriented Particle Impacts. (Arrow Indicates Direction of Particles.)

Target: 410 SS (Annealed)
Test Dust: Al_2O_3, 50μ
Velocity (u): 500 fps
Impingement Angle: 30 deg
Temperature: RT
Magnification: 2400X

Figure 103. Corner-Oriented Impact, Showing Microsmearing of Highly Plastic Metal (A) in Impact Crater.

Because the corner-oriented particle, when slugged, imparts a large portion of its kinetic energy into a small volume of target metal, the intense transfer of energy made available by this impact should promote maximum deformation and deformation heating. Hence, target melting logically should be most plausible for the corner-oriented particle impact. The phenomenological evidence supports this. Dillon (Ref. 25) has shown that for deforming pure aluminum at rapid strain rates, ≈95 percent of the energy expended in plastic working is converted to heat. The

potential for generating extreme temperatures through rapid strain rate was recently demonstrated by Stock and Thompton (Ref. 26), who studied the microstructures of aluminum alloys penetrated by high-velocity projectiles (600-3000 fps). They found definite evidence of target melting within adiabatic shear bands adjacent to the impact zones.

Moreover, work in explosive welding (Ref. 27) has established that when two metal surfaces collide at ballistic velocities (e.g., 1000-3000 fps), very high shock pressures are generated, ranging from 1.5-4.5 million psi at the points of contact. If the analogy can be drawn for dust particles striking a metal target at comparable velocities, the relative resistances to low- and intermediate-temperature surface deformation and flow provided by different heat-treat and cold-work conditions and different carrier-gas temperature would be meaningless (by being effectively erased) at the high pressures and temperatures generated locally.

In general, the average size of impact crater developed by 50μ Al_2O_3 particles was visibly larger on all targets than that developed by SiO_2 particles of comparable diameter and energy level (Test Series I). This is in line with the greater erosiveness observed for Al_2O_3 in Series I. The reason Al_2O_3 particles are more erosive than SiO_2 is believed to be their greater hardness, atomic-bond strength and related refractoriness, factors that should help resist disintegration and/or thermal softening and distortion of the penetrating particle corner during impact. It was also observed that the depths of craters formed at the higher impingement angles (60 and 90 degrees) generally were greater than those for the lower angles studied (20 and 37.5 degrees). Figure 104 is an example of a 50μ Al_2O_3 particle impact on 2024 Al at 90 degrees impingement. The four-sided crater in the photo center shows an outline of the four crystalline faces of the penetrating particle corner. (This demonstration of structural stability of the Al_2O_3 particle corner supports the concept relating particle refractoriness with erosiveness.) This crater is about 8 microns deep, and illustrates the somewhat diminished tendency for directional ridge formation typical of the higher impingement angles.

COMPARISON OF METAL DEFORMATION AND METAL REMOVAL PROCESSES

The erosion or metal removal process is apparently very inefficient, when target erosion loss is contrasted with the average volume of target metal displaced and deformed per particle impact. Typical volume ratios of target metal for the two processes are on the order of 300/1 to 400/1. For example, in Series II, a typical (measured) crater volume $\approx 1200\mu^3$, while the (calculated) average erosion loss per particle is only $\approx 3.5\mu^3$, corresponding to a cube of target metal just $\approx 1.5\mu$ on a cube edge. (This volume corresponds to a minuscule speck on the

Target: 2024-Al (Annealed)
Test Dust: Al_2O_3, 50μ
Velocity (u): 500 fps
Impingement Angle: 90 deg
Temperature: RT
Magnification: 2400X

Figure 104. Impact Crater, Showing Crystalline Faces of the Penetrating Particle.

crater impression; see Figure 105.) Erosion products of this small size (or likely smaller if multiples are formed) could readily pass through the "1μ" fiber-glass collection filters and escape detection. More probably, most of these small erosion products burn up (oxidize) in the air carrier gas before they even reach the filter, particularly if they are hot when formed.

However, evidence of micron- and submicron-size debris is repeatedly observed deposited on erosion surfaces adjacent to many corner-oriented impacts (Figure 106). The size of the apparently molten and resolidified droplets of debris (all targets) is the same order as that predicted by the bulk volume loss data (0.1 - 2.0μ). In addition, standard erosion tests conducted with helium or helium-rich carrier gas invariably produce a deposit of fine metallic particles on the test chamber walls, (presumably unoxidized erosion products) of the same size and general appearance as the debris deposited on the target surfaces (Figure 107). It is believed that these particles collected from the chamber walls are the actual target erosion products, identical in composition and origin to the occasional target surface deposits. Electron diffraction analysis of the collected particles failed to yield an identifiable structure, presumably because of partial surface oxidation. However, it is felt that the collected particles are in fact metallic and not test dust fragments, because of their high electronic conductivity. Because the erosion products are so small (colloidal size), they can readily be suspended in the carrier gases, much like smoke, and be carried throughout the test chamber.

Apparently then, most of the kinetic energy absorbed by the target surface is channeled into "massive" surface deformation and surface heating effects, with actual physical removal (i.e., erosion) of the target surface constituting only about

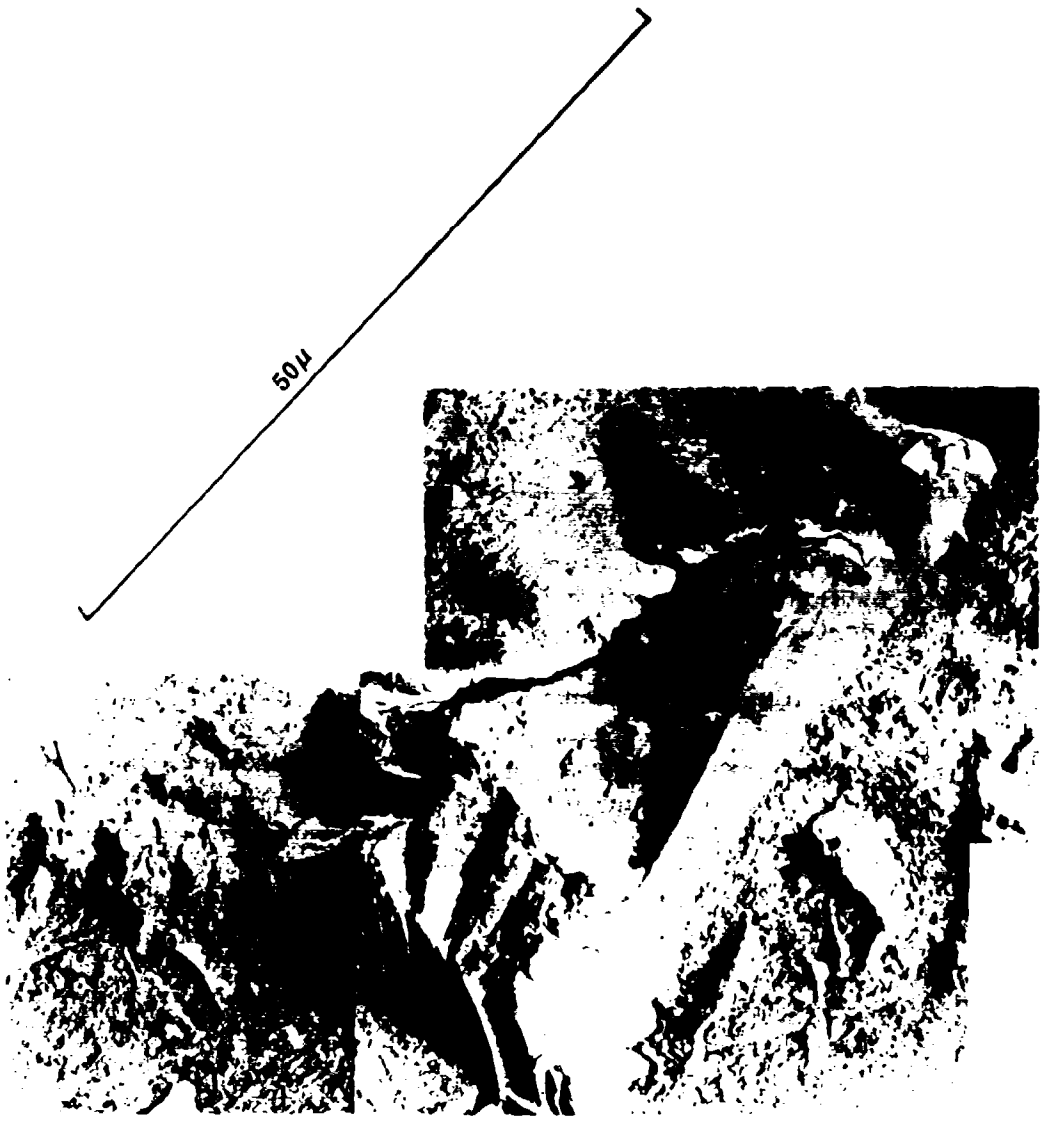

Target: 2024-Al (Annealed)
Test Dust: AR Dust, 43-74μ
Velocity (u): 650 fps
Impingement Angle: 60 deg
Temperature: 400° F
Magnification: 2400X

Figure 105. Typical Crater Size, Corner-Oriented Impact in Aluminum.

Target: Ti-6Al-4V (Annealed)
Test Dust: AR Dust, 43-74μ
Velocity (u): 650 fps
Impingement Angle: 60 deg
Temperature: RT
Magnification: 2400X

Figure 106. Splattered Debris on Target Surface.

Transmission Electron Micrograph
Magnification: 12,000X

Figure 107. Micron-Size Erosion Products (Ti-6Al-4V Target).

1/300-1/400 the total volume of surface metal plastically deformed or displaced per particle. Hence, erosion, per se, is only a very minor by-product of the principal dust-target reactions occurring at the erosion interface.

It is difficult to assess the importance of the metal deformation process to the metal erosion process. Presumably, the majority of the heat generated on impact derives from the plastic straining (deformation) of the target metal. It is interesting that erosion surfaces produced just above the erosion threshold look very

similar to those produced below the threshold (constant particle variety and size and target alloy), where erosion has ceased. That is, myriads of impact craters are seen below the threshold (u = 110 fps) that are just slightly smaller than those above it (u = 178 fps), where the erosion mechanism definitely is functioning (see Figure 108). This is a strong indication that the metal deformation process and the erosion process are not synonymous, but are functionally separate.

SYNTHESIS OF PROBABLE EROSION MECHANISMS

One plausible explanation of the erosion phenomena observed is that, above the threshold energy for erosion, the energy transfer on particle impact (corner-oriented) is sufficient to cause localized target melting in the crater region and subsequent spraying or splattering of micron-size droplets of molten and semi-molten target metal into the gas stream under the high pressures generated by impact. Below the threshold energy for erosion, there is insufficient energy available for significant metal melting and/or splattering. Metal splattering would be most feasible (reasonable) for the corner-oriented impact, where the particle is decelerated over the smallest total contact area, promoting most intense heat buildup, maximum pressurization, and maximum opportunity for target liquating and spraying. In Appendix VI it is shown that there is ample kinetic energy per particle to melt the amount of material removed per particle.

Another possible erosion process is suggested by the frequent observation of broken particle corners embedded (mechanically bonded) in the impact craters they have formed (Figure 109). The sharply outlined cleavage facets of the brittle particle contrast with the smoother deformation-flow pattern of the target metal. This is clear evidence that dust particles can be bonded mechanically to the target surfaces on (corner-oriented) impact. Ostensibly, this bonding is a transient condition; most particles subsequently are extracted from the craters with whatever residual energy they possess or by subsequent particle impacts. But in the extraction process, some bonded target metal may adhere to the particle surface and be removed. The viscous, pock-marked crater surfaces shown in Figures 103 and 110 indicate that this erosion process could be analogous to extracting a rock from soft adherent mud.

At this stage of understanding, it is not possible to say which of the two induced erosion processes is the most influential in setting erosion rate. However, the possible relationships of the two erosion processes are discussed hypothetically in the section, "Development of a Mathematical Model for the Ductile Erosion Mechanism", page 226.

6400X

NO METAL REMOVED

u = 110 fps

7600X

Erosion Threshold

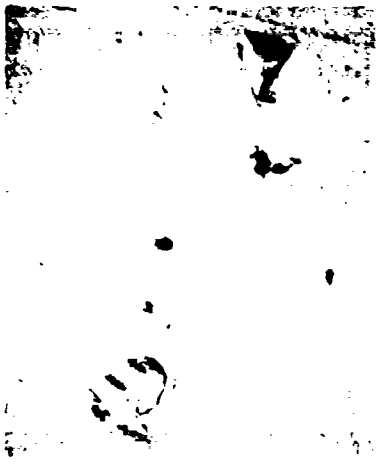

4500X

METAL REMOVED

u = 178 fps

7600X

Target: 410 SS (Annealed)
Test Dust: AR Dust, 0-43μ
Velocity (u): 110 fps and 178 fps
Impingement Angle: 37.5 deg
Temperature: RT

Figure 105. Impact Craters in a 410 SS Target Just Above and Just Below the Erosion Threshold.

Target: Ti-6Al-4V (Annealed)
Test Dust: AR Dust, 43-74μ
Velocity (u): 650 fps
Impingement Angle: 60 deg
Temperature: 400° F
Magnification: 24 0X

Figure 109. Fractured Dust Particle Embedded in Target Surface.

Target: 2024-Al (Annealed)
Test Dust: AR Dust, 43-74μ
Velocity: 650 fps
Impingement Angle: 37.5 deg
Temperature: RT
Magnification: 2400X

Figure 110. Viscous, Pock-Marked Crater Surface.

OBSERVATIONS USING SCANNING ELECTRON MICROSCOPY

Standard replica electron microscopy had been used to this point to observe eroded surfaces. With this technique, a very thin replica of the target surface is examined, and the minimum magnification available is 2400X. With scanning electron microscopy, the eroded target metal is viewed directly from 50 to 30,000X magnification. Furthermore, the extremely large depth of focus available with a scanning electron microscope provides the actual three-dimensional appearance of the surface.

To confirm and further elucidate the standard electron microscope results, scanning electron microscopy was used on a few carefully selected erosion specimens. Figure 111 shows a 2024 aluminum surface eroded at 37.5 degrees. This specimen was chosen specifically to examine the ripples that occur on heavily eroded surfaces. The light areas in the picture correspond to the crests of the ripples. Figure 112 is a portion of Figure 111 at a higher magnification. The eroded surface is quite rough, and no evidence of micromachining is observed. Rather, the surface is one of extreme plasticity containing many small discrete metallic particles on the order of 1μ. To the authors' knowledge, this is the first conclusive evidence of micron-size erosion products (in situ). The size of the particles compares well with that predicted from weight loss data and observed previously with replica electron microscopy.

Figure 113 is also a portion of Figure 111 at a higher magnification. The arrow indicates a dust particle that is embedded in the eroded surface. With scanning electron microscopy, it is simple to differentiate between metallic and nonmetallic particles, because a nonconducting material will become charged by the electron beam and cause distortion of the photograph. In Figure 113, the dark band on either side of the particle is a result of the electrically charged dust particle.

Single particle impacts on polished target surfaces were also examined. Figure 114 is an example of an Arizona Road Dust particle impact on 410 stainless steel. The velocity was 650 fps at an impingement angle of 37.5 degrees. The particle has created a crater on the polished surface, and the metal has been extruded up around the circumference of the crater. The most interesting feature of this photograph is the 1μ, rounded metallic particle (residual erosion product) residing in the bottom of the crater. The physical appearance of the dust particle/target metal collision is one of extreme plasticity of the metal, indicating that high localized heating occurred during impact.

The results of the scanning electron microscopy observations further confirm the conclusions arrived at previously by standard electron microscopy methods. The surface of a heavily eroded specimen appears to have been in a molten or semi-molten state, containing much debris in the form of discrete micron- and sub-micron-size metallic particles. Dust particles frequently are found embedded in the target surface. The erosion mechanisms induced from prior studies of erosion phenomena (liquid-metal splattering and particle/target metal bonding) are supported substantially by the scanning electron microscopy work.

SUMMATION OF ALL MECHANISM-RELATED FINDINGS

Corner-oriented particle impacts cause the preponderance of erosion damage to metal targets. The energy absorbed by the target is translated into both metal

Target: 2024-Al (Annealed)
Test Dust: AR Dust, 43-74μ
Velocity (u): 650 fps
Impingement Angle: 37.5 deg
Temperature: RT
Magnification: 170X

Figure 111. Ripple Formation on Eroded Surface of Aluminum (Scanning Electron Microscopy).

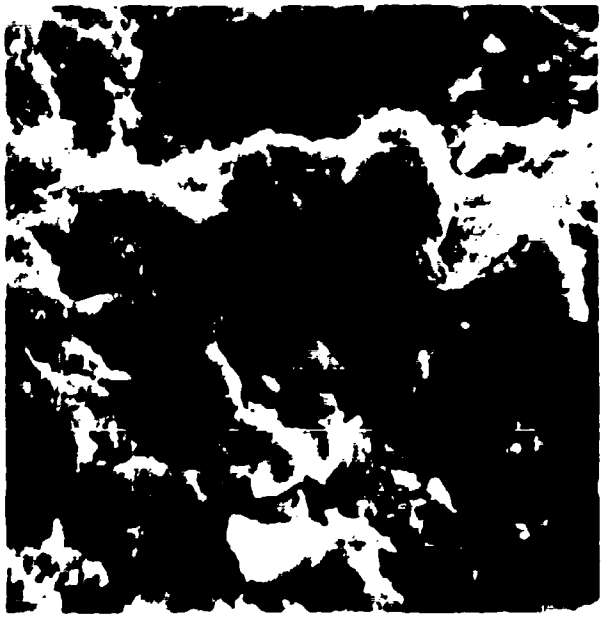

Target: 2024-Al (Annealed)
Test Dust: AR Dust, 43-74μ
Velocity (u): 650 fps
Impingement Angle: 37.5 deg
Temperature: RT
Magnification: 1700X

Figure 112. Magnified View of Figure 111 Showing Metallic Debris.

Target: 2024-Al (Annealed)
Test Dust: AR Dust, 43-74μ
Velocity (u): 650 fps
Impingement Angle: 37.5 deg
Temperature: RT
Magnification: 850X

Figure 113. Magnified View of Figure 111 Showing an Embedded Dust Particle.

Target: 410 SS (Annealed)
Test Dust: AR Dust, 43-74μ
Velocity (u): 650 fps
Impingement Angle: 37.5 deg
Temperature: RT
Magnification: 4250X

Figure 114. Impact Crater, Corner-Oriented Impact (Scanning Electron Microscopy).

deformation and metal removal, the metal deformed (per impact) typically being 300-400 times greater in volume than that removed or eroded.

Two probable erosion processes have been induced from the phenomenological study. Both processes rely upon the intense heat generated by kinetic energy conversion on particle impact. The first is the splattering of submicron-size droplets of molten target metal from the impact crater. The second is the mechanical bonding of highly plastic target metal to the particle surface.

The amount of erosion per particle is proportional to the particle kinetic energy. Inasmuch as the quantity of target metal that can be heated to melting also is proportional to available particle energy, the erosion-energy correlation seems logical.

Because of the implication that local surface temperatures are at or near the target melting point during the erosion process, it is not surprising that variations in low temperature strength and hardness characteristics have little or no bearing on relative erosion resistance within a given target material.

DEVELOPMENT OF A MATHEMATICAL MODEL FOR THE DUCTILE EROSION MECHANISM

Erosion data on ductile metals indicate that the amount of material removed, per particle impinging on the target surface, is proportional to the particle kinetic energy. The results show that this dependence is true over a wide range of particle sizes, velocities, and energies. In addition to this behavior, the weight loss due to erosion was found to be strongly dependent on impingement angle. In all instances the maximum weight loss occurred at angles in the 30- to 40-degree range.

Examination of the eroded target surface by electron microscopy provided considerable information about the erosion mechanism for ductile metals. The results of these studies indicate that corner-oriented impacts are responsible for the majority of the material removal, and that erosion occurs by localized melting and splattering or adherence to the particles.

Based on the experimental evidence, an approximate theory for erosion of ductile materials can be developed that properly describes the angle of impingement effect while retaining the correct dependence on particle kinetic energy. The overall mechanism is assumed to be composed of two separate erosion mechanisms, called mechanism 1 and mechanism 2. Mechanism 1 characterizes the erosion due to localized melting followed by partial splattering. Mechanism 2 accounts for material removal due to the process of localized melting, partial adherence or bonding to the particle, and subsequent dislodgement by later impacts.

If we assume that the particles that are "snagged" by the target transfer all of their kinetic energy into localized melting of the target, then the amount melted is given by the expression

$$W = \varphi(\alpha)\left[\frac{\frac{1}{2}\,Nu^2}{Q}\right], \tag{17}$$

where W is the grams of target material melted by particles of mass N and velocity u, Q is the energy required to heat and melt 1 gram of target, and $\varphi(\alpha)$ is the probability that a particle impacting the target at an angle α will be snagged by the target. The energy Q required for melting 1 gram of target material may be calculated from the equation

$$Q = C_{p,t}\Delta T + H_F \tag{18}$$

where $C_{p,t}$ is the specific heat of the target, H_F is the heat of fusion of the target, and ΔT is the difference between the actual target temperature and its melting temperature.

We shall assume that the probability of snagging is proportional to the ratio of the normal component of the particle force to the total force; i.e.,

$$\varphi(\alpha) \propto \frac{F \sin\alpha}{F} = \sin\alpha\,,$$

or

$$\varphi(\alpha) = \varphi(90 \text{ deg}) \sin\alpha\,. \tag{19}$$

Here φ(90 degrees) is the probability of snagging when α = 90 degrees. Combining equations (17) and (19) yields the following relationship between the amount melted and the impact angle:

$$W = \varphi(90 \text{ deg}) \sin\alpha \left[\frac{\frac{1}{2}\,Nu^2}{Q}\right] \tag{20}$$

MECHANISM 1 (MELTING AND SPLATTERING)

The majority of the melted material is created in the vicinity of point P (see Figure 115) on the target crater-particle interface. This point coincides with the particle corner causing the erosion, since, in first approximation, maximum

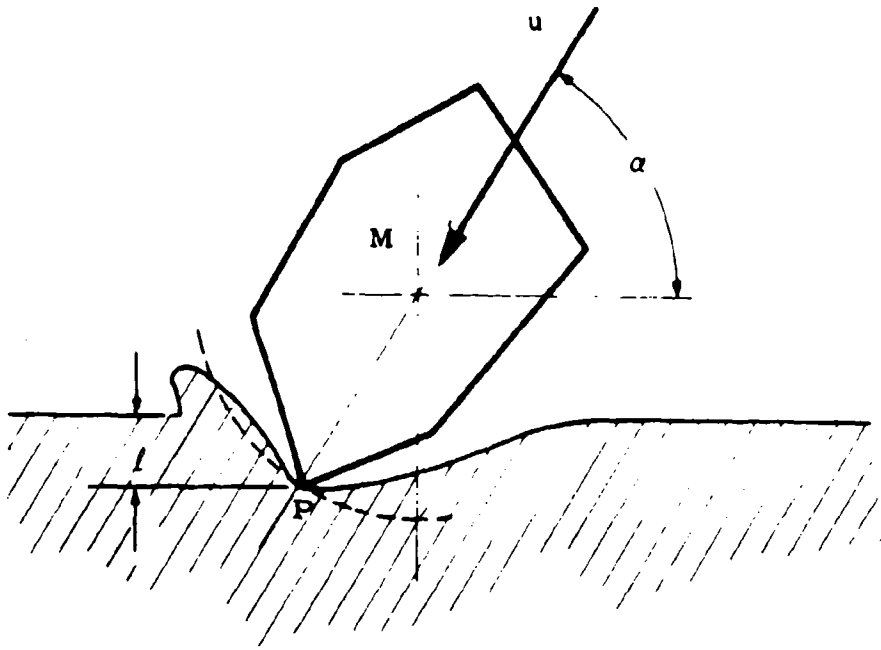

Figure 115. Erosion Due to a Corner-Oriented Impact.

liquation is expected to occur in the vicinity of the particle corner. A portion of this liquid material is squeezed out of the vicinity of point P. The probability that this material will escape from the interface should be a function of how far point P is below the target surface. This distance is shown in Figure 115 as ℓ. If the crater can be assumed to be roughly spherical, then the distance ℓ can be related to the angle of impact by an equation of the form

$$\ell = \ell_{max} \sin \alpha ,$$

where ℓ_{max} is the depth of point P when α = 90 degrees. Now the probability ψ, for splattering of the liquid at point P, is 1 when ℓ = 0 and 0 when $\ell = \ell_{max}$. Thus

$$\psi(\alpha) = (\ell_{max} - \ell)/\ell_{max} = 1-\sin\alpha . \qquad (21)$$

It then follows from equations (20) and (21) that the amount of material removed by splattering (mechanism 1) is given by the expression

$$W_{R,1} = \eta\psi(\alpha)W$$

$$= \eta\psi(90 \text{ deg}) \sin\alpha (1-\sin\alpha)\left[\frac{\frac{1}{2} Nu^2}{Q}\right] , \qquad (22)$$

where η is the fraction of the splattered material that acually escapes; i.e., $1 - \eta$ is the fraction that redeposits on the target surface. We note that this mechanism shows maximum erosion at an angle of 30 degrees and zero erosion at angles of 0 and 90 degrees.

MECHANISM 2 (MELTING + BONDING + DISLODGEMENT)

Since $\psi(\alpha)$ is the probability for splattering of the melted material, then $1 - \psi$ is the probability that the melted material will remain in the vicinity of point P, and $(1 - \psi)W$ represents the amount of target material remaining at the interface. This material may solidify and become partially bonded to the snagged particle. Later impacts may then dislodge the particle, causing it to carry away a portion of the solidified target material. We define ζ as the fraction of $(1 - \psi)W$ that is carried away by this mechanism; i.e.,

$$W_{R,2} = \zeta(1 - \psi)W$$
$$= \zeta(90 \text{ deg}) \sin^2\alpha \left[\frac{\frac{1}{2} Nu^2}{Q}\right], \quad (23)$$

where $W_{R,2}$ stands for the amount of target material removed by mechanism 2. This mechanism shows maxtmum erosion at an impact angle of 90 degrees.

CORRELATION WITH EXPERIMENTAL RESULTS

The overall erosion mechanism must be a combination of mechanisms 1 and 2; i.e.,

$$W_R = W_{R,1} + W_{R,2}$$
$$= K_{R,1}\left(\frac{1}{2} Nu^2\right)[\sin\alpha (1 - \sin\alpha)] + K_{R,2}\left(\frac{1}{2} Nu^2\right)\sin^2\alpha, \quad (24)$$

where

$$K_{R,1} = \epsilon(90 \text{ deg})\eta/Q \text{ and } K_{R,2} = \epsilon(90 \text{ deg})\zeta/Q . \quad (25)$$

Equation (24) may now be used in conjunction with the experimental data to evaluate the constants $K_{R,1}$ and $K_{R,2}$. Figures 116 through 123 show the experimentally determined weight erosion factor versus impingement angle curves for a number of target materials and two different particle types. The weight erosion factor ϵ is defined as the target weight loss in milligrams per gram of impacting particles.

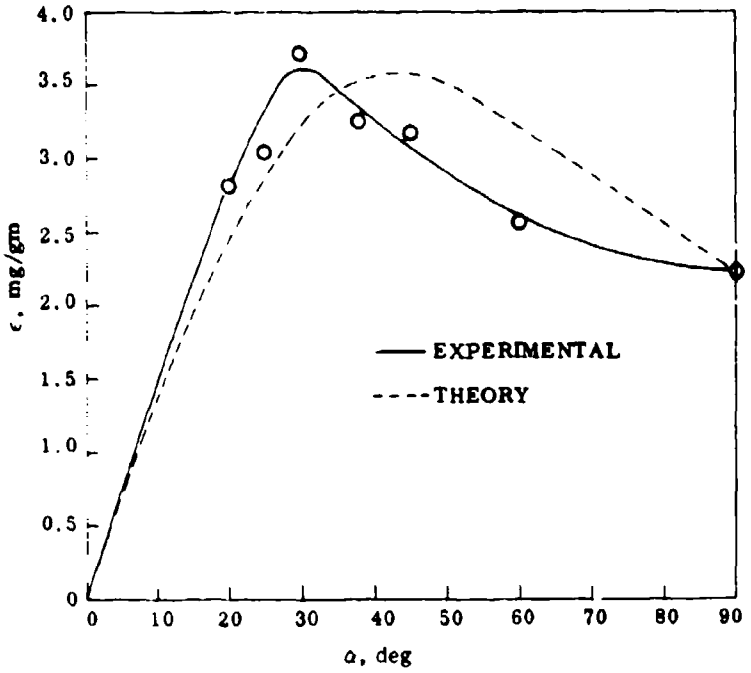

Figure 116. Weight Erosion Factor Versus Impingement Angle for 50μ Al_2O_3 Particles Impacting Ti-6Al-4V at a Velocity of 500 fps.

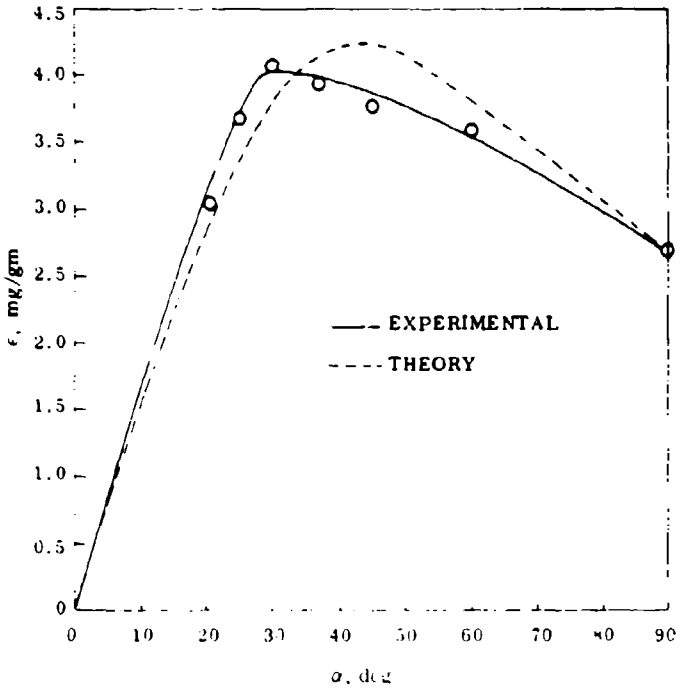

Figure 117. Weight Erosion Factor Versus Impingement Angle for 50μ Al_2O_3 Particles Impacting 17-7PH Stainless Steel at a Velocity of 500 fps.

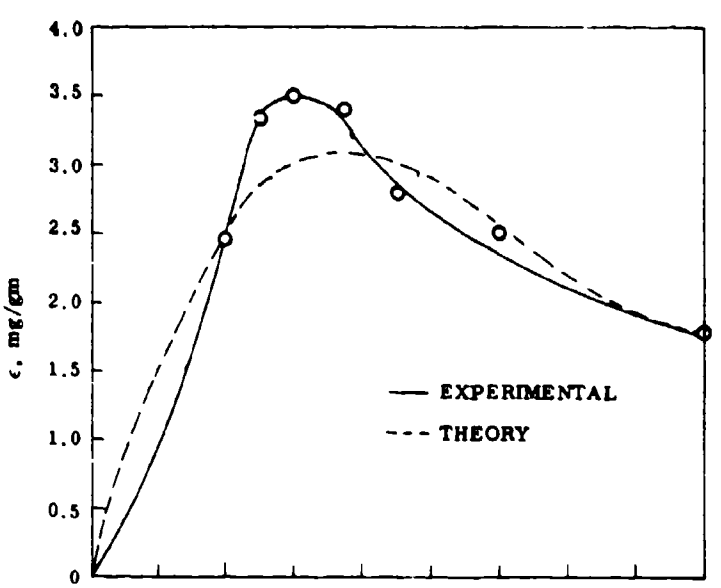

Figure 118. Weight Erosion Factor Versus Impingement Angle for 50μ Al_2O_3 Particles Impacting 2024 Al at a Velocity of 500 fps.

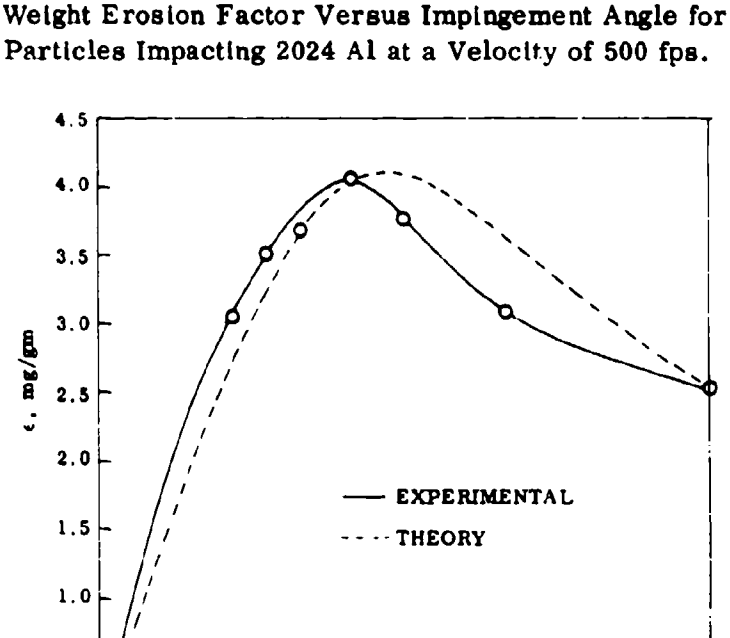

Figure 119. Weight Erosion Factor Versus Impingement Angle for 50μ Al_2O_3 Particles Impacting 410 Stainless Steel at a Velocity of 500 fps.

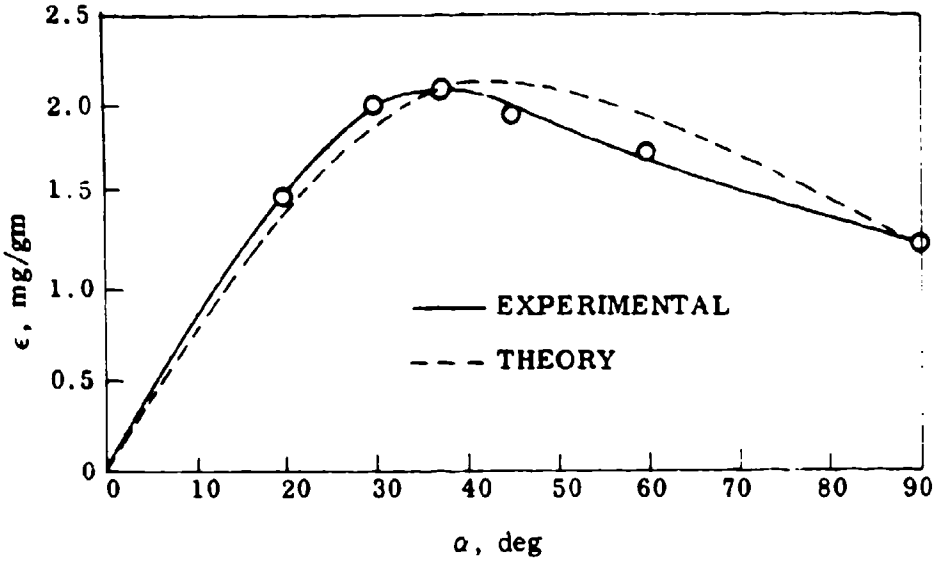

Figure 120. Weight Erosion Factor Versus Impingement Angle for 43-74μ Arizona Road Dust Impacting Ti-6Al-4V at a Velocity of 650 fps.

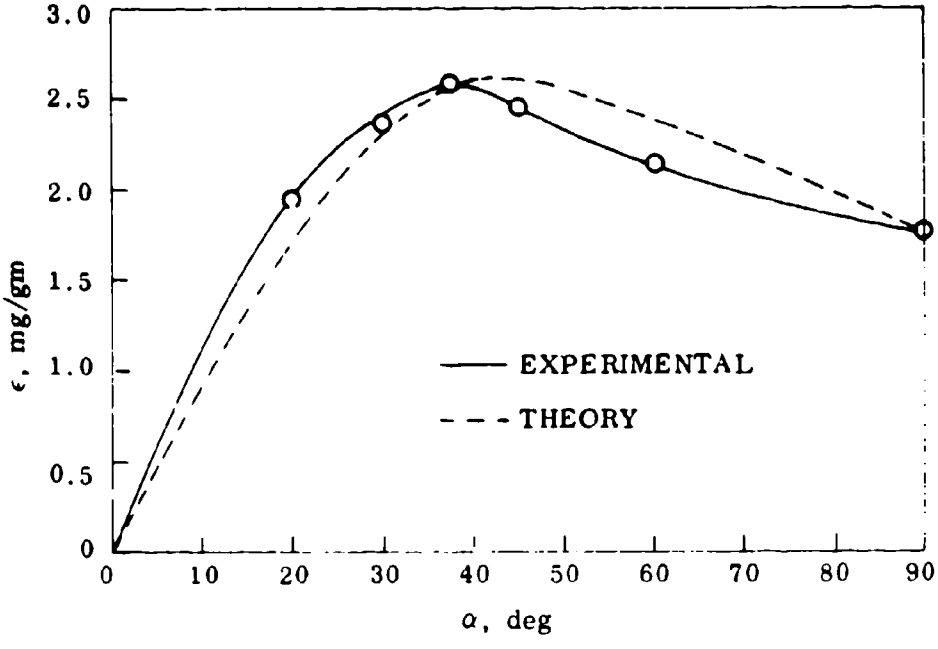

Figure 121. Weight Erosion Factor Versus Impingement Angle for 43-74μ Arizona Road Dust Impacting 17-7PH Stainless Steel at a Velocity of 650 fps.

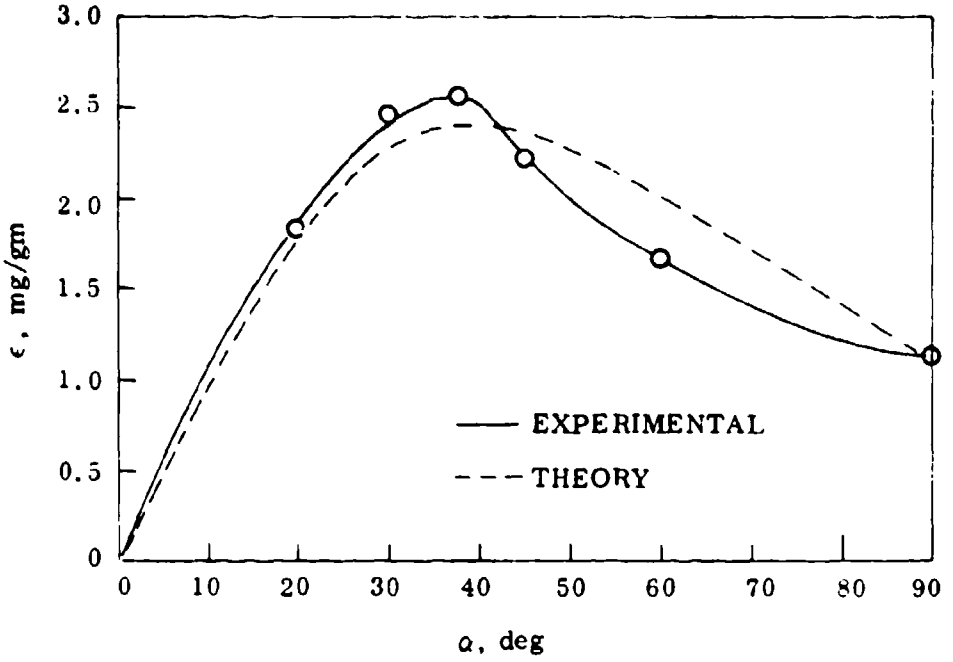

Figure 122. Weight Erosion Factor Versus Impingement Angle for 43-74μ Arizona Road Dust Impacting 2024 Al at a Velocity of 650 fps.

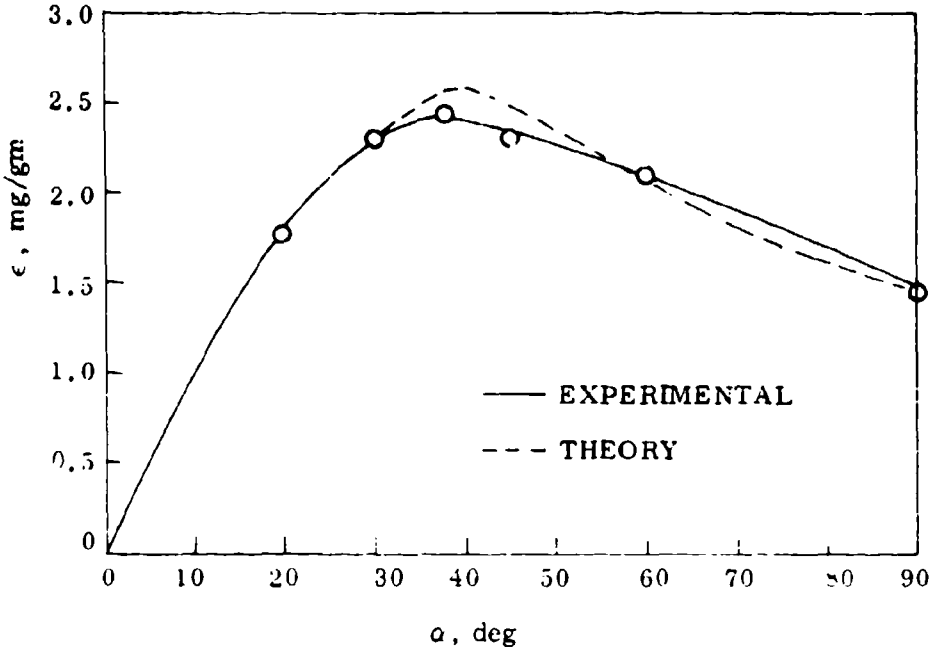

Figure 123. Weight Erosion Factor Versus Impingement Angle for 43-74μ Arizona Road Dust Impacting 410 Stainless Steel at a Velocity of 650 fps.

In terms of the weight erosion factor, equation (24) becomes

$$\epsilon_m = \epsilon_1 + \epsilon_2$$

$$= K_{R,1}\left(\frac{1}{2}u^2\right)\left[\sin\alpha(1 - \sin\alpha)\right] + K_{R,2}\left(\frac{1}{2}u^2\right)\sin^2\alpha\,, \qquad (26)$$

where the subscript m denotes theoretical erosion due to mechanisms 1 and 2. Now at $\alpha = 90$ degrees, $\epsilon_1 = 0$ and

$$\epsilon_m = \epsilon_2 = K_{R,2}\left(\frac{1}{2}u^2\right).$$

Thus, from the experimental data, and knowing the particle velocity, the constant $K_{R,2}$ can easily be found. Knowing $K_{R,2}$, the erosion (ϵ_2) due to mechanism 2 can be calculated as a function of impact angle. Subtracting ϵ_2 from ϵ then gives ϵ_1, the weight erosion factor for mechanism 1 alone. The constant $K_{R,1}$ can then be evaluated by fitting the first term (ϵ_1) of equation (26) to the $\epsilon - \epsilon_2$ curve, treating $K_{R,1}$ as an adjustable constant. With $K_{R,1}$ and $K_{R,2}$ known, the theoretical weight erosion factor ϵ_m can be determined as a function of α from equation (26). Figures 116 through 123 compare the theory and experimental data. Agreement is fairly good, particularly with the Arizona Road Dust. Table XXVI lists the constants $K_{R,1}$, $K_{R,2}$ and the ratio $K_{R,2}/K_{R,1}$ for each of the target material-particle combinations.

The notable (and unpredictable) variation of the system constants $K_{R,1}$ and $K_{R,2}$ tends to confirm the complexity of the (inferred) material property parameters controlling erosion. The subject constants (and related parameters) are obviously functions of certain (as yet unidentified) target material and dust material properties, and probably the carrier-gas properties as well (Ref. Test Series V and VI). Cursory plots of erosion loss (pure metals) versus such target material properties as elastic modulus, absolute melting temperature, heat required for melting unit mass ($C_{p,t}\Delta T + H_F$), and liquid metal surface tension all give the correct relative order of erosion values, but not a high degree of absolute predictability. However, all of these material parameters are directly relatable to the basic atomistic makeup of a material and its structure; i.e., atomic bond strength and stored potential energy, etc. The size (length) of the impact craters studied indicates that particle kinetic energy is transferred to the target very rapidly, on the order of microseconds. Hence, erosion conceivably could be considered a dynamic process, wherein the normal static, time-dependent processes such as deformation and diffusion do not apply (insufficient time for their activation). In this context, erosion might occur simply from decohesion of the target material. In either case (i.e., decohesion or melting), the basic target

TABLE XXVI. EROSION CONSTANTS

Target Material	Dust Variety	Particle Velocity (fps)	$K_{R,1}$ (gm/ft-lb$_f$) (x 10^{-3})	$K_{R,2}$ (gm/ft-lb$_f$) (x 10^{-4})	$K_{R,2}/K_{R,1}$
2024 Al	Al_2O_3 (50μ)	500	1.22	2.10	0.173
Ti-6Al-4V	↓		0.825	2.60	0.315
17-7PH			0.973	3.15	0.323
410 SS			0.948	2.96	0.314
2024 Al	Arizona Road Dust (43-47μ)	650	0.365	0.788	0.216
Ti-6Al-4V	↓		0.277	1.01	0.365
17-7PH			0.342	1.22	0.356
410 SS			0.370	0.809	0.218

material properties discussed would tend to relate to the disposition of particle energy absorbed. In all probability, the actual material removal process is further complicated by such parameters as the oxidation potential of the target.

LITERATURE CITED

1. Finnie, I., EROSION OF SURFACES BY SOLID PARTICLES, Wear, Vol. 3, 1960, pp. 87-103.

2. Sheldon, G. L., and Finnie, I., MECHANISMS OF MATERIAL REMOVAL IN THE EROSIVE CUTTING OF BRITTLE MATERIALS, ASME Paper No. 65-WA/Prod-8.

3. Sheldon, G. L., and Finnie, I., ON THE DUCTILE BEHAVIOR OF NOMINALLY BRITTLE MATERIALS DURING EROSIVE CUTTING, ASME Paper No. 65-WA/Prod-7.

4. Finnie, I., Wolak, J., and Kabin, Y., EROSION OF METALS BY SOLID PARTICLES, Journal of Materials, Vol. 2, No. 3, Sept. 1967, pp. 682-700.

5. Bitter, J. G. A., A STUDY OF EROSION PHENOMENA, PARTS I AND II, Wear, Vol. 6, 1963, pp. 5-21 and 169-190.

6. Wood, C. D., and Espenschade, P. W., MECHANISMS OF DUST EROSION, SAE Transactions, Vol. 73, 1965, pp. 515-523.

7. Neilson, J. H., and Gilchrist, A., EROSION BY A STREAM OF SOLID PARTICLES, Wear, Vol. 11, 1968, pp. 111-112.

8. Head, W. J., Pacela, T., and Poole, J., THE ALLISON-PURDUE DUST TECHNOLOGY PROGRAM, Allison Division of General Motors Corporation, Indianapolis, Indiana, Final Report on Phase I, 1 March 1967.

9. Compton, W. A., and Steward, K. P., DUST EROSION OF COMPRESSOR MATERIALS - EXPERIENCE AND PROSPECTS, paper presented at the Gas Turbine Conference and Products Show, Washington, D.C., March 17-21, 1968 (ASME Publication No. 68-GT-55).

10. Compton, W. A., Steward, K. P., and Mnew, H., COMPOSITE MATERIALS FOR TURBINE COMPRESSORS, Final Technical Report AFML-TR-68-31, Air Force Materials Laboratory, Wright-Patterson Air Force Base, Ohio, June 1968.

11. Finnie, I., and Kabil, Y. H., ON THE FORMATION OF SURFACE RIPPLES DURING EROSION, Wear, Vol. 8, 1965, pp. 60-69.

12. Miller, Lt. Roger A., FIELD TESTING THE ARL DUST SEPARATOR, Research Review, Office of Aerospace Research, Vol. VI, No. 1, January 1967.

13. DUST CONCENTRATION MEASUREMENTS ON THE U.S. ARMY OVERLAND TRAIN MARK II, TRECOM Tech. Report 64-16, April 1964.

14. Rapp, G. C., and Rosenthal, S. H., PROBLEMS AND SOLUTIONS FOR SAND ENVIRONMENT OPERATION OF HELICOPTER GAS TURBINES, paper presented at the Gas Turbine Conference and Products Show, Washington, D. C., March 17-21, 1968 (ASME Publication No. 68-GT-37).

15. Spooner, S. H., THE V/STOL AIRCRAFT ENVIRONMENT, paper presented at the Gas Turbine Conference and Products Show, Washington, D.C., March 17-21, 1968 (ASME Publication No. 68-GT-40).

16. Rogers, Sheridan J., EVALUATION OF THE DUST CLOUD GENERATED BY HELICOPTER ROTOR DOWNWASH, USAAVLABS Technical Report No. 67-81, U.S. Army Aviation Materiel Laboratories, Fort Eustis, Va., March 1968.

17. Montgomery, J. E., and Clark, J. M., Jr., DUST EROSION PARAMETERS FOR A GAS TURBINE, SAE Summer Meeting, Atlantic City, N.J., June 1962.

18. Thomas, Gary E., EFFECTIVENESS OF AN INERTIAL AIR CLEANER IN EXTENDING GAS TURBINE LIFE IN A DUSTY ENVIRONMENT, Final Technical Report No. QR-643, for the U.S. Army Mobility Equipment Research and Development Center by Southwest Research Institute, San Antonio, Texas, March 1968.

19. Journal of the Armed Forces, 6 August 1966.

20. Bianchini, V., and Koschman, R. B., T63 ENGINE SAND AND DUST TOLERANCE, Report No. 66-ENV-18 of Allison Division, General Motors Corporation, 1966.

21. Clark, J. M., Jr., and Wolfe, E. J., FOR INDUSTRY, GAS TURBINE VS. RECIPROCATING ENGINE, Mechanical Engineering, Vol. 88, Nov. 1966, pp. 58-61.

22. Letter comment on preceding article by R. P. Allen of General Electric Co., Mechanical Engineering, Vol. 89, March 1967, pp. 79-80.

23. Sage, W., and Tilly, G. P., THE SIGNIFICANCE OF PARTICLE SIZE IN SAND EROSION OF SMALL GAS TURBINES, The Aeronautical Journal of the Royal Aeronautical Society, Vol. 73, May 1969, pp. 427-428.

24. Tilly, G. P., and Sage, W., A STUDY OF THE BEHAVIOR OF PARTICLES AND MATERIALS IN EROSION PROCESSES, paper No. 69-WA/Met.-6, presented at the ASME Winter Annual Meeting, Los Angeles, Calif., Nov. 16-20, 1969.

25. Dillon, O. W., MECHANICAL BEHAVIOR OF MATERIALS UNDER DYNAMIC LOADS, Springer-Verlag, New York, 1968, pp. 53.

26. Stock, T. A. C., and Thompson, K. R. L., PENETRATION OF ALUMINUM ALLOYS BY PROJECTILES, Metallurgical Transactions, Vol. 1, Jan. 1970, pp. 219-224.

27. Carlson, R. F., Linse, V. D., and Wittman, R. H., EXPLOSIVE WELDING BONDS METALS OVER LARGE AREAS, Materials Engineering, July 1968, pp. 70-75.

28. Shapiro, A. H., THE DYNAMICS AND THERMODYNAMICS OF COMPRESSIBLE FLUID FLOW. Ronald Press Co., New York, N.Y., 1953, Vol. 1, pp. 171.

29. Kennan, J. H., and Kaye, J., GAS TABLES, John Wiley and Sons, New York, N.Y., 1949.

30. Perry, J. H., CHEMICAL ENGINEERING HANDBOOK, McGraw-Hill, New York, N.Y., 1963.

APPENDIX I

SOME FLOW PARAMETERS FOR PARTICULATE CLOUDS

A measure of the drag and inertia of a particle is the "range" or "carry". This is the distance the particle will travel in the direction of its initial velocity when projected into a motionless viscous fluid. The time to travel this distance is theoretically infinite, but the "range" concept is useful as a criterion for the threshold size for particle damage to surfaces. For example, if the range is less than the boundary layer thickness, then the particle will never reach the surface. Also, the range concept will give a measure (it is simply related to the inertia parameter discussed elsewhere) of the departure of the particle trajectories from the fluid streamlines in the vicinity of a solid body. The larger the range, the more the trajectories will depart from the streamlines in curving flow.

For spherical particles in the Stokesian motion regime ($Re \ll 1.0$), the drag coefficient $C_D = 24/Re$, where the particle Reynolds number, $Re = V D_p/\nu$,

and ν = kinematic viscosity - ft^2/sec

V = velocity - fps

D_p = diameter of particle - ft

The equation of motion of the particle in the direction of the initial velocity, assuming that the fluid drag is the only force acting in this direction, is:

$$m \frac{dV}{dt} = -C_D \frac{1}{2} \rho V^2 A \qquad \text{with } V = V_o \text{ when } t = 0,$$

i.e.,

$$\rho_p \frac{\pi D_p^3}{6} \frac{dV}{dt} = -\frac{24\nu}{V D_p} \frac{1}{2} \rho V^2 \frac{\pi D_p^2}{4}$$

or

$$\frac{dV}{dt} = -\frac{18\mu V}{\rho_p D_p^2} \qquad (27)$$

where m = mass of particle - slugs

ρ_p = density of particle - $slugs/ft^3$

A = projected area of particle - ft^2

ρ = density of fluid - $slugs/ft^3$

μ = absolute viscosity of fluid = $\rho\nu$ slug/ft sec

Solutions of this equation are

$$V = V_o \epsilon^{-\frac{18\mu}{\rho_p D_p^2} t} = V_o \epsilon^{-\frac{t}{\tau}} \qquad (28)$$

$$S = V_o \tau (1 - \epsilon^{-\frac{t}{\tau}}) = S_o (1 - \epsilon^{-\frac{t}{\tau}}) \qquad (29)$$

where $\tau = \rho_p D_p^2 / 18\mu$ is a time constant related to $S_o = V_o \tau$, the "range" or "carry".

It is apparent that τ is the time for the velocity to drop to 36.8 percent of its initial value V_o when the distance travelled will be 63.2 percent of S_o.

The range S_o can also be thought of as the distance that the particle would travel in time τ if its initial velocity V_o were maintained. Plots of velocity and distance against time make these points clear.

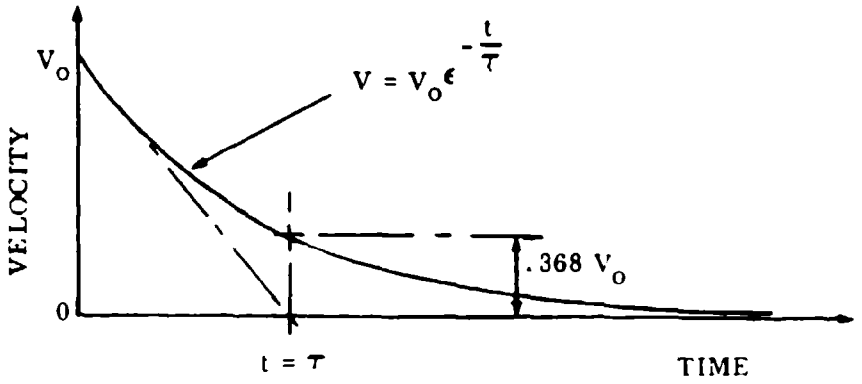

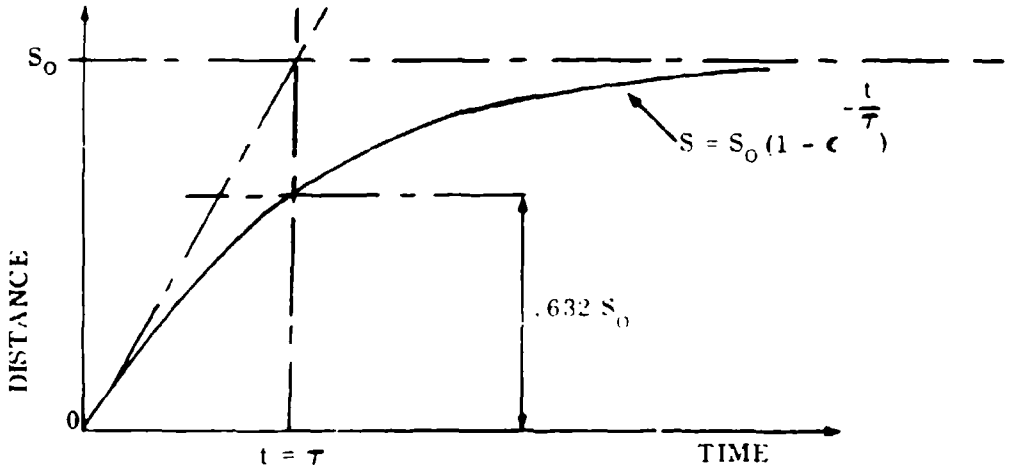

For flow in the vicinity of a solid body, the trajectories of the particles will be determined by the ratio of the range to a characteristic length of the body. For a sphere or cylinder in crossflow, this length has (traditionally) been taken as the radius, giving rise to the so-called inertia parameter $K = 2S_o/D$

$$K = \frac{\rho_p D_p^2 V_o}{9\mu D} \tag{30}$$

The inertia parameter is clearly dimensionless, and the trajectories of all particles with the same value K will be geometrically similar so long as the particle can be regarded as a massive point (i.e., its dimensions are small compared to the impacting body) and its presence does not interfere with the flow pattern (i.e., the concentration is sufficiently small).

For flow of particles in a fluid falling under the influence of gravity, the particles will accelerate until the drag plus bouyancy forces just balance the gravitational force. The terminal (or settling) velocity so reached is given when

$$\frac{1}{2}\rho V_t^2 C_D A + mg\left(\frac{\rho}{\rho_p}\right) = mg \tag{31}$$

where m = mass of the particle - slugs

ρ_p = density of the particle - slugs/ft^3

ρ = density of fluid - slugs/ft^3

A = drag area of particle - ft^2

C_D = drag coefficient

V_t = terminal velocity - fps

g = gravitational acceleration - ft/sec^2

For a spherical particle in the Stokesian regime, this becomes

$$\frac{1}{2}\rho V_t^2 \frac{24}{Re} \frac{\pi D_p^2}{4} = \frac{\pi D_p^3}{6}(\rho_p - \rho) g$$

or

$$V_t = \frac{gD_p^2}{18\mu}(\rho_p - \rho)$$

$$= \frac{gD_p^2 \rho_p}{18\mu}\left(1 - \frac{\rho}{\rho_p}\right) \qquad (32)$$

Substituting from (31) into (32), we get

$$V_t = \frac{gKD}{2V_o}\left(1 - \frac{\rho}{\rho_p}\right)$$

or

$$\frac{V_t V_o}{gD} = \frac{K}{2}\left(1 - \frac{\rho}{\rho_p}\right) \qquad (33)$$

The quantity $V_t V_o / gD$ is called the separation number and is also dimensionless like the inertia parameter K. If the density of the particles is large compared to the density of the propelling fluid, then the separation number = 1/2 the inertia parameter. The separation number is related to a body with characteristic dimension D and is a measure of the separation (or collection) efficiency of that body when impacted by a particulate cloud.

DYNAMICS OF PARTICULATE CLOUDS

Equation of Motion - A particle moving through a fluid with instantaneous velocity $\vec{V}$ will experience a resisting force given by

$$\vec{F} = -\frac{1}{2}\rho(\vec{V} - \vec{U})^2 C_D A \hat{K}$$

$$= -\frac{1}{2}\rho(\vec{W})^2 C_D A \hat{K} \qquad (34)$$

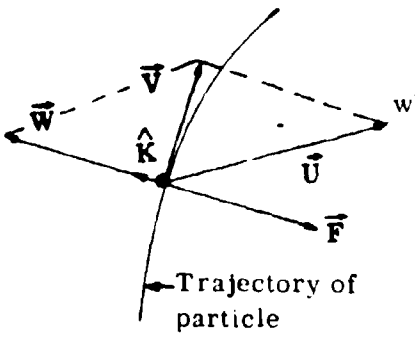

where $\vec{U}$ = local velocity of the fluid

$\vec{W}$ = velocity of the particle relative to the fluid = $\vec{V} - \vec{U}$

ρ = density of the fluid

C_D = drag coefficient of the particle

A = relevant projected area of the particle for the given drag coefficient

$\hat{K}$ = unit vector in the direction of relative motion

Neglecting all other body forces (including gravity), the equation of motion of the particle will be

$$m \frac{d\vec{V}}{dt} = \vec{F} = -\frac{1}{2} \rho (\vec{W})^2 C_D A \hat{K} \tag{35}$$

where m = mass of the particle

or

$$\frac{d}{dt} (\vec{U} + \vec{W}) = -\frac{C_D A \rho}{2m} (\vec{W})^2 \hat{K} \tag{36}$$

SPHERICAL PARTICLE IN UNIFORM VELOCITY FIELD

If the particle is spherical of diameter D_p and density ρ_p, then

$$m = \rho_p \frac{D_p^3}{6} \tag{37}$$

and a good approximation to the drag coefficient (see Figure 124) is

$$C_D = .4 + \frac{24}{Re} \tag{38}$$

with $A = \frac{\pi D^2}{4}$ the projected frontal area

Also,

$$Re = \frac{|\vec{W}| D_p \rho}{\mu} \tag{39}$$

where μ = absolute viscosity of the fluid

If additionally, $\vec{V}$ is in the same direction as $\vec{U}$, then $-\vec{W}$ is also in this same direction, and with $\vec{U} = -U\hat{K}$, $\vec{V} = -V\hat{K}$, and $\vec{W} = W\hat{K}$, we get the scalar equations

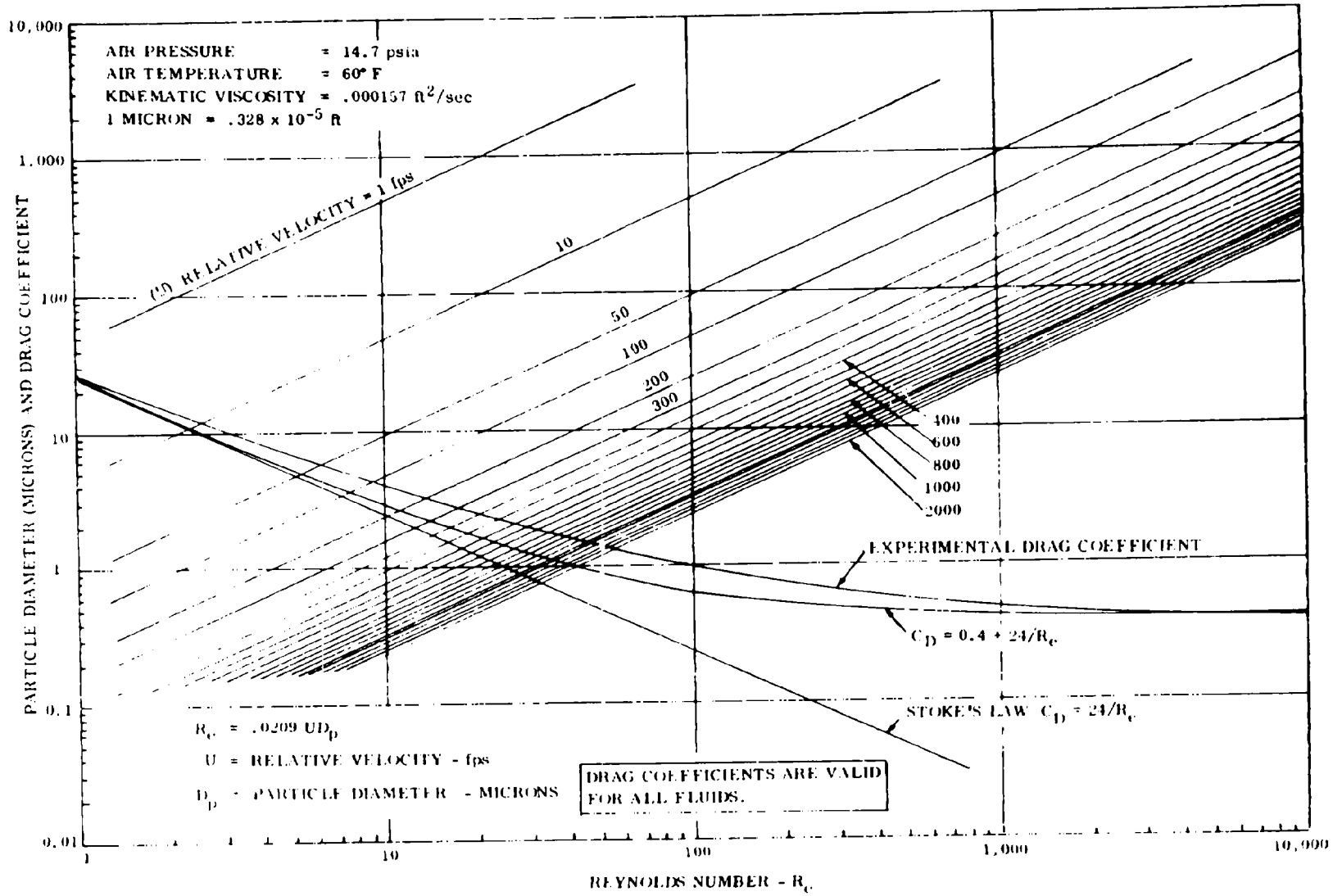

Figure 124. Drag Coefficient and Reynolds Numbers For Spherical Particles in Air.

$$W = U - V$$

and $$\frac{d}{dt}(-U + W) = -\frac{1}{2}\frac{6}{\pi \rho_p D_p^3}\left(.4 + \frac{24\mu}{W D_p \rho}\right)\rho\frac{\pi D^2}{4} W^2$$

$$= -\frac{.3\rho}{\rho_p D_p} W^2 + \frac{18\mu}{\rho_p D_p^2} W) \qquad (40)$$

The factor $18\mu/\rho_p D_p^2 = 1/\tau$ where τ is the Stokesian time constant associated with the range when U = 0. Also, if U is a constant velocity (i.e., a uniform fluid velocity field), then

$$\frac{d}{dt}(-U + W) = \frac{dW}{dt}$$

Putting $$\frac{.3\rho}{\rho_p D_p} = \frac{1}{\delta}$$, we get

$$\frac{dW}{dt} = -\frac{1}{\tau}\left(W + \frac{\tau}{\delta} W^2\right) \qquad (41)$$

which is the differential equation for the relative velocity W.

The solution of this equation is

$$\frac{t}{\tau} = \text{const} - \log\left(\frac{W}{1 + \frac{\tau}{\delta} W}\right)$$

If $$W = W_o \text{ when } t = 0,$$

then $$\text{const} = \log\left[\frac{W_o}{1 + \frac{\tau}{\delta} W_o}\right]$$

and $$t = \tau \log\left[\frac{W_o}{W}\frac{1 + \frac{\tau}{\delta} W}{1 + \frac{\tau}{\delta} W_o}\right] \qquad (42)$$

giving the time to reach a relative velocity W from an initial relative velocity W_o. It will be noted that the time for W to become zero is infinitely large. Also, when $t = \tau$ we have

$$\epsilon = \frac{W_o}{W}\left[\frac{1 + \frac{\tau}{\delta} W}{1 + \frac{\tau}{\delta} W_o}\right]$$

or

$$W = \frac{W_o}{\epsilon}\left\{1 + \frac{\tau}{\delta} W_o \left(1 - \frac{1}{\epsilon}\right)\right\}^{-1}$$

$$= .368\, W_o \left\{1 + .632 \frac{\tau}{\delta} W_o\right\}^{-1} \qquad (43)$$

This shows the influence of the stronger drag coefficient as compared to the Stokesian solution. For Stokesian flow, τ is the time for the relative velocity to drop to 36.8 percent of the initial value, whereas with the stronger drag forces the relative velocity drops to somewhat less than 36.8 percent in time τ, depending on the value of $(\tau/\delta) W_o$. Also, for $1/\delta = 0$ or $W_o \to 0$, the Stokesian equations are regained.

Now equation (41) may be rewritten as

$$W \frac{dW}{dS_{rel}} = -\frac{1}{\tau}\left(W + \frac{\tau}{\delta} W^2\right)$$

or

$$\frac{dW}{dS_{rel}} = -\frac{1}{\tau}\left(1 + \frac{\tau}{\delta} W\right) \qquad (44)$$

where S_{rel} is the distance that the particle travels relative to the fluid.

The solution to equation (44) is

$$\frac{S_{rel}}{\tau} = \text{constant} - \frac{\delta}{\tau} \log\left(1 + \frac{\tau}{\delta} W\right)$$

when

$$S_{rel} = 0 \qquad W = W_o \qquad \text{const} = \frac{\delta}{\tau}\left(1 + \frac{\tau}{\delta} W_o\right)$$

Then,
$$S_{rel} = \delta \log \left(\frac{1 + \frac{\tau}{\delta} W_o}{1 + \frac{\tau}{\delta} W} \right) \tag{45}$$

The distance the particle will travel in time t is given by

$$S = \int V \, dt = \int (U - W) \, dt$$

So
$$S = Ut - \int W \, dt$$

$$= Ut - S_{rel} \tag{46}$$

Substituting for t from equation (42) and S_{rel} from equation (45) gives

$$S = U\tau \log \left[\frac{W_o}{W} \frac{1 + \frac{\tau}{\delta} W}{1 + \frac{\tau}{\delta} W_o} \right] - \delta \log \left[\frac{1 + \frac{\tau}{\delta} W_o}{1 + \frac{\tau}{\delta} W} \right]$$

$$= U\tau \log \left[\frac{W_o}{W} \left(\frac{1 + \frac{\tau}{\delta} W}{1 + \frac{\tau}{\delta} W_o} \right)^{1 + \frac{\delta}{U\tau}} \right] \tag{47}$$

and this is the distance travelled by the particle to attain a relative velocity W from an initial relative velocity W_o in a uniform fluid velocity field of value U.

If the particle is introduced into the stream with initial velocity zero, then the initial relative velocity $W_o = U$ and the instantaneous relative velocity $W = U - V$. Equation (47) becomes

$$S = U\tau \log \left[\left(\frac{U}{U - V} \right) \left(\frac{1 + \frac{\tau}{\delta} (U - V)}{1 + \frac{\tau}{\delta} U} \right)^{1 + \frac{\delta}{U\tau}} \right]$$

or putting
$$\lambda = \frac{V}{U},$$

$$S = U\tau \log \left[\left(\frac{1}{1-\lambda} \right) \left(\frac{1 + \frac{\tau U}{\delta}(1-\lambda)}{1 + \frac{\tau U}{\delta}} \right)^{1 + \frac{\delta}{U\tau}} \right] \qquad (48)$$

Similarly, equation (42) for the time becomes

$$t = \tau \log \left[\left(\frac{1}{1-\lambda} \right) \frac{1 + \frac{\tau U}{\delta}(1-\lambda)}{1 + \frac{\tau U}{\delta}} \right] \qquad (49)$$

Now $\tau U/\delta = \rho D_p U/60\mu = Re_o/60$, where Re_o is the Reynolds number for the particle based on fluid velocity U. Also writing $U\tau = S_o$ - the "range" for Stokesian motion, equations (48) and (49) may be written

$$\frac{S}{S_o} = \log \left(\frac{1}{1-\lambda} \right) + \left(1 + \frac{60}{Re_o} \right) \log \left[1 - \frac{\lambda}{1 + \frac{60}{Re_o}} \right] \qquad (50)$$

and

$$\frac{t}{\tau} = \log \left(\frac{1}{1-\lambda} \right) + \log \left[1 - \frac{\lambda}{1 + \frac{60}{Re_o}} \right] \qquad (51)$$

For pure Stokesian motion, these equations reduce to the limiting equations as $Re_o \rightarrow 0$

$$\frac{S}{S_o} = \log \left(\frac{1}{1-\lambda} \right) - \lambda \qquad (52)$$

and

$$\frac{t}{\tau} = \log \left(\frac{1}{1-\lambda} \right) \qquad (53)$$

All four above equations are dimensionless and will therefore be valid for any spherical particle in any viscous fluid. The parameters Re_o, S_o and τ will, however, depend on the properties of the particular fluid and particle considered.

It should be noted that

$$S_o = U\tau = U D_p^2 \rho_p / 18\mu = \left[\frac{D_p \rho_p}{18 \rho}\right] Re_o \qquad (54)$$

Equation (50) has been plotted on Figure 125 as $\lambda = V/U$ against S/S_o, with Re_o as parameter and on Figure 126 as S/S_o versus Re_o with $\lambda = V/U$ as parameter.

These plots can be used in conjunction with Figures 124 and 127 to find the acceleration distances of spherical particles (or equivalent Stokesian spheres) in viscous fluids as follows:

Example: 200μ Arizona Road Dust Sphere in a 1000 fps stream of 60° F, 14.7 psia air

$$\rho_{air} = 2.7 \times \frac{14.7}{520} = 0.0765 \text{ lb/ft}^3$$

$$\mu_{air} = .0432 \text{ lb/hr-ft (From Figure 128)}$$

$$D_p = 200\mu = 6.56 \times 10^{-4} \text{ ft}$$

$$\therefore Re_o = \frac{U D_p \rho_{air}}{\mu_{air}} = \frac{3600 \times .0765}{.0432} \times (.328 \times 10^{-5}) U D_p$$

$$= .0209 U D_p \qquad \text{where U is in fps, } D_p \text{ is in microns}$$

$$= 4180$$

(or, directly from Figure 124, $Re_o = 4120$)

$$\tau = \frac{\rho_p D_p^2}{18\mu_{air}}$$

$$\rho_p = 2.46 \times 62.4 \text{ lb/ft}^3$$

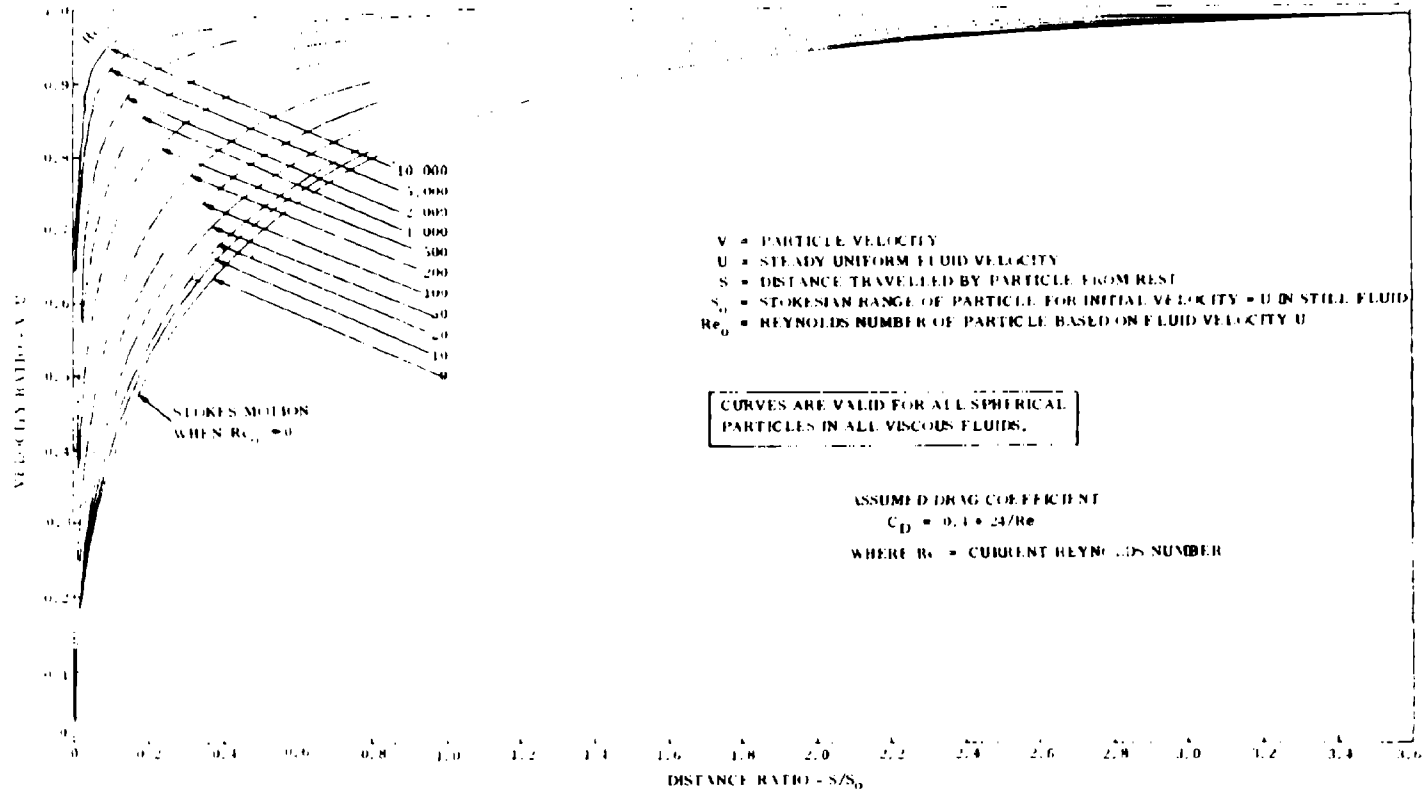

Figure 125. Acceleration Distances of Spherical Particles in a Viscous Fluid With Uniform Steady Velocity.

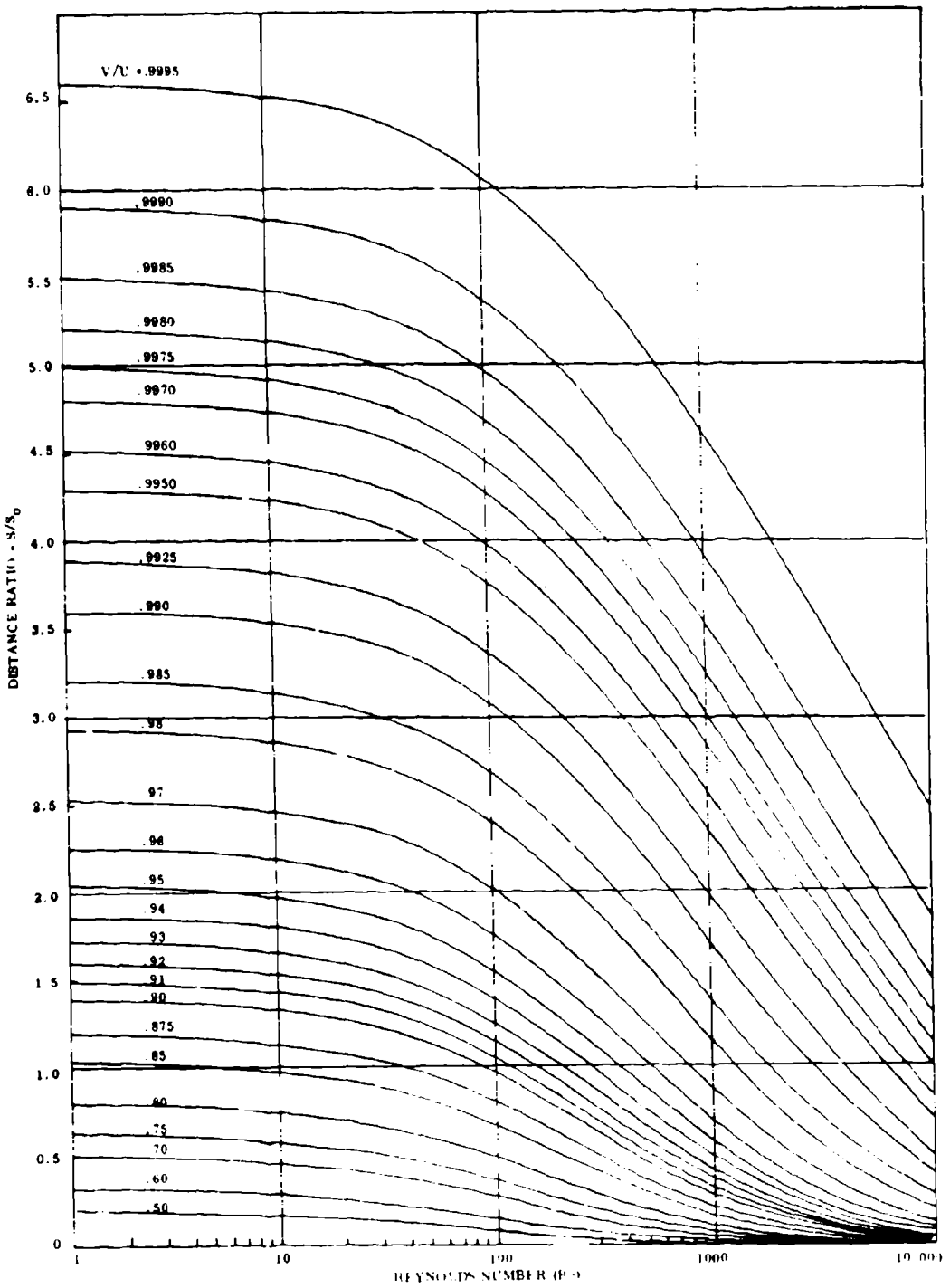

Figure 126. Acceleration Distances Versus Reynolds Number (Based on Particle Velocity (V)/Fluid Velocity (U) Ratio; See Figure 125).

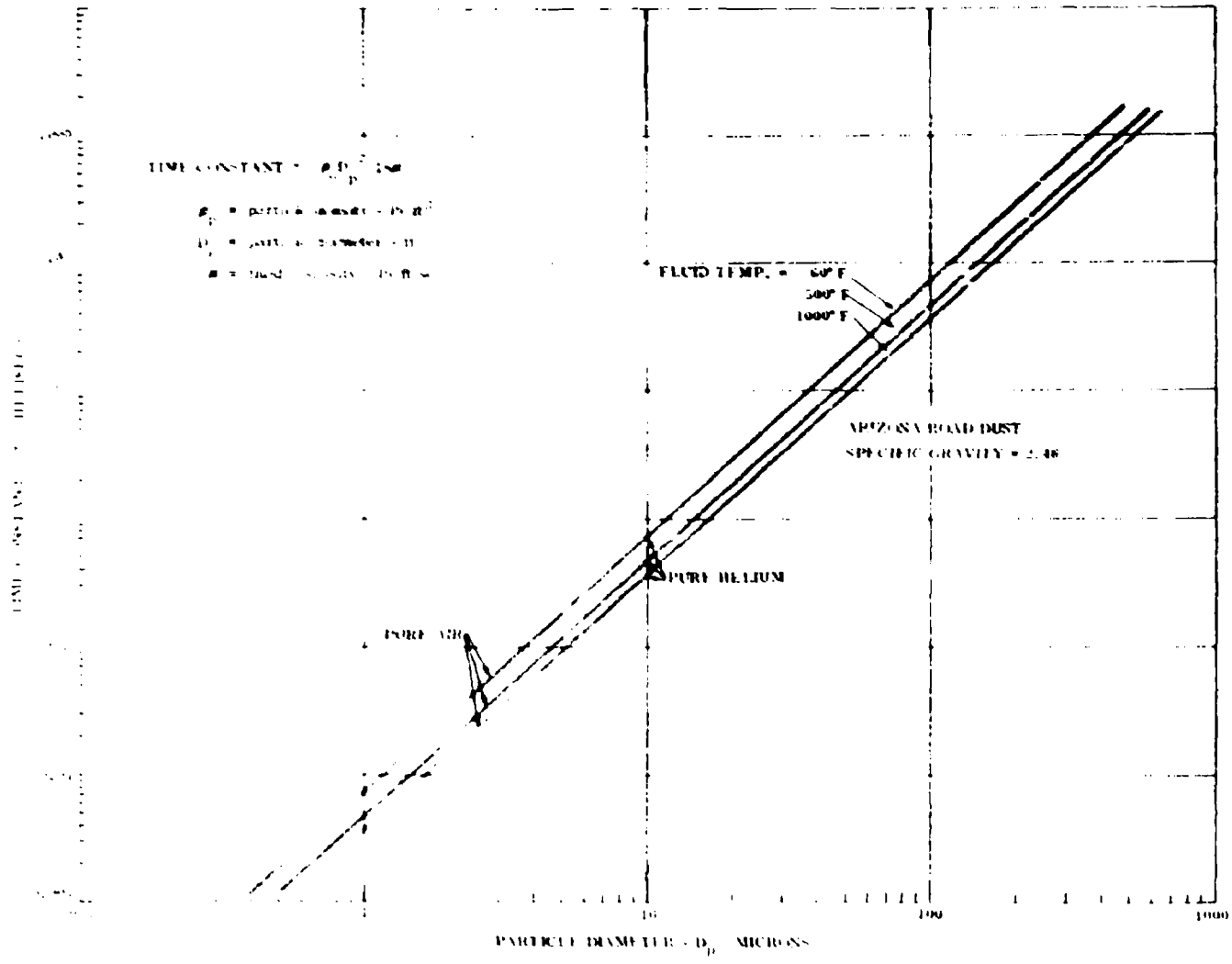

Figure 127. Time Constants For Spherical Particles (Arizona Road Dust) in Viscous Fluids.

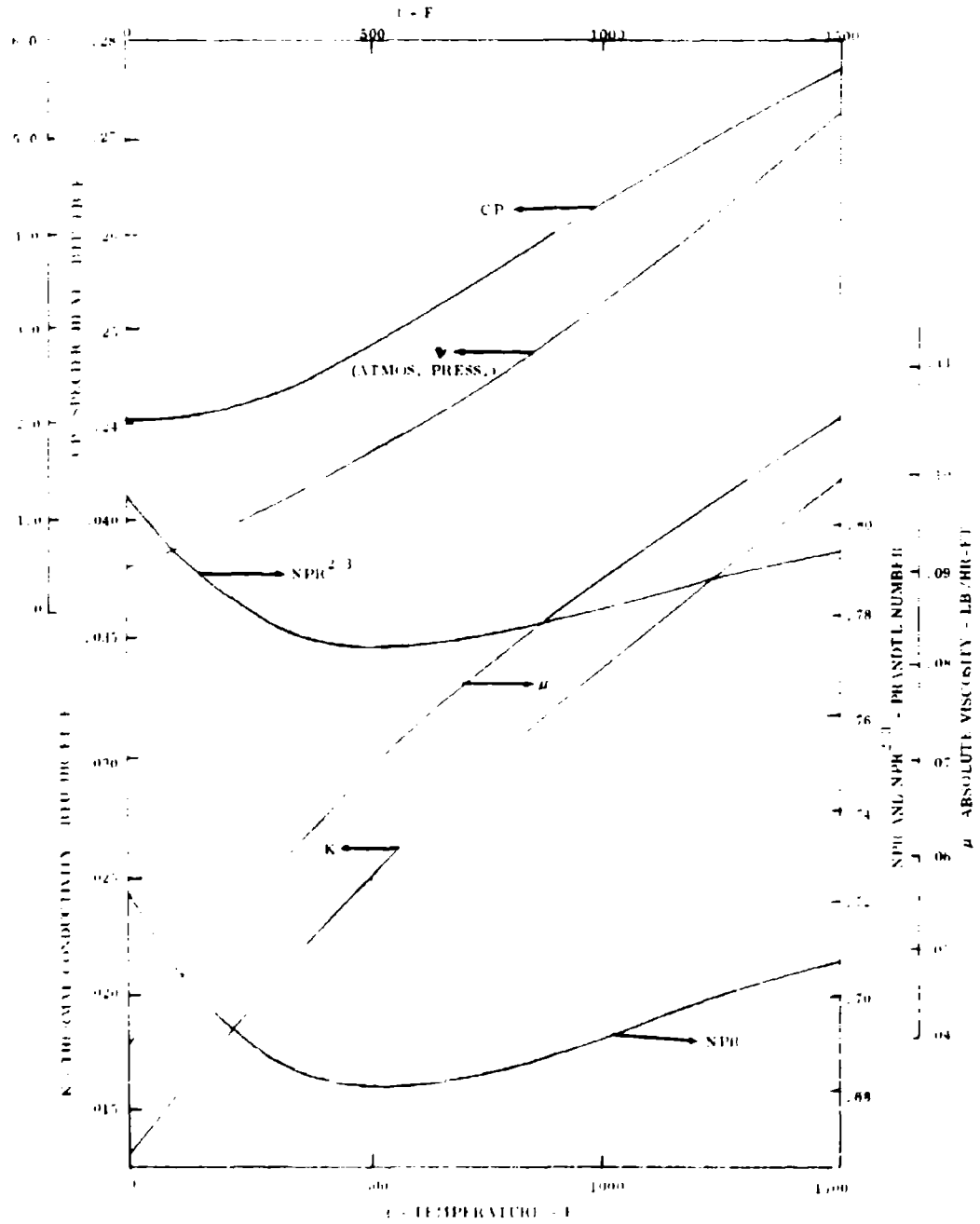

Figure 128. Thermal Properties of Air

$$\therefore \tau = \frac{2.46 \times 62.4 \times \left[.328 \times 10^{-5}\right]^2 \times 3600}{18 \times .0432} D_p^{\,2}$$

$$= .0764564\left(\frac{D_p}{100}\right)^2 \text{ sec, where } D_p \text{ is in microns}$$

Thus, $\tau = 4 \times .0764564$

$= .306$ sec

(or, directly from Figure 127, τ = 310 millisecs)

From Figure 126, with Re_o = 4180, the following table may be constructed.

$\lambda = V/U$	.75	.8	.85	.9	.95	.99	.995	.999	.9995
S/S_o	.020	.025	.05	.09	.20	.82	1.28	2.66	3.31

Now $S_o = U\tau = 1000 \times 306$

$= 306$ feet

S feet	6.12	7.35	15.3	27.55	61.2	251	391	814	1013
V fps	750	800	850	900	950	990	995	999	999.5

Thus, an acceleration length of about 400 feet is required to get a 200μ Arizona Road Dust particle (equivalent Stokes spherical diameter) up to 995 fps in a 1000 fps air-stream. However, a speed of 900 fps can be achieved in a 28-foot length.

As a further example, the air velocity required to accelerate the above particle to 1000 fps in a 20-foot length will be determined.

In this case, $V = 1000$ fps
$S = 20$ ft
$\tau = .306$ sec
$Re_o = 4.18\,U$
$S_o = U\tau = .306\,U$ feet

and U is to be determined.

Choose	$\lambda = V/U$	.75	.8	.90	.875
	$U = V/\lambda = 1000/\lambda$	1333.3	1250	1111.1	1145
	$Re_o = 4.18\ U$	5590	5230	4650	4790
	S/S_o from Figure 126	.020	.025	.13	.06
	$S_o = .306\ U$	408	382.5	340	350
	$S = (S/S_o) \times S_o$	8.16	9.57	44.2	21.0

and the solution is $U \simeq 1150$ fps required.

If this 200μ particle is a member of a group ranging in size from 148μ to 210μ, then the velocity spread in the group can be obtained as follows:

$$U = 1150 \text{ fps}$$

$$S = 20 \text{ ft}$$

$$Re_o = .0209\ U D_p = 24.05\ D_p \quad \left\{ D_p \text{ in microns} \right.$$

$$S_o = U\tau = 1150 \times .0764564 \left(\frac{D_p}{100}\right)^2 \quad \left\{ D_p \text{ in microns} \right.$$

$$= 86.7 \left(\frac{D_p}{100}\right)^2$$

D_p micron	148	160	180	200	210
S_o feet	190	222	281	347	382
Re_o	3560	3845	4330	4810	5050
$S/S_o = 20/S_o$	.105	.090	.0711	.0575	.0523
$\lambda = V/U$ (Figure 126)	.89	.885	.875	.864	.863
V fps	1022	1018	1005	993	991

There will be a velocity spread of ±15.5 fps about a mean value of 1006.5 fps, i.e., ±1.54 percent.

It will be noted that Figure 126 is not particularly accurate for velocity ratios below about 0.9 with Reynolds numbers above 3000, but the "ball park" results obtained indicate the feasibility of using shorter acceleration barrels than was

originally anticipated. Greater accuracy could be obtained by either replotting the curves in this region to a larger scale or by programming equation (50) for a computer with optional procedures according to the problem type. Even if greater numerical accuracy is obtained in this way, the results are still only valid for truly spherical particles under the assumed approximate correlation of drag coefficient against Reynolds number. Figure 124 shows that this correlation is conservative, leading to lower than experimental values for drag coefficient at Reynolds numbers below 2000. Thus, the estimated barrel lengths will be somewhat longer than is physically required. Also, the asphericity of the actual dust particles will likely contribute to higher drag coefficients than for true spheres.

For other particle species (e.g., laterite) and fluids (i.e., He-air mixes), it will be necessary to adjust the values of Re_o, S_o and τ for the new values of particle density and fluid viscosity. A change in dust species alone will affect the results through change in particle density (i.e., only τ and S_o will change). Therefore, since S_o and τ are directly proportional to particle density, acceleration distances (all other things being equal) can be directly scaled using ratios of particle density or specific gravity. For example, the calculation beginning on page 251 will be valid for laterite if all lengths (and times) are multiplied by, say $3.5/2.46 = 1.422$, where 3.5 is the specific gravity of laterite and 2.46 is the specific gravity of Arizona Road Dust.

A change in fluid will change all three of the parameters Re_o, S_o and τ by the change in fluid viscosity and density. In this case, no simple scaling method is available.

APPENDIX II
PROPERTIES OF HELIUM-AIR MIXTURES

INTRODUCTION

The use of helium and helium-air mixtures as particle propellant gases is necessary in this program to avoid compressibility effects at the higher programmed particle velocities (≥1000 fps). Helium and helium-air mixtures possess appreciably higher limiting sonic velocities than air. Therefore, their use as carrier gases will enable attainment of high particle velocities (up to 1100 fps) without problems of choking and shock wave interactions within the acceleration nozzle and at the nozzle exit, such as would occur if transonic or supersonic operation were attempted with air carrier gas. To attain such nonchoked, shock-free operation, it is preferable to adjust the properties of the gas such that the Mach numbers of the flowing gas and/or the relative Mach number of a particle is a maximum of .6 at the target, which should be well below the critical Mach number for incident flow and in the nonchoked regime for passage and nozzle flow. It should be noted that choking and shock effects can occur because of frictional effects in pipe flow. The Mach number in pipe flow with friction always tends toward unity along the Fanno line through the initial condition. The maximum length-to-diameter ratio for a friction factor of .0025 is given below:

Initial Mach Number	0	.25	.50	.75	1.0
L max/Dia	∞	850	110	12	0

This table is extracted from Reference 28, and gives the length-to-diameter ratio at which the flow becomes sonic under the given assumed friction factor and initial Mach number conditions.

As a preliminary to calculating such effects, and to estimate mass flow and particle velocity requirements related to the mixture proportions, it is necessary to investigate the thermodynamic and transport properties of helium-air mixtures. For this purpose, the thermodynamic properties of air are taken from Reference 29. These data are claimed to be accurate to within .5 percent up to 400 psia (27 atmospheres). The thermodynamic properties of helium have been assumed to be (independent of both temperature and pressure):

Specific Heat at Constant Pressure	C_p	1.24 BTU/lb° F
Ratio of Specific Heats	γ	1.667
Molecular Weight	MW	4.0
Gas Constant	R	386.3 ft lb/lb° F

The following equation has been used for absolute viscosity (assumed independent of pressure):

$$\mu = \mu_{392} \left|\frac{590}{198 + t}\right| \left|\frac{t}{392}\right|^{1.5} \text{ lb/hr ft} \qquad (55)$$

where t = static temperature in °R
and μ_{392} = .0346 for air = .0363 for helium

THERMODYNAMIC PROPERTIES

Let X be the fraction of helium by weight in a mixture of air and helium.

Then
$$\frac{1}{(MW)_{mix}} = \frac{(1 - X)}{(MW)_{air}} + \frac{X}{(MW)_{He}}$$

$$= \frac{1 - X}{28.97} + \frac{X}{4.00} \qquad (56)$$

and
$$R_{mix} = \frac{R \text{ universal}}{(MW)_{mix}} = 1545.32 \left|\frac{1 - X}{28.97} + \frac{X}{4.00}\right|$$

$$= R_{air} (1 - X) + R_{He} X$$

$$= 53.34 (1 - X) + 386.3X \qquad (57)$$

also
$$C_{p_{mix}} = C_{p_{air}} (1 - X) + C_{p_{He}} X \qquad (58)$$

now $C_{p_{air}}$ varies with temperature although $C_{p_{He}}$ does not. So in calculating $C_{p_{mix}}$, temperature variation must be included.

Finally,
$$\gamma_{mix} = \left(\frac{1}{1 - \frac{R_{mix}}{J\, C_{p_{mix}}}}\right) \qquad (59)$$

and again temperature variation must be included.

The above thermodynamic properties have been plotted in Figure 129, which

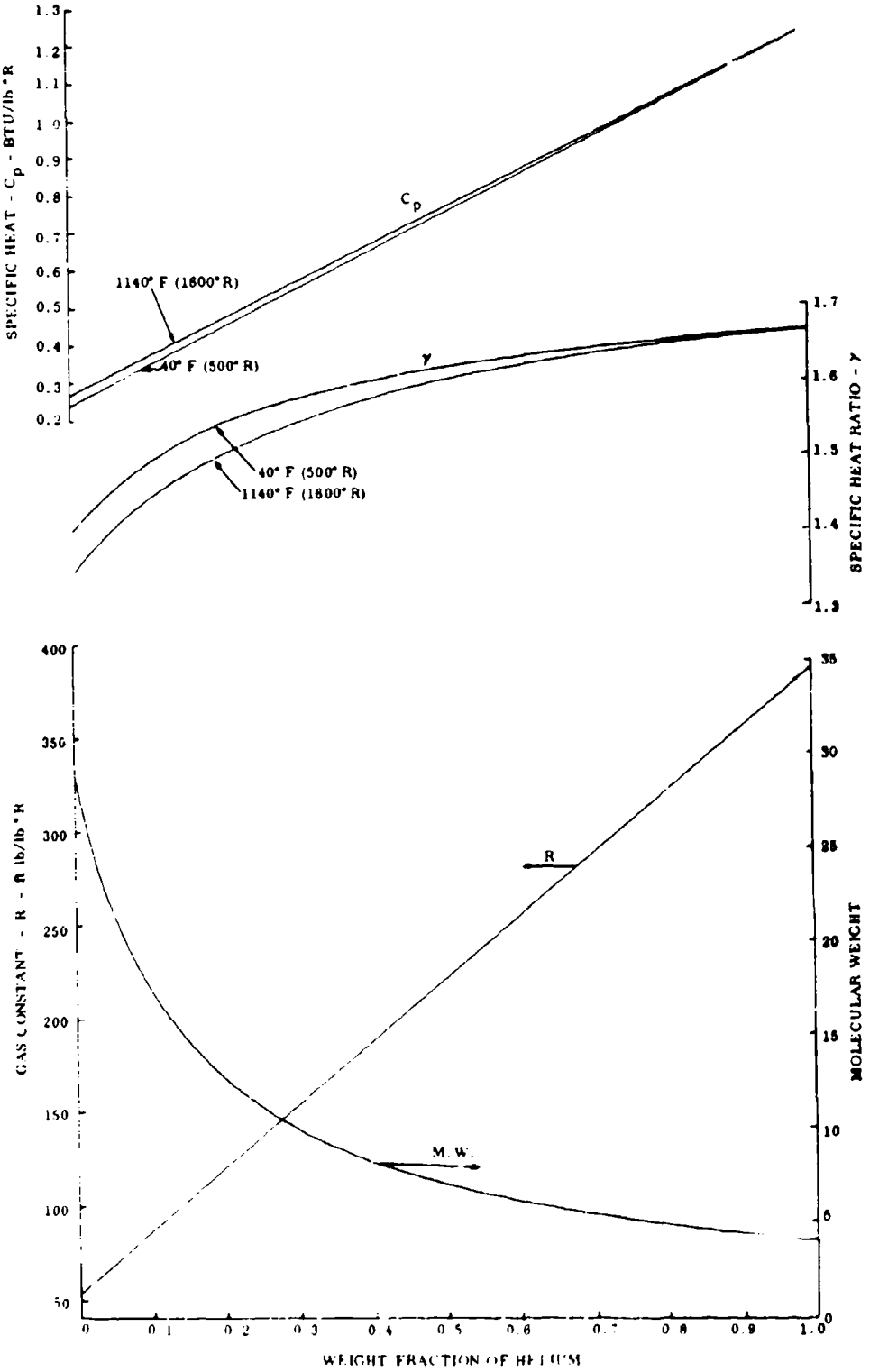

Figure 129. Thermodynamic Properties of Air -Helium Mixtures (at Low Pressures < " Atms.).

illustrates the influence of temperature on $C_{p_{mix}}$ and γ_{mix}.

TRANSPORT PROPERTIES

For adiabatic flow processes, the only transport property of immediate interest is the absolute viscosity. A suitable equation for calculating the viscosity of a gaseous mixture is given in Reference 30 as

$$\mu_{mix} = \frac{\Sigma\, y_i\, \mu_i\, (M_i)^{1/2}}{\Sigma\, y_i\, (M_i)^{1/2}} \tag{60}$$

where y_i = mole fraction of i'th component

M_i = molecular weight of i'th component

μ_i = viscosity of i'th component

If X is the weight fraction of helium in an air-helium mixture, we get

$$\mu_{mix} = \frac{(1 - X)\,\mu_{air} + X\,\mu_{He}\left(\frac{MW_{air}}{MW_{He}}\right)^{1/2}}{(1 - X) + X\left(\frac{MW_{air}}{MW_{He}}\right)^{1/2}}$$

and substituting from equation (55) for μ_{air} and μ_{He}, this results in

$$\mu_{mix} = f(X) \cdot \mu_{air_{392}} \cdot g(t) \tag{61}$$

where

$$f(X) = \frac{1 + 1.823415X}{1 + 1.691189X} \tag{62}$$

$$\mu_{air_{392}} = .0346 \text{ lb/ft hr}$$

$$g(t) = \left|\frac{590}{198 + t}\right| \left|\frac{t}{392}\right|^{3/2} \tag{63}$$

and t is the static temperature in °R. This equation has been evaluated over a suitable range of temperatures with values of X from 0 to 1.0 and plotted on Figure 130.

SONIC VELOCITY OF HELIUM-AIR MIXTURES

The sonic velocity is given by

$$a = \sqrt{g \gamma R t} = \sqrt{g \gamma R T} \left(\frac{t}{T}\right)^{1/2} \qquad (64)$$

where a = sonic velocity, fps

g = gravitational constant = 32.2 fps^2

γ = ratio of specific heats

R = gas constant, ft lb/lb °R

t = static temperature, °R

T = stagnation temperature, °R

At zero Mach number, $t/T = 1.0$

At unity Mach number, $t/T = 2/(\gamma + 1)$

Equation (64) has been evaluated (using the previously generated thermodynamic properties of helium-air mixtures) for both the zero and unity Mach number cases; the results are plotted on Figure 131. This curve shows variation in sonic velocity with temperature and percentage of helium by weight. Two sets of curves are shown labeled zero Mach number and unity Mach number respectively. Although these two sets of curves are true for the sonic velocity at zero and unity stream Mach number, alternative interpretations apply in that at a given sonic velocity, the temperature corresponding to zero Mach number is the stream static temperature and the temperature corresponding to unity Mach number is the relative stagnation temperature for an object moving at relative unity Mach number through the stream. The difference between the two temperatures is the temperature equivalent of the sonic velocity, whether this velocity is due to motion of the gas stream itself or motion of a body relative to the gas stream.

These curves will be useful for judging temperatures and mixture proportions required to suppress undesirable compressibility effects in jet flow and short length pipe flow. For flow in long pipes, however, some Fanno line investigation will be required to determine the influence of frictional effects.

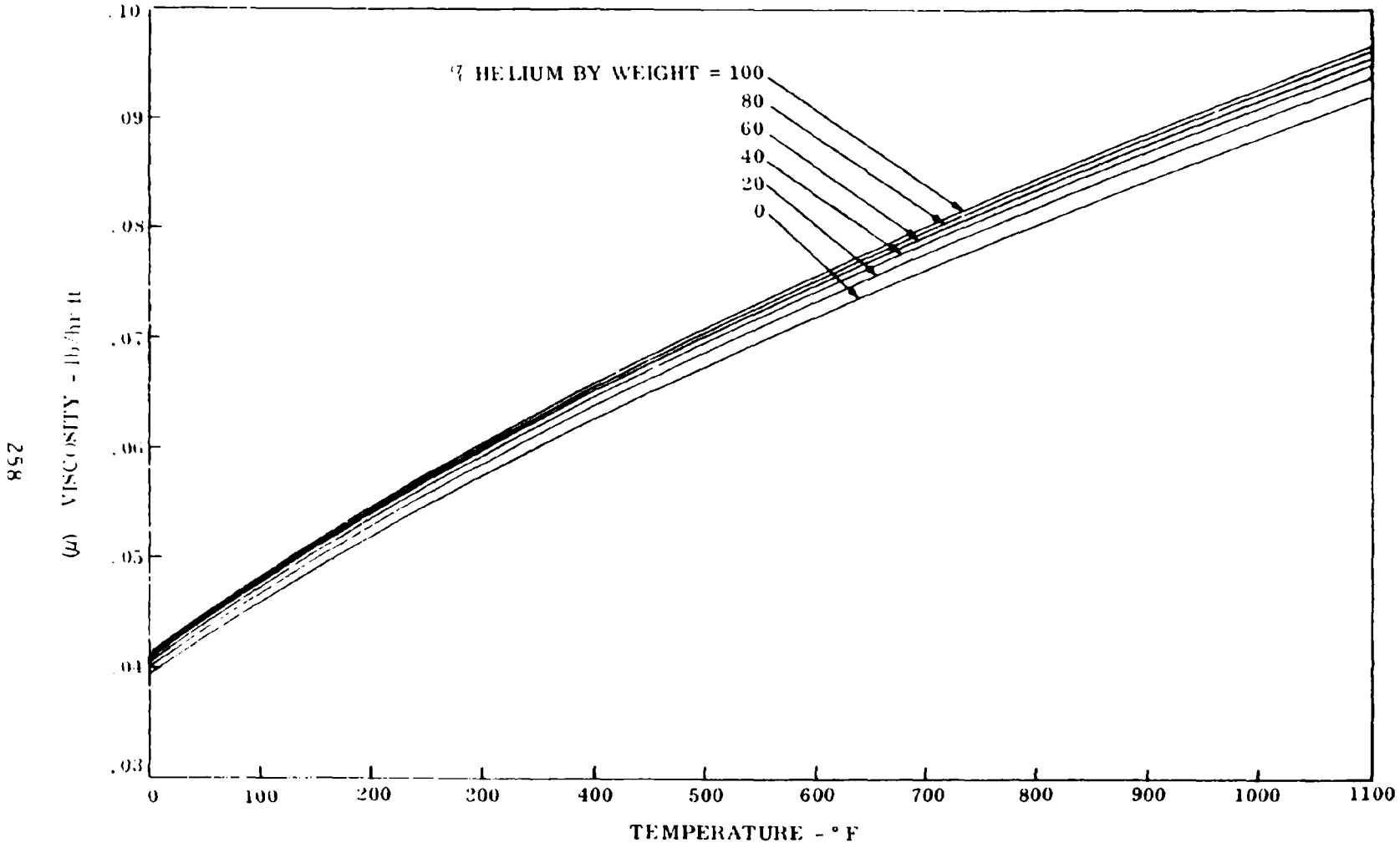

Figure 130. Absolute Viscosity of Air-Helium Mixtures at Low Pressures.

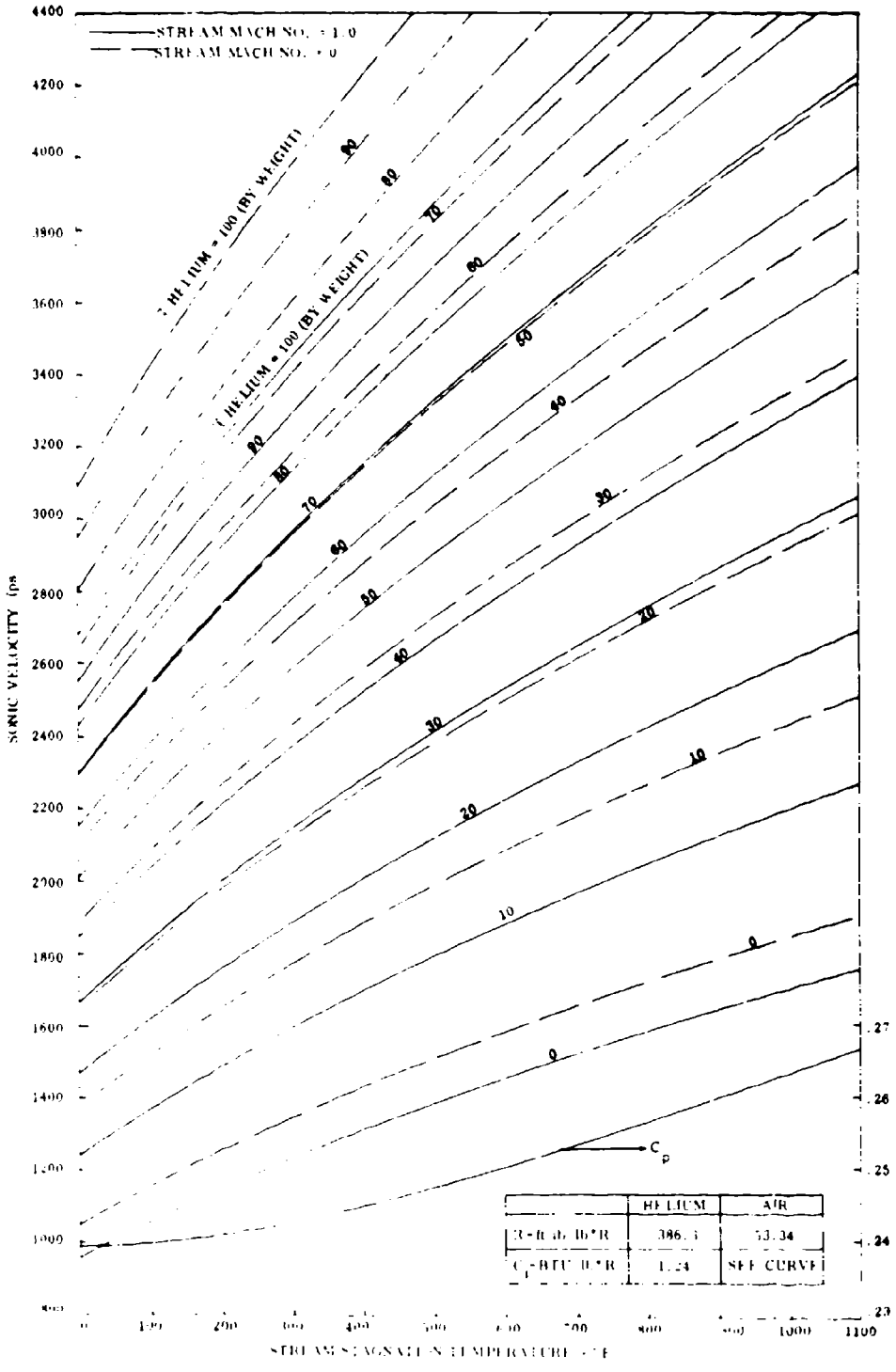

Figure 131. Sonic Velocities of Air-Helium Mixtures at Low Pressures.

APPENDIX III
DESIGN AND OPERATION OF NEW GRAVITY-FEED DUST METER

Fine test dusts have a disturbing tendency to cake together and clog the feeder orifice of rotary-type dust feeders, preventing uniform dust metering and often stopping flow altogether. Inasmuch as a wide variety of dust sizes and types are required on the subject program, it was desired to have a single dust feeder available with sufficient flexibility to meter all test dusts uniformly. The Gianinni rotary-type feeder proved to be incapable of handling the 0-43μ size powders (both Arizona Road Dust and Vietnamese laterite). Consequently, a simple gravity-type feeder was devised at Solar with an adjustable oscillating plunger to provide the necessary agitation of the dust feeding into the orifice to eliminate caking and clogging problems. A schematic of the new feeder showing the relationship of the orifice and the mating plunger is illustrated in Figure 132. The plunger is activated by a variable-speed, electric-motor-controlled cam. The orifice opening (clearance) can be controlled between 0-1/8 inch by adjusting the length of the plunger rod. The rate of plunger oscillation can be controlled continuously between 20-200 cycles per minute.

To ensure a uniform feeding rate during actual erosion testing, preliminary metering runs are made with the prescribed size, type, and charge weight of test dust, to collect and weigh the quantities of dust metered out each minute of a simulated test run. The cam speeds and plunger-orifice clearances are varied experimentally during each run until a uniform metering rate is obtained. A distinct advantage of the new meter is that the quantity of test dust is preweighed for each test, eliminating possible error in the amount of dust ingested from test to test.

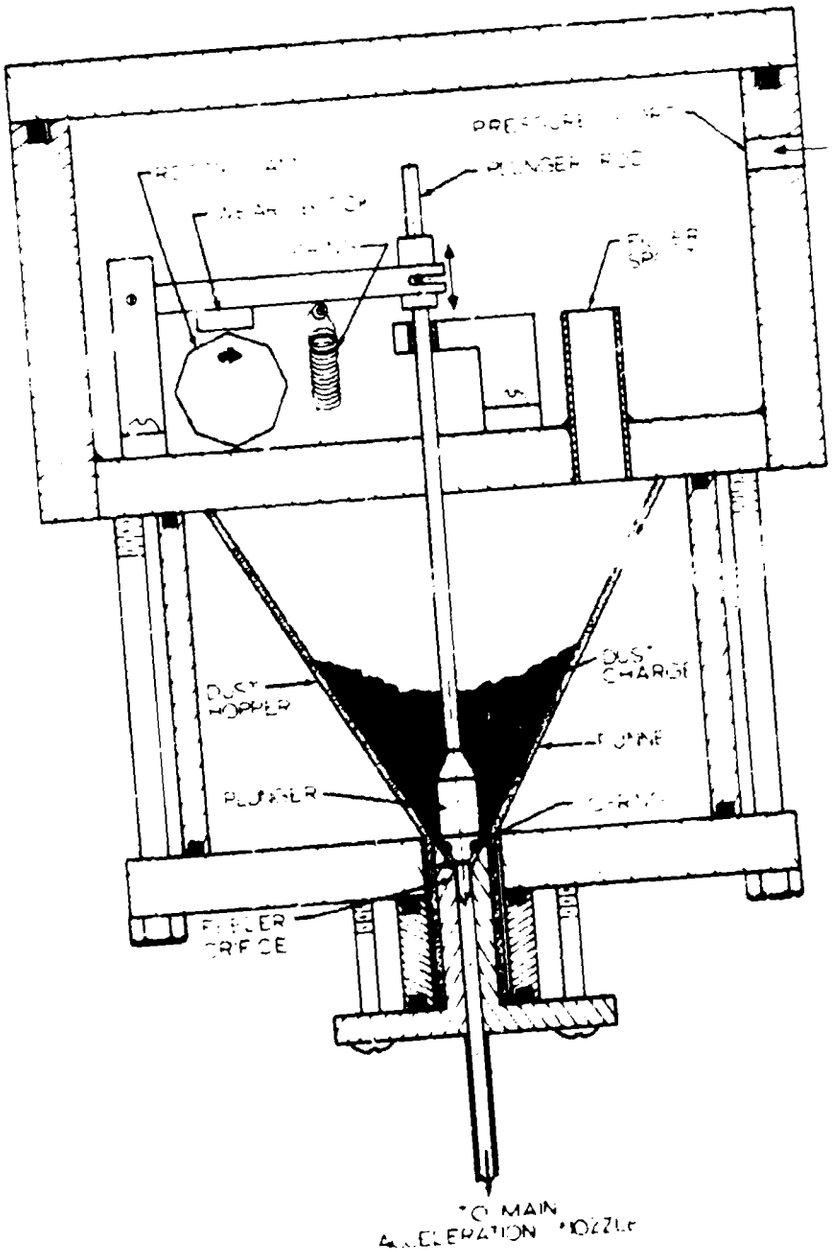

Figure 132. Sketch of Gravity Feed Meter.

APPENDIX IV

PETROGRAPHIC ANALYSIS OF VIETNAM DUST SAMPLES

(MICHIGAN TECHNOLOGICAL UNIVERSITY)
HOUGHTON, MICHIGAN

Three samples of dust from Vietnam were submitted for cursory petrographic analyses. The unopened samples were sterilized in an autoclave at 125° C and 15 pounds pressure for 15 minutes to destroy viral and bacterial contaminants.

Photomicrographs were made of each sample, and for ease of comparison were taken under the same set of conditions: petrographic microscope; 125 magnifications; plane polarized light; refractive index 1.652. For further comparison, a photomicrograph of -100/+200 mesh Arizona Road Dust (Figure 133) was also taken. The results of petrographic examination are as follows:

SAMPLE 1 (AN KHE)

This sample (Figure 134) is gray colored and appears to have resulted from the disintegration, partially by mechanical action, of a granitic rock. About half of the sample is coarser than 0.5 mm. Quartz is the predominant mineral and constitutes about 75 percent of the sample. It is slightly iron stained, has an irregular shape in the coarse fraction, but is sharp and angular, as if crushed, in the fine fraction. Muscovite mica, which is most abundant in this sample, and the feldspars each constitute about 10-12 percent of total mineral content. Hematite, magnetite, hornblende and euhedral apatite and zircon are present in minor amounts.

SAMPLE 2 (PLEIKU)

This sample (Figure 135) is brown and appears to be 80-90 percent clay. A small portion was treated to break up the clay aggregates and free the included mineral grains. The clay particles cannot be resolved with light microscopy. The included grains are less than 75 microns in size and are predominantly quartz and feldspar with magnetite, hematite, mica, apatite, and zircon. These grains (except the euhedral apatite and zircon) are fragments with sharp angular surfaces.

SAMPLE 3 (CAM RANH BAY)

This sample (Figure 136) is tan, and of the three, shows the greatest range of particle size. Composite particles (those composed of more than one mineral) are as large as 7 mm in diameter. The predominant minerals are quartz and feldspar; they are present in about equal proportions and constitute about 95 percent of the

Magnification: 125X
Refractive Index: 1.652

The Sample is Predominantly Quartz and Feldspar.

Figure 133. Arizona Road Dust (-100/+200 Mesh Fraction)

Magnification: 125X
Refractive Index: 1.652

Grains Are Mostly Quartz (Sharp and Angular) and Feldspar (Not Completely Transparent). Round Grain With High Relief at Top Right is Zircon.

Figure 134. Sample 1; Dust From An Khe

Magnification: 125X
Refractive Index: 1.652

Sharp Angular Grains of Quartz and Euhedral Apatite are Surrounded by Aggregates of Clay (Black).

Figure 135. Sample 2; Dust From Pleiku

Magnification: 125X
Refractive Index: 1.652

Grains are Mostly Irregular Angular Quartz and Feldspar. A Crystal of Apatite is Seen at Top.

Figure 136. Sample 3; Dust From Cam Ranh Bay

sample. Other minerals include fragments of magnetite, hematite, goethite, hornblende, garnet, mica, marine shell, clay minerals, and crystals of apatite and zircon. This type of mineral assemblage, with the exception of the marine shell, is typical of a disintegrated granite. Very few grains are rounded; most of them retain their irregular angular form.

APPENDIX V
THE PROBABILITY OF INTERPARTICLE COLLISIONS AT THE EROSION INTERFACE

If interparticle collisions at the erosion interface are responsible for a significant and progressive reduction in erosion factor (ϵ) with increasing dust concentrations, then the following two assumptions can be made:

1. Erosion factor (ϵ) and erosion efficiency are reduced by incoming particles colliding with rebounding particles and being deflected.

2. Interparticle collisions must have a reasonable degree of probability (e.g., $\geq 5\%$) for at least the higher dust concentrations of interest, which (probability) increases with increasing dust concentration.

The maximum probability for interparticle collision in a typical Series I erosion test should exist under the following test conditions:

- The heaviest dust concentration, 160 mg/ft^3 (test dust: 50μ Al_2O_3).
- The impingement angle of 90 degrees, to obtain the smallest target impingement area (area = πR^2, where R is the radius of the impingement circle; 0.1875 in. or 4.77 x 10$^3\mu$).
- Maximum incoming particle velocity of 600 fps.

The greatest probability of a rebounding particle colliding with an incoming particle should exist for the following specific events:

- The rebounding particle initially strikes the center of the target impingement area and moves (rebounds) out at a low grazing angle in any direction. The low grazing angle is compatible with the suppressing influence of the high-velocity gas jet.
- Due to a ductile, highly inelastic impact with the target, the rebounding particle slows to about 5 percent of its preimpact velocity (30 fps).

The area on the impingement circle swept by the rebounding particle (i.e., the area in which potential collisions with incoming particles must occur) is approximately 4r (R), where r is the particle radius (r = 25μ). This swept area (4r units wide and R units long) can be called the "collision strip" for convenience. The time, τ,

required for the rebounding particle to traverse the collision strip is R/v, where v = the velocity of the rebounding particle (30 fps or 360 ips).

$$\therefore \tau = .1875 \text{ in.}/360 \text{ ips} = 520 \text{ microseconds}$$

The effective number of 50μ Al_2O_3 particles in the carrier-gas jet at a dust concentration of 160 mg/ft^3 is equivalent to 2.5×10^5 particles per cubic foot. This computes out to 61.5 particles impacting the target every 520 microseconds (τ). On the collision strip, this number of impacts (Y) dwindles to

$$Y = 61.5 \times \frac{4rR}{\pi R^2} = \frac{4r}{\pi R} \times 61.5 = 0.41 \text{ particle (average)},$$

assuming a uniform or symmetrical pattern of impacts within the target circle and a randomly oriented collision strip or radial element.

The target area assigned to each impacting particle (100% probability of striking) can be expressed as $\pi R^2/61.5$. Consequently, the approximate probability of a single incoming particle impacting the collision strip during time interval, τ, is proportional to the ratio of these two areas; i.e.,

$$\frac{4rR \times 100}{\pi R^2/61.5} = 41.0\%$$

The more pertinent (coincidental) probability, P_1, of the incoming particle colliding in the strip and with the (single, specific) rebounding particle as well is then approximated by

$$P_1 \cong 0.41 \times \frac{2r}{R} \times 100 = 0.43\%,$$

assuming little or no interference from other rebounding particles.

P_1 is the probability of a single rebounding particle colliding with any available incoming particle during the traverse time, τ. In the following example, the approximate probability, P_2, of a single incoming particle colliding with any available rebounding particle on the impingement area is calculated. The total number of available rebounding particles is the maximum number that can coexist on the impingement area during the traverse time interval, τ = 520 microseconds. Over the time interval, τ, 61.5 particle impacts occur. For the maximum number of rebounding particles to coexist in the target area (and to maximize the probability of interparticle collision, P_2), assume that all (61.5) incoming particles

strike the target center point and rebound radially in random directions. Assume also that one particle strikes every 520 microseconds/61.5 = 8.5 microseconds.

The probability, P_2, that the next incoming single particle (the 62nd or 63rd) will strike one of the rebounding particles is approximated by the ratio of the sum of the projected areas of the rebounding particles over the total available impingement area:

$$P_2 \cong \frac{61.5 \times \pi r^2}{\pi R^2} \times 100 = 0.17\%$$

The very low probability of interparticle collisions indicates that such collisions must play an extremely minor role in the erosion mechanism, at this and all lower dust concentrations.

APPENDIX VI

ENERGY CONSIDERATIONS WITH REGARD TO EROSION MECHANISM

The principal erosion mechanism, based upon prior structure studies, is assumed to be the splattering of liquid target metal (droplets), formed in the impact craters of corner-oriented particle collisions. To test this assumption and show plausibility of the concept, computations were made to determine whether the kinetic energy possessed by a single incoming dust particle is sufficient (on total conversion) to heat and melt the average quantity of target material eroded per impact. Conditions of the hypothetical particle and target selected are similar to those employed in the prior structures studies:

Particle: 60μ SiO_2 particle (cube), travelling at 650 fps (u)
Mass: 4.8×10^{-7} gm (M)
Kinetic Energy = $1/2\ Mu^2 = 95$ ergs $\cong 2.3 \times 10^{-6}$ calories

Target: Pure Iron (m.p. $\approx 1500°$ C)
Average Mass of Target Removed per Impact $\cong 1.0 \times 10^{-9}$ gm (Erosion Product)

(a) Energy Required to Heat Erosion Product to Its Melting Point $\cong 2.7 \times 10^{-7}$ calories

(b) Energy Required to Melt Erosion Product $\cong 0.7 \times 10^{-7}$ calories (Heat of Fusion)

(c) Total Energy Requirement for Melting (a + b) $\cong 3.4 \times 10^{-7}$ calories

It is apparent that the particle's kinetic energy is ≈ 7 times greater than the energy requirement for heating and melting of the erosion product. This energy relationship for a typical erosion situation supports the concept of liquid-metal splattering.

DISTRIBUTION

Army Materiel Command	2
Army Aviation Systems Command	9
Director of Defense Research and Engineering	2
Chief of R&D, DA	4
Army R&D Group, Europe	2
Army Air Mobility Research and Development Complex	2
Army Aviation Materiel Laboratories	14
Army Aviation Systems Test Activity	2
Army Ballistic Research Laboratories	1
Army Aeronautical Research Laboratory, Ames	2
Army Aeronautical Research Laboratory, Langley	2
Army Aeronautical Research Laboratory, Lewis	2
Army Research Office-Durham	1
Army Materials and Mechanics Research Center	6
Plastics Technical Evaluation Center	1
Army Test and Evaluation Command	1
Army Materiel Systems Analysis Agency	1
Army Combat Developments Command Experimentation Command	1
Army Combat Developments Command Aviation Agency	3
Army Combat Developments Command Transportation Agency	1
Army Ordnance Weapons Command	1
Ordnance Special Weapons-Ammunitions Command	1
Army Medical R&D Command	1
Army Advanced Materiel Concepts Agency	1
Army Picatinny Arsenal	1
Army Frankford Arsenal	1
Army Aviation School	1
Assistant Chief of Staff for Force Development, DA	1
Army Aviation Test Board	2
Army Board for Aviation Accident Research	1
1st Cavalry Division (Airmobile)	1
Air Force Office of Scientific Research	1
HQ, USAF, Washington, DC	1
Air Force Flight Test Center, Edwards AFB	1
Army Field Office, AFSC, Andrews AFB	1
Air Force Materials Laboratory, Wright-Patterson AFB	3
Air Force Flight Dynamics Laboratory, Wright-Patterson AFB	1
Naval Air Systems Command	8
Naval Research Laboratory	1
Naval Air Station, Norfolk	1
Naval Air Test Center, Patuxent River	1
Naval Air Propulsion Test Center, Philadelphia	1
Naval Weapons Laboratory, Dahlgren	1

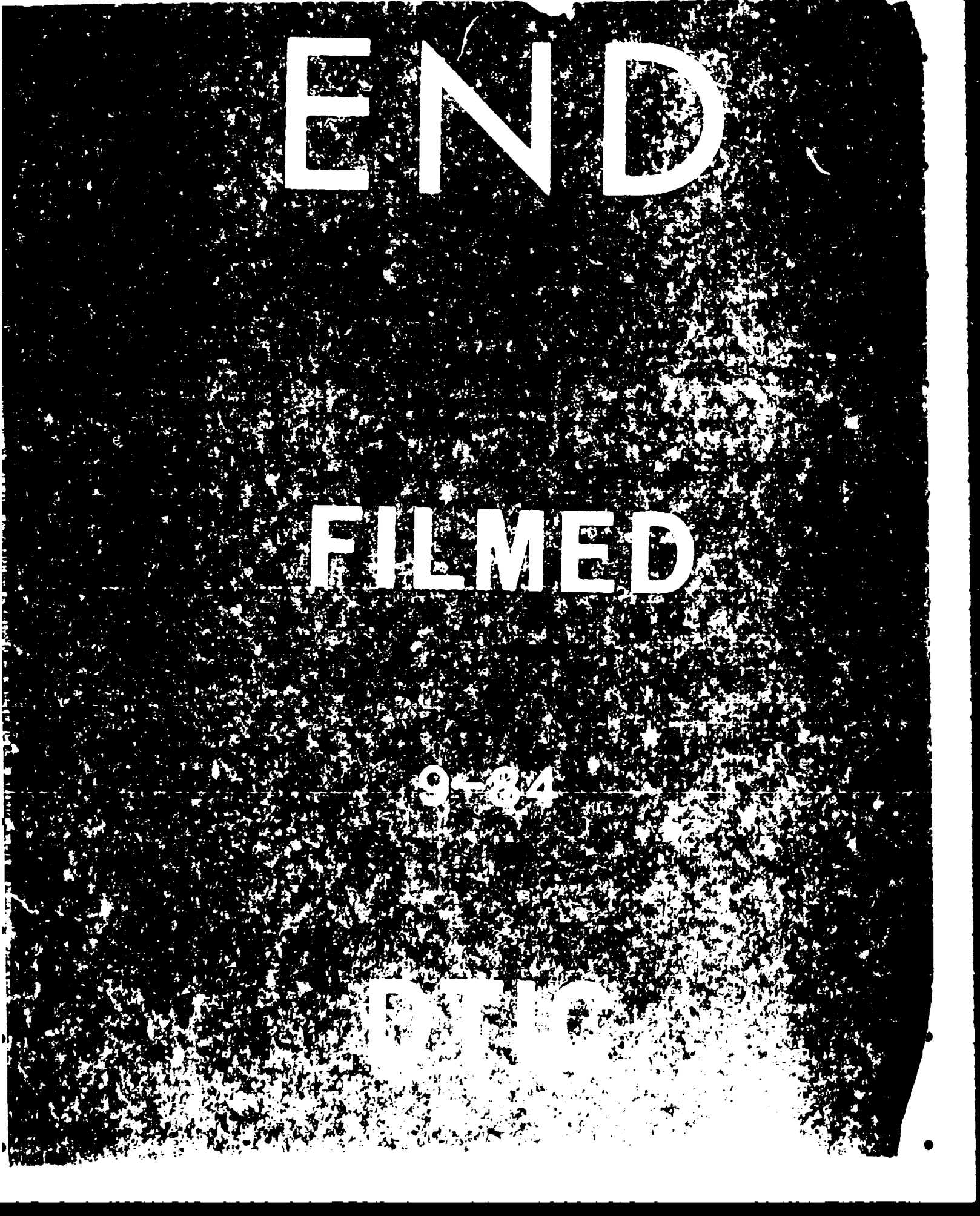
END
FILMED
9-84
DTIC